https://ntrs.nasa.gov/search.jsp?R=19970025057 2020-06-16T02:19:09+00:00Z

FIBER-OPTIC TEMPERATURE SENSOR

USING

A THIN-FILM FABRY-PEROT INTERFEROMETER

by

GLENN BEHEIM

Submitted in partial fulfillment of the requirements

for the degree of Doctor of Philosophy

Thesis Adviser: Professor Massood Tabib-Azar

Department of Electrical Engineering and Applied Physics

CASE WESTERN RESERVE UNIVERSITY

FIBER-OPTIC TEMPERATURE SENSOR USING A THIN-FILM FABRY-PEROT INTERFEROMETER

Abstract

by

Glenn Beheim

A fiber-optic temperature sensor was developed that is rugged, compact, stable, and can be inexpensively fabricated. This thin-film interferometric temperature sensor was shown to be capable of providing a ±2 °C accuracy over the range of -55 to 275 °C, throughout a 5000 hr operating life.

A temperature-sensitive thin-film Fabry-Perot interferometer can be deposited directly onto the end of a multimode optical fiber. This batch-fabricatable sensor can be manufactured at a much lower cost than can a presently available sensor, which requires the mechanical attachment of a Fabry-Perot interferometer to a fiber. The principal disadvantage of the thin-film sensor is its inherent instability, due to the low processing temperatures that must be used to prevent degradation of the optical fiber's buffer coating.

The design of the stable thin-film temperature sensor considered the potential sources of both short and long term drifts. The temperature-sensitive Fabry-Perot interferometer was a silicon film with a thickness of $\sim 2\ \mu m$. A laser-annealing process was developed which crystallized the silicon film without damaging the optical fiber. The silicon film was encapsulated with a thin layer of Si_3N_4 overcoated with aluminum. Crystallization of the silicon and its encapsulation with a highly stable, impermeable thin-film structure were essential steps in producing a sensor with the required long-term stability.

ACKNOWLEDGEMENTS

I would like to thank my dissertation adviser Professor Massood Tabib-Azar for his guidance and encouragement. I was greatly assisted by my co-workers at NASA Lewis Research Center in all aspects of this research project. Those individuals whose help was especially significant are listed below, following the area of their contribution:

(a) Thin-film deposition--Dak Knight, Carl Salupo,

(b) Laser annealing--Jorge Sotomayor, Ken Weiland,

(c) Sensor testing--John Heisler, Jorge Sotomayor,

(d) Data acquisition--Joseph Flatico,

(e) Optical analysis of thin films--John Heisler, Margaret Tuma,

(f) Auger and XPS analysis--Don Wheeler, Liang-Yu Chen, Jeremy Petit,

(g) SEM--Drago Androjna.

I would also like to express my appreciation for the support provided by my supervisors at NASA Lewis, especially Gary Seng, Bill Nieberding, Norm Wenger, Dan Williams, and Walt Merrill.

TABLE OF CONTENTS

Title page i

Abstract by Glenn Beheim ii

Acknowledgements iv

Table of Contents v

List of Figures x

List of Tables xxi

1. INTRODUCTION 1

    1.1 Fiber-Optic Temperature Sensors for Aircraft 1

    1.2 Fabry-Perot Temperature Sensor 3

    1.3 References 5

2. REVIEW OF FIBER-OPTIC TEMPERATURE SENSOR 7

    2.1 Introduction 7

    2.2 Optically Emissive, Thermally Powered Sensors 10

    2.3 Optically Emissive, Optically Powered Sensors 14

    2.4 Intensity-Modulating (Non-Emissive) Sensors 18

    2.5 Distributed Sensors 32

    2.6 Concluding Remarks 35

2.7 References 37

3. REVIEW OF FABRY-PEROT TEMPERATURE SENSORS 55

3.1 Introduction 55

3.2 Advantages of Wavelength-Encoded Temperature Measurements 56

3.3 Wavelength-Encoded Temperature Measurements Using Fabry-Perot Interferometry 57

3.4 Concluding Remarks 67

3.5 References 68

4. PRELIMINARY DESIGN OF A FABRY-PEROT TEMPERATURE SENSOR 73

4.1 Introduction 73

4.2 Optical Fiber System 74

4.3 Ideal Fabry-Perot Temperature Sensor 78

4.4 Selection of Temperature-Sensitive Material 83

4.5 Determination of the Fabry-Perot Temperature Sensor's Thickness 90

4.6 Sensitivity to Pressure 98

4.7 Conclusion 99

4.8 References 100

5. DESIGN OF ENCAPSULATING STRUCTURE 105

5.1 Encapsulation Requirements 105

5.2 Effects of Silicon Oxidation 107

5.3 Encapsulant Design 114

5.4 Effects of Si_3N_4 Oxidation 122

5.5 Effects of Temperature on Si_3N_4 126

5.6 Concluding Remarks 128

5.7 References 129

6. SILICON DEPOSITION AND ANNEALING 141

6.1 Introduction 141

6.2 Optimization of Silicon Deposition Process 148

6.3 Deposition of Silicon on Fibers 155

6.4 Spectral Reflectometry 157

6.5 Laser Annealing 163

6.6 Analysis of Annealed Silicon Films 170

6.7 Conclusion 181

6.8 References 182

7. TEMPERATURE SENSOR ENCAPSULATION 216

7.1 Introduction 216

7.2 Silicon Nitride Deposition Methods 216

7.3 Optimization of Si_3N_4 Deposition Process 223

7.4 Effect of an Oxidizing Environment on Si_3N_4 Encapsulant 237

7.5 Characteristics of the Aluminum Encapsulating Layer 254

7.6 Conclusion 259

7.7 References 259

8. TEMPERATURE SENSOR CHARACTERIZATION 279

8.1 Introduction 279

8.2 Sensor Fabrication and Initial Characterization 279

8.3 Sensor Calibration 286

8.4 Effects of Connector Remating 288

8.5 Effects of Wavelength-Dependent Changes in the Transmissivity of the Fiber Link 289

8.6 Effects of Fiber Bending 290

8.7 Long-Term Stability 292

8.8 Conclusion 296

8.9 References 297

9. CONCLUSION 318

10. BIBLIOGRAPHY 320

11. APPENDIX ON OPTICAL THEORY 337

11.1 Plane Wave Propagation in Homogeneous Media 337

11.2 Reflection and Transmission
at an Interface Between Two Materials 341

11.3 Reflection From a Single Layer 344

11.4 Reflection From a Multilayer Stack of Films 350

11.5 Basic Ellipsometric Relations 356

11.6 Effective Medium Theory 357

11.7 References 361

LIST OF FIGURES

Figure 2.1 Fiber-optic thermometer using a thermally emissive sensor.

Figure 2.2 Optical spectra $i_E(\lambda)$ radiated from a black body with an area $a = 1$ cm^2, for temperatures between 1000 K and 2000 K.

Figure 2.3 Schematic of optically linked electronic temperature sensor showing thermocouple (TC), photovoltaic array (PVA), voltage regulator (V Reg.), long-wavelength pass filters (LWP), photodiode (PD), lenses (L), and laser diode (LD).

Figure 2.4 Temperature dependence of the fluorescence decay time of chromium-activated magnesium fluorogermanate.

Figure 2.5 Excitation spectrum and fluorescence spectra of AlGaAs sensor at different temperatures.

Figure 2.6 GaAs absorption-edge fiber-optic thermometer.

Figure 2.7 Transmissivities $H_S(\lambda)$ at different temperatures of Nd-doped fiber.

Figure 2.8 Integrated-optic interferometer for temperature measurements.

Figure 2.9 Birefringent-crystal fiber-optic temperature sensor.

Figure 2.10 Fabry-Perot interferometer comprised of a material of thickness L and refractive index n_1 surrounded by a material with an index n_0.

Figure 2.11 Reflectivities R_F, as functions of one-way phase-shift Φ, for Fabry-Perot interferometers having different mirror reflectivities R.

Figure 2.12 Input and output spectra of silicon Fabry-Perot temperature sensor at 25 and 125 °C, using an LED source.

Figure 2.13 Fiber-optic temperature sensor using a thin-film Fabry-Perot interferometer.

Figure 2.14 Optical spectra transmitted and reflected by a fiber Bragg grating, using a white light source.

Figure 4.1 Schematic of fiber-optic thermometer using a Fabry-Perot sensor.

Figure 4.2 Thin-film Fabry-Perot interferometer.

Figure 4.3 Maximum phase sensitivity of Fabry-Perot interferometer $| dR_F/d\Phi |_{MAX}$ as a function of mirror reflectivity R.

Figure 5.1 Calculated oxide thickness L_{ox} as a function of time, for silicon in dry O_2 at 300 °C.

Figure 5.2 Dual-cavity thin-film Fabry-Perot interferometer.

Figure 5.3 Calculated reflectivities $R_{123}(\lambda)$ of Si_3N_4-coated aluminum, in a silicon ambient, for different Si_3N_4 thicknesses L_2, where n and k of all the materials are fixed at the values for $\lambda = 830$ nm.

Figure 5.4 Refractive index n and extinction coefficient k of single-crystal silicon as functions of wavelength.

Figure 5.5 Refractive indexes of Si_3N_4 and SiO_2 as functions of wavelength.

Figure 5.6 Refractive index n and extinction coefficient k of aluminum as functions of wavelength.

Figure 5.7 Calculated reflectivities $R_{123}(\lambda)$ of Si_3N_4-coated aluminum, in a silicon ambient, for different Si_3N_4 thicknesses L_2, where the λ-dependent n and k values have been used.

Figure 5.8 Calculated phase changes ϕ_{123} on reflection from Si_3N_4-coated aluminum, in a silicon ambient, as functions of wavelength, for different Si_3N_4 thicknesses L_2, where the λ-dependent n and k values have been used.

Figure 5.9 Reflectivities $R_F(\lambda)$ of Fabry-Perot interferometers using 1.6-μm-thick silicon layers, for silicon embedded in SiO_2 and for silicon encapsulated with 88-nm-thick Si_3N_4 overcoated with aluminum.

Figure 6.1 Imaginary part of the pseudo-dielectric function $<\varepsilon_2(E)>$, where E is the photon energy, for silicon sputter-deposited at different pressures.

Figure 6.2 Measured and calculated $\psi(\lambda)$ for silicon sputter-deposited at 4.0 mTorr pressure and 400-W RF power.

Figure 6.3 Measured and calculated $\Delta(\lambda)$ for silicon sputter-deposited at 4.0 mTorr pressure and 400-W RF power.

Figure 6.4 Measured $n(\lambda)$ and $k(\lambda)$ for sputter-deposited silicon films.

Figure 6.5 Real part of the dielectric function $\varepsilon_1(E)$ for sputter-deposited a-Si, evaporated a-Si and LPCVD a-Si.

Figure 6.6 Imaginary part of the dielectric function $\varepsilon_2(E)$ for sputter-deposited a-Si, evaporated a-Si and LPCVD a-Si.

Figure 6.7 Fiber holder for sputter deposition.

Figure 6.8 Schematic of fiber-coupled spectrometer showing microscope objectives (MO), fibers (F) and coupler pigtails (CP).

Figure 6.9 Transmissivities of 1.5-m fiber and connector $H_{F1}C_{F1\text{-}F2}(\lambda)$ showing effects of connector remating.

Figure 6.10 Transmissivities of fiber and connector $H_{F1}C_{F1\text{-}F2}(\lambda)$ for 1.5-m and 10-m long fibers.

Figure 6.11 Round-trip transmissivity $H_{CP}(\lambda)$ of coupler and mechanically aligned splice.

Figure 6.12 Measured and calculated reflectivity $R_f(\lambda)$ of silicon film sputter-deposited on fiber end (sensor 294).

Figure 6.13 Nomarski-microscope image of silicon film sputter-deposited on fiber end.

Figure 6.14 Schematic of laser-annealing apparatus.

Figure 6.15 Silicon film annealed for 2 s with 1-W laser beam focused to a 66-μm-diameter spot.

Figure 6.16 Silicon film annealed for 10 s with 1-W laser beam focused to a 66-μm-diameter spot.

Figure 6.17 Silicon film annealed for 0.5 s with 2-W laser beam focused to a 66-μm-diameter spot.

Figure 6.18 Silicon film annealed for 2 s with 1-W laser beam focused to a 378-μm-diameter spot.

Figure 6.19 Reflectivities $R_f(\lambda)$ of silicon films annealed for 0.5 s and 2 s. For the case of the 0.5 s anneal, the R_f values have been multiplied by 0.58.

Figure 6.20 Measured and calculated $\psi(\lambda)$ for silicon rapid thermal annealed at 900 °C. Here, an EMA of a-Si, c-Si and void was used to model the film.

Figure 6.21 Measured and calculated $\psi(\lambda)$ of RTA silicon, for $\lambda < 500$ nm.

Figure 6.22 Measured and calculated $\Delta(\lambda)$ of RTA silicon, for $\lambda < 500$ nm.

Figure 6.23 Measured and calculated $\psi(\lambda)$ of RTA silicon, for $\lambda > 500$ nm.

Figure 6.24 Measured and calculated $\Delta(\lambda)$ of RTA silicon, for $\lambda > 500$ nm.

Figure 6.25 Calculated $n(\lambda)$ and $k(\lambda)$ for silicon rapid thermal annealed at 900 °C.

Figure 6.26 Real part of the dielectric function $\varepsilon_1(E)$, where E is the photon energy, for sputter-deposited a-Si, RTA poly-Si and c-Si.

Figure 6.27 Imaginary part of the dielectric function $\varepsilon_2(E)$, where E is the photon energy, for sputter-deposited a-Si, RTA poly-Si and c-Si.

Figure 6.28 Measured and calculated reflectivity $R_f(\lambda)$ of silicon film laser annealed for 2 s (sensor 294).

Figure 6.29 Measured and calculated reflectivity $R_f(\lambda)$ of silicon film laser annealed for 0.5 s.

Figure 7.1 Void fractions f_V of SiN_x films as functions of sputtering gas pressure, measured on four different occasions.

Figure 7.2 Etch rates in buffered HF of SiN_x films as functions of sputtering gas pressure, for 10-min and 30-min etches.

Figure 7.3 Void fraction f_V as a function of sputtering gas pressure for SiN_x films on silicon substrates that were subjected to etch-rate testing.

Figure 7.4 Survey spectrum of electron binding energies for SiN_x sputter deposited in 2.3 mTorr N_2.

Figure 7.5 Survey spectrum of electron binding energies for SiN_x sputter deposited in 4.7 mTorr N_2.

Figure 7.6 Measured and calculated $\psi(\lambda)$ for Si_3N_4 sputter deposited on silicon in 3.5 mTorr N_2.

Figure 7.7 Measured and calculated $\Delta(\lambda)$ for Si_3N_4 sputter deposited on silicon in 3.5 mTorr N_2.

Figure 7.8 Void fractions of Si_3N_4 films on silicon as functions of sputtering gas pressure, as deposited and after annealing.

Figure 7.9 Composition profile for Si_3N_4 film on silicon, as sputter deposited.

Figure 7.10 Composition profile for oxidized Si_3N_4 film on silicon.

Figure 7.11 Thicknesses of Si_3N_4 and SiO_2 layers, L and L_{ox}, respectively, as functions of etching time in buffered HF.

Figure 7.12 Silicon oxidation--measured and calculated thicknesses L_{ox} of SiO_2 layers on silicon as functions of oxidation times in wet O_2, at different temperatures.

Figure 7.13 Si_3N_4 oxidation--measured and calculated thicknesses L_{ox} of SiO_2 layers on Si_3N_4 as functions of oxidation times in wet O_2, at different temperatures.

Figure 7.14 Log-log plots of Si_3N_4 oxidation data.

Figure 7.15 Oxygen concentration profile of aluminum film as deposited.

Figure 7.16 Oxygen concentration profile of oxidized aluminum film.

Figure 8.1 Reflectivity $R_f(\lambda)$ of silicon film on fiber end (sensor 294), as sputter-deposited and after laser annealing.

Figure 8.2 Measured and calculated reflectivities $R_f(\lambda)$ of laser-annealed silicon on fiber end (sensor 291).

Figure 8.3 Measured and calculated reflectivities $R_f(\lambda)$ of laser-annealed silicon on fiber end after encapsulation with Si_3N_4 and aluminum (sensor 291, fully fabricated).

Figure 8.4 Transmissivities $H_S(\lambda)$ of sensor 293 at -55 °C and 278 °C for 500 nm $< \lambda < 1$ μm.

Figure 8.5 Transmissivities $H_S(\lambda)$ of sensor 292 at -55 °C and 278 °C for $800 < \lambda < 900$ nm.

Figure 8.6 Average, for sensors 291-294, of the normalized resonance shifts $\gamma(T) = [\lambda_m(T)-\lambda_m(T_0)]/\lambda_m(T_0)$, where $T_0 = 96$ °C.

Figure 8.7 Deviations of the normalized resonance shifts $\gamma(T)$ from the quadratic fit to the average, expressed in terms of the measured temperature T_M.

Figure 8.8 Transmissivities $H_S(\lambda)$ of sensor 291 at 278 °C showing effects of remating connectors.

Figure 8.9 Deviations of the measured temperatures T_M from the mean values, at $T = 20$ °C, caused by remating the connectors (all four sensors).

Figure 8.10 Variations in fiber-link transmissivities H_{FO}, relative to the means, caused by remating connectors.

Figure 8.11 Calculated sensor transmissivities $H_S(\lambda)$ showing effects of wavelength-dependent transmissivity changes with different slopes α (in units of nm^{-1}) for sensors having different fringe visibilities η_{VIS}.

Figure 8.12 Changes in measured temperatures T_M caused by wavelength-dependent transmissivity changes for sensors having fringe visibilities η_{VIS} ranging from 0.3 to 1.0 in increments of 0.1.

Figure 8.13 Changes in measured temperature T_M caused by bending sensor fiber.

Figure 8.14 Changes in fiber-link transmissivity H_{FO} caused by bending sensor fiber.

Figure 8.15 Changes in measured temperature T_M caused by bending input fiber.

Figure 8.16 Changes in fiber-link transmissivity H_{FO} caused by bending input fiber.

Figure 8.17 Changes in measured temperatures T_M as functions of time of exposure to 278 °C.

Figure 8.18 Changes in measured temperatures T_M that were calculated based on the changes in the resonant wavelengths of sensors 292 and 293 and the emission wavelength of the HeNe laser, as functions of time.

Figure 8.19 Changes in the measured temperatures T_M as functions of time of exposure to 278 °C for a-Si sensors (131-135).

Figure 11.1 Transmission and reflection at an interface between two materials with complex refractive indexes N_0 and N_1.

Figure 11.2 Transmission and reflection from a single film.

Figure 11.3 Reflectivities R_F of ideal Fabry-Perot interferometers as functions of the one-way phase shift Φ, for different mirror reflectivities R.

Figure 11.4 Transmission and reflection from a multilayer stack.

LIST OF TABLES

Table 4.1 Properties of candidate Fabry-Perot materials.

Table 4.2 Properties of Faby-Perot temperature sensors fabricated from candidate materials.

Table 7.1 Results of ellipsometric analyses of SiN_x films sputter deposited at different pressures.

Table 7.2 Effects of annealing on sputter-deposited Si_3N_4 film.

Table 7.3 Measured thicknesses of SiO_2, Si_2N_2O and Si_3N_4 layers, L_{ox}, L_{on} and L, respectively, and void fraction of Si_3N_4 layer f_V as functions of cumulative etch time t in buffered HF.

Table 7.4 Etch sequence of oxidized Si_3N_4. Provided are the thicknesses of SiO_2, SiO_xN_y and Si_3N_4 etched during each time interval ending at time t.

Table 7.5 Parabolic rate constants for wet oxidation of (100) Si.

Table 7.6 Rate constants for wet oxidation of Si_3N_4, where $L_{ox} = A_E t^{2/3} + L_0$.

Table 8.1 Sensor characteristics measured at T = 20 °C.

1. INTRODUCTION

1.1 Fiber-Optic Temperature Sensors for Aircraft

The application of fiber-optic technologies to the measurement of physical parameters can alleviate many of the problems that are encountered when using electrical sensors.[1,2] The greatest advantage is obtained when electrically passive optical sensors are connected solely by fibers to their opto-electronic interfaces, which can be located in benign environments remote from the hostile measurement sites. Advantages of fiber-optic sensors include immunity to electromagnetic interference (EMI) and elimination of ground loops. Fiber-optic sensors can provide ready isolation from high voltages, and they can be constructed using all-dielectric materials in order to minimize errors due to self-heating in RF fields. Further, fiber-optic sensors can eliminate the shock hazard to subjects of in-vivo measurements; they can be inherently safe in the presence of flammable gases; and they can be constructed of inert materials for use in reactive environments.

Fiber-optic sensors are of interest for aircraft systems because their immunity to EMI can provide a significant weight savings through the elimination of cable shielding and surge-protection electronics.[3-6] A further weight savings can be realized by using the high bandwidth of optics to multiplex the sensor outputs, thereby reducing the fiber count.

When combined with optically controlled actuators and optical data links, fiber-optic sensors can effectively isolate an aircraft's control electronics from potentially damaging EMI, such as that which is generated by a lightning strike. Implementation of such a "fly-by-light" engine control system would require an optical inlet-air temperature sensor, in addition to optical sensors of actuator positions, shaft speeds and the temperatures of the hot gases produced by combustion.[4,5] Control of a supersonic fighter engine requires an inlet-air temperature sensor with a range of -55 to 275 °C and an accuracy of ± 2 °C. A sensor that meets these requirements could also be used in a subsonic transport, in which case, the inlet-air temperature range is -55 to 125 °C.

In order to prove economically advantageous, a fiber-optic inlet-air temperature sensor must have maintenance requirements comparable to those of the platinum resistance thermometer that it would replace. Since in-situ

calibration is not feasible, the sensor must have a high immunity to cable and connector effects (i.e. a high short-term stability) so that the factory calibration is maintained during installation. Also, the sensor's long-term stability must be sufficient to provide a lifetime of 5000 engine-operating hours without recalibration.

A fluorescent-decay-rate type of fiber-optic temperature sensor has been developed for engine-inlet air-temperature measurements by Rosemount Inc.[7] The principal drawback of this sensor is the incompatibility of its time-based encoding mechanism with the wavelength-based method used by wavelength-division-multiplexed (WDM) position encoders, which are, at present, the optical position transducers best accepted for aircraft.[8]

1.2 Fabry-Perot Temperature Sensor

A fiber-linked Fabry-Perot interferometer can provide a wavelength-encoded temperature measurement from a very compact and rugged sensor. Typically, the Fabry-Perot temperature sensor is a thin platelet of a material that has a temperature-dependent refractive index.[9,10] The surfaces of the platelet are flat and parallel so that optical resonance is produced at

wavelengths that are submultiples of the temperature-dependent difference in the optical paths of successive reflected beams. At resonance, the reflectivity of the interferometer is a minimum, and the wavelength of one of these reflectivity minima can serve as a signal-level-insensitive indicator of temperature.

A fiber-optic Fabry-Perot temperature sensor has been devised, in which the temperature-sensitive interferometer is constructed from thin films that are deposited directly onto the end of an optical fiber.[11] The annealing and encapsulation of such a thin-film interferometer are critical steps in fabricating a stable sensor, as has not been well recognized in previous work on such devices. An especially high degree of stability is required for the aircraft engine application. This level of stability has not yet been demonstrated by any fiber-optic temperature sensor.

The objective of the research described here is the design and fabrication of a thin-film Fabry-Perot temperature sensor with sufficient stability for use in aircraft-engine control systems. Design rules will be developed and a preliminary design undertaken, following reviews of fiber-optic techniques for temperature measurement and fiber-optic Fabry-Perot temperature sensors.

The sensor design will be predicated on the analysis of its spectral reflectance using an AlGaAs LED together with a grating spectrometer and silicon photodetector array. Following the selection of a temperature-sensitive material, the optimum thickness of the temperature-sensing film will be determined, and a thin-film encapsulating structure will be designed. The thin-film deposition and annealing processes will then be devised and optimized, and the individual films characterized. Finally, a set of completed sensors will be characterized in terms of thermal response, sensitivity to disturbances that occur over short time intervals (such as connector remating and fiber bending), and long-term stability at the maximum temperature of the intended application.

1.3 References

1. T.G. Giallorenzi, J.A. Bucaro, A. Dandridge, G.H. Sigel, Jr., J.H. Cole, S.C. Rashleigh, and R.G. Priest, "Optical Fiber Sensor Technology," IEEE J. Quantum Electron. QE-18, 626 (1982).

2. G.D. Pitt, P. Extance, R.C. Neat, D.N. Batchelder, R.E. Jones, J.A. Barnett and R.H. Pratt, "Optical-Fibre Sensors," IEE Proc. 132, Pt. J, 214 (1985).

3. D.J. Poumakis and W.J. Davies, "Fiber Optic Control System Integration," NASA CR-179569 (1986).

4. G.L. Poppel, W.M. Glasheen, J.C. Russell, "Fiber Optic Control System Integration", NASA CR-179568 (1987).

5. G.L. Poppel, W.M. Glasheen, "Electro-optic Architecture for Servicing Sensors and Actuators in Advanced Aircraft Propulsion Systems," NASA CR-182269 (1989).

6. W.L. Glomb, Jr., "Electro-Optic Architecture (EOA) for Sensors and Actuators in Aircraft Propulsion Systems," NASA CR-182270 (1989).

7. R.W. Phillips and S.D. Tilstra, "Design of a Fiber Optic Temperature Sensor for Aerospace Applications," in **Temperature: Its Measurement and Control in Science and Industry**, J.F. Schooley, ed., Vol. 6, Part 2, pp. 721-724 (American Institute of Physics, New York, 1992).

8. G. Beheim and K. Fritsch, "Spectrum-Modulating Fiber-Optic Sensors for Aircraft Control Systems," NASA TM-88968 (1987).

9. G. Beheim, "Fiber-Optic Thermometer Using Semiconductor-Etalon Sensor," Electron. Lett. 22, 238-239 (1985).

10. J.C. Hartl, E.W. Saaski, and G.L. Mitchell, "Fiber Optic Temperature Sensor Using Spectral Modulation," in **Fiber Optic and Laser Sensors V**, R.P. DePaula and E. Udd, eds., Proc. SPIE 838, pp. 257-261 (1987).

11. L. Schultheis, H. Amstutz, and M. Kaufmann, "Fiber-Optic Temperature Sensing With Ultrathin Silicon Etalons," Opt. Lett. 13, 782 (1988).

2. REVIEW OF FIBER-OPTIC TEMPERATURE SENSORS

2.1 Introduction

The objective of this review of fiber-optic temperature sensors is to illustrate, through examples, each of the most prominent sensing techniques. The benefits of fiber optics are fully realized only if the remotely located sensor is linked solely by fibers, therefore, this chapter will not discuss sensors that require electrical power connections. Fiber-linked optical temperature sensors can be categorized on the basis of their method of signal generation, as follows:

(a) Optically emissive, thermally powered,

(b) Optically emissive, optically powered,

(c) Intensity modulating (non-emissive).

An elegant fiber-based method of measuring temperature uses the thermal energy of the sensed medium to power a radiant probe. At lower temperatures, where the thermal radiation is inadequate, an emissive sensor can be powered by an external light source using one of two means. In the first

method, an optical-to-electrical conversion powers electronic circuitry which processes the output of an electrical sensor, such as a thermocouple. The measurement is then transmitted optically, using an electro-optic emitter. In a purely optical approach, optical excitation of the sensor produces a temperature-dependent emission, typically via fluorescence.

Non-emissive sensors encode the measured temperature via the intensity modulation of fiber-transmitted light. Typically, this intensity modulation is performed in some wavelength-dependent manner to reduce the sensitivity to variations in the fiber link's transmissivity. There are two intensity-modulation mechanisms which have proven to be useful. The first approach uses a material which absorbs light in a temperature-dependent manner. The other approach exploits a thermally induced change in refractive index, which, by interferometry, is converted to an intensity change.

Some of these sensing methods are suited to the measurement of the temperature profile along the length of an optical fiber. Because of their unique capabilities, these distributed temperature sensors will be discussed in a separate section, even though they can be classified as either intensity modulating or optically emissive and optically powered.

An important attribute of a fiber-optic sensor is its ability to encode the measurement information so that it is not corrupted during transmission. Cable effects pose an especially severe problem for the optical transmission of quasi-static analog signals. For example, simply remating a connector can produce a transmissivity change of 10%, while a fiber bend of moderate curvature can cause a change of several percent. The variability of fiber and connector losses necessitates the use of some type of compensation scheme in order to obtain the required accuracy, which is typically about 1% of the temperature span.

There are two types of encoding schemes for fiber-optic temperature sensors that have been shown to provide a reasonable degree of immmunity to cable effects. Generally the most robust encoding methods are the time-based type. Here, the temperature is encoded as a frequency, typically in the audio to RF range, or as a time delay, such as the time constant of an exponentially decaying signal. Alternatively, a loss-insensitive signal can be produced by a spectral-encoding method. Here, the sensor's output spectrum contains some temperature-indicating feature, for instance a minimum, the position of which varies as a function of temperature. In another widely used spectrum-modulating approach, the output spectrum is sampled at two wavelengths, and the temperature determined as a function of the ratio of the intensities.

2.2 Optically Emissive, Thermally Powered Sensors

A fiber-optic thermometer that uses the thermally generated light from an emissive probe has the unique advantage of requiring no electro-optical source. This instrument is also readily calibrated since its thermal response can be derived from fundamental physical laws. The light emitted by the sensor is transmitted by a fiber to an analyzer, which measures the radiant intensity in two separate wavelength bands. Figure 2.1 shows a sensor marketed by Luxtron's Accufiber Division. This black-body probe is made by sputter depositing a high-emissivity coating onto the tip portion of a single-crystal sapphire fiber.[1] For length-to-diameter ratios greater than about 10, this beveled-bottom cylindrical chamber radiates a spectrum approximately equal to that emitted by an ideal black body, i.e.

$$i_E(\lambda, T) = \frac{a c_1}{\lambda^5 [\exp(c_2/\lambda T) - 1]} \quad . \tag{1}$$

Here a is the area of the cavity exit, the first radiation constant c_1 is 3.7418×10^{-16} W m^2, the second radiation constant c_2 is 1.43879×10^{-2} m K, λ is the wavelength in vacuum, and T is the absolute temperature. Figure 2.2

shows $i_E(\lambda)$ for various temperatures between 1000 and 2000 K (730 and 1730 °C), for a = 1 cm^2.

By integrating Eq. 1 over all λ one obtains the Stefan-Boltzman relation for total emitted intensity,

$$I_E = \sigma T^4 , \qquad (2)$$

where σ is 5.67×10^{-8} W m^{-2} K^{-4}. Differentiating Eq. 1 provides the wavelength of peak spectral density, which is given by Wien's displacement law,

$$\lambda_{peak} = \frac{C_0}{T} , \qquad (3)$$

where $C_0 = 2.897 \times 10^{-3}$ m K.

In the first implementation of the Accufiber instrument, a silicon photodiode and optical bandpass filter were used to integrate $i_E(\lambda)$ over a 100-nm-wide band centered at 600 nm. The range of this instrument was 700 to 1000 °C. Here, a high sensitivity was obtained by sampling the radiant spectrum at $\lambda < \lambda_{peak}$. For λ = 600 nm and T = 1000 °C, a 1% change in the absolute temperature causes a 20% change in i_E.

A high degree of immunity to cable and connector effects has been realized, in later versions of this instrument, by using a ratiometric loss-compensation technique. A second photodiode is used to sample the radiant spectrum at $\lambda = 700$ nm. The temperature is then determined as a function of the ratio of the two intensities. If the two monitored wavelengths are designated λ_1 and λ_2, then, for the temperatures and wavelengths of interest, the ratiometric signal is approximately given by

$$\frac{i_E(\lambda_1, T)}{i_E(\lambda_2, T)} \approx \frac{\lambda_2^5}{\lambda_1^5} \exp\left[-c_2 \frac{\lambda_1 - \lambda_2}{\lambda_1 \lambda_2} \frac{1}{T}\right]. \tag{4}$$

The effectiveness of this ratiometric technique relies on a constant ratio of the fiber link's transmissivities, $H_{FO}(\lambda_1)/H_{FO}(\lambda_2)$, which is more nearly obtained if $\lambda_1 \approx \lambda_2$. For example, if the fiber absorptivities at λ_1 and λ_2 are α_{FO1} and α_{FO2}, then the ratio of the transmissivities, for a fiber of length L_{FO}, is $\exp[(\alpha_{FO2}-\alpha_{FO1})L_{FO}]$. This ratio will be independent of the length of the fiber link only if $\alpha_{FO1} = \alpha_{FO2}$, which will be approximated if $\lambda_1 \approx \lambda_2$.

Degradation of this probe's thermally emissive coating can be a problem in extremely harsh environments, such as in the turbine region of an aircraft engine where the sensor is subjected to an extremely hot, high-velocity,

oxidizing gas flow. An emissive probe which has proven quite durable in this environment was developed by Conax Corp.[2] A hole is drilled in the end of a sapphire lightguide and a highly stable emissive material, chromium oxide, is inserted and then capped with a sapphire plug. This instrument also uses a ratiometric method. A silicon photodiode integrates the short-wavelength radiation, between 0.5 and 1.1 μm, and a germanium diode integrates the radiation between 1.1 and 1.8 μm. This probe has a demonstrated temperature range of 600 to 1900 °C and has been extensively tested in gas turbine engines.[3]

Because the radiant intensity decreases rapidly with decreasing temperature, as indicated by Eq. 2, temperatures below 600 °C are not readily measured using a fiber-linked radiant probe. At these temperatures, the radiant emission has shifted well into the infrared, which necessitates the use of IR detectors and special IR-transmitting fibers. Using a 5-m fiber of polycrystalline thallium-bromoiodide (KRS-5), together with a HgCdTe detector that was cooled to 77 K, temperatures as low as 60 °C were measured with a signal-to-noise ratio greater than 10 dB.[4] Drawbacks of IR-transmitting fibers can include high costs, poor mechanical properties, low softening temperatures, water solubility and toxicity. Despite the prevalence of optically emissive,

thermally powered sensors for high-temperature applications, for the measurement of temperatures below 600 °C there are a number of competitive approaches.

2.3 Optically Emissive, Optically Powered Sensors

An electrically active sensor can be fully fiber linked through the use of an optical-to-electrical converter and an optical transmitter. The key to success with this approach is to minimize the sensor's power consumption to allow it to be powered by a standard 5-mW-output AlGaAs laser diode. Higher power laser diodes are available, but they are expensive, they can pose an eye hazard, and they are not usable in explosive environments. Figure 2.3 shows a thermocouple-based sensor whose sole connecting link is an optical fiber.[5] This provides ready electrical isolation in high-voltage regions; also, a high degree of immunity to electromagnetic interference was demonstrated.

The 5-mW output from a laser diode is transmitted by a fiber to the sensor, where it is directed onto a series-connected array of silicon photovoltaic cells. The photovoltaic array powers special low-current circuitry which converts the thermocouple voltage to a pulse-position modulated (PPM) LED

current. Long-wavelength-pass (LWP) optical filters are used at both ends of the optical fiber to combine and separate the 780-nm power and 880-nm data signals. The PPM coding mechanism allows the LED to be operated with a very low duty cycle, which is essential since the LED draws 50 mA of current. The total electrical power consumption is less than 100 μW, which can be supplied optically through a fiber as long as 70 m.

The temperature range of this type of device is of course limited to that of the electronics, which for conventional silicon technologies is no greater than about 150 °C. The maximum operating temperature may actually be considerably below 150 °C because the photovoltaic efficiency is severely degraded at elevated temperatures. An important advantage of this sensor is the high degree of immunity to cable effects which is provided by its time-based encoding mechanism.

Another time-based means of encoding a temperature measurement uses a fluorescent material whose emission, after cessation of the optical excitation, decays exponentially with a temperature-dependent rate. For a common type of fluorescent material, consisting of activator ions in an insulating host, the absorption of a photon excites an ion to a higher energy level. One of the

processes by which this ion can relax to a lower level is via the emission of a photon. Besides this radiative process, there are competing nonradiative relaxation processes which will shorten the lifetime of the excited state. Let N be the population of the excited state, and let τ be its lifetime, so that $1/\tau = 1/\tau_R + 1/\tau_{NR}$, where $1/\tau_R$ and $1/\tau_{NR}$ are the probabilities per unit time of a radiative and a nonradiative transition. Then, since $dN/dt = -N/\tau$, and since the emitted intensity is proportional to N/τ_R, both N and the emission will decay exponentially with a time constant τ. An increase in temperature will generally cause τ_{NR} to decrease, while τ_R remains largely unchanged, so that τ can be expected to decrease as a function of temperature over at least some range.

An instrument manufactured by Luxtron uses an ultraviolet light pulse from a xenon flashlamp to excite the fluorescence of magnesium fluorogermanate activated with tetravalent manganese.[6,7] The fluorescence decay time decreases from more than 5 ms at -200 °C to 0.5 ms at 450 °C, as shown by Fig. 2.4. An alternative fluorescent material, one that could be excited with red or near-IR light, would have the advantage of permitting the

use of a solid-state source. Also, the optical fiber could be longer in this case, since the fiber losses are lower at the longer wavelengths.

A number of fluorescent temperature sensors using solid-state sources have been reported. A sensor using a chromium-doped yttrium-aluminum-garnet (YAG) crystal, whose fluorescence is excited using a 635-nm laser diode, was tested from -25 to 500 °C.[8] Over this range τ decreased from about 30 ms to less than 0.5 ms. The fluorescent decay rates of both chromium-doped sapphire (ruby),[9] excited at 560 nm, and neodymium-doped glass,[10] excited at 810 nm, have been used to sense temperatures in the range of approximately -50 to 200 °C. Rosemount has developed a fluorescent probe for the measurement of inlet air temperature in aircraft engines.[11,12] This sensor uses a proprietary material that is excited using a 680-nm LED; the material fluoresces in the 700-900 nm range with a decay time that decreases by almost an order of magnitude from -75 to 350 °C.

The insertion loss of these sensors is generally quite high because of the inefficiency of the emission process and the low coupling of the nondirectional emission to the fiber. The insertion loss generally becomes exceptionally high as the temperature approaches the fluorescence quench point. The Rosemount

probe's output intensity remains approximately constant between -55 and 300 °C. For temperatures greater than 300 °C, the fluorescence decreases linearly and is reduced by a factor of 20 at 500 °C.[12]

A fluorescent temperature sensor that encodes the measurement via the emission wavelength was developed by ASEA.[13] The wavelength of an AlGaAs heterostructure's emission increases as a function of temperature, due to the decrease in the bandgap energy E_g. Figure 2.5 shows the spectrum of the LED excitation together with the emitted spectra for temperatures between 0 and 100 °C. The fluorescence is split into its components above and below 890 nm, and the intensity ratio is used to determine the temperature. This two-wavelength ratiometric type of compensation method will be discussed extensively in section 2.4.

2.4 Intensity-Modulating (Non-Emissive) Sensors

Non-emissive fiber-optic sensors can be characterized by their temperature-dependent transmittances, $H_S(\lambda,T)$, which relate their input and

output spectra, $i_1(\lambda)$ and $i_2(\lambda,T)$, through

$$i_2(\lambda, T) = H_S(\lambda, T)\, i_1(\lambda)\ . \qquad (5)$$

Unlike fluorescent sensors, the output spectra of intensity-modulating sensors contain only the spectral components emitted by the source. In order to reduce the sensitivity to the effects of variations in the fiber and connector losses, the sensor generally imposes some type of temperature-sensitive feature on the transmitted spectrum. For example, the temperature might be encoded via the position of a minimum or an edge, or it might be determined from the ratio of the sensor's transmissivities at two wavelengths.

A temperature-indicating spectral edge can be provided by a semiconductor material with a temperature-dependent bandgap E_g. Sufficiently thick samples of many semiconductors have transmissivities which approximate that of an ideal long-wavelength-pass (LWP) filter, where the cut-on wavelength is $\lambda_g = hc/E_g$. Of course, λ_g must lie within the spectral range of the source, so that GaAs is an obvious sensor material for use with an AlGaAs LED.

Figure 2.6 shows an implementation of this approach.[14] The 0.2-mm-thick GaAs platelet is interrogated by a AlGaAs LED. The LED has an 880-nm center wavelength and a 150-nm spectral width. As the temperature of the GaAs increases so does λ_g; this reduces the width of the transmitted portion of the LED's spectrum. At $\lambda = 1.3\ \mu m$, however, the sensor is transparent throughout its -10 to 300 °C range. Therefore, the temperature can be determined from the ratio of the transmissivities. This ratiometric approach eliminates the effects of incidental transmissivity variations common to both wavelengths. To obtain accurate transmissivity measurements, the outputs of the LEDs must be monitored to correct for intensity drifts.

This two-wavelength ratiometric technique requires much lower spectral resolution than would be required to directly measure λ_g, which might be accomplished using a grating spectrometer. A disadvantage of this simple approach is its sensitivity to temperature-induced changes in the source wavelength. The temperature sensitivity of the AlGaAs LED's output is 0.35 nm/°C, essentially the same as $d\lambda_g/dT$. The measured temperature, therefore, has a sensitivity to the LED temperature of -1 °C/°C. This necessitates thermo-electric control of the LED's temperature. Another disadvantage of the ratiometric technique used here is the need to calibrate each

sensor with a specific LED, since the LED spectra will vary somewhat between devices.

Another ratiometrically compensated temperature sensor uses a short length of neodymium-doped fiber as the sensing element.[15] Here the sampled wavelengths are much closer together, which, in principle, should provide greater immunity to cable effects. For trivalent Nd ions incorporated in a glass host, absorption of a near-infrared photon of wavelength λ is accompanied by the excitation of an ion from a low-lying energy level to a state having an energy hc/λ higher. The probability of this transition is proportional to the number of ions in the initial state, which is thermally populated in accordance with Boltzman statistics. As the temperature changes, some absorption lines will become stronger while the strengths of others will diminish, depending upon the changes in the populations of the asssociated initial levels.

Figure 2.7 shows the spectral transmissivity of a 3.8-cm length of Nd-doped fiber for temperatures between 20 and 900 °C. Over this temperature range the transmissivities at 840 and 860 nm are grossly dissimilar functions of temperature, therefore, their ratio can be used as a temperature indicator. The sources are LEDs whose spectra are narrowed using

10-nm-wide bandpass filters. This sensor also exhibits high sensitivity to source spectral changes. Narrower bandpass filters could reduce this sensitivity, but would also reduce the signal-to-noise ratio.

When designing an intensity-modulating sensor, a greater flexibility is obtained if the sensor is based on a temperature-dependent change in refractive index rather than absorption. In this case, an interferometer is used to convert the refractive-index changes to changes in the sensor's transmissivity. This interferometer can be tuned for a particular measurement range simply by adjusting the length of the temperature-sensitive component. In a two-beam interferometer, a splitter divides the optical input into two beams. These beams then travel paths of lengths L_1 and L_2, through media having refractive indexes of n_1 and n_2, before they are recombined. The transmissivity of a two-beam interferometer is given by

$$H_S(\lambda, T) = \frac{1}{2} A_1 \left[1 + A_2 \cos \left[\frac{2\pi}{\lambda} \Lambda_{OPD}(T) \right] \right], \quad (6)$$

where A_1 and A_2 are 1 for the ideal case of zero losses and 50:50 beamsplitters, and where Λ_{OPD} is the interferometer's optical path difference,

or OPD, which is given by

$$\Lambda_{OPD}=n_1L_1-n_2L_2\,. \tag{7}$$

In general, n_1, n_2, L_1, and L_2 will all vary as functions of temperature. The sensor should be designed so that Λ_{OPD} is a sensitive and repeatable monotonic function of temperature. The temperature can then be determined by measuring the phase of the sinusoidal component of H_S as a function of $1/\lambda$. Equivalently, the wavelength of a fixed phase can be measured, for example, by measuring the position of one of the minima in $H_S(\lambda)$. The range using either of these approaches is limited to a phase change of 2π or $\Delta\Lambda_{OPD} = \lambda_0$, where λ_0 is either the wavelength at which the phase is measured or the initial position of of the tracked minimum.

A larger range can be provided by measuring the free spectral range, $\Delta\lambda_{FSR}$, which is the wavelength change corresponding to a phase change of 2π, i.e. the period of $H_S(\lambda)$. However, for interferometers of large order, i.e. $\Lambda_{OPD} >> \lambda$, this approach requires a very high spectral resolution. For

sufficiently large fringe orders, the free spectral range is given by

$$\Delta\lambda_{FSR} = \frac{\lambda^2}{\Lambda_{OPD}} \,. \tag{8}$$

The wavelength resolution required to measure a given OPD change is therefore given by

$$\delta\,[\Delta\lambda_{FSR}] = \frac{\lambda^2}{\Lambda_{OPD}^2}\;\delta\Lambda_{OPD} \,. \tag{9}$$

Figure 2.8 shows a temperature sensor which is based on an integrated-optic Mach-Zehnder interferometer.[16] Single-mode waveguides and two Y-junction splitter-combiners are fabricated in a lithium-niobate substrate by titanium diffusion. This interferometer's OPD is equal to $n_{EFF}\,\Delta L$, where $\Delta L = L_1 - L_2$ and the waveguide's effective index is given by $n_{EFF} = c\,/\,v_p$, where v_p is the phase velocity of the guided light. Here both arms are exposed

to the sensed temperature, which gives

$$\frac{d\Lambda_{OPD}}{dT} = \Delta L \left[\frac{dn_{EFF}}{dT} + n_{EFF}\kappa_L \right], \tag{10}$$

where the thermal expansion coefficient is $\kappa_L = L^{-1}\, dL/dT$. The effective index n_{EFF} lies between the substrate's refractive index and the slightly higher index of the titanium-doped core. By substituting the material properties of lithium niobate into Eq. 10, the OPD's temperature sensitivity is determined to be $(\Delta L)^{-1}\, d\Lambda_{OPD}/dT \approx 7.5 \times 10^{-5}/\ °C$. For $\Delta L = 0.06$ mm and $\lambda = 630$ nm, a 2π phase change will be produced by a temperature change of 140 °C.

Another temperature sensor has been reported which uses an integrated-optic Michelson interferometer.[17] Here, the optical combiner is absent and the ends of the interferometer's arms are reflectively coated so that the optical splitter also combines the two beams. Disadvantages of these integrated-optic temperature sensors include their relatively large size, and the very small cross-section of their single-mode waveguides, which necessitates precise and highly stable fiber coupling. Also, single-mode-fiber connectors are more expensive and less reliable than are connectors for multimode fibers.

A more compact interferometric sensor, which is compatible with multimode fibers, directs two orthogonally polarized beams along the same path through a birefringent crystal. These polarization eigenmodes propagate with different phase velocities, yielding an OPD that will, in general, be temperature dependent. This type of sensor, shown in Fig. 2.9, has been constructed by sandwiching a 0.55-mm thick slice of y-cut lithium niobate between crossed polarizers oriented at ±45° to the z (or optical) axis.[18] The crystal decomposes the 45° polarized light into equal-amplitude eigenmodes. These are polarized along the x and z axes and have phase velocities determined by n_o and n_e, which are the material's ordinary and extraordinary refractive indexes. The orthogonally polarized beams are made to interfere by the output polarizer. The sensor's transmissivity $H_S(\lambda,T)$ is given by Eq. 6, in which A_2 = -1, and

$$\Lambda_{OPD}=(n_e-n_o)\,L, \tag{11}$$

where L is the length of the crystal. Here, the temperature sensitivity of the OPD is almost entirely due to the birefringence change, the effect of thermal expansion being considerably smaller.

A single-ended probe, which would be preferred in most applications, has been fabricated by applying a reflective coating to the back surface of the crystal.[19] The output spectra of one of these sensors has been analyzed using discrete Fourier techniques to determine the temperature-indicating phase shift.[20] A disadvantage of these sensors is the requirement for collimating lenses, which causes the sensors to be larger than is usually desired. Dichroic-film polarizers also have a limited temperature range. Prism polarizers can be used at much higher temperatures,[21] however, they are large and expensive.

The smallest interferometric sensors are the Fabry-Perot type. Section 3 provides a comprehensive review of Fabry-Perot temperature sensors. The optical properties of Fabry-Perot interferometers are derived in the appendix. Only the most significant features of Fabry-Perot temperature sensors will be described here.

Figure 2.10 shows a solid Fabry-Perot interferometer, or etalon, which has a thickness of L and a refractive index of n_1. The etalon is surrounded by a material of index n_0, where $n_1 > n_0$. The surfaces of this ideal interferometer are perfectly flat and parallel, and the materials are lossless, while the incident light is assumed to be collimated. The reflectivity of the

etalon's surfaces is R, where $R = (n_1-n_0)^2/(n_1+n_0)^2$. The interferometer is operated reflectively, as this provides for a more compact single-ended probe. The reflectivity of the ideal Fabry-Perot interferometer is given by Airy's formula, which is

$$R_F(\Phi) = \frac{F \sin^2(\Phi)}{1 + F \sin^2(\Phi)}, \tag{12}$$

where

$$F = \frac{4R}{(1-R)^2}, \tag{13}$$

and

$$\Phi = \frac{\pi}{\lambda} \Lambda_{OPD}. \tag{14}$$

Here, Λ_{OPD} is

$$\Lambda_{OPD} = 2n_1 L \cos\theta_1, \tag{15}$$

where θ_1 is the internal angle of incidence. Figure 2.11 shows $R_F(\Phi)$ for different values of R. The interferometer's reflectivity is a minimum ($R_F = 0$) at resonance, $\Phi = \pi m$, where m is an integer. In terms of wavelength, the resonance condition is $\lambda = \lambda_m$, where $m\lambda_m = \Lambda_{OPD}$.

A commercial Fabry-Perot temperature sensor, available from Photonetics, is fabricated using a ~1-μm-thick slice of single-crystal silicon.[22] The fragile piece of silicon is protected by electrostatically bonding it between two thicker pieces of Pyrex glass. The large refractive index discontinuities at the silicon/glass interfaces give $R = 0.18$. The glass-encased silicon etalon is bonded to a glass capillary, inside of which is affixed an optical fiber. No collimating lens is required since the silicon is quite thin; also its refractive index is very high, 3.7 at 830 nm, which greatly reduces the internal divergence. Figure 2.12 shows the spectrum of the LED source and the sensor's output spectra at 25 and 125 °C. The reflectance minima shift to longer wavelengths with increasing temperature, primarily due to the refractive index change, which is about 0.01%/°C. An optical edge filter splits the sensor's output spectrum into its components above and below 840 nm. The ratio of these intensities is used to determine the temperature over the range of -40 to 300 °C.

A SiC Fabry-Perot temperature sensor with a range of 20 to 1000 °C has been demonstrated.[23] This Fabry-Perot sensor is a several-μm-thick layer of crystalline SiC, on a much thicker silicon substrate, which is cemented onto the end of a ceramic tube. A graded-index rod lens collimates the light emitted

by the fiber and directs it down the tube to the reflective SiC film. This approach allows the fiber and collimating lens to be located outside the hot environment. The collimator effectively eliminates the effects of fiber bending on the angular distribution of the light inside the etalon. Without the collimating lens, a 2 °C accuracy is not readily obtained because of the sensitivity to the modal power distribution.[24] The modal sensitivity is greater for SiC than it is for silicon because of the lower refractive index, $n_1 = 2.6$ instead of 3.7 at 830 nm. A lower n_1 causes the light rays inside the Fabry-Perot etalon to be more divergent, since the range of angles of incidence is given by $|\theta_1| \leq \sin^{-1}(NA/n_1)$, where NA is the fiber's numerical aperture.

A silicon Fabry-Perot sensor can be fabricated less expensively by depositing the silicon directly onto the end of an optical fiber.[25] Figure 2.13 shows such a temperature sensor, which is the subject of the research described here. The silicon film, which is amorphous as deposited, is crystallized using an argon-ion laser. Then, two encapsulating layers are deposited; first, a thin layer of Si_3N_4, which is followed by ~ 1 μm of aluminum. The Si_3N_4-coated aluminum serves as the Fabry-Perot interferometer's second reflector, the first being the fiber/silicon interface.

Yet another type of interferometric temperature sensor is based on Bragg diffraction from an in-fiber grating.[26] A Bragg grating of several-mm length is formed in a single-mode fiber by the use of intense ultraviolet radiation which produces a permanent modulation of the refractive index. The fiber is exposed, from the side, with UV light, the intensity of which varies sinusoidally along the fiber's length, with a period L_B. This UV exposure produces, in proportion to its intensity, a refractive-index change which is quite stable despite subsequent annealing at temperatures as high as 350 °C.[27] The Bragg grating's operation can be understood by considering a square-wave index modulation of amplitude Δn, which is superimposed on the fiber's effective index n_{EFF}, where $\Delta n << n_{EFF}$. Each refractive index step Δn produces a small reflected wave; these wavelets will interfere constructively if $\lambda = 2n_{EFF}L_B$, which is the Bragg condition. The large number of interfering wavelets (several thousand per mm of filter length) causes the spectral reflectance peak to be extremely narrow, as shown by Fig. 2.14. Because the thermo-optic coefficient, $\kappa_n = n^{-1}dn/dT$, for fused silica is only about 9×10^{-6}/°C, the thermally induced resonance shift is quite small, about 0.01 nm/°C at $\lambda = 1300$ nm. The sharpness of the reflectance peak makes it possible to resolve temperature changes of 1 °C or smaller, but the

requirements for a wavelength-tunable laser and single-mode fibers make this sensor relatively expensive.

An interesting type of intensity-modulating temperature sensor uses optical power to produce, through purely optomechanical means, a frequency-encoded modulation of an externally supplied probe beam.[28] Through the photothermal effect, a modulated optical signal causes the vibration of a micromachined silicon cantilever beam which has a temperature-dependent resonant frequency. The beam's vibration amplitude is detected interferometrically, using a second light source and optical fiber. The frequency of the excitation is then adjusted to maximize the vibration amplitude, thereby determining the resonant frequency. Since only relative and not absolute measurements of the vibration amplitude are required, this sensor has a high degree of immunity from cable effects. Also, the frequency-encoded output is readily interfaced to a computer.

2.5 Distributed Sensors

Several groups have achieved significant success in measuring the temperature distribution along the length of an optical fiber. Such a distributed

temperature sensor has a number of interesting applications, the requirements of which are not readily met using electrical sensors. The general principle is that of optical time domain reflectometry (OTDR), in which a short-duration optical pulse is injected into the fiber and the backscattered light monitored as a function of time. If a pulse of energy E_0, at time t = 0, is injected into the fiber end face, position x = 0, then the backscattered power is

$$I_S(t) = \frac{1}{2} E_0 v_g \, S(v_g t/2) \, \exp\left[-2 \int_0^{v_g t/2} \alpha(x)\, dx\right] , \qquad (16)$$

where v_g is the fiber's group velocity, S(x) is the scattering coefficient, and $\alpha(x)$ is the fiber's attenuation.

Distributed temperature measurements were performed using a Nd-doped fiber and a 904-nm diode laser.[29] At this wavelength, the absorption of the Nd-doped fiber has a temperature coefficient, $\alpha^{-1}\, d\alpha/dT = 2 \times 10^{-3}/°C$. Here, S(x) is caused by Rayleigh backscattering and is constant, and the temperature-dependent absorption, $\alpha(x)$, is determined from the time derivative of $\log[I_S(t)]$. Due to the low levels of backscattering, 10^5 waveforms were averaged over a period of 2.5 min in order to provide a signal-to-noise ratio sufficient to

resolve a 2 °C change. The accuracy from -40 to 80 °C was estimated to be 10 °C, with a spatial resolution of 15 m out of a total measurement distance of 140 m.

A temperature-dependent scattering coefficient S(x) can be obtained using Raman scattering. The Raman-scattered light has two components, the Stokes and anti-Stokes emissions, which have frequencies of ν_0 - ν_S and $\nu_0 + \nu_S$, respectively, where ν_0 is the frequency of the incident light and the frequency shift ν_S is determined by the material, which has a vibrational energy level $h\nu_S$. The Stokes emission occurs after the absorption of a photon of frequency ν_0 by a molecule which is initially in the ground state. This molecule is then left in the higher energy level after the emission of a photon of frequency ν_0 - ν_S. The anti-Stokes emission requires that the molecule be in the excited state when the incident photon is absorbed. The intensities of the Raman emissions are proportional to the populations of the associated initial energy levels, which can be determined using Maxwell-Boltzman statistics. The ratio of the scattered intensities is given by

$$\frac{S_{AS}(x)}{S_S(x)} = \frac{(\nu_0+\nu_S)^4}{(\nu_0-\nu_S)^4} \exp\left(\frac{-h\nu_S}{kT(x)}\right). \tag{17}$$

Since $h\nu_S >> kT$, the anti-Stokes emission is several orders of magnitude lower in intensity than the Stokes emission, which in turn is much lower than the Rayleigh backscattering. A distributed temperature sensor based on the Raman effect has been described which uses a 900-nm laser diode.[30] The reported resolutions were 10 °C and 3 m over a fiber length of 180 m.

More recently, a Raman-scattering distributed temperature sensor has been described which has a ± 1 °C accuracy, a -50 to 150 °C range, and a 1-m distance resolution over 2 km of fiber.[31] Using an optical source with a wavelength of 1.55 μm, the wavelength of minimum absorption for fused-silica fiber, another group has reported distributed temperature sensing over a 30-km distance.[32]

2.6 Concluding Remarks

For temperatures greater than 600 °C, thermally emissive sensors have the considerable advantage of simplicity, which is essential for reliable operation at these temperatures. At lower temperatures, a number of different modulation mechanisms have been used, none of which has been shown to be clearly superior to the others. Optically powered electrical sensors do not have

all the advantanges of all-dielectric optical sensors, such as freedom from self-heating in RF fields, and their temperature range is limited. These sensors have limited capabilty for multiplexing; their power requirements generally dictate that an expensive laser diode be dedicated to each sensor. However, they can provide exceptional accuracy and stability, because they use technologically mature electrical sensors such as thermocouples. Also, they offer excellent immunity to cable effects, provided the power margin is sufficient.

Sensors based on a fluorescence decay rate also offer low sensitivity to cable effects, but they have similar power margin problems. Since the fluorescence decay time is a property of the bulk material, these sensors should not require individual calibration. This desirable feature is less readily obtained with intensity-modulating temperature sensors because their outputs can be quite sensitive to small dimensional changes; interferometric sensors more so than the absorptive types. Intensity-modulating sensor are, in general, more prone to errors due to cable effects, because their spectrally encoded outputs can be affected by wavelength-dependent changes in the fiber link's transmissivity. Another cause of errors is source spectral shifts due to temperature changes, aging, or parts substitution. On the positive side, some

of these spectrum-modulating sensors, in particular, the thin-film Fabry-Perot sensors, have the advantages of exceptionally small size, low cost and ruggedness.

2.7 References

1. R.R. Dils, "High-Temperature Optical Fiber Thermometry," J. Appl. Phys. 54, 1198 (1983).

2. G. Tregay, P. Calabrese, P. Kaplin, and M. Finney, "Fiber Optic Sensor for Turbine Engine Gas Temperature from 600 to 1900 °C," NASA CR-187048 (1990).

3. G.W. Tregay, P.R. Calabrese, M.J. Finney, and K.B. Stukey, "Durable Fiber Optic Sensor for Gas Temperature Measurement in the Hot Section of Turbine Engines," in **Fly-by-Light**, E. Udd and D. Varyshneya, eds., Proc. SPIE 2295 (1995).

4. M. Shimizu, M. Shimoishizaka, and S. Yoshida, "Radiometric Temperature Measurement Using Infrared Optical Fibers," in **Second International Conference on Optical Fiber Sensors**, Proc. SPIE 514, pp. 161-164 (1984).

5. A. Ohte, K. Akiyama and I. Ohno, "Optically-Powered Transducer with Optical-Fiber Data Link," in **Fiber Optic and Laser Sensors II**, E.L. Moore and O.G. Ramer, eds., Proc. SPIE 478, pp. 33-38 (1985).

6. K.A. Wickersheim, "A New Fiberoptic Thermometry System for Use in Medical Hyperthermia," in **Optical Fibers in Medicine II**, A. Katzir, ed., Proc. SPIE 713, pp. 150-157 (1986).

7. M. Sun, "Fiberoptic Thermometry Based on Photoluminescent Decay Times," in **Temperature: Its Measurement and Control in Science and**

Industry, J.F. Schooley, ed., Vol. 6, Part 2, pp. 731-734 (American Institute of Physics, New York, 1992).

8. V. Fernicola and L. Crovini, "A High-Temperature Digital Fiber-Optic Thermometer," in **Tenth International Conference on Optical Fiber Sensors**, B. Culshaw and J.D.C. Jones, eds., Proc. SPIE 2360, pp. 211-214 (1994).

9. K.T.V. Grattan, R.K. Selli, and A.W. Palmer, "Phase Measurement Based Ruby Fluorescence Fiber Optic Temperature Sensor," in **Optical Fiber Sensors, 1988 Technical Digest Series**, Vol. 2, pp. 490-494 (Optical Society of America, Washington, D.C. 1988).

10. K.T.V. Grattan, A.W. Palmer, and C.A. Willson, "A Miniaturized Microcomputer-Based Neodymium 'Decay-Time' Temperature Sensor," J. Phys. E: Sci. Instrum. 20, 1201 (1985).

11. R.W. Phillips and S.D. Tilstra, "Design of a Fiber Optic Temperature Sensor for Aerospace Applications," in **Temperature: Its Measurement and Control in Science and Industry**, J.F. Schooley, ed., Vol. 6, Part 2, pp. 721-724 (American Institute of Physics, New York, 1992).

12. S.C. Jensen, S.D. Tilstra, G.A. Barnabo, D.C. Thomas, and R.W. Phillips, "A Fiber Optic Temperature Sensor for Aerospace Applications," in **Fiber Optic Systems for Mobile Platforms**, N.E. Lewis and E.L. Moore, eds., Proc. SPIE 1369, pp. 87-95 (1990).

13. C. Ovren, M. Adolfsson, and B. Hok, "Fiber-Optic Systems For Temperature and Vibration Measurements in Industrial Applications," in **Proc. Int. Conf. on Optical Techniques in Process Control** (BRHA Fluid Engineering Publications, Cranfield, UK, 1983) pp. 67-81.

14. K. Kyuma, S. Tai, T. Sawada and M. Nunoshita, "Fiber-Optic Instrument for Temperature Measurement," IEEE J. Quantum Electron. QE-18, 676 (1982).

15. E. Snitzer, W.W. Morey and W.H. Glenn, "Fiber Optic Rare Earth Temperature Sensors," in **Optical Fibre Sensors**, IEE CP-221 (IEE, London, 1983) pp. 79-82.

16. L.M. Johnson, F.J. Leonberger, and G.W. Pratt, Jr., "Integrated Optical Temperature Sensor," Appl. Phys. Lett. 41, 134 (1982).

17. M. Izutsu, A. Enokihara, and T. Sueta, "Integrated Optic Temperature and Humidity Sensors," J. Lightwave Technol. LT-4, 833 (1986).

18. J.M. Knox, P.M. Marshall, and R.T. Murray, "Birefringent Filter Temperature Sensor," in **Optical Fibre Sensors**, IEE CP-221 (IEE, London, 1983) pp. 1-5.

19. C. Mariller and M. Lequime, "Fiber-Optic White Light Birefringent Temperature Sensor," in **Fiber Optic Sensors II**, A.M. Scheggi, ed., Proc. SPIE 798, pp. 121-130 (1987).

20. H. van de Vaart, S.M. Emo, DM. Gualtieri, J. Hou, T.R. Kinney, and R.C. Morris, "Fringe Pattern Analysis of a Birefringent Modified Spectrum to Determine Environmental Temperature," US Patent #5255068 (1993).

21. L. Fiorina, S. Mezetti, and P.L. Pizzolati, "Thermometry in Geothermal Wells: An Optical Approach," Appl. Opt. 24, 402 (1985).

22. J.C. Hartl, E.W. Saaski, and G.L. Mitchell, "Fiber Optic Temperature Sensor Using Spectral Modulation," in **Fiber Optic and Laser Sensors V**, R.P. DePaula and E. Udd, eds., Proc. SPIE 838, pp. 257-261 (1987).

23. G. Beheim, Fiber-Optic Thermometer Using Semiconductor-Etalon Sensor," Electron. Lett. 22, 238-239 (1985).

24. G. Beheim, K. Fritsch, and D.J. Anthan, "Fiber-Optic Temperature Sensor Using a Spectrum-Modulating Semiconductor Etalon," in **Fiber Optic and Laser Sensors V**, R.P. DePaula and E. Udd, eds., Proc. SPIE 838, pp. 238-246 (1987).

25. G. Beheim, J.L. Sotomayor, M.L. Tuma, and M. Tabib-Azar, "Fiber-Optic Temperature Sensor Using Laser Annealed Silicon Film," in **Integrated Optics and Microstructures II**, Proc. SPIE 2291, M. Tabib-Azar, D.L. Polla, and K.K. Wong, eds., pp. 92-98 (1994).

26. W.W. Morey, G. Meltz, and W.H. Glenn, "Bragg-Grating Temperature and Strain Sensors," in **Optical Fiber Sensors, Proceedings of the 6th International Conference**, H.J. Arditty, J.P. Dakin, and R.T. Kersten, eds. (Springer-Verlag, Berlin, 1989) pp. 526-531.

27. W.W. Morey, G. Meltz, and J.M. Weiss, "High Temperature Capabilities and Limitations of Fiber Grating Sensors," in **Tenth International Conference on Optical Fiber Sensors**, B. Culshaw and J.D.C. Jones, eds., Proc. SPIE 2360 pp. 234-237 (1994).

28. D. Angelidis, P. Parsons, "Optical Micromachined Pressure Sensor for Aerospace Applications," Opt. Eng. 31, 1638 (1992).

29. M.C. Farries, M.E. Fermann, R.I. Laming, S.B. Poole, D.N. Payne, and A.P. Leach, "Distributed Temperature Sensor Using Nd^{3+}-Doped Optical Fibre," Electron. Lett. 22, 418 (1986).

30. J.P. Dakin and D.J. Pratt, "Distributed Optical Fibre Raman Temperature Sensor Using a Semiconductor Light Source and Detector," Electron Lett. 21, 570 (1985).

31. O. Iida, T. Iwamura, K. Hashiba, Y. Kurosawa, "A Fiber Optic Distributed Temperature Sensor for High-Temperature Measurements," in **Temperature: Its Measurement and Control in Science and Industry**, J.F. Schooley, ed., Vol. 6, Part 2, pp. 745-749 (American Institute of Physics, New York, 1992).

32. T. Wakami and S. Tanaka, "1.55 μm Long-Span Fiber-Optic Distributed Temperature Sensor," in **Tenth International Conference on Optical Fiber Sensors**, B. Culshaw and J.D.C. Jones, eds., Proc. SPIE 2360, pp. 134-137 (1994).

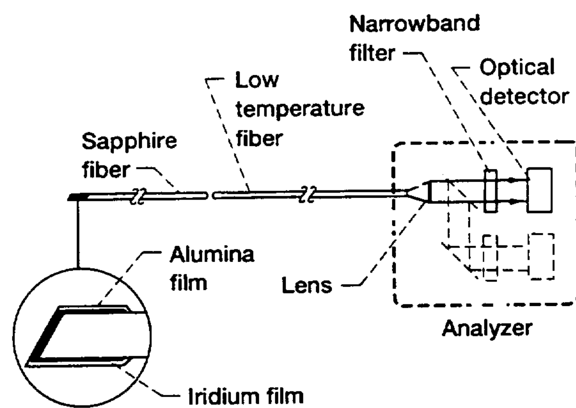

Figure 2.1 Fiber-optic thermometer using a thermally emissive sensor.

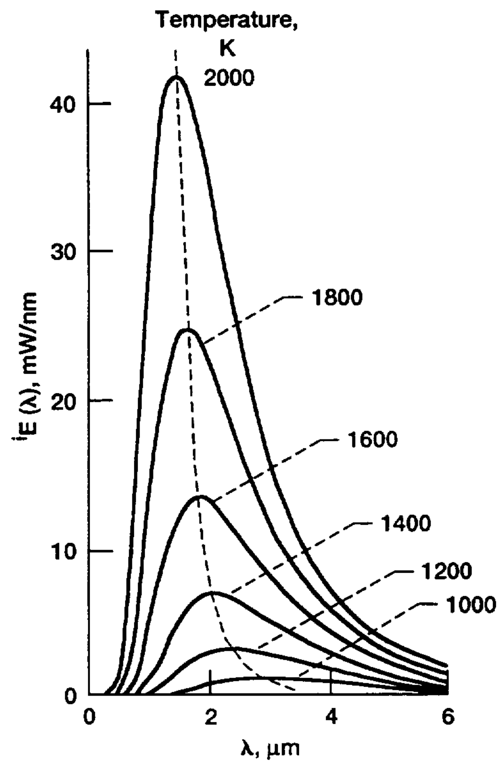

Figure 2.2 Optical spectra $i_E(\lambda)$ radiated from a black body with an area $a = 1\ cm^2$, for temperatures between 1000 K and 2000 K.

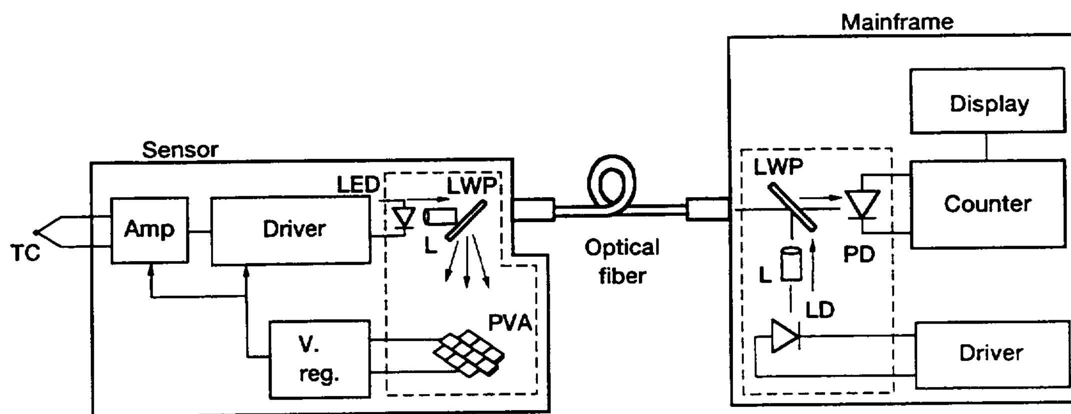

Figure 2.3 Schematic of optically linked electronic sensor showing thermocouple (TC), photovoltaic array (PVA), voltage regulator (V Reg.), long-wavelength pass filters (LWP), photodiode (PD), lenses (L), and laser diode (LD).

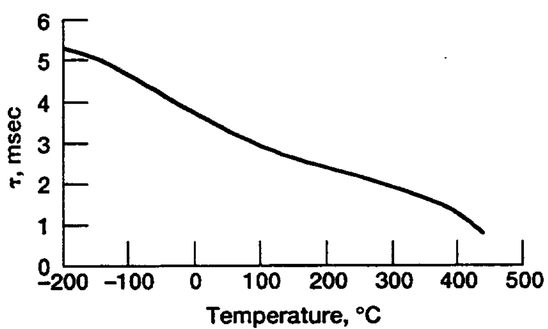

Figure 2.4 Temperature dependence of the fluorescence decay time of chromium-activated magnesium fluorogermanate.

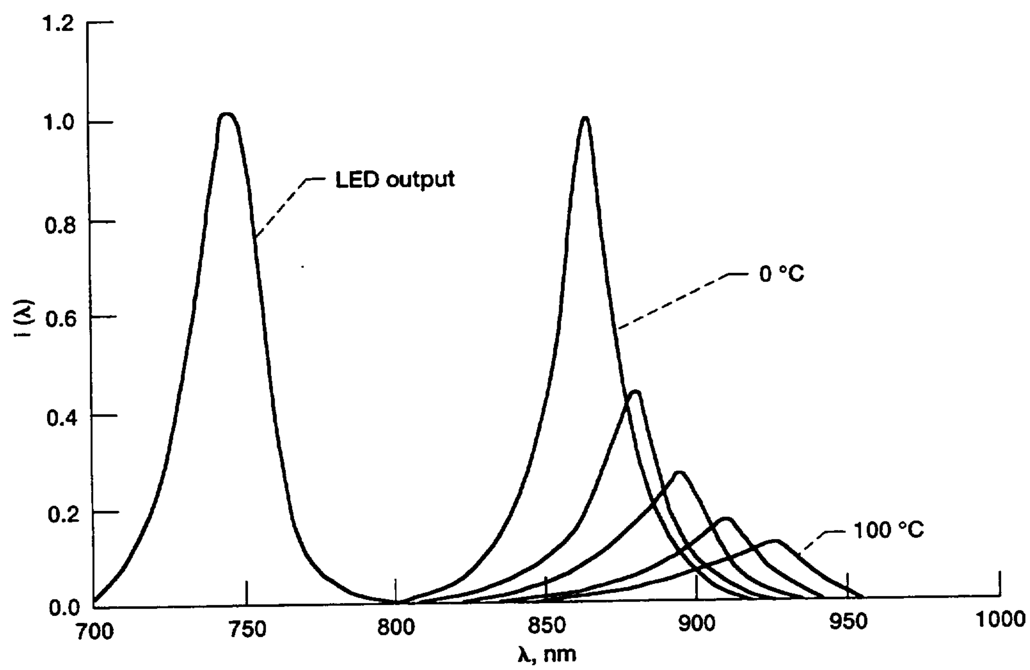

Figure 2.5 Excitation spectrum and fluorescence spectra of AlGaAs sensor at different temperatures.

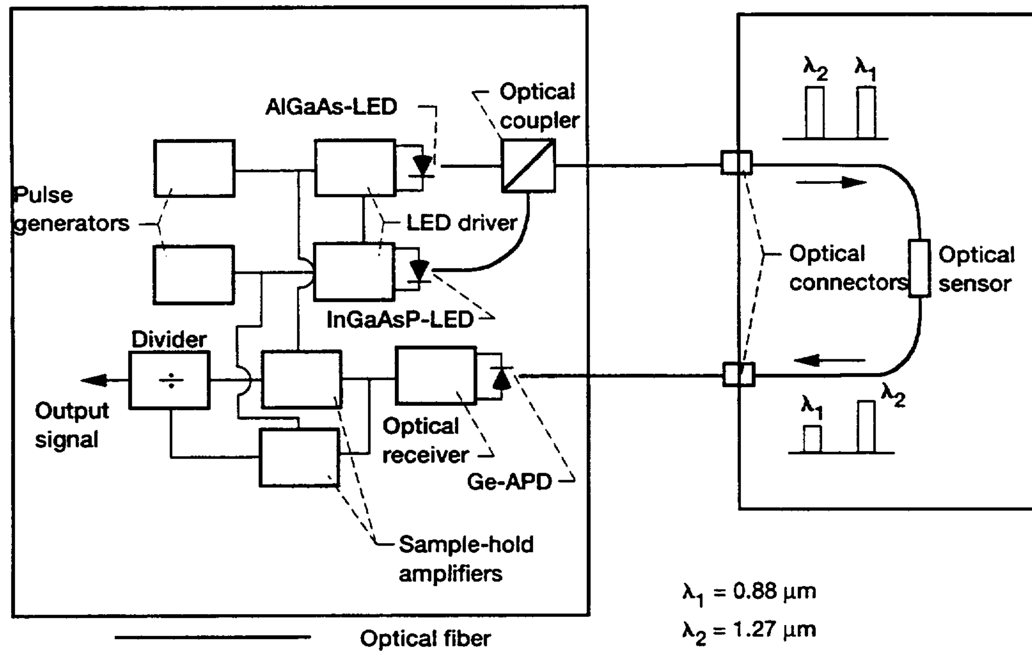

Figure 2.6 GaAs absorption-edge fiber-optic thermometer.

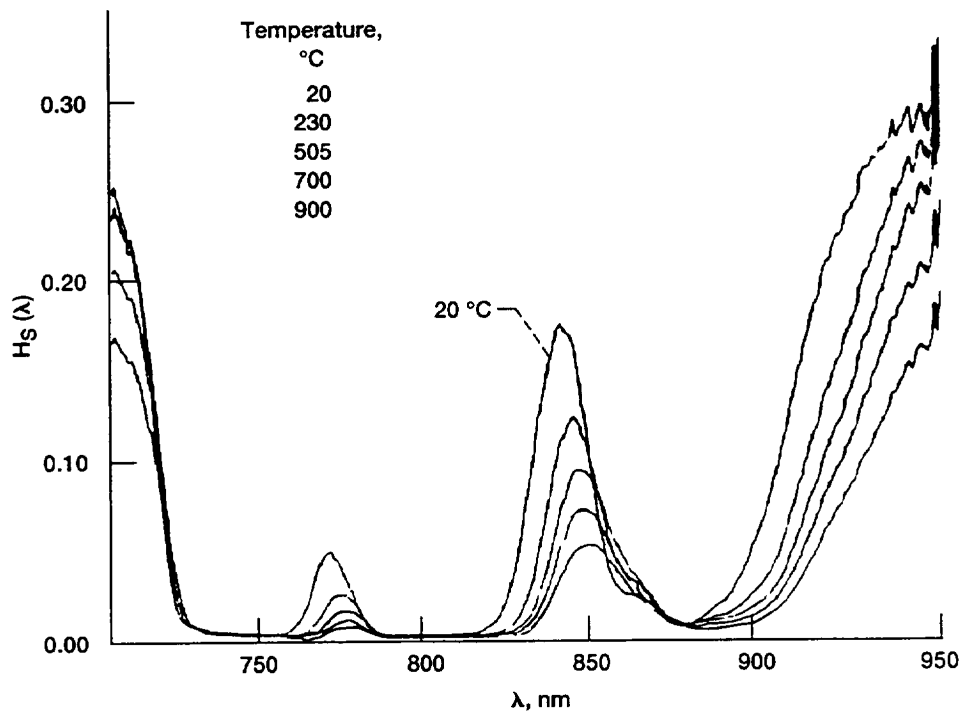

Figure 2.7 Transmissivities $H_S(\lambda)$ at different temperatures of Nd-doped fiber.

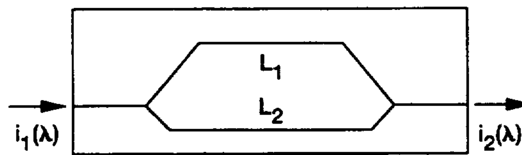

Figure 2.8 Integrated-optic interferometer for temperature measurements.

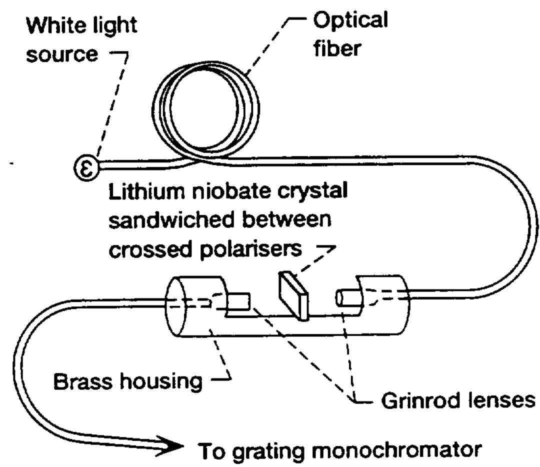

Figure 2.9 Birefringent-crystal fiber-optic temperature sensor.

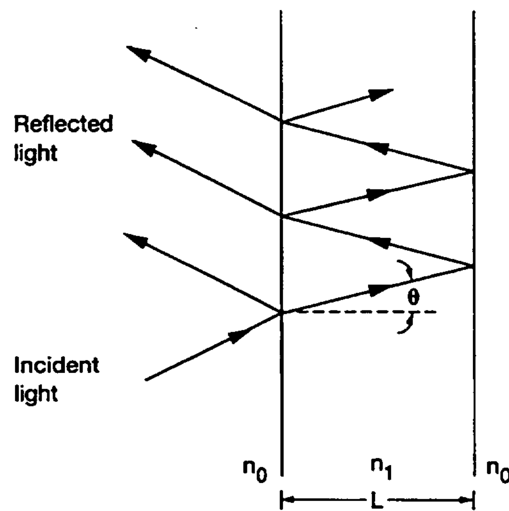

Figure 2.10 Fabry-Perot interferometer comprised of a material of thickness L and refractive index n_1 surrounded by a material with an index n_0.

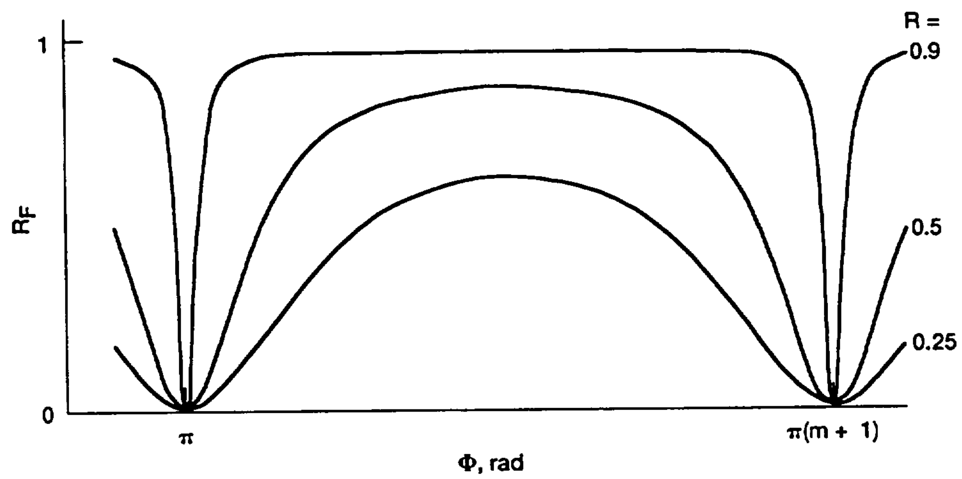

Figure 2.11 Reflectivities R_F, as functions of one-way phase-shift Φ, for Fabry-Perot interferometers having different mirror reflectivities R.

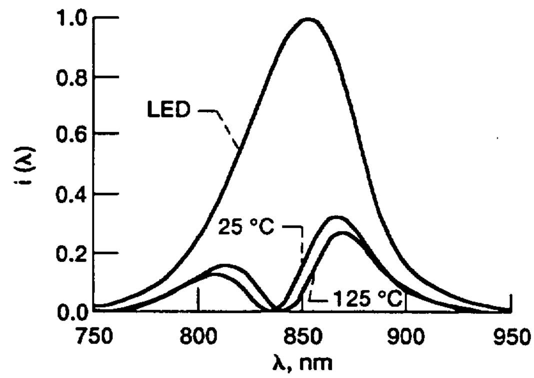

Figure 2.12 Input and output spectra of silicon Fabry-Perot temperature sensor at 25 and 125 °C, using an LED source.

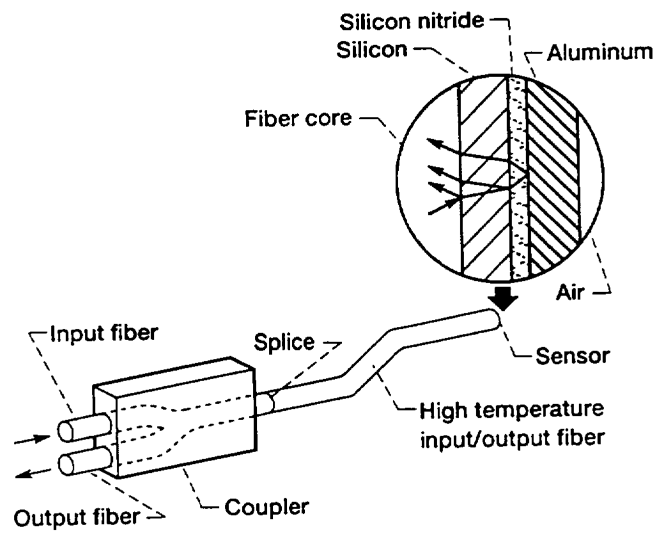

Figure 2.13 Fiber-optic temperature sensor using a thin-film Fabry-Perot interferometer.

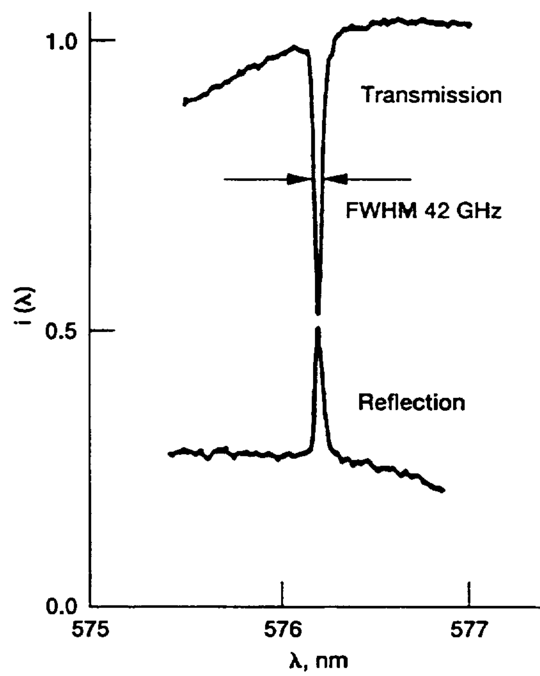

Figure 2.14 Optical spectra transmitted and reflected by a fiber Bragg grating, using a white light source.

3. REVIEW OF FABRY-PEROT TEMPERATURE SENSORS

3.1 Introduction

An instrumentation manufacturer has developed, for aircraft applications, a fluorescence-based fiber-optic temperature sensor which has a time-encoded output. This sensor largely meets the requirements for inlet-air temperature measurements in aircraft engine control systems. This section begins with a brief discussion of this sensor's principal limitation, its incompatability with wavelength-division multiplexed (WDM) digital position transducers. This limitation motivated the continued development of a thin-film Fabry-Perot temperature sensor, which is fully described in the following sections of this manuscript. The bulk of this section constitutes a review of fiber-optic Fabry-Perot temperature sensors. These sensors were discussed only briefly in the preceding section, which reviewed fiber-optic temperature sensors in general.

3.2 Advantages of Wavelength-Encoded Temperature Measurements

The fluorescence-based fiber-optic temperature sensor developed by Rosemount has a -55 to 260 °C range.[1-4] A pulse of light from a 660-nm wavelength LED excites a fluorescent emission with a wavelength of ~800 nm. After cessation of the excitation, the intensity of fluorescence decays exponentially. The time constant of decay decreases from ~300 μs at -75 °C to ~30 μs at 350 °C.[4]

A disadvantage of this sensor, for fly-by-light control systems, is its incompatibility with WDM transducers. A WDM digital position transducer encodes its measurement via the presence or absence of light at a series of wavelengths, each of which represents one of the bits of the binary-coded measurement.[5] The set of sensors for control of an aircraft engine consists in large part of position transducers. Control of a prototypical advanced-technology supersonic fighter requires continuous monitoring of 44 engine parameters, half of which are positions.[6] These position measurements are used for closed-loop control of linear actuators which adjust various aspects of the engine geometry, such as the angles of the compressor guide vanes.

In order to minimize the control system's size, weight and cost, the sensors should, whenever practical, use a common signal-encoding method so they can share the same source and receiver. Wavelength-division multiplexed encoders are presently the best accepted optical position sensors for aircraft. A grating spectrometer and two-dimensional photodiode array can be used to demultiplex the wavelength-encoded outputs of all the control system's position sensors. The same spectrometer can also analyze the radiant output spectra of the four thermally emissive probes that monitor the turbine exhaust temperature. The temperature sensor based on fluorescent decay rate, however, is incompatible with these wavelength-encoded sensors, so that it requires a dedicated opto-electronics interface. A temperature sensor with a wavelength-encoded output would therefore be preferable.

3.3 Wavelength-Encoded Temperature Measurements Using Fabry-Perot Interferometry

A wavelength-encoded temperature measurement can be provided by a temperature-sensitive Fabry-Perot interferometer. The essential feature of a Fabry-Perot interferometer is two parallel flat reflective surfaces, which are separated by a distance L. If the interferometer is operated in reflection, only

the first reflector need be partially transmissive, otherwise, both reflectors must be transmissive. The light is assumed to be collimated, with an internal angle of incidence θ_1. The Fabry-Perot interferometer's optical path difference is then given by $\Lambda_{OPD} = 2n_1L\cos\theta_1$, where n_1 is the refractive index between the reflectors. To sense temperature, Λ_{OPD} must vary as a monotonic function of temperature. This can be effected by changes in n_1 or L.

At resonance, $\lambda = \lambda_m$, where the resonant wavelength of integer-order m is given by $m\lambda_m = \Lambda_{OPD}$, the interferometer's spectral reflectance $R_F(\lambda)$ is minimized (here it is assumed that the phase changes on internal reflection are zero). The sensed temperature can be determined by tracking the position of one of the minima in $R_F(\lambda)$, since λ_m is proportional to the temperature-dependent Λ_{OPD}. This wavelength-based measurement method, because it is signal-level insensitive, has a high degree of immunity to the effects of changes in the transmissivities of the optical fibers and connectors.

The first temperature measurements using a fiber-linked Fabry-Perot interferometer were described by Christensen in 1974.[7,8] He tested two sensors: a fused-silica window, 3.2-mm thick, and a glass window, 0.145-mm thick. Multilayer dielectric mirrors were deposited on both surfaces of each

window. The high reflectivities of these mirrors provided a high finesse, which is a measure of the optical resonator's quality factor. The temperature ranges were 11 °C and 150 °C for the fused-silica and glass interferometers, respectively. If the sensed temperature is inferred from one of the resonant wavelengths λ_m, then the temperature range is that ΔT which causes a change in Λ_{OPD} equal to the initial value of λ_m.

Yoshino et al., in 1982, described the temperature sensitivity of a guided-wave Fabry-Perot interferometer that was made from a single-mode fiber with a length of several cm.[9] A high finesse was obtained by evaporating multilayer dielectric mirrors onto the ends of the fiber. Since then, other groups have used fiber Fabry-Perot interferometers to sense temperature.[10-17] The deposition of mirrors on the fiber ends has the disadvantage of requiring precise and stable mechanical alignment of the sensing fiber with a single-mode transmission fiber. A more robust approach was devised by Lee et al., who evaporated a thin TiO_2 coating onto the end of the sensing fiber prior to fusion splicing it to a transmission fiber.[12-15] Lee's group found that the reflectivity of the splice could be controlled via the fusion parameters; by the continued application of heat the titanium was made to diffuse further into the surounding SiO_2, thereby reducing the splice's reflectivity.

Temperature sensors based on optical-fiber interferometers are described only briefly here, since this approach is, at the present time, not well suited for aircraft because it uses single-mode fibers. Single-mode-fiber connectors are considerably less robust than are multimode connectors. Also, they are not yet available in the multipin configurations required for aircraft. The remainder of this review, therefore, will concentrate on Fabry-Perot sensors that are compatible with multimode optical fibers.

During the early 1980's, James and Quick developed a fiber-optic thermometer which used an air-spaced Fabry-Perot interferometer.[18-22] This sensor was designed for use at temperatures as high as 1000 °C and was tested from 20 °C to 400 °C. The interferometer's first reflector was the back surface of a thin fused-silica window; its second reflector was the top of a pedestal which was made of a material having an ultra-low thermal-expansion coefficient κ_L. Both reflecting surfaces were uncoated, and the length of the pedestal was several mm. The gap between the reflectors L, which was nominally 1 μm, was made to vary as a function of temperature by the thermal expansion of a fused-silica collar. This collar fit around the slightly shorter pedestal and was bonded, at its ends, to the first reflector and the pedestal's base. By transferring the thermal expansion of the relatively long collar to the

three-orders-of-magnitude smaller gap L, the temperature-sensitivity of the resonant wavelengths, $\lambda_m^{-1}d\lambda_m/dT$, was caused to be reasonably large despite the low κ_L of SiO_2. Disadvantages of this sensor are its mechanical complexity and large thermal mass.

In 1983, Cox and Jones described a temperature sensor which was a polymer Fabry-Perot interferometer.[23] First, a partially transmissive mirror was fabricated by evaporating a thin aluminum film on a glass cover slip. Then a 4-μm polymer film (methylmethacrylate) was applied using a photoresist spinner, and another alumimum mirror was evaporated onto the polymer. This Fabry-Perot interferometer was highly temperature sensitive because of the large changes in the polymer film's thickness and refractive index. Softening of the polymer, however, precluded the measurement of temperatures above 80 °C.

In 1985, Boreman et al. measured temperature by analyzing the spectral transmissivity of a fiber-linked all-dielectric bandpass filter.[24] The bandpass filter was a common type which uses a thin-film Fabry-Perot interferometer. On a glass substrate, a spacer film is sandwiched between two partially transmissive multilayer mirrors. The mirrors are made by stacking quarter-

wave layers of high and low index materials, alternately. So that only one of the Fabry Perot's resonant wavelengths is transmitted, multilayer blocking filters are deposited on the same substrate. Graded-index rod lenses were used to direct light from the input fiber through the filter into an output fiber. A temperature range of 20 to 150 °C was demonstrated. Sensitivity of the resonant wavelength to temperature was quite low, 0.007 nm/°C.

In 1986, using a SiC Fabry-Perot interferometer, Beheim demonstrated a temperature resolution of 1 °C over the 20 °C to 1000 °C range.[25] The temperature-sensitive material was cubic SiC, with a thickness of 18 μm, that was deposited on a silicon wafer. A SiC/Si chip was cemented, silicon side out, onto the end of a 2.5-mm-diameter alumina tube. A 1.8-mm-diameter graded-index rod microlens, positioned at the other end of the 5-cm-long tube, was used to couple light between an optical fiber and the SiC film. The ceramic tube and collimating lens allowed the fiber to be located outside of the high-temperature environment.

Using this sensor, temperature could be measured without ambiguity over any 400 °C span within the 20 °C to 1000 °C range. A temperature increase of 400 °C increased Λ_{OPD} by an amount equal to the nominal operating

wavelength of 840 nm. This caused the initial $R_F(\lambda)$ to be approximately recovered, as the next-higher-order resonance λ_{m+1} was shifted to the initial value of λ_m. Temperature could be measured, with no ambiguity, over a larger span of the 1000 °C range by reducing the thickness of the SiC film, since $d\Lambda_{OPD}/dT$ is proportional to L. The penalty associated with a reduction in L is, potentially, a degraded temperature resolution, since the reflectance minima will be broadened about the resonant wavelengths.

In 1987, Beheim described a more compact sensor in which the SiC Fabry-Perot interferometer was positioned close to the end of the fiber, without an intervening lens. The SiC-on-Si chip was cemented to the end of a ceramic ferrule, inside of which was affixed the optical fiber.[26,27] Since the fiber, in this case, is exposed to the measured temperature, the maximum temperature is limited to that of the fiber's buffer material. This sensor was tested between room temperature and 260 °C. A disadvantage of this sensor is its high sensitivity to fiber bending; a bend with a radius of 1.5 cm was found to shift the measured temperature by 2.5 °C. The modes of the optical fiber will have different angles of incidence θ_1 when they are coupled into the SiC film, therefore each mode will resonate at slightly different wavelengths. Fiber bending can alter the modal power distribution, thereby shifting the perceived

resonances. The previously described SiC sensor achieved a very high immunity to the effects of fiber bending through its use of a collimating microlens.

Besides the use of a collimating lens, another means to reduce the sensitivity to the modal power distribution is to increase the index n_1 so that refraction causes the light to be less divergent inside the interferometer. Also, higher index materials generally have a greater thermo-optic coefficient, $\kappa_n = n^{-1}dn/dT$, which further reduces the sensitivity to modal effects. In 1986, Saaski et al. described a compact Fabry-Perot temperature sensor that used single-crystal silicon as the temperature-sensitive material.[28-32] The refractive index of silicon is much larger than that of SiC, 3.7 instead of 2.6 at $\lambda = 825$ nm, and its sensitivity κ_n is almost an order of magnitude greater. The superior properties of silicon provide an adequate immunity to the effects of fiber bending without requiring collimation of the light emitted by the fiber. Of the Fabry-Perot temperature sensors described here, this has been the one most fully developed and has been marketed for a number of years under the Metricor name, presently by Photonetics.

The Metricor temperature sensor is fabricated by first diffusing a boron etch stop into a silicon wafer. The doped silicon surface is then anodically bonded to a 7740 glass substrate which provides mechanical support when the silicon is thinned to a thickness of ~ 1 μm, first by polishing and then by etching in ethylene diamine pyrocatechol (EDP). A second piece of 7740 glass, with a thickness of about 0.2 mm, is bonded to the thinned silicon, and the wafers are diced into 0.5 mm squares. The silicon and glass sandwiches are then bonded onto the ends of glass capillaries, inside of which are affixed the optical fibers. These sensors have a temperature range of -40 to 300 °C; the upper limit is imposed by the adhesives used to mount the fibers in the capillaries.

A disadvantage of this type of sensor is the labor-intensive fabrication process. In 1988, Shultheis and co-workers at ASEA described a silicon Fabry-Perot temperature sensor that was fabricated using a batch-compatible process, the silicon film being deposited directly onto the end of the fiber by electron-beam evaporation.[33-35] The amorphous silicon film was annealed for one hour at 400 °C and then coated with a protective layer of polyimide. This sensor was tested between room temperature and 400 °C. In 1989, Berthold described a similar thin-film silicon sensor that was sputter deposited.[36,37] This

amorphous-silicon film was not coated. It was annealed at 400 °C and then tested from 20 to 400 °C.

In 1989, Beheim described a Fabry-Perot temperature sensor that was fabricated by sputter-depositing, onto the end of a fiber, a three-layer structure; a one-μm silicon resonator was overcoated with two encapsulating layers.[38-40] This inorganic encapsulant was intended to provide a greater long-term stability than could be obtained using a polyimide coating, which would do little to protect the silicon from oxidation. The silicon was coated first with a 140-nm SiO_2 layer and then with about one μm of a FeCrAl alloy. The FeCrAl layer, which forms a largely impervious oxide scale, was intended to protect the silicon from oxidation. The purpose of the thin SiO_2 layer was to prevent interactions of the silicon and metal which could alter the silicon film's thickness or refractive index. After this sensor was annealed at 310 °C, it was subjected to 230 °C for 300 hrs, which was found to produce an output drift of 11 °C. These were the first reported measurements of the long-term drift of a Fabry-Perot temperature sensor.

Chao and Neudeck, in 1994, described a Fabry-Perot sensor that used a 2-μm layer of poly-crystalline silicon.[41] Multilayer dielectric mirrors were

used on both sides of the polysilicon layer to increase the interferometer's finesse. These mirrors were comprised of quarter-wave layers of polysilicon and SiO_2, three layers of each material, applied alternately. The polysilicon was deposited in a reduced-pressure epitaxial reactor at 1015 °C using dichlorosilane. This method provided a very high rate of deposition onto the silicon substrates. This sensor was not mounted on an optical fiber. A labor-intensive approach, similar to that of the Metricor sensor, would be required.

3.4 Concluding Remarks

If fiber-optic sensors are to find application in aircraft control systems, their operating lifetimes must be comparable to those of the electrical sensors that they would replace. A fiber-optic engine-inlet temperature probe should therefore maintain its ± 2 °C accuracy throughout several thousand hours of engine operation. Long-term stability is a particularly significant issue for the deposited silicon Fabry-Perot sensors, because the deposited silicon is more sensitive to thermally induced structural changes than is single-crystal silicon. Also, like single-crystal silicon, the deposited silicon is subject to oxidation, which can be significant because the exposure times are extremely long. The goal of the research described here is the development of a thin-film

Fabry-Perot sensor that is stable enough to find application in aircraft control systems. The specifications for this application are a -55 to 275 °C range and a ±2 °C accuracy throughout 5000 hrs of engine operation.

3.5 References

1. S.C. Jensen, S.D. Tilstra, G.A. Barnabo, D.C. Thomas, and R.W. Phillips, "A Fiber Optic Temperature Sensor for Aerospace Applications," **Fiber Optic Systems for Mobile Platforms IV**, N.E. Lewis and E.L. Moore, eds., Proc. SPIE 1369, pp. 87-95 (1990).

2. S.D. Tilstra, "A Fluorescence-Based Fiber Optic Temperature Sensor for Aerospace Applications," **Specialty Fiber Optic Systems for Mobile Platforms**, N.E. Lewis and E.L. Moore, eds., Proc. SPIE 1589, pp. 32-37 (1991).

3. R.W. Phillips and S.D. Tilstra, "Design of a Fiber Optic Temperature Sensor for Aerospace Applications," in **Temperature: Its Measurement and Control in Science and Industry**, J.F. Schooley, ed., Vol. 6, Part 2, pp. 721-724 (American Institute of Physics, New York, 1992).

4. K.A. Bauer, S. Gerson, D.M. Griffith, A.K. Trikha, and E.J. Woods, "Fly-By-Light/Power-By-Wire Integrated Requirements Analysis and Preliminary Design--Boeing Results," NASA CR-4590, pg. 117 (1994).

5. K. Fritsch and G. Beheim, "Wavelength-Division Multiplexed Digital Optical Position Transducer," Opt. Lett. 11, 1 (1986).

6. G.L. Poppel, W.M. Glasheen, J.C. Russell, "Fiber Optic Control System Integration", NASA CR-179568 (1987).

7. D.A. Christensen, "Temperature Measurement Using Optical Etalons," Annual Meeting of the Optical Society of America, Houston, Texas, October 15-18, 1974.

8. D.A. Christensen, "An Optical Etalon Temperature Probe for Biomedical Applications," 28th ACEMB, Paper D4a.1, Fairmont Hotel, New Orleans, Louisiana, Sept. 20-24, 1975.

9. T. Yoshino, K. Kurosawa, K. Itoh, and T. Oze, "Fiber-Optic Fabry-Perot Interferometer and Its Sensor Applications," IEEE J. Quantum. Electron. QE-18, 1624 (1982).

10. R. Kist, S. Drope, and H. Wolfelshneider, "Fiber-Fabry-Perot (FFP) Thermometer for Medical Applications," in **Second International Conference on Fiber Optic Sensors**, Proc. SPIE 514, pp. 165-170 (1984).

11. P. Akhavan Leilabady and M. Corke, "All-Fiber-Optic Remote Sensing of Temperature Employing Interferometric Techniques," Opt. Lett. 12, 772 (1987).

12. C.E. Lee and H.F. Taylor, "Interferometric Optical Fiber Sensors Using Internal Mirrors," Electron. Lett. 24, 193 (1988).

13. C.E. Lee, R.A. Atkins, and H.J. Taylor, "Performance of a Fiber-Optic Temperature Sensor From -200 to 1050 °C," Opt. Lett. 13, 1038 (1988).

14. Y. Yeh, C.E. Lee, R.A. Atkins, W.N. Gibler, and H.F. Taylor, "Fiber Optic Sensor for Substrate Temperature Monitoring," J. Vac. Sci. Technol. A 8, 3247 (1990).

15. C.E. Lee and H.F. Taylor, "Fiber-Optic Fabry Perot Temperature Sensor Using a Low-Coherence Light Source," J. Lightwave Technol. 9, 129 (1991).

16. K.A. Murphy, M.F Gunther, A.M. Vengsarkar, and R.O. Claus, "Quadrature Phase-Shifted, Extrinsic Fabry-Perot Optical Fiber Sensors," Opt. Lett. 16, 273 (1991).

17. A. Wang, S. Gollapudi, K.A. Murphy, R.G. May, and R.O. Claus, "Saphire-Fiber-Based Intrinsic Fabry-Perot Interferometer," Opt. Lett. 17, 1021 (1992).

18. K.A. James, W.H. Quick, and V.H. Strahan, "Analysis and Preliminary Design of Optical Sensors for Propulsion Control," NASA CR-159519 (1979).

19. K.A. James, W.H. Quick, and V.H. Strahan, "Optical Temperature Sensors for Propulsion Control Systems (Fabry-Perot)," NASA Report No. C81-341/201.

20. W.H. Quick, K.A. James, and J.E. Coker, "Fiber Optics Sensing Techniques," in **Optical Fibre Sensors**, IEE CP-221 (IEE, London, 1983) pp. 6-9.

21. K. James and W. Quick, "Fiber-Optic, Fabry-Perot Temperature Sensor," NASA CR-174712 (1984).

22. K.A. James, W.H. Quick, and V.H. Strahan, U.S. Patent 4,329,058 (11 May 1982).

23. E.R. Cox and B.E. Jones, "Fibre Optic Colour Sensors Based on Fabry-Perot Interferometry", in **Optical Fibre Sensors**, IEE CP-221 (IEE, London, 1983) pp. 122-126.

24. G. Boreman, R. Walters, and D. Lester, "Fiber Optic Thin Film Temperature Sensor," **Fiber Optic and Laser Sensors III**, E.L. Moore and O.G. Ramer, eds., Proc. SPIE 566, 312-316 (1986).

25. G. Beheim, "Fibre-Optic Thermometer Using Semiconductor- Etalon Sensor," Electron. Lett. 22, 238 (1986).

26. G. Beheim and K. Fritsch, "Spectrum-Modulating Fiber-Optic Sensor For Aircraft Control Systems," NASA TM-88968 (1987).

27. G. Beheim, K. Fritsch, and D.J. Anthan, "Fiber-Optic Temperature Sensor Using a Spectrum-Modulating Semiconductor Etalon," **Fiber Optic and Laser Sensors V**, R.P. DePaula and E. Udd, eds., Proc. SPIE 838, 238-246 (1988).

28. E.W. Saaski, J.C. Hartl, G.L. Mitchell, R.A. Wolthuis, and M.A. Afromowitz, "A Family of Fiber Optic Sensors Using Cavity Resonator Microshifts," Technical Digest OFS '86: 4th International Conference on Optical Fiber Sensors, Tokyo, October 7-9, 1986, pp. 11-14 (Institute of Electronics and Communications Engineers of Japan, Tokyo, 1986).

29. E. Saaski and J. Hartl, U.S. Patent 4,678,904 (7 July 1987).

30. J.C. Hartl, E.W. Saaski, and G.L. Mitchell, "Fiber Optic Temperature Sensor Using Spectral Modulation," in **Fiber Optic and Laser Sensors V**, R.P. DePaula and E. Udd, eds., Proc. SPIE 838, 257-261 (1988).

31. E.W. Saaski and J.C. Hartl, "Thin-Film Fabry Perot Temperature Sensors," in **Temperature: Its Measurement and Control in Science and Industry**, J.F. Schooley, ed., Vol. 6, Part 2, pp. 731-734 (American Institute of Physics, New York, 1992).

32. Technical Literature, Photonetics, Inc., 401 Edgewater Place, Suite 140, Wakefield, Massachusetts, 01880.

33. L. Shultheis, H. Amstutz, and M. Kaufmann, "Fiber-Optic Temperature Sensing With Ultrathin Silicon Etalons," Opt. Lett. 13, 782 (1988).

34. L. Shultheis, "A Simple Fiber-Optic Fabry-Perot Temperature Sensor," in **Optical Fiber Sensors, 1988 Technical Digest Series**, Vol. 2 (Optical Society of America, Washington, D.C., 1988) pp. 506-509.

35. M. Kaufmann and L. Shultheis, UK Patent Application GB 2,204,948A (11 May 1988).

36. J.W. Berthold, S.E. Reed, and R.G. Sarkis, "Simple, Repeatable, Fiber Optic Intensity Sensor for Temperature Measurement," **Fiber Optic and Laser Sensors VII**, E. Udd and R.P. DePaula, eds., Proc. SPIE 1169, pp. 512-520 (1990).

37. J.W. Berthold, S.E. Reed, and R.G. Sarkis, "Reflective Fiber Optic Temperature Sensor Using Silicon Thin Film," Optical Eng. 30, 524 (1991).

38. G. Beheim, K. Fritsch, J.M. Flatico, and M. Tabib-Azar, "Silicon-Etalon Fiber Optic Temperature Sensor," **Fiber Optic and Laser Sensors VII**, E. Udd and R.P. DePaula, eds., Proc. SPIE 1169, pp. 504-511 (1990).

39. G. Beheim, K. Fritsch, and M. Tabib-Azar, "Sputtered Thin-Film Fiber-Optic Temperature Sensor," Proceedings of Sensors Expo, Cleveland, Ohio, September 12-14, 1989, paper #204B (Helmers Publishing, Peterborough, NH, 1989).

40. G. Beheim, K. Fritsch, and M. Tabib-Azar, "Sputtered Thin Film Fiber-Optic Temperature Sensor," Sensors Vol. 7, No. 1, January, 1990, pp. 37-43.

41. H.C. Chao and G.W. Neudeck, "Polysilicon Fabry-Perot Cavities Deposited With Dichlorosilane in a Reduced Pressure Chemical Vapor Deposition Reactor for Thermal Sensing," Electron. Lett. 30, 80 (1994).

4. PRELIMINARY DESIGN
OF A FABRY-PEROT TEMPERATURE SENSOR

4.1 Introduction

This section will develop a preliminary design for a fiber-optic Fabry-Perot temperature sensor that meets the requirements of an aircraft engine's control system for inlet air temperature measurements. Briefly, these requirements are:

(a) -55 to 275 °C range,

(b) ±2 °C accuracy,

(c) 5000 hr lifetime,

(d) portable calibration.

With the aircraft application in mind, this design will be predicated on the use of multimode optical fibers, SMA single-channel or military-style multipin connectors, solid-state optical sources, and spectrometers which are based on inexpensive photodiode arrays. The principal objectives of this

section are the selection of a temperature-sensitive material and an approximate determination of the thickness of the thin-film interferometer.

4.2 Optical Fiber System

Figure 4.1 shows a schematic of the temperature-sensing system. Multimode, rather than single-mode, optical fibers are used because multimode interconnects are less expensive and more reliable (core diameters of multimode fibers are typically 100 μm as opposed to ~ 8 μm for single-mode fibers). Also, multimode optical fibers with high-temperature buffer coatings are available off-the-shelf, while high-temperature single-mode fibers would have to be specially fabricated. The standard fiber for aircraft applications is fused silica with 100/140 μm core/cladding diameters, either step or graded index.

The thin-film Fabry-Perot interferometer is deposited on the cleaved end of a short length of high-temperature optical fiber. Fused-silica, rather than plastic, fibers are of course most suitable for this application. Both the core and cladding are fused silica, with dopants incorporated into one or both to raise the core index relative to that of the cladding. Fused-silica fibers must

be coated with a buffer material to protect the surface of the glass from abrasion as well as moisture and other corrosive chemicals. Uncoated fibers will develop microcracks in the glass surface, which cause stress concentrations that lead eventually to breakage. Readily available buffer materials that are rated for use at 275 °C are polyimide, gold and aluminum. Polyimide is the least expensive, but it gradually degrades at about 300 °C. Polyimide coatings are more appropriate for the coupler and interconnect fibers, which are located in a -55 to 200 °C ambient.

Gold and aluminum coated fibers also were tested in a furnace at temperatures from 300 to 500 °C for periods up to several days. The aluminum-coated fibers were found to be quite reliable despite prolonged exposure to 300 °C, but they became brittle after ~24 hours at 400 °C. The gold fibers were found to be generally unreliable. The gold coating may be less effective than the aluminum at holding the glass surface in compression. The aluminum-coated optical fiber that was selected for sensor fabrication had a step-index profile, with 100/140 μm core/cladding diameters, and a 0.20 NA.

The high-temperature optical fiber, with the temperature-sensitive thin-film interferometer on its distal end, is permanently fused to the unpaired port

of a 3-dB 2 x 1 fiber-optic coupler. Separate input and output fibers link the remotely located sensor, and dematable connectors are used only in these fibers. Hence, any light reflected from the connectors is strongly attenuated, since the interfering light must twice pass through the sensor (thereby undergoing four transits of the 3-dB coupler) en route from the source to the receiver. Locating the coupler locally and using a single fiber to connect the remote sensor is ruled out by the large (and variable) offsets that would be caused by reflections from the connectors. If such a bi-directional link were used, light could travel from the source to a connector and then back to the receiver, without encountering the sensor. In this case, the back-reflected light could very well be equal in intensity to the light returned from the sensor.

Back reflections are a characteristic of single-channel SMA connectors and the multipin connectors, based on electrical shells, that are preferred for aircraft applications. In such connectors the fiber ends are separated by about 20 μm. Some connector designs, such as FC and ST, obtain low back reflections by a convex end polish and spring-loaded ferrules, which cause the fiber cores to be optically contacted. This approach, of course, can be made ineffective by debris, which is prevalent on aircraft. Also, it is more successful for single-mode fibers, as it is not possible to maintain optical

contact over a larger-diameter core. The use of index matching gels inside FC or ST connectors can provide very low back reflections with multimode fibers, but this method is unsuitable for aircraft.

On an aircraft, a grating spectrometer will be used to analyze the sensor's output spectrum. A miniature spectrometer which employs a two-dimensional photodiode array can analyze the spectrally encoded outputs of a network of temperature, pressure and position sensors.[1,2] Silicon photodiode arrays are far less expensive and more reliable than are detector arrays which respond to longer wavelengths. Two-dimensional silicon CCD arrays are available for less than $50. For transmission through fused-silica fibers and detection by silicon photodiodes, AlGaAs LEDs are the solid-state sources of choice. The wavelength of peak intensity is typically 830 nm ± 50 nm, and the spectral width (FWHM) is about 60 nm. In the laboratory, a tungsten lamp together with a scanning monochromator and a single silicon photodiode were used to characterize the temperature sensors. This appproach provided the best attainable spectral resolution and range.

4.3 Ideal Fabry-Perot Temperature Sensor

A model of the thin-film Fabry-Perot temperature sensor will be developed here. This model will provide a basis for a preliminary sensor design which consists of the selection of a material and the determination of the optimum thickness range. An idealized model will be used which neglects absorption and assumes equal reflectivities at both surfaces of the film. Encapsulating layers will not be considered until the following section.

Consider the thin-film Fabry-Perot interferometer shown in Fig. 4.2. The film has a thickness of L and a refractive index of n_1. It is surrounded by a material of index n_0, where $n_1 > n_0$. Collimated light is assumed, and the materials are assumed to be lossless. Then, as derived in the appendix, the interferometer's reflectance is

$$R_F(\Phi) = \frac{F\sin^2(\Phi)}{1+F\sin^2(\Phi)} . \qquad (1)$$

Here, the (one-way) phase shift Φ is given by

$$\Phi = \pi \frac{\Lambda_{OPD}}{\lambda} , \tag{2}$$

where the optical path difference Λ_{OPD} is

$$\Lambda_{OPD} = 2 n_1 L \cos\theta_1 . \tag{3}$$

The coefficient F is given by

$$F = \frac{4R}{(1-R)^2} , \tag{4}$$

where R is the reflectivity of the film's surfaces,

$$R = \frac{(n_1 - n_0)^2}{(n_1 + n_0)^2} . \tag{5}$$

The coefficient F determines the interferometer's finesse, $(\pi/2)\ F^{1/2}$, which is analogous to the quality factor of a resonant circuit. A higher R sharpens the reflectance minima, or fringes, as shown by Fig. 2.11 which gives $R_F(\Phi)$ for various values of R.

The interferometer's reflectance is minimized at resonance, or $\Phi = \pi m$, where m is an integer. For the ideal Fabry-Perot interferometer, $[R_F]_{MIN} = 0$.

In terms of wavelength, the resonance condition is $\lambda = \lambda_m$, where

$$\lambda_m = \Lambda_{OPD}/m. \tag{6}$$

The maximum reflectance, which occurs at $\Phi = \pi(m+1/2)$, is given by

$$[R_F]_{MAX} = \frac{F}{1+F}. \tag{7}$$

The interferometer's phase sensitivity is obtained by differentiating Eq. 1, which gives[3]

$$\frac{dR_F}{d\Phi} = \frac{F\,\sin 2\Phi}{(1+F\,\sin^2\Phi)^2}. \tag{8}$$

The phase sensitivity is a maximum at $\Phi = \pi m \pm \Phi_0$, where

$$\Phi_0 = \frac{1}{2}\cos^{-1}\left(\frac{1}{2}\sqrt{9+4/F+4/F^2} - \frac{1}{F} - \frac{1}{2}\right). \tag{9}$$

For R small, $\Phi_0 \approx \pi/4$. As R increases and begins to approach 1, Φ_0 approaches 0. For a given Λ_{OPD}, the wavelengths of maximum sensitivity are equal to $\Lambda_{OPD}/(m \pm \Phi_0/\pi)$.

The Fabry-Perot interferometer's maximum phase sensitivity is

$$\left|\frac{dR_F}{d\Phi}\right|_{MAX} = \frac{1}{F}\left[\frac{1}{\sin^3 2\Phi_0} - \frac{1}{\sin 2\Phi_0}\right]. \tag{10}$$

Figure 4.3 shows the dependence of $|dR_F/d\Phi|_{MAX}$ on R. For R sufficiently large, the Fabry Perot has a greater phase sensitivity than does a two-beam interferometer. The transmissivity of an ideal Michelson interferometer is given by

$$H_M(\Phi) = \frac{1}{2}\ (1-\cos 2\Phi)\ , \tag{11}$$

where Φ is still $\pi\Lambda_{OPD}/\lambda$, but, in this case, $\Lambda_{OPD} = 2n_1L$, where L is the imbalance in the lengths of the Michelson's arms. Maximum phase sensitivity is obtained at $\Phi = \pi(m \pm 1/4)$, and is equal to 1 rad^{-1}. As shown by Fig. 4.3, the phase sensitivity of a Michelson interferometer is exceeded by an ideal Fabry Perot if $R > 0.3$.

If the RMS detector noise is δi_N, then the minimum detectable phase shift is given by

$$\delta \Phi_N = \left[S_D \; H_{FO} \; I_0 \left| \frac{dR_F}{d\Phi} \right|_{MAX} \right]^{-1} \delta i_N, \qquad (12)$$

where S_D is the detector's sensitivity, H_{FO} is the optical system's transmissivity, and I_0 is the input optical intensity. If a grating spectrometer and photodiode array are used to analyze the interferometer's reflectance, then $I_0 = i_0(\lambda_p)\delta\lambda_A$, where $i_0(\lambda)$ is the source spectrum, λ_p is the wavelength incident on photodiode p, and $\delta\lambda_A$ is the analyzer's spectral bandwidth. The phase sensitivity will vary as a function of the detected wavelength, with the maximum sensitivity provided by the photodiodes for which $\Phi = \pi m \pm \Phi_0$. The instrument's ultimate phase resolution will depend on the procedure used to determine Φ from $R_F(\lambda)$, but can be no better than the value of $\delta\Phi_N$ for the optimally positioned diodes divided by the square root of the number of diodes.

The temperature sensitivity of the Fabry Perot's phase shift is given by

$$\frac{d\Phi}{dT} = \pi \frac{\Lambda_{OPD}}{\lambda} \kappa_\Phi, \qquad (13)$$

where

$$\kappa_\Phi = \kappa_n + \kappa_L . \tag{14}$$

Here, κ_n is the thermo-optic coefficient,

$$\kappa_n = \frac{1}{n_1}\frac{dn_1}{dT} , \tag{15}$$

and κ_L is the thermal-expansion coefficient,

$$\kappa_L = \frac{1}{L}\frac{dL}{dT} . \tag{16}$$

The temperature sensitivity of the Fabry Perot's reflectance can be determined by substituting from Eqs. 8 and 13 into $dR_F/dT = (dR_F/d\Phi)\,(d\Phi/dT)$.

4.4 Selection of Temperature-Sensitive Material

As the first step in the selection of a thin-film interferometer material, the temperature sensitivities of various candidate materials will be compared. This requires a sensitivity figure-of-merit which is independent of the film thickness. Assume that the temperature is determined as a function of one of the resonant wavelengths λ_m. The relative temperature sensitivity of λ_m is

given by

$$\kappa_S = \frac{1}{\lambda_m} \frac{d\lambda_m}{dT} . \qquad (17)$$

Here, $\kappa_S = \kappa_\Phi$. Table 4.1 ranks the candidate materials in descending order of κ_Φ. This table also provides n, κ_n and κ_L, together with the wavelengths at which the optical properties were measured. In the case of all the materials except aluminum, the Fabry-Perot interferometer is assumed to be a thin film. The κ_L of aluminum provides the sensitivity of an interferometer which is comprised of two mirrors separated by an aluminum spacer. The sensitivity of this air-spaced resonator is relatively low. Since this sensor is also relatively large and difficult to fabricate, it will not be considered further.

For all the optical materials listed in Table 4.1, $\kappa_n >> \kappa_L$, so the temperature-induced phase change is almost entirely caused by the change in refractive index. The temperature sensitivity κ_n is greatest for the high-index semiconductors, which are, in descending order of sensitivity, GaAs, Ge and Si. For these semiconductors, κ_n is highly wavelength dependent. With decreasing λ, κ_n generally increases, as shown by the entries in Table 4.1 for silicon.

Table 4.1 Properties of candidate Fabry-Perot materials. Units of κ_n, κ_L and κ_Φ are 10^{-6}/°C.

Material	λ, μm	n	κ_n	κ_L	κ_Φ, 10^{-6}/°C
GaAs	0.9	3.6 [4]	120 [4]	5.7 [5]	126
Ge	2.55	4.06 [6]	100 [6]	5.7 [7]	106
Si	2.5	3.44	46 [6]	2.6 [8]	
	1.5	3.5	53 [9]		
	1.26	3.51 [10]	59 [10]		
	0.78	3.695 [11]	76 [11]		79
CdTe	1.15	2.79 [12]	53 [12]	5.0 [12]	58
TiO_2	0.7	2.55,n_o [7]	16 [5]	7.1 [5]	23
(Rutile)		2.83,n_e [7]	35 [5]	9.2 [5]	44
ZnS	0.63	2.35 [12]	27 [12]	6.9 [12]	34
Al	---	----	--	23	23
MgO	0.77	1.74 [5]	8.1 [5]	14 [5]	22
Si_3N_4	0.80	2.01 [13]	NA	2.8 [14]	19 [15]
SiC	0.83	2.61 [16]	NA	4.2 [14]	17 [16]
SiO_2	0.63	1.46 [7]	15 [7]	0.5 [7]	15
Al_2O_3	0.85	1.76 [7]	10 [7]	5 [7]	15

Of the three materials with the largest values of κ_Φ, silicon is best suited for this application. The material with the highest temperature sensitivity, GaAs, is not sufficiently stable at the sensor's maximum temperature of 275 °C. Evaporation of arsenic from GaAs has been detected after only 10 min at 450 °C.[17] Also, stoichiometric GaAs cannot readily be deposited on the end of a fiber. Germanium, which has the second highest κ_Φ, is readily sputter-deposited, however, it is highly absorbing at the emission wavelengths

of AlGaAs LEDs. At 830 nm, the absorption coefficient of germanium is 4.5×10^4 cm^{-1}, so that transmission through 1 μm produces a 20-dB loss.[13] At 1.3 μm, α is much lower, 0.68×10^4 cm^{-1}, but this wavelength is outside the range of inexpensive silicon photodiode arrays. Silicon is preferrable to germanium for this application, because its absorption coefficient is much lower at the AlGaAs emission wavelengths. At 830 nm, $\alpha = 0.19 \times 10^4$ cm^{-1}, which causes a 17% absorption in 1 μm.[13]

In addition to a high κ_Φ, the Fabry-Perot material should have a high refractive index. A higher value of n provides a larger R, which increases the maximum reflectivity $[R_F]_{MAX}$ and the maximum phase sensitivity $|dR_F/d\Phi|_{MAX}$. Assume that the film is deposited on the end of a fused-silica fiber and is overcoated by a very thick layer of SiO_2, so that $n_0 = 1.46$. Table 4.2 provides, for each of the candidate materials, $|dR_F/d\Phi|_{MAX}$ and $[R_F]_{MAX}$, both of which increase with increasing n_1. Once again, absorption of these materials is neglected to simplify this preliminary design. For silicon, $[R_F]_{MAX} = 0.53$, which provides sufficient sensitivity that no reflectivity-enhancing coatings are necessary.

Table 4.2 Properties of Fabry-Perot temperature sensors fabricated from candidate materials.

Material	n	$\lvert dR_F/d\Phi \rvert_{MAX}$	$[R_F]_{MAX}$	δT_θ, °C
GaAs	3.6	0.58	0.51	12
Ge	4.06	0.71	0.59	12
Si	3.695	0.60	0.53	19
CdTe	2.79	0.34	0.32	44
TiO_2	2.55, n_o	0.26	0.26	130
	2.83, n_e	0.35	0.34	58
ZnS	2.35	0.20	0.20	110
MgO	1.74	0.03	0.03	300
Si_3N_4	2.01	0.10	0.10	250
SiC	2.61	0.28	0.27	170
SiO_2	1.46	0	0	630
Al_2O_3	1.76	0.03	0.03	430

In selecting a Fabry-Perot material, another factor which should be considered is the interferometer's sensitivity to the angular distribution of the light. Higher-order modes have a larger propagation angle in the fiber so they will have a larger angle of incidence, θ_1, once they are coupled into the thin-film interferometer. The measured $R_F(\lambda)$ is a power-weighted average of the reflectances of the individual modes. These modal reflectances will differ from each other because Φ is θ_1 dependent, as indicated by Eqs. 2 and 3. The

maximum value of θ_1 is given by

$$[\theta_1]_{MAX}=\sin^{-1}(NA/n_1)\,, \tag{18}$$

where NA is the fiber's numerical aperture, which, for fused-silica multimode fibers, is typically between 0.2 and 0.3. For $0 \leq \theta_1 \leq [\theta_1]_{MAX}$, Φ varies from Φ_0 to $\Phi_0 - \delta\Phi_\theta$, where Φ_0 is the phase shift for normal incidence and

$$\delta\Phi_\theta=\pi\frac{\Lambda_{OPD}}{\lambda}\frac{(NA)^2}{2n_1^2}\,. \tag{19}$$

Here it has been asssumed that $(NA/n_1)^2 << 1$. For a fixed Λ_{OPD}, $\delta\Phi_\theta$ can be decreased by increasing n_1. The value of $\delta\Phi_\theta$ must be smaller than $\pi/2$ to prevent a significant degradation of the interferometer's fringe visibility (if $\delta\Phi_\theta > \pi$ then the fringes will be essentially washed out). This dictates a limit to Λ_{OPD}/λ, once the material has been selected and the value of n_1 defined.

The modal power distribution can be expected to vary due to perturbations, such as fiber bending (macro and micro), which cause coupling between modes. Such modal variations may shift the perceived values of λ_m, thereby shifting the measured temperature. The difference in Φ between the lowest and highest angles of incidence, $\delta\Phi_\theta$, is equivalent to a temperature

difference of

$$\delta T_\theta = \frac{(NA)^2}{2n_1^2\kappa_\Phi} . \tag{20}$$

A lower δT_θ, therefore, indicates a lower modal sensitivity. Table 4.2 provides δT_θ for the candidate sensor materials, assuming that NA = 0.2. The lowest values of δT_θ are provided by GaAs, germanium and silicon. All the other materials have considerably higher modal sensitivities. For silicon, δT_θ = 19 °C. In practice, the temperature variations due to modal effects will be considerably smaller than δT_θ, since the mode of the lowest or highest order is never solely present; all the modes will be populated to some extent. The actual sensitivity to modal effects can only be determined by experiment, and will be addressed fully in section 8.

Based on the above considerations, silicon was determined to be the best material for the fabrication of a thin-film Fabry-Perot temperature sensor. The following subsection will develop the criteria used to determine the thickness of the temperature-sensitive silicon film.

4.5 Determination of the Fabry-Perot Temperature Sensor's Thickness

An important design parameter is the interferometer's fringe order, which is given by $m = \Lambda_{OPD} / \lambda_m$, where λ_m is the monitored resonant wavelength and m is an integer. As shown by Eq. 13, increasing m increases the temperature sensitivity of the phase shift Φ. Increasing m also decreases the period of $R_F(\lambda)$, so that analysis of R_F requires the resolution of smaller wavelength differences. The wavelength change corresponding to $\Delta\Phi = \pi$ is termed the free spectral range, $\Delta\lambda_{FSR}$. For moderately large m,

$$\frac{\Delta\lambda_{FSR}}{\lambda_m} \approx \frac{\lambda_m}{\Lambda_{OPD}} . \tag{21}$$

It has been assumed throughout this section that the analyzer's spectral bandwidth $\delta\lambda_A$ and the wavelength sampling interval $\delta\lambda_S$ are both sufficiently small to allow the fringes of $R_F(\lambda)$ to be resolved. For the instrument under consideration here, $\delta\lambda_A > \delta\lambda_S$, so $\delta\lambda_A$ is the resolution-limiting factor. A typical photodiode array has a center-to-center spacing of 25 μm. Since the width of the photodiodes is significantly less than the 100-μm diameter of the fiber core, the analyzer's spectral bandwidth $\delta\lambda_A$ is approximately equal to the

product of the core diameter and the spectral dispersion, $d\lambda/dx$. The wavelength sampling interval $\delta\lambda_S$, which is the product of the dispersion and the diode spacing, is, for this instrument, a factor of 4 lower than $\delta\lambda_A$.

For low values of R, $R_F(\lambda)$ is approximately sinusoidal (for sufficiently large m) and $\delta\lambda_A$ can be as large as $\Delta\lambda_{FSR} / 2$. As R is increased, $R_F(\lambda)$ becomes less sinusoidal and is increasingly constituted by components of higher order. Therefore, a smaller $\delta\lambda_A$ is required. For large R, $\delta\lambda_A$ should be smaller than the fringe width (FWHM), which is approximately $\Delta\lambda_{FSR}$ divided by the finesse.

The spectral width of the optical source $\Delta\lambda_{LED}$, imposes a lower bound on the fringe order. It is assumed here that the source spectrum is a subset of the analyzer's range. To determine Φ independently of the received signal level, $\Delta\lambda_{LED}$ should be large enough to permit the analysis of a good portion, at least 1/2, of a free spectral range. The requirement that $\Delta\lambda_{LED} \geq \Delta\lambda_{FSR}/2$ gives

$$\frac{\Delta\lambda_{LED}}{\lambda_m} \geq \frac{\lambda_m}{2\Lambda_{OPD}} . \qquad (22)$$

The required measurement range also needs to be considered in determining a design value of m. The temperature increase that causes a phase change $\Delta\Phi = \pi$, thereby shifting λ_{m+1} to the original position of λ_m, is inversely proportional to m and is given by

$$\Delta T_{FSR} = \frac{\lambda_m}{\Lambda_{OPD}\,\kappa_\Phi}\ . \qquad (23)$$

If the temperature is determined from the resonant wavelength λ_m, or, equivalently, if the temperature is determined by measuring Φ at a fixed wavelength, then the measurement range, T_{MAX} - T_{MIN}, can be no greater than ΔT_{FSR}.

A greater temperature range can be provided by using an alternative technique, which is based on a measurement of the period of the cyclic component of $R_F(\lambda)$, i.e. $\Delta\lambda_{FSR}$, instead of the phase. The opportunity to extend the range beyond $\Delta\Phi = \pi$ arises because ΔT_{FSR} is λ dependent, so that the initial form of $R_{FP}(\lambda)$ is not fully recovered for any nonzero ΔT.

Since $\Delta\lambda_{FSR} = \lambda_m - \lambda_{m+1}$, the temperature sensitivity of $\Delta\lambda_{FSR}$ is

$$\frac{d(\Delta\lambda_{FSR})}{dT} = -\frac{\lambda_m^2 \kappa_\Phi}{\Lambda_{OPD}} . \tag{24}$$

In order to resolve a temperature change δT, $\Delta\lambda_{FSR}$ must be measured with a resolution of $\delta[\Delta\lambda_{FSR}]$, where

$$\frac{\delta\,[\Delta\lambda_{FSR}]}{\Delta\lambda_{FSR}} \leq \kappa_\Phi\ \delta T. \tag{25}$$

Since the required temperature resolution is about 1 °C and κ_Φ is no greater than $\sim 10^{-4}$/°C, this analysis method requires an exceptionally accurate measurement of $\Delta\lambda_{FSR}$. Because of its impracticality for this application, this technique will not be further considered.

The wide measurement range of this period-based approach can be maintained, and the required accuracy of the $\Delta\lambda_{FSR}$ measurement significantly relaxed, if the $\Delta\lambda_{FSR}$ measurement is combined with a measurement of the phase of the cyclic component of $R_F(\lambda)$. Here the phase measurement determines the value of Φ modulo π, while the integer value of Φ/π is determined from the measured $\Delta\lambda_{FSR}$. Equivalently, two adjacent resonances λ_m and λ_{m+1} can be tracked. If the temperature range is greater than ΔT_{FSR},

then the fringe order of these resonances will be initially unknown, but can be determined from the measured free spectral range, $\Delta\lambda_{FSR} = \lambda_m - \lambda_{m+1}$. To determine m, the accuracy of the $\Delta\lambda_{FSR}$ measurement must be less than the change produced by one fringe shift, which implies that

$$\frac{\delta\,[\Delta\lambda_{FSR}]}{\Delta\lambda_{FSR}} \leq \frac{\lambda_m}{\Lambda_{OPD}}\,. \tag{26}$$

The various constraints on the fringe order can be summarized as follows:

(a) To obtain a temperature resolution of δT, the resonant wavelength must be determined with a resolution of

$$\delta\lambda_m = \lambda_m\,\kappa_\phi\,\delta T. \tag{27}$$

The required resolution in λ_m, therefore, is independent of m. However, m can determine the value of $\delta\lambda_m$, because a larger m sharpens the fringes and makes the resonances easier to locate. This effect is made apparent when δT

is related to the minimum resolvable phase change $\delta\Phi$, which gives

$$m \geq \frac{\delta\Phi}{\pi \kappa_{\phi} \delta T} . \tag{28}$$

The minimum resolvable phase change $\delta\Phi$ can be no less than the noise-equivalent phase change $\delta\Phi_N$. In choosing m, it should be kept in mind that, for a given δT, a higher fringe order allows a larger $\delta\Phi$. For silicon, if L = 2 μm, then δT = 1 °C requires that $\delta\Phi$ = 4 mrad.

(b) A lower bound on m is imposed by the requirement that the source spectral width $\Delta\lambda_{LED}$ encompass at least half a free spectral range, which gives

$$m \geq \frac{\lambda_m}{2\ \Delta\lambda_{LED}} . \tag{29}$$

For a typical AlGaAs LED, λ = 830 nm and $\Delta\lambda_{LED}$ = 60 nm, which gives m $\geq$ 7. For silicon, this corresponds to L $\geq$ 0.8 μm.

(c) An upper bound on m is imposed by the analyzer's spectral bandwidth $\delta\lambda_A$,

$$m \leq \frac{\lambda_m}{2\delta\lambda_A} . \tag{30}$$

This is not a difficult requirement to fullfill. If $\delta\lambda_A = 10$ nm then m must be less than 40.

(d) By requiring that the intermodal phase differences be sufficiently small that the fringe visibility is not severely degraded, i.e. $\delta\Phi_\theta < \pi/2$, one obtains

$$m \leq \frac{n_1^2}{(NA)^2} , \tag{31}$$

where NA is the fiber's numerical aperture. If NA = 0.2, and the resonator material is silicon, then m must be less than 330. This requirement also is irrelevant in this case.

(e) Assume that the temperature is determined, over the range from T_{MIN} to T_{MAX}, as a function of resonant wavelength λ_m. Then T_{MAX} can be no greater

than the temperature at which $\lambda_{m+1}(T) = \lambda_m(T_{MIN})$. Thus,

$$m \leq \frac{1}{\kappa_{\Phi} \ (T_{MAX} - T_{MIN})} \ . \qquad (32)$$

For a silicon sensor with a -55 to 275 °C range, m must be less than 38, which gives L < 4.3 μm. Deposition of silicon films onto the ends of fibers with thicknesses greater than 4 μm was found to be impractical. Therefore, the change in Φ, at a given λ, will be less than π over the -55 to 275 °C range. For completeness, if the fringe order were to be determined from a measurement of $\Delta\lambda_{FSR}$, then this would require that

$$m \leq \frac{\Delta \lambda_{FSR}}{\delta \ [\Delta \lambda_{FSR}]} \ , \qquad (33)$$

where $\delta[\Delta\lambda_{FSR}]$ is the resolution of the free spectral range measurement.

In practice, the maximum fringe order may be determined by the stress and the thickness nonuniformity of the deposited films. Thicker silicon films can be expected to be more susceptible to cracking and peeling because of stresses caused by the difference in the thermal-expansion coefficients of silicon and fused silica. Preliminary experiments determined that the yield of Fabry-Perot interferometers with L > 2 μm was severely reduced by the

nonuniformity of the silicon films deposited on fiber ends. To prevent severe degradation of the interferometer's fringe visibility, the phase shift Φ must deviate by less than $\pi/2$ over the 100-μm-diameter fiber core. This gives, in terms of L,

$$\delta L \leq \frac{\lambda_m}{4n_1} . \tag{34}$$

For silicon, $\delta L \leq 60$ nm, so a nonuniformity less than 0.7% is required for L = 4 μm. For silicon thin-film interferometers with L $\approx$ 2 μm, the observed fringe visibility was approximately equal to that which was calculated assuming ideal uniformity. For L $\approx$ 4 μm, the observed fringe visibility was significantly reduced, which is indicative of excessive nonuniformity.

4.6 Sensitivity to Pressure

When installed in the inlet of an aircraft engine, this sensor will be exposed to a variable air pressure. The effect of pressure on the refractive index of the silicon Fabry-Perot interferometer was estimated by assuming that the refractive index changes can be related to the changes in the bandgap energy E_g. Since dE_g/dT = -.046 eV/°C and $dE_g/dP = -1.7 \times 10^{-7}$ eV/psi,[18]

$n^{-1}dn/dP = -2.8 \times 10^{-10}$/psi is obtained based on the published value for κ_n of $n^{-1}dn/dT = 7.6 \times 10^{-5}$/°C. The effect of pressure changes on the interferometer's thickness was determined from $L^{-1}dL/dP = -(1-2\nu)/E$. Using the published values for the Young's modulus E and Poisson's ratio ν,[19] it was determined that $L^{-1}dL/dP = -3.0 \times 10^{-8}$/psi. Combining the effects of changes in n and L, the sensitivity to pressure of the sensor's output was determined to be $dT_M/dP = -4 \times 10^{-4}$ °C/psi. This degree of cross sensitivity is insignificant for this application, where the range of pressures will be much less than 100 psi.

4.7 Conclusion

Figures of merit were developed and used to rank a number of candidate materials based on their suitability for this application. Silicon was selected, because of its high sensitivity to temperature, its low sensitivity to modal-power fluctuations, its low absorption, and its ease of deposition. Rules were developed to determine the thickness of the Fabry-Perot temperature sensor, and it was determined that the thickness of the silicon film should fall within the range of 0.8 μm to 4.3 μm. Greater sensitivity is obtained at the high end of this range, however, nonuniformity has been found to impose an upper

thickness limit of about 2 μm. The cross sensitivity to pressure was determined to be negligible for this application.

4.8 References

1. G. Beheim and K. Fritsch, "Spectrum-Modulating Fiber-Optic Sensor for Aircraft Control Systems," NASA TM-88968 (1987).

2. D.W. Seal, T.L. Weaver, B.L. Kessler, C.A. Bedoya, R.E. Mattes, "Fiber Optic Control System Integration for Advanced Aircraft," NASA CR-191194 (1994).

3. S.J. Petuchowski, T.G. Giallorenzi, and S.K. Sheem, "A Sensitive Fiber-Optic Fabry-Perot Interferometer," IEEE J. Quantum. Electron. QE-17, 2168 (1981).

4. D.T.E. Marple, "Refractive Index of GaAs," J. Appl. Phys. 35, 1241 (1964).

5. S.S. Ballard, K.A. McCarthy, W.L. Wolfe, "Optical Materials for Instrumentation," University of Michigan Report No. 2389-11-S (1959).

6. H.W. Icenogle, B.C. Platt, W.L. Wolfe, "Refractive Indexes and Temperature Coefficients of Germanium and Silicon," Appl. Opt. 15, 2348 (1976).

7. W.G. Driscoll, ed., **Handbook of Optics** (McGraw-Hill, New York, 1978).

8. S.M. Sze, **Physics of Semiconductor Devices**, 2nd Edition (John Wiley & Sons, New York, 1981) pg. 851.

9. G. Cocorullo and I. Rendina, "Thermo-Optical Modulation at 1.5 μm in Silicon Etalon," Electron. Lett. 28, 83 (1992).

10. H.H. Li, "Refractive Index of Silicon and Germanium and its Wavelength and Temperature Derivatives," J. Phys. Chem. Ref. Data 9, 561 (1980).

11. G.E. Jellison, Jr. and F.A. Modine, "Optical Functions of Silicon at Elevated Temperatures," J. Appl. Phys. 76, 3758 (1994).

12. R.J. Harris, G.T. Johnston, G.A. Kepple, P.C. Krok, and H. Mukai, "Infrared Thermooptic Coefficient Measurement of Polycrystalline ZnSe, ZnS, CdTe, CaF_2, and BaF_2, Single Crystal KCl, and TI-20 Glass," Appl. Opt. 16, 436 (1977).

13. E.D. Palik, ed., **Handbook of Optical Constants of Solids** (Academic Press, Orlando, 1985).

14. W.J. Lu, A.J. Steckl, T.P. Chow, and W. Katz, "Thermal Oxidation of Sputtered Silicon Carbide Thin Films," J. Electrochem. Soc. 131, 1907 (1984).

15. G. Beheim, unpublished data.

16. G. Beheim, K. Fritsch, and D.J. Anthan, "Fiber-Optic Temperature Sensor Using a Spectrum-Modulating Semiconductor Etalon," NASA TM-100153 (1987).

17. J.M. Molarius, E. Kolawa, K. Morishita, M-A. Nicolet, J.L. Tandon, J.A. Leavitt, and L.C. McIntyre, Jr., "Tantalum-Based Encapsulants For Thermal Annealing of GaAs," J. Electrochem. Soc. 138, 834 (1991).

18. S.M. Sze, **Physics of Semiconductor Devices**, 2nd edition (John Wiley and Sons, New York, 1981) pp. 15-16.

19. K.E. Petersen, "Silicon as a Mechanical Material," Proc. IEEE 70, 420 (1982).

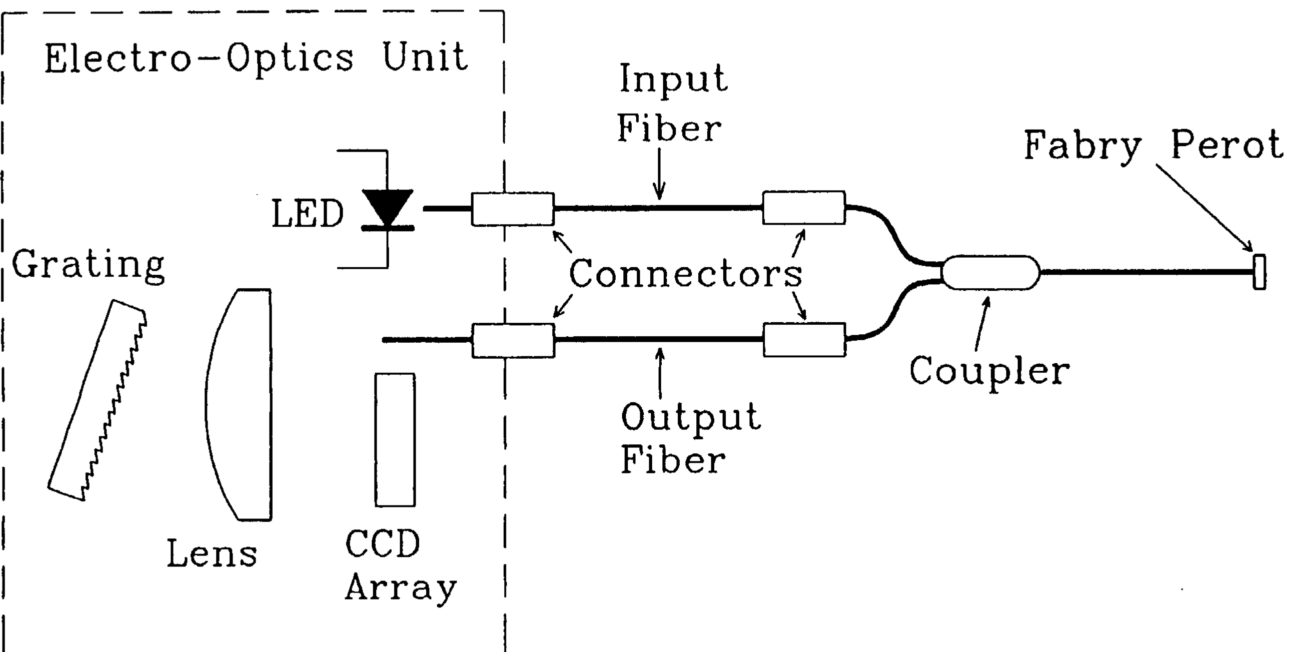

Figure 4.1 Schematic of fiber-optic thermometer using a Fabry-Perot sensor.

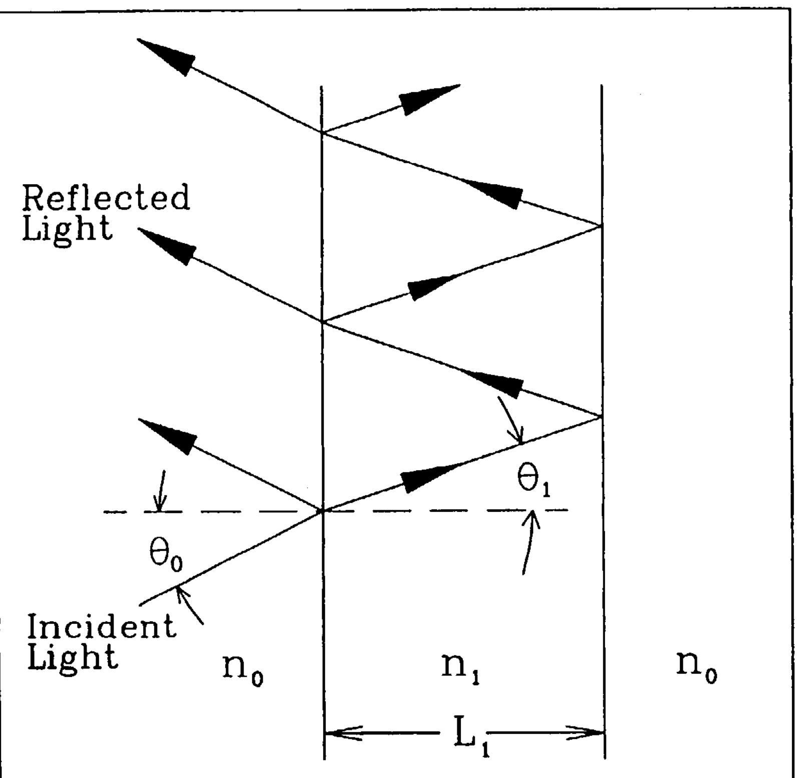

Figure 4.2 Thin-film Fabry-Perot interferometer.

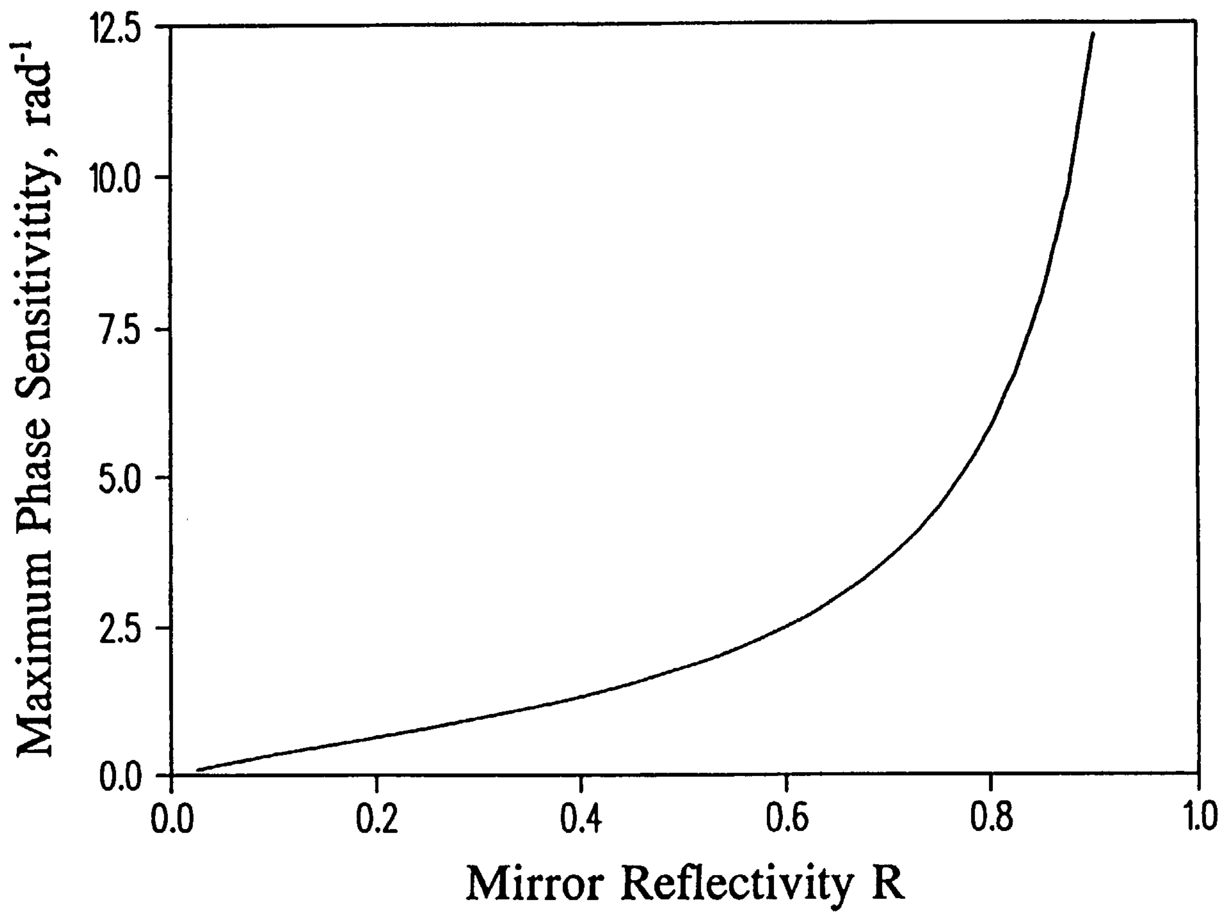

Figure 4.3 Maximum phase sensitivity of Fabry-Perot interferometer $|dR_F/d\Phi|_{MAX}$ as a function of mirror reflectivity R.

5. DESIGN OF ENCAPSULATING STRUCTURE

5.1 Encapsulation Requirements

A critical function of the Fabry-Perot sensor's encapsulating layers is the protection of the silicon surface from dirt and other contaminants. The encapsulant should therefore be opaque, to prevent the guided light from interacting with contaminants and also to block any external light. Further requirements arise because of the extremely high sensitivity of the measured temperature to changes in the refractive index and thickness of the silicon layer. The interface between the encapsulant and the silicon must be extremely stable, with no optically detectable reaction or diffusion of the constituents of the films, throughout the sensor's operational life. To protect the silicon from oxidation, the encapsulant should be an effective barrier to the diffusion of oxidizing species. Further, the optical properties of the encapsulant, itself, should be highly stable. Finally, the encapsulant should have a reflectivity which provides the thin-film interferometer with a high fringe visibility.

Aluminum has proven to be a superior coating for the environmental protection of fused silica fibers at temperatures as high as 400 °C. It was

determined to use aluminum as the thin-film interferometer's outermost encapsulating layer, since it can provide the required light-blocking and reflectance-enhancing functions. Since the oxide of aluminum, Al_2O_3, is strongly adherent and highly impermeable, aluminum oxidizes very slowly.[1] Therefore, a dense aluminum coating could protect the silicon layer from oxidation. However, aluminum deposited on a low-temperature substrate by evaporation or sputtering typically has a columnar structure.[2] A high reliance, therefore, was not placed on the oxidant-blocking abilities of this type of film. In any event, an intermediate diffusion barrier is required to prevent dissolution of the silicon in the aluminum, as the solubility of silicon in aluminum, at 300 °C, is ~0.1% by weight.[3]

In an early version of this sensor, which was coated with FeCrAl instead of aluminum, the metal-silicon diffusion barrier was SiO_2, which is permeable to oxygen and water.[4] In this sensor, the coating of FeCrAl, which forms an impermeable scale, was intended to protect the silicon from oxidation. However, like aluminum, sputter-deposited FeCrAl has a tendency towards a columnar structure. As a metal-silicon diffusion barrier, Si_3N_4 has a considerable advantage over SiO_2 because it is also an extremely good barrier

to the diffusion of water and oxygen. The need for an oxidant-impermeable encapsulant is discussed in the following subsection.

5.2 Effects of Silicon Oxidation

If it is not satisfactorily encapsulated, the silicon Fabry-Perot interferometer will oxidize during use. This can cause the sensor's output to drift at a rate that is unacceptable for many applications. For the aircraft-engine application under consideration here, a $\pm$ 2 °C accuracy must be maintained throughout 5000 hrs of exposure to temperatures as high as 275 °C. Although the maximum temperature of this application is much lower than the temperatures used to purposefully oxidize silicon, the time of exposure is orders of magnitude greater here. Also, the growth of a very thin oxide is sufficient to produce an unacceptably large error, since the thermally induced changes in the interferometer's optical path difference are extremely small.

For the ideal Fabry-Perot sensor described in section 4, the measured temperature T_M is affected by changes in the silicon film's refractive index n_1

and thickness L, thusly

$$\delta T_M = \frac{1}{\kappa_\Phi}\left[\frac{\delta L}{L} + \frac{\delta n_1}{n_1}\right], \tag{1}$$

where $\kappa_\Phi = 7.9 \times 10^{-5}$ /°C was obtained using published material properties for silicon. From Eq. 1, if L = 2 μm, then a 1 °C change in T_M will be caused by the consumption of only 1.6 Å of silicon by oxidation. This analysis neglects the light reflected from the outer surface of the SiO_2, which has a thickness L_{ox} = 3.6 Å in this instance (since $\delta L_{ox} = -2.27\ \delta L$). The light reflected from the oxide/air interface will have the effect of reducing δT_M for a given oxide growth. For purposes of this discussion, however, only approximate results are necessary, since the objective here is to demonstrate the desirability of an oxidant-impermeable encapsulant. With this objective in mind, an estimate will be made of the time of exposure to 300 °C which would cause a 1 °C shift in the output of an unencapsulated silicon sensor.

Very little data is available on the oxidation of silicon at temperatures as low as 300 °C. An initial approximation can be made by extrapolating the linear-parabolic rate constants of Deal and Grove.[5] The rate constants measured by Deal and Grove were well fit by Arrhenius relations over the full

range of temperatures used in their study, which were 700 to 1200 °C in dry O_2 and 920 to 1200 °C in wet O_2. The linear rate constant B/A, rather than the parabolic rate constant B, is of interest here because its effect is predominant for thin oxides. Extrapolating to 300 °C gives $B/A = 1.9 \times 10^{-7}$ Å/hr in dry O_2 and $B/A = 7.1 \times 10^{-6}$ Å/hr in wet O_2. These extrapolated rates indicate that negligible drift should result due to oxidation, despite 10^5 hrs of exposure to 300 °C, even with no protection from the oxidizing ambient. However, studies of silicon oxidation at low temperatures show that these extrapolated rate constants severely underestimate the oxide growth.

Goodman and Breece[6] measured the oxidation rates of silicon, at 600 °C, in dry O_2 and in water vapor. In dry O_2, the oxide growth was approximately linear after 25 Å, with a rate of 1.2 Å/hr. This rate is considerably higher than the 0.20 Å/hr obtained by extrapolating the B/A measurements of Deal and Grove. In water vapor, Goodman and Breece measured a rate of 5 Å/hr, which compares more favorably with the extrapolated B/A of 5.8 Å/hr. The large discrepancy in the case of dry O_2 is primarily due to the inappropriate application of the linear-parabolic rate constants to a very different oxidation regime. The dry oxidation data of

Goodman and Breece terminate at L_{ox} = 34 Å. The linear-parabolic model of Deal and Grove, on the other hand, is applicable only if L_{ox} > 300 Å, for dry oxidation. The kinetic model of Deal and Grove accounts for the rapid initial oxidation, prior to the onset of linear-parabolic growth, by the incorporation of a time offset which provides L_{ox} = 230 Å at t = 0.

Additional measurements in the regime of rapid initial oxidation were performed by Fehlner,[7] who measured the oxide growth on silicon at 400 °C in dry O_2. From an initial thickness of 10 Å, the SiO_2 layer grew to 17 Å after 16 hrs, which corresponds to a linear rate 4 orders of magnitude larger than that which is obtained by extrapolating the Deal and Grove B/A measurements. Clearly, extrapolation of the Deal and Grove rate constants will not be of much asssistance in estimating the oxidation rate at 300 °C.

The oxide-Debye length provides an approximate demarcation between the regimes of rapid initial oxidation, which is presumed to be field driven, and linear-parabolic oxidation, which is thermally driven. The oxide-Debye length

is given by

$$L_D = \left[\frac{K_0 \varepsilon_0 kT}{2q^2 C^*} \right]^{1/2}, \tag{2}$$

where K_0 is the dielectric constant of SiO_2 and C^* is the equilibrium concentration of the oxidant in the oxide.[5] For oxidation in dry O_2 at 1000 °C, $L_D \approx 150$ Å.[5] At 300 °C, if the same value of C^* is assumed, $L_D = 100$ Å. Since C^* will more likely be lower at this temperature, 100 Å can be presumed to be a lower bound on L_D at 300 °C. For the case of wet oxidation, the initial rapid growth is generally not detected, since $L_D = 6$ Å at 1000 °C. However, at a temperature of 400 °C, the oxidation rate in moist O_2, as measured by Fehlner, was much higher than the extrapolated value of B/A. At such low temperatures, L_D may be significantly larger than its value at 1000 °C due to the reduced solubility of water in SiO_2. Published measurements of wet-oxidation rates at low temperatures are almost non-existent, due to the experimental difficulties and absence of practical benefits. Therefore, this approximate analysis will be based on dry oxidation rates.

For $L_{ox} < L_D$, the oxidation kinetics have been successfully modeled using the theory of Cabrera and Mott.[8] Here, the rate-limiting process is

presumed to be the field-driven migration of oxygen ions through the oxide. Electrons tunnel through the thin oxide to fill surface states which are provided by the adsorbed oxygen molecules. At steady state, the potential across the oxide is that which causes the equalization of the surface state levels and the Fermi level of the silicon. This contact potential is of the order of 1 V, so that very high fields are produced in the thin oxide.

The Cabrera-Mott equation, which is applicable for $L_{ox} << x_1$, is

$$\frac{dL_{ox}}{dt} = u \exp(x_1/L_{ox}) , \quad (3)$$

where

$$u = N\Omega\nu \exp(-W/kT) , \quad (4)$$

$$x_1 = \left| \frac{qaV}{kT} \right| . \quad (5)$$

Here, N is the surface density of potentially mobile ions, W is the activation energy for ion movement, V is the voltage across the oxide, 2a is the ion-jump distance, ν is the frequency of vibration, q is the effective ion charge and Ω is the oxide volume per ion. An approximate solution for Eq. 3,

since $L_{ox} << x_1$, is

$$\frac{x_1}{L_{ox}} = -\ln[x_1 u(t+\tau)/L_{ox}^2] , \qquad (6)$$

where τ is determined by the initial oxide thickness. This expression is approximately inverse-logarithmic over the applicable range of L_{ox}.

Fehlner[9] found that the Cabrera-Mott relation accurately represented his measurements of oxide growth at 400 °C in dry oxygen,[7] as well as the measurements for 600 °C and dry O_2 by Goodman and Breece.[6] He also found that it accurately modeled the measurements of Kamigaki and Itoh[10] at temperatures from 950 to 1100 °C in low partial pressures of oxygen. The values of log(u) and x_1 obtained from these measurements were found to be linear with respect to 1/T, as predicted by theory.[9] Extrapolating to 300 °C gives $u = 2.3 \times 10^{-6}$ Å/hr and $x_1 = 140$ Å. Using these coefficients, the oxide growth in dry O_2 at 300 °C was calculated. These results are plotted in Fig. 5.1.

After 1 hr in dry O_2 at 300 °C, a 10.9-Å oxide is formed. After an additional 40 hrs, L_{ox} will increase by 3.6 Å, thereby shifting T_M by -1 °C (for

these approximate calculations, the light reflected from the SiO_2/air interface is neglected). The sensor's oxidation-induced drift can be reduced by a pre-calibration burn-in. After a 100-hr burn-in at 300 °C, it will take 650 hrs to grow 3.6 Å of oxide. A 1000-hr anneal provides 2900 hrs at 300 °C before T_M is shifted by -1 °C. By annealing at higher temperatures, the burn-in times can be reduced, but the optical fiber's aluminum coating is made brittle by exposure to temperatures greater than 400 °C. Also, because of the presence of moisture, the in-service oxidation rate will be significantly greater than is indicated by the data of Fig. 5.1. Fehlner found that the introduction of moisture, by bubbling oxygen through water at 20 °C, increased the oxidation rate at 400 °C by ~50%.[7] Clearly, the encapsulant should be impermeable to oxidants to obtain the required sensor lifetime.

5.3 Encapsulant Design

Silicon nitride oxidizes very slowly and is largely impermeable to oxygen and water.[11] For these reasons it is widely used as a mask for the selective oxidization of silicon.[12] For this purpose, Si_3N_4 is usually deposited at temperatures between 700 and 800 °C using low-pressure chemical vapor deposition (LPCVD).[13] These temperatures greatly exceed the maximum

temperature of aluminum-coated optical fibers. Dense stoichometric Si_3N_4 films, however, can be deposited at temperatures well below 300 °C using reactive sputtering.[14] Initial efforts to reactively sputter Si_3N_4 were sufficiently encouraging that it was determined to optimize this process for deposition of the sensor's diffusion barrier.

If Si_3N_4 is used as a diffusion barrier, its oxidation, although quite slow, is a potential source of drift. More stable would be an oxide, such as Al_2O_3, through which oxygen and water diffuse quite slowly. When deposited onto low-temperature substrates, however, Al_2O_3 films typically have a porous columnar structure.[15,16] Bombarding the substrate with oxygen ions during deposition can disrupt the columnar growth and densify the Al_2O_3 film.[17] Preliminary experiments were performed in which an Al_2O_3 target was reactively sputtered in an oxygen plasma. These experiments were not successful at producing low-void films.

The optical properties of the three-film sensor structure, $Si/Si_3N_4/Al$, will now be considered. The Si_3N_4 layer constitutes a second Fabry-Perot resonator which is coherently coupled to the much thicker silicon resonator.

Normal incidence will be assumed. The complex phase shift (one-way) of the silicon resonator is then

$$\Omega_1 = \frac{2\pi}{\lambda} N_1 L_1 . \tag{7}$$

The real part of Ω is

$$\Phi_1 = \frac{2\pi}{\lambda} n_1 L_1 . \tag{8}$$

Since $k_2 = 0$, the phase shift of the Si_3N_4 resonator is real so that $\Omega_2 = \Phi_2$, where

$$\Phi_2 = \frac{2\pi}{\lambda} n_2 L_2 . \tag{9}$$

To be an effective diffusion barrier, the Si_3N_4 layer need not be thick, $L_2 > 10$ nm is adequate. Because of the disparity in L_1 and L_2, it makes intuitive sense to model the sensor as a silicon Fabry-Perot interferometer, the second mirror of which is nitride-coated aluminum. Because the Si_3N_4 layer can be very thin, its order of interference can be chosen so that the reflectivity of the nitride-coated aluminum does not vary significantly over the spectral range of the LED.

Figure 5.2 shows the three-film sensor structure. Here, materials 0 through 3 are the SiO_2 optical fiber, the silicon, the Si_3N_4, and the aluminum films, respectively. Following the derivation in the appendix, the sensor's amplitude reflectance is determined to be

$$r_F = \frac{-r_{10} + r_{123}\exp(j2\Omega_1)}{1 - r_{10}r_{123}\exp(j2\Omega_1)}, \tag{10}$$

where the amplitude reflectance of the nitride-coated aluminum is

$$r_{123} = \frac{-r_{21} + r_{23}\exp(j2\Phi_2)}{1 - r_{21}r_{23}\exp(j2\Phi_2)}. \tag{11}$$

The reflectivity of the nitride-coated aluminum, $R_{123} = |r_{123}|^2$, is maximized (assuming all n and k are λ independent) at the anti-resonance condition, which is

$$2\Phi_2 + \phi_{21} + \phi_{23} = \pi(2p+1), \tag{12}$$

where ϕ_{21} and ϕ_{23} are the phase shifts associated with r_{21} and r_{23} and p is an integer. Since k_1 is small and $n_1 > n_2$, $\phi_{21} \approx \pi$. If the aluminum is modeled as an ideal metal (i.e. k_3 infinite), then $\phi_{23} = -\pi$. The reflectivity R_{123} is then a maximum for $\Phi_2 = \pi(p + 1/2)$. The zeroth-order reflectance maximum, $\Phi_2 = \pi/2$, is in this case provided by a quarter-wave layer, i.e. $L_2 = 103$ nm

for λ = 830 nm. If n and k values from the literature are used to accurately determine ϕ_{21} and ϕ_{23}, then the zeroth-order reflectance maximum is more precisely determined to occur at λ = 830 nm if L_2 = 88 nm.

At λ = 830 nm, the complex refractive indexes are N_1 = 3.673 + j 0.005, N_2 = 2.01, and N_3 = 2.94 + j 7.76. Figure 5.3 shows $R_{123}(\lambda)$, which was calculated using these refractive index values, for L2 = 0, 100 and 300 nm. The nonzero values of L_2 are approximately the thicknesses that provide zeroth and first-order constructive interference at λ = 830 nm (more accurately, these thicknesses are 88 and 294 nm). As shown by Fig. 5.3, a larger interference order requires more precise control of the film's thickness, if one is to obtain an $R_{123}(\lambda)$ that is approximately constant over the LED's spectral width. Since a thicker nitride layer provides no apparent benefit, L_2 was fixed at 88 nm.

The thin-film interferometer was more accurately modeled using the wavelength-dependent refractive index data compiled by Palik.[18] The n and k data are shown in Figs. 5.4 to 5.6. The properties of polycrystalline aluminum films, prepared in ultra-high vacuum (UHV), were measured by Mathewson and Myers[19] using in-situ ellipsometry. The Si_3N_4 properties were determined

by Philipp[20] using Kramers-Kronig analysis of reflectance and absorptance measurements. These Si_3N_4 films were prepared by pyrolysis at 1000 °C. In the 500 nm to 1.1 μm region, Philipp determined k to be zero. The properties of single-crystal silicon were ellipsometrically determined by Aspnes and Theeten,[21] who mathematically eliminated the effect of the wafer's native oxide to obtain the bulk n and k. The data of Aspnes and Theeten extend from the UV to 827 nm. For longer wavelengths, n was obtained by interpolation, using a 1.12 μm data point of Primak,[22] who determined n from the angle of minimum deviation. Beyond the range of the data of Aspnes and Theeten, k was assumed to linearly decrease to 0 at 1.12 μm. The precise value is not critical in this region, since k is small.[23] Finally, the SiO_2 refractive index was measured by Brixner[24] using a prism method. All the tabulated n and k data were linearly interpolated as functions of λ.

Figure 5.7 shows $R_{123}(\lambda)$ for L_2 = 0 and 88 nm. Here, the reflectance of the nitride-coated aluminum was calculated using the λ-dependent n and k values, instead of the 830-nm values used to calculate the R_{123} functions shown in Fig. 5.3. The reflectivity of the nitride-coated aluminum is approximately constant, as is desired, over the spectral width of an 830-nm wavelength LED, which is typically ~60 nm (FWHM). Besides the reflectance magnitude, the

phase change on reflection is also important, as the phase change ϕ_{123} determines the resonance condition of the encapsulated silicon interferometer. At resonance,

$$2\Phi_1+\phi_{123}+\phi_{10}=2\pi m, \qquad (13)$$

where m is an integer. Figure 5.8 shows $\phi_{123}(\lambda)$, for L_2 = 0 and 88 nm. For L_2 = 88 nm, ψ_{123} = 0 at λ = 830 nm. In the vicinity of λ = 830 nm, ψ_{123} is approximately a linear function of λ, decreasing from 0.05 rad at 800 nm to -0.05 rad at 860 nm. Because R_{123} is approximately constant and $\phi_{123} \approx 0$ for 800 nm $< \lambda <$ 860 nm, $R_F(\lambda)$ of the dual-cavity interferometer is very similar in form, over the LED's spectral range, to $R_F(\lambda)$ of the uncoated silicon Fabry-Perot interferometer.

Figure 5.9 shows $R_F(\lambda)$ for L_1 = 1.6 μm and L_2 = 88 nm, over the wavelength range of 500 nm to 1.1 μm. Also shown is $R_F(\lambda)$ for a 1.6 μm-thick silicon film embedded in an SiO_2 ambient. In the vicinity of λ = 830 nm, the R_F minima are obtained, in both instances, at about the same wavelengths. However, because of the considerably higher reflectivity of the encapsulated silicon's back surface, the minimum values of $R_F(\lambda)$ are in this case significantly greater.

Since $\eta_{VIS} = \{[R_F]_{MAX}-[R_F]_{MIN}\}/\{[R_F]_{MAX}+[R_F]_{MIN}\}$, the maximum fringe visibility of 1 is obtained if $[R_F]_{MIN} = 0$. From Eq. 9, $[R_F]_{MIN} = 0$ if $R_{10} = R'_{123}$, where R'_{123} is given by

$$R'_{123} = R_{123}\exp(-2\alpha_1 L_1)\ , \tag{14}$$

where $\alpha_1 = 4\pi k_1/\lambda$. Thus, R'_{123} is the apparent reflectivity of the silicon Fabry Perot's back surface, as viewed from the front surface. In the case of the silicon film embedded in SiO_2, $R_{12} = R_{10}$, and the fringe visibility increases with increasing λ because α decreases. In the case of the encapsulated silicon, $R_{123} > R_{10}$ so that the fringe visibility reaches its peak value of 1 at about $\lambda = 650$ nm. For $\lambda > 650$ nm, the fringe visibility decreases since the imbalance of R'_{123}/R_{10} increases with increasing λ.

A high fringe visibility, in the wavelength range of operation, is desired as this makes it possible to more accurately determine the interferometer's resonant wavelength, in spite of perturbations to the spectrum which are caused by the fiber-optic link. The wavelength of peak fringe visibility can be shifted further towards the infrared by modifications such as increasing L_1 or substituting a metal having a lower reflectivity. Such design modifications, however, were made unnecessary by the higher absorptivity, relative to single

crystal, of the polycrystalline silicon films of the actual sensors. This higher absorption was sufficient to move the wavelength of maximum fringe visibility to about 750 nm, very close to the wavelength range of operation.

5.4 Effects of Si_3N_4 Oxidation

If oxygen and water are able to migrate through the pores of the aluminum layer, then the underlying Si_3N_4 will oxidize. Since there is reason to suspect that the aluminum layer might be porous, the effect of Si_3N_4 oxidation should be considered. Assume that the measured temperature T_M is determined from the wavelength of one of the interferometer's resonances. From Eq. 13, an oxidation-induced change in ϕ_{123} of $\delta\phi_{123}$ will shift the resonant value of Φ_1 by an amount $\delta\Phi_1 = -\delta\phi_{123}/2$. Since

$$\frac{d\Phi_1}{dT} = \frac{2\pi}{\lambda} n_1 L_1 \kappa_\Phi , \tag{15}$$

then

$$\delta T_M = -\frac{\lambda}{4\pi n_1 L_1 \kappa_\Phi} \delta\phi_{123} . \tag{16}$$

Substituting the material properties for silicon gives, for $\delta T_M = 1$ °C, $\delta\phi_{123} = -7.9 \times 10^{-3}$ rad.

The phase shift on reflection from a $Si_3N_4/SiO_2/Al$ structure, in a silicon ambient, was calculated using the method of Abeles, which is described in the appendix. A baseline ϕ_{123} was calculated, with the thicknesses of the Si_3N_4 and SiO_2 layers equal to 100 nm and 0, respectively. Then the SiO_2 thickness was increased to 10 Å and the Si_3N_4 thickness decreased by 5.5 Å in accordance with the conversion ratio measured by Fourrier, et al.[25] The phase change, at $\lambda = 830$ nm, that was produced by this 10-Å oxide growth was $\delta\phi_{123} = 7.2 \times 10^{-3}$ rad, which corresponds to $\delta T_M = -0.9$ °C.

To determine whether or not Si_3N_4 oxidation might cause the sensor's output to drift appreciably, an estimate was made of the oxidation rate for Si_3N_4 directly exposed to the atmosphere. For this purpose, oxidation rates measured at temperatures of 900 °C and higher had to be extrapolated. At 900 °C in wet O_2, the oxide growth on Si_3N_4 was found to be parabolic for thicknesses between 10 and 60 Å, which was the full range of the study by Lee et al.[26] For thinner oxides, oxidation occcurs via a different mechanism, since a ~10-Å oxide grows very rapidly at room temperature. The oxidation studies reported by Enomoto[27] and Fourrier[25] also included oxides thinner than 100 Å. After 10 hrs at 900 °C in wet O_2, both these groups measured $L_{ox} = 120 \pm 5$ Å. The measurements performed by Lee et al. were

terminated at 5 hrs, but parabolic extrapolation of their data gives L_{ox} = 120 Å, as well, after 10 hrs. Fourrier's group also measured the oxide growth at 1000 °C. The data of Fourrier yield, for wet oxidation, B = 1.46 x 10^3 $Å^2$/hr at 900 °C and B = 1.69 x10^4 $Å^2$/hr at 1000 °C. The corresponding activation energy is 3.2 eV. This is comparable to the 3.0 eV activation energy of the parabolic rate constant that was determined for oxidation in wet O_2 at temperatures between 1100 and 1240 °C by Choi's group.[28]

The oxidation of Si_3N_4 differs from that of silicon in that it produces a duplex scale; a layer of silicon oxynitride is formed between the Si_3N_4 and the SiO_2 outer scale. The oxynitride layer, nominally Si_2N_2O, has been found to have a thickness which is about 1/8 of the thickness of the SiO_2 layer.[29] Since the structure of Si_2N_2O is considerably more dense than is that of SiO_2, the rate-limiting step during parabolic oxidation is the diffusion of the oxidant through the oxynitride layer. Therefore, as for the oxidation of silicon, the activation energy of B should be comparable to the activation energy for diffusion of the oxidant. In dry O_2 at temperatures from 1100 to 1400 °C, Du et al.[29] determined that the activation energy of the parabolic rate constant was 5.0 eV. This was felt to provide a plausible characterization of oxygen

diffusion in Si_2N_2O. The activation energy for oxidation in wet O_2, which was determined to be 3.2 eV, should therefore be characteristic of the diffusion of water in Si_2N_2O. These activation energies seem plausible based on the similar difference in activation energies for diffusion in SiO_2, which are 1.17 eV for oxygen and 0.80 eV for water.[5]

The parabolic rate constants that fit the data of Fourrier were extrapolated to lower temperatures, using an activation energy of 3.2 eV, in order to estimate the temperature at which 5000 hrs of exposure would cause an oxidation-induced drift of 1 °C. For this purpose, a native oxide of thickness 10 Å was assumed to have been present on the surface of the Si_3N_4 when the sensor was calibrated. Once again, the aluminum layer is assumed present for the purpose of optical calculations, but it is assumed to have no effect on the Si_3N_4 oxidation rate. A -1 °C output shift, caused by an increase in the oxide thickness of 11 Å, was determined to result after 5000 hrs at 615 °C. At this temperature B = 0.068 Å^2/hr. This determination of the maximum operating temperature, based on oxidation-induced drift, is not particularly sensitive to the assumed initial oxide thickness. At lower temperatures, of course, the oxidation rates are greatly reduced. At 500 °C, the time required to increase the oxide thickness from 10 to 21 Å is

2.4 x 10^6 hrs. At 300 °C, therefore, oxidation of the Si_3N_4 is not expected to be a significant error source, assuming that parabolic growth is obtained for oxides as thin as 10 Å, as was reported by Lee for oxidation at 900 °C.

5.5 Effects of Temperature on Si_3N_4

In section 4, the temperature sensitivity, $\kappa_S = \lambda^{-1}d\lambda_m/dT$, of an unencapsulated silicon Fabry-Perot interferometer was determined to be 7.9 x 10^{-6}/°C, based on published properties of silicon. Encapsulation with Si_3N_4 and aluminum should increase κ_S since the nitride layer's temperature coefficients of n and L will both be positive. The effect on κ_S, however, will be relatively small, because of the gross disparity in the optical path differences of the coupled resonators.

No value of $\kappa_n = n^{-1}dn/dT$ for Si_3N_4 could be found in the literature, so an experimentally determined value of κ_ϕ will be used here. An 840-nm-thick Si_3N_4 film was deposited on the end of an optical fiber by reactive sputtering, as will be described in section 7. From spectral reflectance measurements, κ_ϕ was determined to be (1.9 $\pm$ 0.2) x 10^{-5}/°C from 20 to 550 °C. This κ_ϕ is a factor of 4 smaller than the value for silicon.

If ϕ_{123} is temperature dependent, then Eq. 12 gives

$$\kappa_S = \kappa_{\Phi 1} + \frac{1}{\Phi_1} \frac{d\Phi_{123}}{dT}, \tag{17}$$

where $\kappa_{\Phi 1}$ is κ_Φ for silicon. This equation can be rewritten as

$$\kappa_S = \kappa_{\Phi 1} + \alpha_{123} \frac{\Phi_2}{\Phi_1} \kappa_{\Phi 2}, \tag{18}$$

where $\kappa_{\Phi 2}$ is κ_Φ for Si_3N_4 and

$$\alpha_{123} = \frac{1}{2} \frac{d\Phi_{123}}{d\Phi_2}. \tag{19}$$

For the case of interest here, L_2 = 88 nm so that $\Phi_2 = -\phi_{23}/2$ and R_{123} is maximized at λ = 830 nm. For purposes of this analysis, it is assumed that $\phi_{21} = 0$, i.e. $k_1 = k_2 = 0$, which is a valid approximation at λ = 830 nm.

Differentiation of Eq. 11, at the design condition $\Phi_2 = -\phi_{23}/2$, yields

$$\alpha_{123} = \frac{|r_{23}|(1-|r_{21}|^2)}{(|r_{21}|+|r_{23}|)(1+|r_{21}||r_{23}|)} . \qquad (20)$$

Using the material properties at $\lambda = 830$ nm gives $\alpha_{123} = 0.544$. For $L_1 = 1.6\ \mu$m and $L_2 = 88$ nm, $\Phi_2/\Phi_1 = 1/33$, and $\kappa_{\Phi 2}/\kappa_{\Phi 1} = 1/4$, so that $\kappa_S = 1.0040\ \kappa_{\Phi 1}$. The effect of the Si_3N_4 layer on κ_S is therefore negligible.

5.6 Concluding Remarks

The desirability of an oxidant-impermeable encapsulant was demonstrated, and Si_3N_4/Al was proposed as a structure which should provide this oxidation protection. The optimum thickness of the Si_3N_4 layer was determined to be 88 nm. Silicon nitride was shown to be sufficiently oxidation resistant to provide the required long-term stability. The effect of the encapsulating films on the temperature sensitivity κ_S was shown to be negligible. A key property of the Si_3N_4/Al encapsulant, not discussed fully in this section, is the high fringe visibility which it provides at the operating wavelength of 830 nm. Demonstration of this feature must be postponed until

the optical properties of the silicon films on fiber ends have been measured, as these films are considerably more absorptive than single-crystal silicon.

5.7 References

1. J. Grimblot and J.M. Eldridge, "Oxidation of Al Films," J. Electrochem. Soc. 129, 2369 (1982).

2. J.A. Thornton, "Influence of Apparatus Geometry and Deposition Conditions on the Structure and Topography of Thick Sputtered Coatings," J. Vac. Sci. Technol. 11, 666 (1974).

3. D.B. Fraser, "Metallization," in **VLSI Technology**, S.M. Sze, ed. (McGraw-Hill, New York, 1983) pg. 367.

4. G. Beheim, K. Fritsch, M. Tabib-Azar, "Sputtered Thin-Film Fiber-Optic Temperature Sensor," Sensors, vol. 7, no. 1, January, 1990, pp. 37-43.

5. B.E. Deal and A.S. Grove, "General Relationship for the Thermal Oxidation of Silicon," J. Appl. Phys. 36, 3770 (1965).

6. A.M. Goodman and J.M. Breece, "Thin Tunnelable Layers of Silicon Dioxide Formed by Oxidation of Silicon," J. Electrochem. Soc. 117, 982 (1970).

7. F.P. Fehlner, "Formation of Ultrathin Oxide Films on Silicon," J. Electrochem. Soc. 119, 1723 (1972).

8. N. Cabrera and N.F. Mott "Theory of the Oxidation of Metals," Rep. Prog. Phys. 12, 163 (1948-9).

9. F.P. Fehlner, "Low Temperature Oxidation of Metals and Semiconductors," J. Electrochem. Soc. 131, 1645 (1984).

10. Y. Kamigaki and Y. Itoh, "Thermal Oxidation of Silicon in Various Oxygen Partial Pressures Diluted by Nitrogen," J. Appl. Phys. 48, 2891 (1976).

11. C.A. Goodwin, "The Use of Silicon Nitride in Semiconductor Devices," Ceram. Eng. & Sci. Proc. 5, 109 (1985).

12. J.A. Appels, E. Kooi, M.. Paffen, J.J. Schatorjé, and W.H.C.G. Verkuylen, "Local Oxidation of Silicon and its Application in Semiconductor-Device Technology," Phillips Res. Repts. 25, 118 (1970).

13. A.C. Adams, "Dielectric and Polysilicon Film Deposition," in **VLSI Technology**, S.M. Sze, ed. (McGraw-Hill, New York, 1983).

14. S.M. Hu and L.V. Gregor, "Silicon Nitride Films by Reactive Sputtering," J. Electrochem. Soc. 114, 826 (1967).

15. B.A. Movchan and A.V. Deshishin, Fiz. Metalloved. 28, 653 (1969).

16. J.A. Thornton, "Influence of Apparatus Geometry and Deposition Conditions on the Structure and Topography of Thick Sputtered Coatings," J. Vac. Sci. Techno. 11, 666 (1974).

17. P.J. Martin, "Review of Ion-Based Methods for Optical Thin Film Deposition," J. Mater. Sci. 21, 1 (1986).

18. E.D. Palik, ed., **Handbook of Optical Constants of Solids** (Academic Press, Orlando, Florida, 1985).

19. A.G. Mathewson and H.P. Myers, Phys. Scr. 4, 291 (1970).

20. H.R. Phillip, "Optical Properties of Silicon Nitride," J. Electrochem. Soc. 120, 295 (1973).

21. D.E. Aspnes and J.B. Theeten, "Spectroscopic Analysis of the Interface Between Si and Its Thermally Grown Oxide," J. Electrochem. Soc. 127, 1359 (1980).

22. W. Primak, "Refractive Index of Silicon," Appl. Opt. 10 ,759 (1971).

23. G.G. McFarlane and V. Roberts, "Infrared Absorption of Silicon Near the Lattice Edge," Phys. Rev. 98, 1865 (1955).

24. B. Brixner, "Refractive Index Interpolation for Fused Silica," J. Opt. Soc. Am. 57, 674 (1967).

25. A. Fourrier, A. Bosseboeuf, D. Bouchier, and G. Gautherin, "Thermal Oxidation in Wet Oxygen of Reactive Ion-Beam Sputter-Deposited Silicon Nitride Films," J. Electrochem. Soc. 138, 1084 (1991).

26. E.G. Lee and H.B. Im, and J.S. Roh, "Effects of Wet Oxidation on the Properties of Sub-10-nm-Thick Silicon Nitride Films," J. Am. Ceram. Soc. 74, 1563 (1991).

27. T. Enomoto, R. Ando, H. Morita, and H. Nakayama, "Thermal Oxidation Rate of a Si_3N_4 Film and Its Masking Effect Against Oxidation of Silicon," Japanese J. Appl. Phys. 17, 1049 (1978).

28. D.J. Choi, D.B. Fischbach, and W.D. Scott, "Oxidation of Chemically-Vapor-Deposited Silicon Nitride and Single-Crystal Silicon," J. Am. Ceram. Soc. 72, 1118 (1989).

29. H. Du, R.E. Tressler, and K.E. Spear, "Thermodynamics of the Si-N-O System and Kinetic Modeling of Oxidation of Si_3N_4," J. Electrochem. Soc. 136, 3210 (1989).

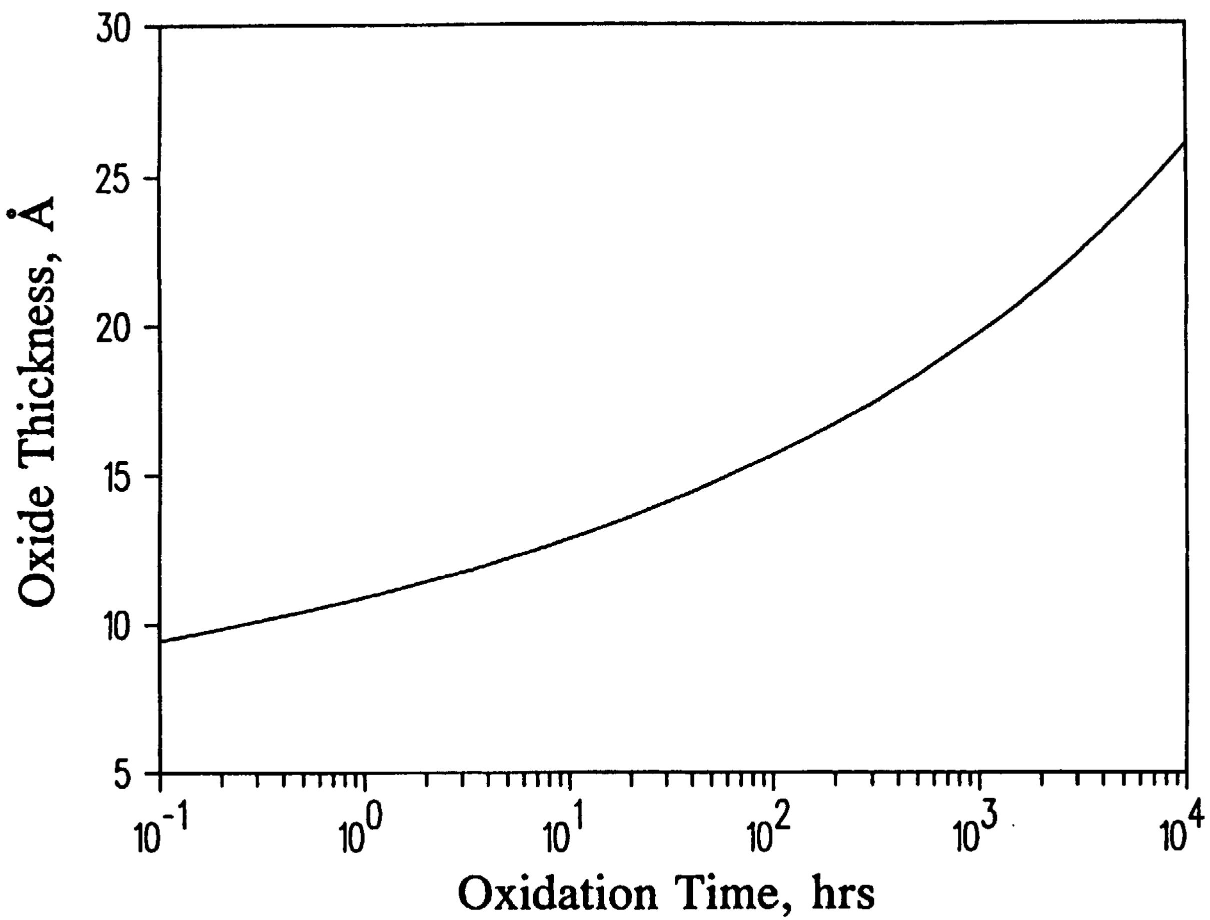

Figure 5.1 Calculated oxide thickness L_{ox} as a function of time, for silicon in dry O_2 at 300 °C.

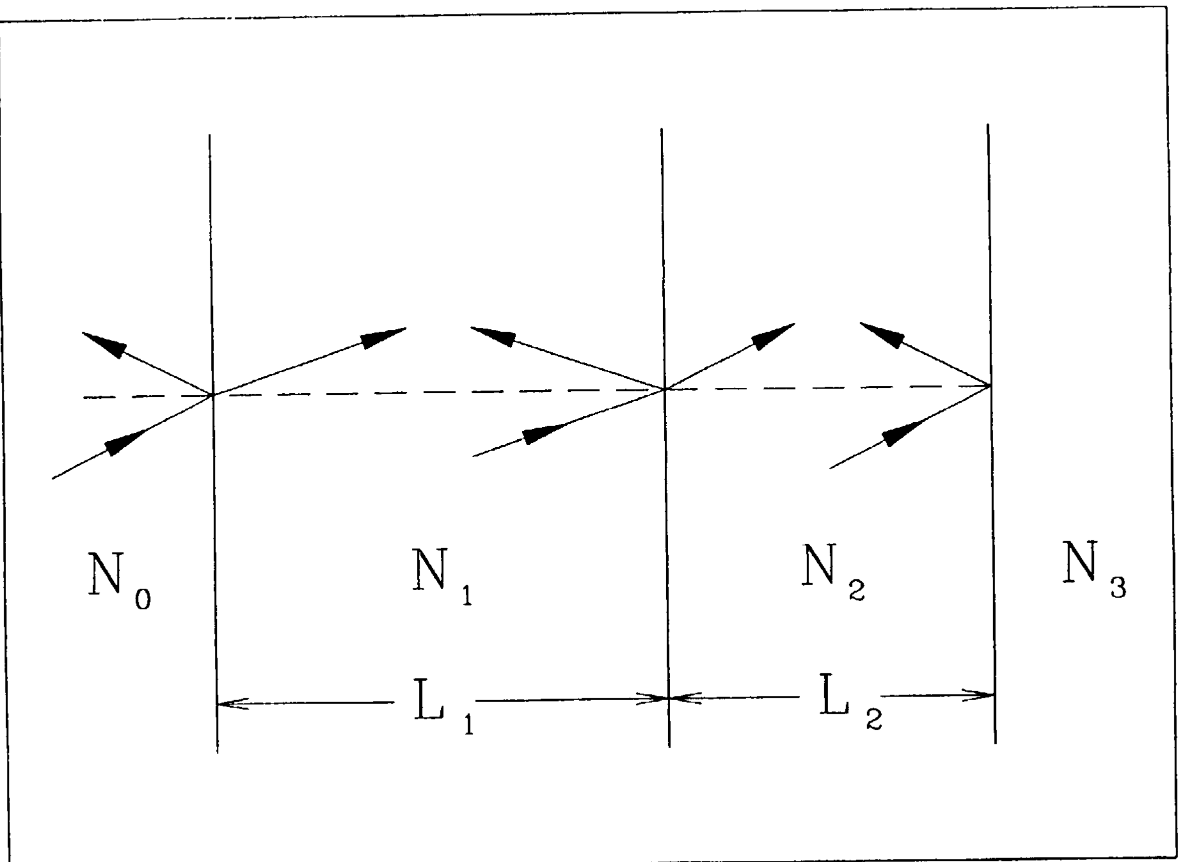

Figure 5.2 Dual-cavity thin-film Fabry-Perot interferometer.

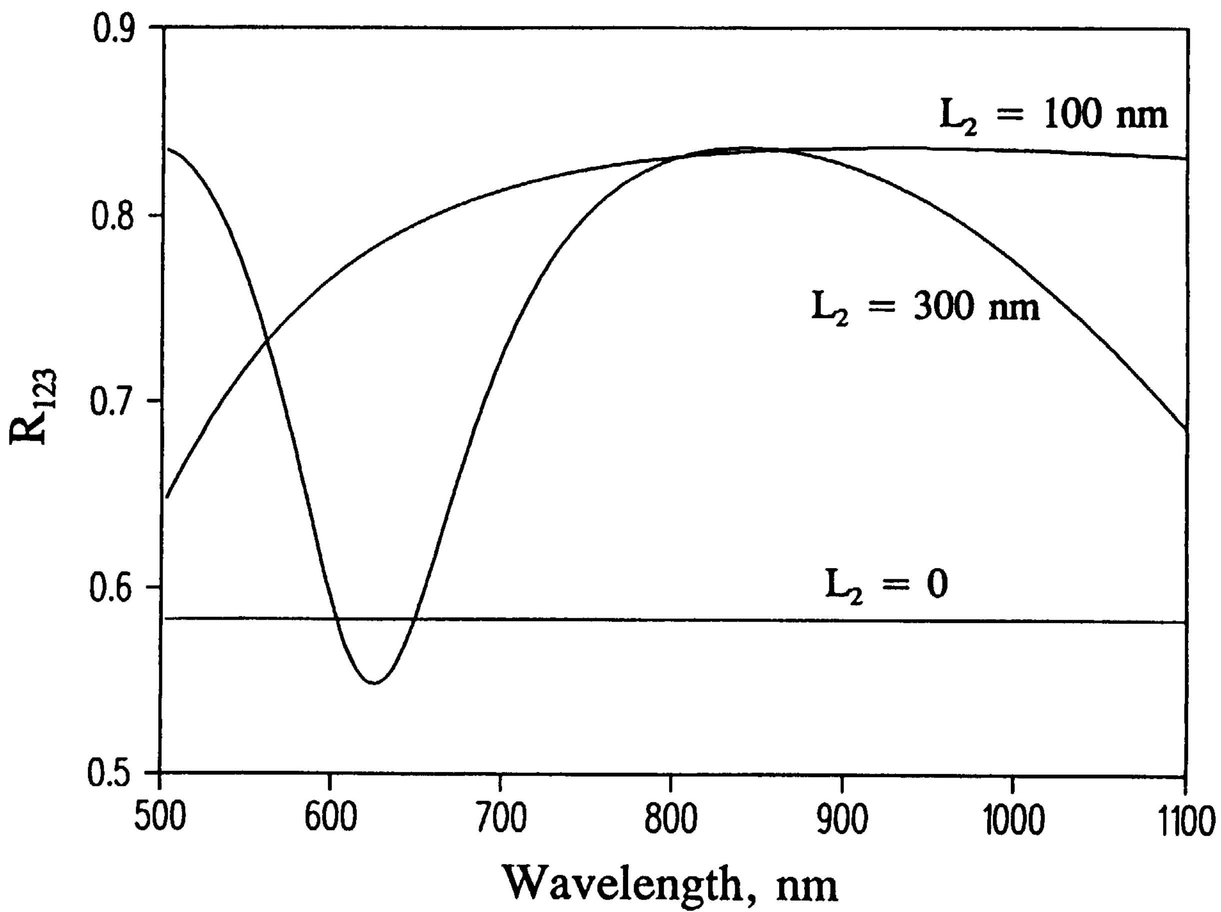

Figure 5.3 Calculated reflectivities $R_{123}(\lambda)$ of Si_3N_4-coated aluminum, in a silicon ambient, for different Si_3N_4 thicknesses L_2, where n and k of all the materials are fixed at the values for $\lambda = 830$ nm.

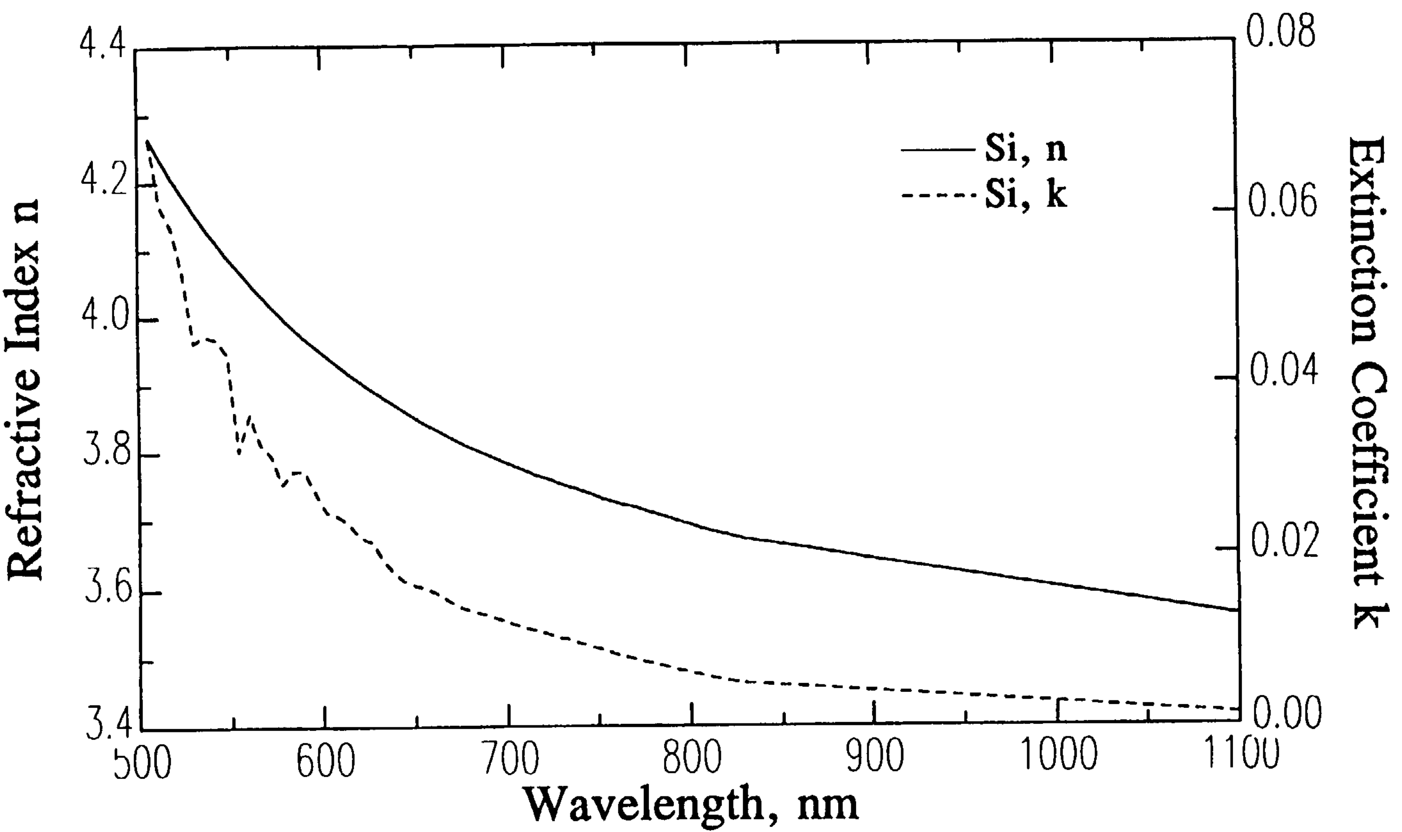

Figure 5.4 Refractive index n and extinction coefficient k of single-crystal silicon as functions of wavelength.

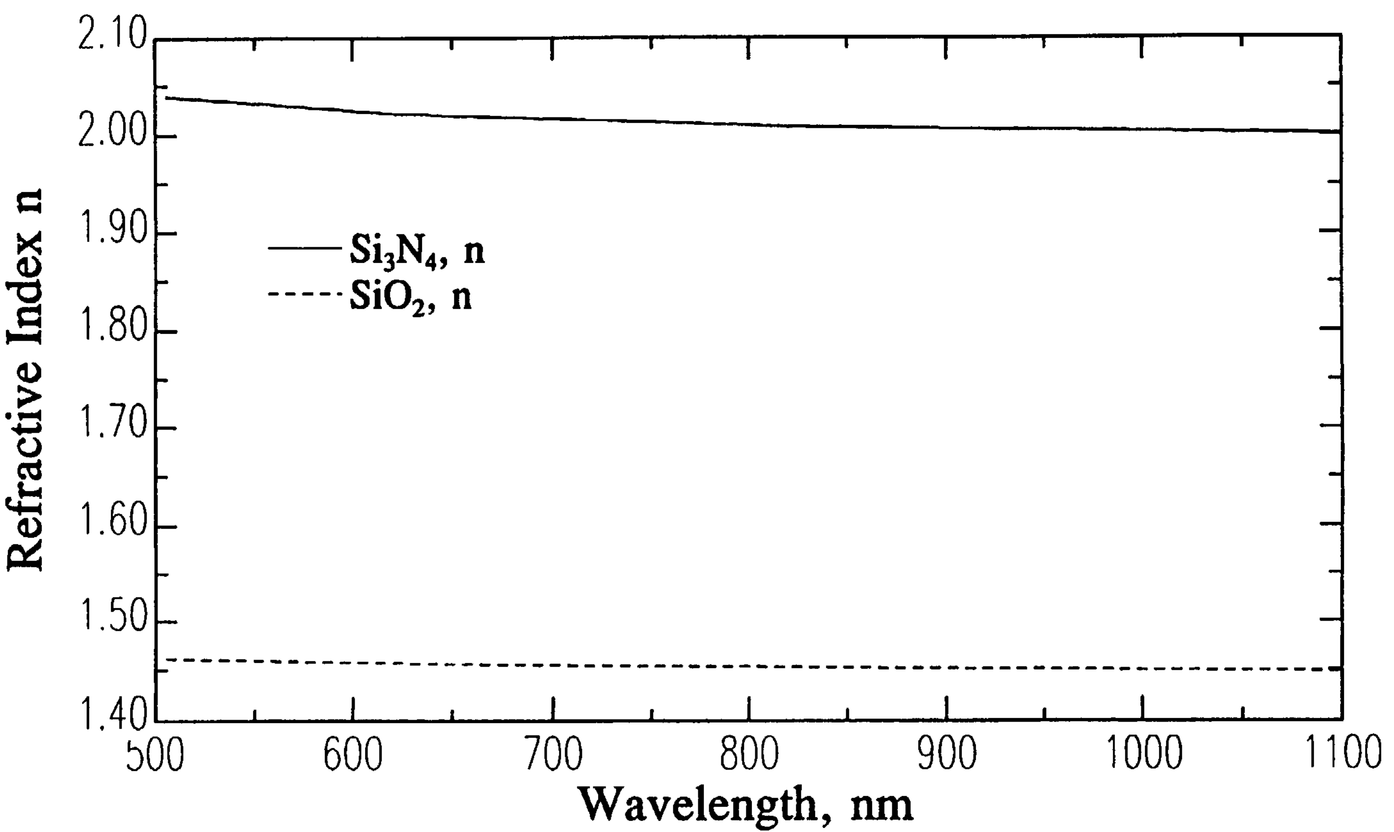

Figure 5.5 Refractive indexes of Si_3N_4 and SiO_2 as functions of wavelength.

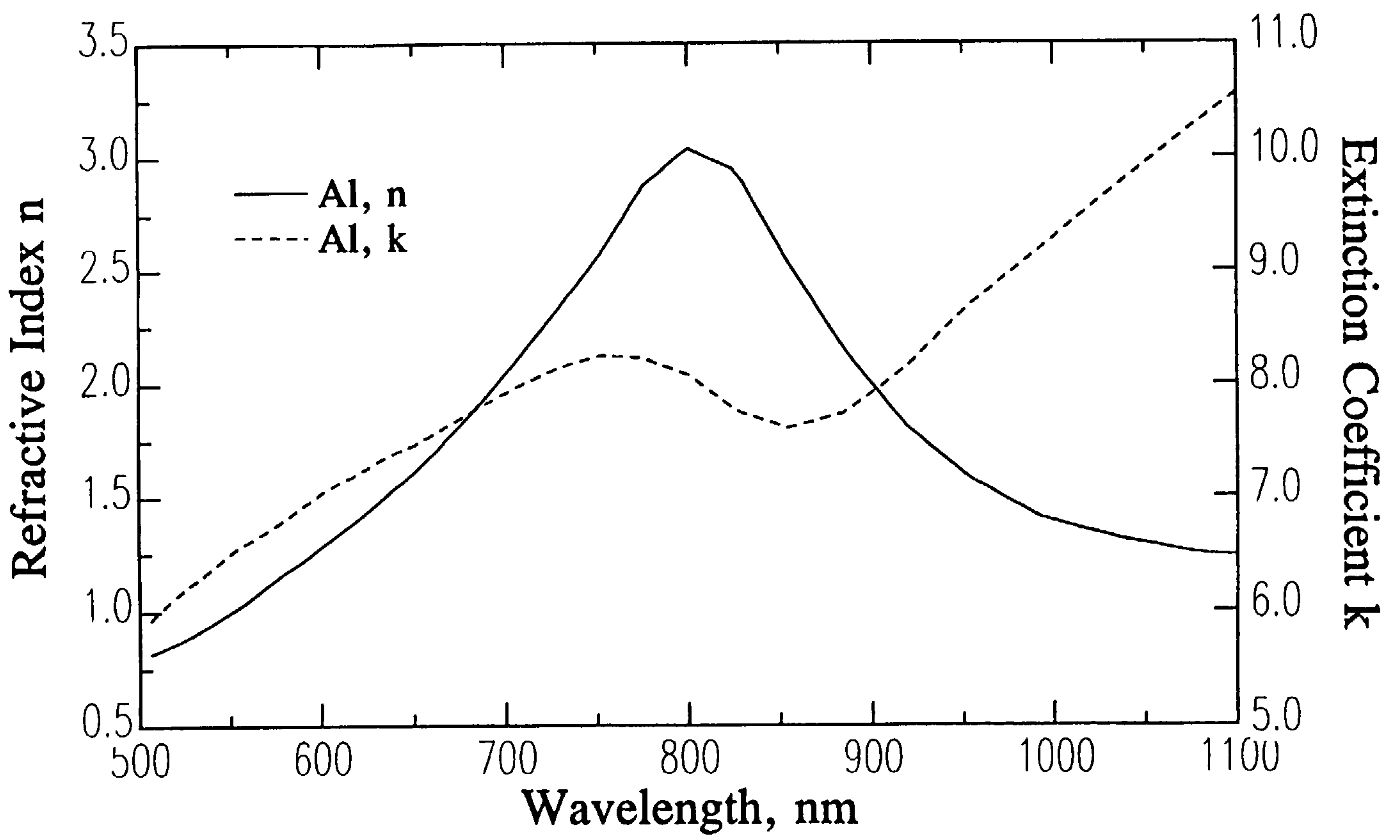

Figure 5.6 Refractive index n and extinction coefficient k of aluminum as functions of wavelength.

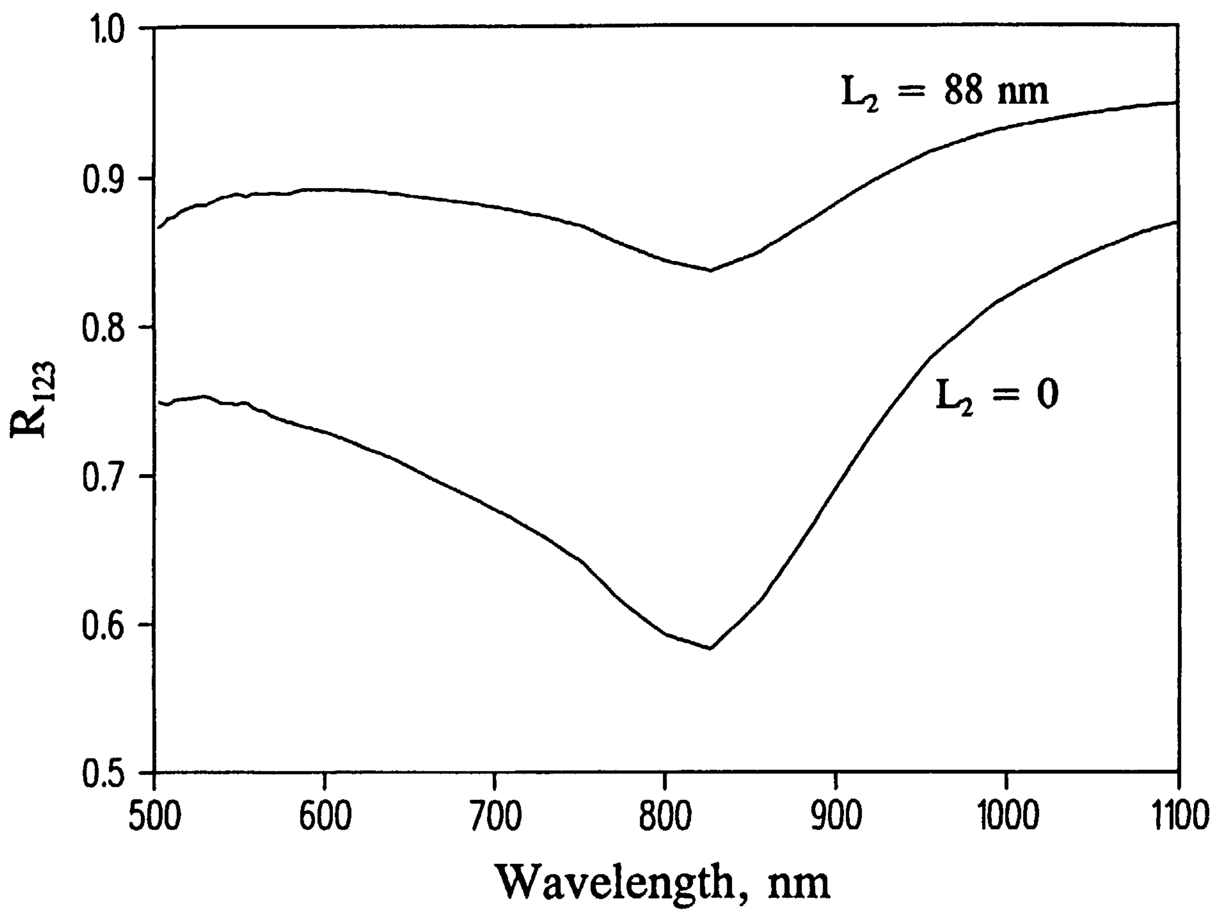

Figure 5.7 Calculated reflectivities $R_{123}(\lambda)$ of Si_3N_4-coated aluminum, in a silicon ambient, for different Si_3N_4 thicknesses L_2, where the λ-dependent n and k values have been used.

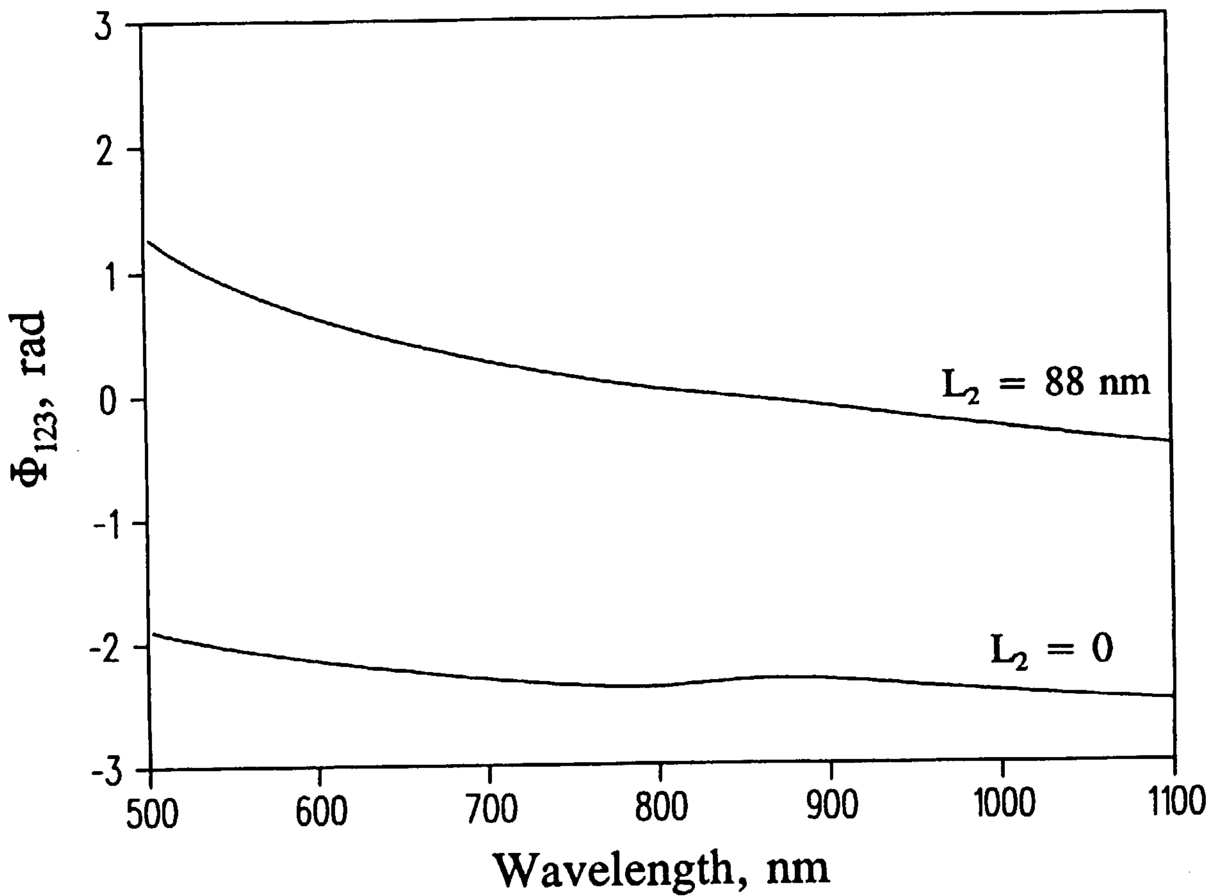

Figure 5.8 Calculated phase changes ϕ_{123} on reflection from Si_3N_4-coated aluminum, in a silicon ambient, as functions of wavelength, for different Si_3N_4 thicknesses L_2, where the λ-dependent n and k values have been used.

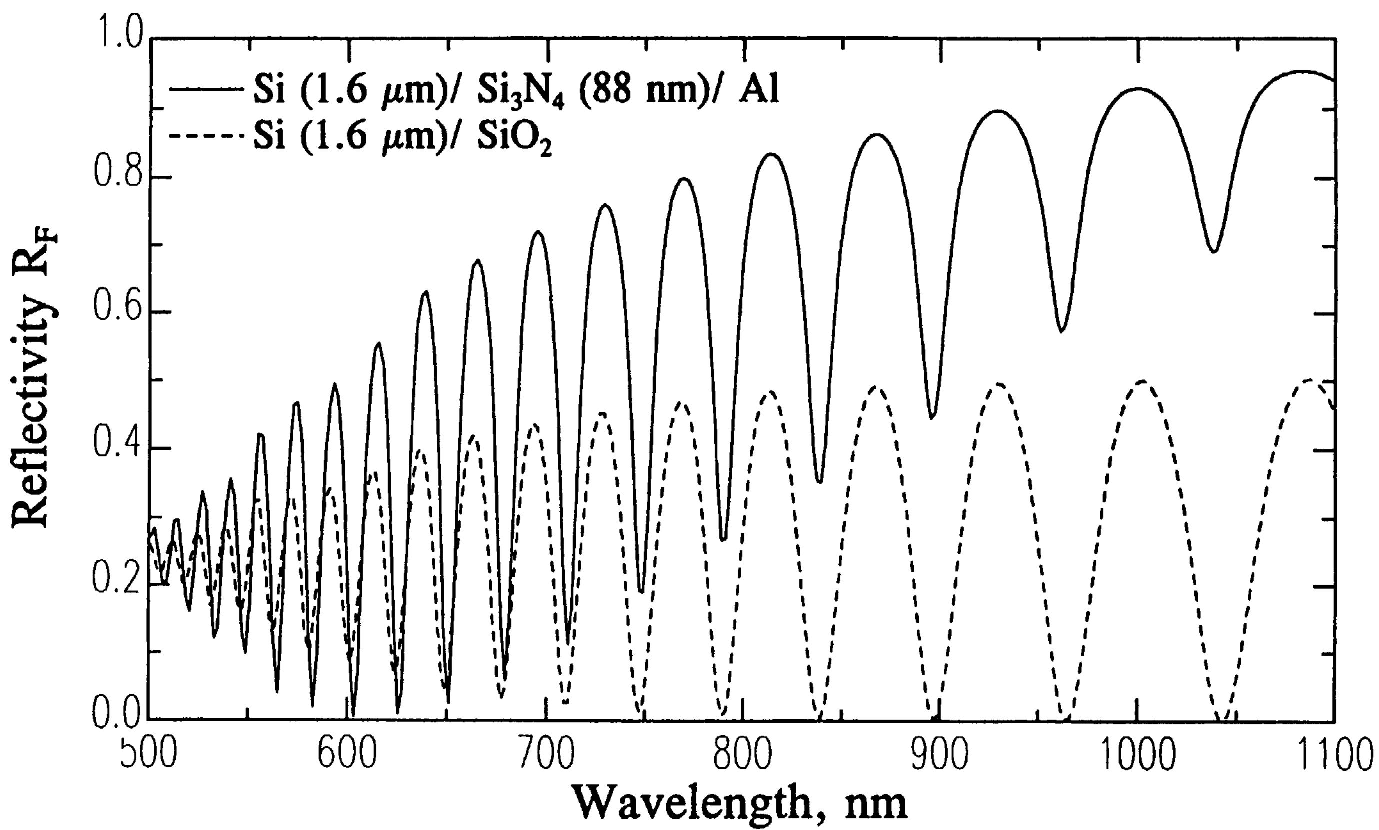

Figure 5.9 Reflectivities $R_F(\lambda)$ of Fabry-Perot interferometers using 1.6-μm-thick silicon layers, for silicon embedded in SiO_2 and for silicon encapsulated with 88-nm-thick Si_3N_4 overcoated with aluminum.

6. SILICON DEPOSITION AND ANNEALING

6.1 Introduction

To prevent damage to the optical fiber's aluminum coating, the temperature-sensing films must be deposited using low-temperature processes. At temperatures greater than 400 °C, the SiO_2 of the fiber reacts with the aluminum buffer coating to produce Al_2O_3 and silicon, which causes the fiber to become brittle.[1] The principal means by which silicon can be deposited at adequately low temperatures are plasma-enhanced chemical vapor deposition (PECVD), evaporation, and sputter deposition. Each of these methods will be briefly considered to justify the selection of magnetron sputtering for sensor fabrication.

Using PECVD, silicon can be deposited at a temperature of 250 °C. This substrate temperature is considerably lower than the ~600 °C which is required for thermally activated CVD. When deposited at 250 °C, PECVD silicon is fully amorphous and typically has a hydrogen content of ~14 atomic percent.[2] As deposited, these films are thermally unstable and therefore

unsuitable for this temperature sensing application. The refractive index is strongly dependent on the hydrogen content and defect density, both of which will be irreversibly altered by exposure to elevated temperatures. For this application PECVD silicon would need to be annealed. To obtain the greatest stability, the silicon should be crystallized. Rapid thermal annealing for 4 min at 700 °C, using a tungsten-halogen lamp, has been shown to fully crystallize 600-nm-thick PECVD silicon films.[3]

The principal drawback of PECVD, for this application, is the incompatibility of commercial reactors with odd-shaped substrates such as optical fibers. In order to be inserted in a standard radial-flow reactor, the fibers would have to be coiled and laid flat, with only their ends tilted upwards. Inside the reactor, there would be insufficient space to bend the fiber ends fully upright, since the minimum bend radius of the fibers is ~5 mm. Instead, the ends of the fibers could be tipped upwards at an angle of only ~30°. Deposition on such a sloped substrate could only produce a highly nonuniform film.

Standard evaporation and sputter-deposition systems can handle a much broader range of substrates. Sputter deposition is preferred for this application,

since it produces a denser film at low temperatures. Evaporated films are generally porous, unless the mobilities of the adatoms are increased by heating the substrate to a temperature close to the deposited material's melting point.[4] Sputter deposition can produce a dense film at low temperatures because it can cause the bombardment of the film with particles (some combination of ions, electrons, and neutrals). This increases the surface mobility of the adatoms and can cause the resputtering of atoms bound in non-optimum sites.

Okamoto and Serikawa[5] showed that magnetron sputtering can produce dense films of amorphous silicon (a-Si) for substrate temperatures below 100 °C. They determined the relative densities of the films, as functions of the deposition conditions, by comparing the surface textures of the films, as deposited and after slight etching in dilute HF. A transmission electron microscope was used to inspect carbon replicas of the film surfaces. The density of the films was found to be strongly influenced by the pressure of the argon sputtering gas. At low argon pressures ($\sim$1.5 mTorr), fine surface roughness, before and after etching, was observed. This is indicative of small, closely packed regions of dense amorphous material (the films were determined to be amorphous using X-ray diffraction). At high pressures ($\sim$40 mTorr), the films were very rough, especially after etching, which produced many

~ 100-nm-diameter pits. These etch pits identified regions of porous material which were intermixed with more slowly etched dense regions. The sizes of these dense and porous regions were found to increase with increasing argon pressure.

Okamoto and Serikawa used Auger electron spectroscopy to determine the composition depth profiles of the sputter-deposited silicon films. If the film was deposited using a low argon pressure, oxygen was localized at the surface. Deposition at a high pressure produced a highly porous film, and oxygen was spread throughout the film's full depth with a concentration of ~2%. Argon content was measured using x-ray microanalysis and found to decrease with increasing argon pressure. If the sputtering gas pressure is sufficiently low, the film will be bombarded by high-energy argon neutrals that are produced by the neutralization and reflection of argon ions at the target. Their energy at the substrate decreases with increasing argon pressure once their mean free path becomes comparable to the target-to-substrate separation. Higher pressure, therefore, incorporates less argon into the film, and, more importantly here, it produces a film of lower density. The general finding of Okamota and Serikawa, that a high sputtering gas pressure produces a density-deficient film,

was duplicated by Pawlewicz,[6] Ross and Messier,[7] and Zaka et al.,[8] all of whom deposited silicon using RF diode sputtering.

Okamato and Serikawa investigated the crystallization behavior of silicon films, which were magnetron sputtered at various argon pressures, by annealing them at 1000 °C for 20 min in nitrogen. Using x-ray diffraction, the grain size was found to be a maximum, 33 nm, for an argon pressure of 15 mTorr. For films deposited using higher pressures, the grain growth was inhibited by oxygen, which was diffused throughout the porous films. For lower pressures, the regions of dense amorphous silicon were smaller and more tightly packed. In this case, grain growth may have been inhibited because these dense regions are readily crystallized. Based on the results of Bhattacharyya and Ritz,[9] who produced large grains by solid-phase crystallization of silicon that had been amorphized by argon implantation, it seems unlikely that the films deposited at lower pressures had a smaller grain size because of their increased argon content.

Upon exposure to a temperature greater than that of deposition, a-Si undergoes a number of thermally induced changes that significantly alter its optical properties. Crystallization is one such process, but its rate is extremely

slow for temperatures less than ~600 °C. If the film contains voids, low-temperature annealing can densify the material, thereby increasing its refractive index.[10] For void-free a-Si, structural relaxation causes the largest refractive index changes prior to the onset of crystallization. Structural relaxation reduces the refractive index of the a-Si while leaving its density unchanged. It occurs via two mechanisms, which are (a) annihilation of network defects such as dangling bonds and (b) a reduction in the bond-angle disorder.[11]

Two optical states were identified for amorphous silicon that was produced by low-temperature ion-implantation of a silicon wafer.[12] This material is essentially identical to dense magnetron-sputtered silicon. The amorphous layer's thickness and refractive index were determined from infrared reflectance measurements. After 2 hrs at 500 °C, the a-Si layer was found to change from its as-implanted defect-saturated state to a thermally stabilized state. The change in state was indicated by a 4% reduction in refractive index, with no further refractive index change after continued annealing at 500 °C (however, the thickness of the a-Si layer decreased continuously due to epitaxial regrowth at the interface). Following the initial relaxation, the subsequent index change was less than the measurement method's resolution, ~1%, despite exposure to 500 °C for 150 additional hrs.

The temperature-sensing silicon film cannot be thermally stabilized by furnace annealing, since a 2-hr exposure to 500 °C would damage the aluminum-coated fiber. Clearly, what is required here is preferential heating of the silicon film together with rapid processing, in order to minimize the conduction of heat to the aluminum buffer coating. Rapid thermal processing was performed using an argon-ion laser, the output from which was focused onto the silicon-coated fiber end. The laser's output power was 1 W and its wavelength was 514 nm. Preliminary calculations indicated that these characteristics are suited to this purpose. If the 1-W beam is entirely incident on the 140-μm diameter fiber, then the average power density is 6.5 kW/cm^2. By focusing the light from a 2-W argon-ion laser to a 100 x 70 μm elliptical spot that was scanned across the film's surface, Lemons et al.[13] crystallized 1-μm-thick silicon films on fused-silica substrates. In this case, the power density of ~30 kW/cm^2 was sufficient to melt the silicon.

Fully crystallized silicon should provide better stability than can be obtained using thermally relaxed a-Si. Extremely high stability is required because, according to the calculations of section 4, only a 79 ppm change in refractive index will shift the sensor's output by 1 °C. Using the Bruggeman effective medium approximation (described in the appendix), it was determined

that a -1 °C output shift would result if only 0.07% of a nominally amorphous film was crystallized. The results of Lemons, et al. suggest that it should be possible to fully crystallize the silicon film using the 1-W argon-ion laser. Even if 1 W is not sufficient to melt the film entirely, solid-phase crystallization should still be possible, and is probably preferrable here. Melting has been shown to be a necessary precondition for the development of large grains.[14] Here, it is more important to maintain an optically smooth, flat surface. This favors crystallization at temperatures below the melting point.

6.2 Optimization of Silicon Deposition Process

Silicon films were sputter-deposited in a cylindrical vacuum chamber, approximately 50 cm in diameter by 50-cm high. Prior to introduction of the sputtering gas, the chamber was evacuated by a turbomolecular pump to a pressure of 10^{-6} Torr. The silicon was deposited by RF magnetron sputtering, using one of three confocally aligned sputter guns (US Flexguns II), that were mounted in the top of the chamber. The substrates were placed at the bottom of the chamber on a platen which was rotated to improve the thickness uniformity. The 75-cm diameter silicon target had a purity of 99.999%. The sputtering gas was ultra-high purity argon. The argon flow rate was set using

a mass flow controller to obtain the desired pressure, as measured by a capacitance manometer. Prior to each deposition, a shutter was interposed between the gun and the substrate, and the target was presputtered for 10 minutes.

The optimum values of argon pressure and RF power were determined by varying both process parameters independently. Nine films were deposited on 7059 glass slides using RF power levels of 300, 400, and 500 W and pressures of 4.0, 8.5, and 14.5 mTorr. The films were analyzed using a rotating-analyzer spectroscopic ellipsometer with a manually variable angle of incidence (Variable Angle Spectroscopic Ellipsometer or VASE).[15] Windows-based analysis software (WVASE), from the manufacturer of the ellipsometer, was used to model the ellipsometric responses of the films. The WVASE software included a linear regression analysis algorithm which adjusted the model parameters to produce the best fit to the experimental data. In this way the void fraction f_V and thickness L of each film was determined. The void fraction was found to be strongly dependent on the argon pressure, and more weakly influenced by the RF power. The RF power was found to principally affect the deposition rate.

The void fraction was found to increase with increasing pressure, in agreement with the results of Okamoto and Serikawa. Figure 6.1 shows $<\varepsilon_2>$, the imaginary part of the pseudo-dielectric function, for films that were deposited using the various argon pressures and a fixed RF power of 400 W (the pseudo-dielectric function is the dielectric function of a hypothetical substrate, reflection from which would produce the measured values of ψ and Δ). In Fig. 6.1, the $<\varepsilon_2>$ values are shown as functions of photon energy E in the spectral region where the films are opaque, $E > 2.5$ eV or $\lambda < 500$ nm. At these wavelengths, light reflects only from the air/silicon interface, and the pseudodielectric function, $<\varepsilon_1> + j<\varepsilon_2>$, is equal to the film's dielectric function, $\varepsilon_1 + j\varepsilon_2$, provided the interface between the film and air is abrupt on an atomic scale. The presence of surface roughness or an oxide layer will cause $<\varepsilon_2>$ to be somewhat less than ε_2, but $<\varepsilon_2>$ can still be used to compare the densities of films with similar surfaces.

In the spectral region where the film is transparent, $\lambda > 500$ nm, ψ and Δ are influenced by the film thickness L. Here, the optical constants cannot be directly determined because of an excess of unknowns. The number of unknown parameters can be reduced by modeling the film as a mixture of already characterized materials.[16] The volume fractions of these constituents

can then be adjusted to produce the best fit to the ψ and Δ data. The quality of the resulting fit gives some indication as to the validity of the model. The sputtered silicon films were modeled as mixtures of amorphous silicon and voids. This reduced the number of unknowns from 2N+1, where N is the number of wavelengths sampled, to just two, the void fraction f_V and film thickness L. Using the WVASE fitting procedure, which is based on the Levenberg-Marquard algorithm,[17] the unknowns f_V and L were adjusted in order to minimize the mean-squared error, which is defined as

$$MSE = \frac{1}{N-1}\sum_{i=1}^{N}\left[\frac{\psi_i-\psi(\lambda_i, f_V, L)}{\sigma_{\psi i}}\right]^2 + \frac{1}{N-1}\sum_{i=1}^{N}\left[\frac{\Delta_i-\Delta(\lambda_i, f_V, L)}{\sigma_{\Delta i}}\right]^2 . \quad (1)$$

Here $\psi(\lambda_i,f_V,L)$ and $\Delta(\lambda_i,f_V,L)$ are the model outputs, and ψ_i and Δ_i are the experimental data points, each of which is the average, at wavelength λ_i, of a number of measurements, the standard deviations of which are $\sigma_{\psi i}$ or $\sigma_{\Delta i}$.

The effects of the void fraction f_V on the optical properties of the films were modeled using the Bruggemann effective medium approximation, which is described in the appendix. The Bruggemann EMA assumes that the heterogeneous material is comprised of randomly distributed homogeneous

grains. These grains must be small compared to the optical wavelength, yet they must still be sufficiently large that they retain the bulk dielectric properties. The measurements of Pierce and Spicer,[18] as tabulated by Palik,[19] were used to represent void-free a-Si. The dielectric function of the 7059 substrate was measured ellipsometrically. The back side of each slide was roughened with a Dremel tool to prevent specular reflection, thereby eliminating this surface from the analysis. The surfaces of the films were assumed to be ideal. The ψ and Δ measurements were fit over the range from 250 to 890 nm (the upper limit was imposed by the range of the a-Si n and k data). Good fits were obtained only for the films sputtered at the lowest argon pressure of 4 mTorr. For this pressure, and an RF power of 400 W, the fitting procedure yielded f_V = -15.2 $\pm$ 0.4 % and L = 197.1 $\pm$ 0.4 nm, which implies a deposition rate of 25 nm/min. The uncertainties in the model parameters were calculated based on the measurement noise, i.e. the measured values of $\sigma_{\psi i}$ and $\sigma_{\Delta i}$. The negative value of f_V indicates that the sputter-deposited silicon is denser than the evaporated material of Pierce and Spicer.

At the same pressure, but a lower power of 300 W, the void fraction was somewhat higher, f_V = -12.1%, and the deposition rate was lower, 20 nm/min. At the highest power, 500 W, a void fraction of -14.1% was

obtained, which is not significantly different from what was obtained at 400 W. The deposition rate at 500 W was higher, 34 nm/min. However, sustained operation at 500 W caused the RF generator to become overly warm. Therefore, the optimum deposition conditions were determined to be 400 W and 4.0 mTorr.

The ellipsometric data for the "best" film were analyzed in more detail. A surface layer, of unknown thickness, was added to the model to simulate the effects of surface roughness. This rough surface overlayer was assumed to be comprised of 50% a-Si and 50% void. By linear regression analysis, the overlayer's thickness was determined to be less than 1 nm, while f_V, the void fraction of the bulk of the film, was found to have the same value as was determined without the overlayer, -15.2%. Introduction of a surface oxide, or for that matter any mixture of SiO_2, a-Si and void, also had negligible effects on the calculated f_V. When combined with a-Si, void and SiO_2 are almost indistinguishable from each other, for 250 nm $< \lambda <$ 1000 nm. Also, for such thin overlayers, the calculated values of f_V and L, which apply to the bulk of the film, are insensitive to the assumed proportions of a-Si, void and SiO_2 in the overlayer.

For wavelengths beyond the range of Pierce and Spicer's data, i.e. $\lambda > 890$ nm, the a-Si dielectric function was determined by directly calculating n and k at each measurement wavelength, using the previously determined film and overlayer thicknesses. Figures 6.2 and 6.3 show the measured values of ψ and Δ as well as the best fits to these data. Figure 6.4 shows the calculated values of n and k for the sputtered a-Si, while Figs. 6.5 and 6.6 show ε_1 and ε_2, the real and imaginary parts of the dielectric function. For comparison, Figs. 6.5 and 6.6 also show the dielectric-function measurements of Pierce and Spicer[18] for silicon evaporated at room temperature and the measurements of Aspnes et al.[20] for a-Si deposited by LPCVD at 570 °C. The ε_2 function of the LPCVD a-Si is typical of well-relaxed amorphous silicon.[21]

The excellent fit provided by the EMA model indicates that the sputter-deposited silicon is fully amorphous. Fitting the experimental data using a three-component EMA comprised of a-Si, void and single-crystal silicon (c-Si), gives an essentially negligible crystalline fraction of 2.0 ± 1.0 %. If present, crystalline grains would be readily detected because of the prominent peaks in the ε_2 function of c-Si at 3.4 eV and 4.2 eV, the E_1 and E_2 critical points.[22] The measured $\varepsilon_2(\lambda)$ is nearly identical to that which was measured for a-Si produced by implantation of Si ions in a silicon wafer.[23] The similarity of

these ε_2 functions shows that the a-Si sputtered at 400 W and 4.0 mTorr argon has approximately the maximum attainable density.

6.3 Deposition of Silicon on Fibers

Temperature sensors were fabricated in batches of 6 or 12. The fibers were first cut to lengths of ~0.5 m using scissors, and ~2 cm of the aluminum buffer coating was removed by etching in photoresist developer. Each fiber was then cleaved at a point 1 to 2 mm beyond the end of the aluminum buffer coating. A vibrating-blade type of fiber cleaver, York Technologies model FK11, was used. After cleaning the fiber with an alcohol-soaked wipe, it was inserted in the cleaver. The fiber was placed under a precisely controlled tension and then contacted by a vibrating diamond blade. If the fiber was cleaved instantly, a good end face was almost always obtained. According to the manufacturer, this cleaver consistently yields end faces that are perpendicular to the fiber axis within ±1°. This claim was supported by measurements that were made on about a dozen cleaved fibers, using a Michelson interferometer. A cleaved end typically appeared smooth and flat, except for a small chip which originated at the blade's point of contact. Usually, this defect was confined to the fiber cladding and so was of no

consequence. If the chip was found to extend into the light-guiding core, the fiber was recleaved. More frequently, fibers had to be recleaved because of debris on the end faces, as such debris was found to be nearly impossible to remove.

The fiber ends were held upright for deposition using a fixture made from aluminum angle stock. Six fibers were laid in vertical grooves that were cut in the angle's upright leg. Each fiber was held in place by a small washer and screw. One or two of these holders full of fibers were placed in the box shown in Fig. 6.7. The free lengths of fiber were coiled inside the box and shielded from deposition by the box's lids, which were installed so that just the fiber ends were exposed to the sputtered flux.

Considerable care was exercised to keep the fiber ends clean. The fibers were cleaved in the class 1000 clean room where the sputtering system was located. After cleaving, the fibers were mounted in holders, inspected under a microscope, and promptly loaded into the vacuum chamber. Deposition time was 45 min at 400 W and 4.0 mTorr argon. The deposition rate was variable, unless the fiber holder was placed each time at the same position on the platen. Another source of variability was repositioning of the flexible sputter guns by

other users of the system. After the fibers were removed from the chamber, the coated ends were inspected. Since the fiber ends were held upright, falling debris was readily incoporated into the films. This necessitated frequent cleaning of the chamber.

6.4 Spectral Reflectometry

Figure 6.8 shows the experimental configuration that was used to analyze the reflectance of the thin-film-coated fibers. Multimode fibers with core diameters of 100 μm, and SMA-type fiber-optic connectors were used exclusively. The light source was a tungsten-halogen lamp, the output from which was chopped at 600 Hz. The lamp's condenser lens and a 10X microscope objective were used to project a demagnified image of the filament onto the end of fiber F1. The objective's numerical aperture of 0.4 was over-filled, so that all of the modes of the 0.2 N.A. optical fibers were excited. A 2 x 1 fiber-optic coupler with a 50:50 splitting ratio directed light from the input fiber F1 to the sensor fiber F3. The coupler then directed about half of the light reflected by the sensor through fiber F2 to a scanning monochromator. The coupler, manufactured by Corning, was an integrated-optic Y-junction, which was fabricated in a glass substrate by ion exchange. The coupler's

pigtails were graded-index fiber, while fibers F1, F2 and F3 had a step index profile. A micropositioner was used to align the uncoated end of the sensor fiber, F3, with the end of the coupler pigtail, CP3. The reflectivity of this connection was minimized using a drop of index-matching fluid.

The monochromator's focal length was 0.25 m, and the grating had a line density of 1200 /mm and a blaze wavelength of 750 nm. A microscope objective was used to project a demagnified image of the end of fiber F2 onto the monochromator's entrance slit. Demagnification, by a factor of ~ 3, provided more efficient transmission through the f/3.6 monochromator. The monochromator's 500-μm-wide entrance and exit slits gave a line width of 1.6 nm FWHM, as measured using a HeNe laser. The detector was a silicon photodiode which was connected directly to the current input of a digitizing lock-in amplifier. The stepping-motor-driven monochromator was controlled by a personal computer. The computer interrogated the lock-in and controlled a wheel of order-sorting filters that were used to block the second-order diffracted light.

The spectrum of the light transmitted through the sensor, as measured

by the fiber-coupled reflectometer of Fig. 6.8, is given by

$$\begin{aligned} i_T(\lambda) &= i_{LAMP}(\lambda) \\ &\times H_{F1}C_{F1-CP1}S_{1-3}C_{CP3-F3}H_{F3}R_F(\lambda) \\ &\times H_{F3}C_{F3-CP3}S_{3-2}C_{CP2-F2}H_{F2}\,. \end{aligned} \tag{2}$$

Here $i_{LAMP}(\lambda)$ is the spectrum that would be measured if the light coupled from the source into fiber F1 were analyzed, $R_F(\lambda)$ is the reflectivity of the thin-film interferometer, H_{FJ} is the transmissivity of fiber J, C_{J-K} is the transmissivity of the connection between fibers J and K, and S_{J-K} is the transmissivity of the coupler from J to K. The H,C and S coefficients can be expected to vary as functions of wavelength, although not as significantly as those variables for which the λ-dependence has been made explicit.

In practice, the transmissivities of the fiber components can be expected to depend to some extent on the modal power distribution of the guided light. An effort has been made to minimize transmissivity variations due to modal effects by overfilling the fiber's acceptance angle at the launch and by selecting mode-insensitive components. For this reason, a Y-junction coupler was used rather than a fused-fiber type of coupler, which tends to more strongly couple the modes of higher order.

For normalization purposes, the source spectrum was measured by linking fibers F1 and F2 to connect the lamp directly to the monochromator. This gives

$$i_0(\lambda) = i_{LAMP}(\lambda)\, H_{F1} C_{F1-F2} H_{F2}\,. \qquad (3)$$

The transmitted spectra were measured over the full range of wavelengths which provided an adequate signal-to-noise ratio, i.e. 500 nm $< \lambda <$ 1.1 μm. The lower wavelength limit was dictated by increasing fiber losses; the upper limit by the decreasing responsivity of the silicon photodiode.

Full characterization of the fiber components can, in principle, permit $R_F(\lambda)$ to be determined from the measured sensor transmissivity $H_S(\lambda)$, where $H_S(\lambda) = i_T(\lambda)/i_0(\lambda)$. However, this is made difficult by the variability of the C coefficients. Each time a fiber connection is remade its transmissivity can be expected to change. Particularly difficult to characterize is C_{CP3-F3}, which changes each time the sensor fiber F_3 is replaced and can only be determined by cutting F_3. Fortunately, the transmissivities of the connectors are largely wavelength insensitive. Also, because the sensor fiber is very short, $H_{F3} \approx 1$. Therefore, by characterizing the coupler to determine the λ-dependent but

stable coefficients $S_{1\text{-}3}$ and $S_{3\text{-}2}$, $R_F(\lambda)$ can be determined from $H_S(\lambda)$, except for a scale factor which is largely λ independent.

To demonstrate the variability of the fiber interconnects, the source spectrum was first measured by connecting the lamp to the monochromator, using only the 1.1-m-long fiber F2. Fiber F1, of length 1.5 m, was then added, and this spectrum was divided by the first to obtain $H_{F1}C_{F1\text{-}F2}$. Prior to each of five subsequent transmissivity measurements, the connector between F1 and F2 was remated. Figure 6.9 shows the six measurements of $H_{F1}C_{F1\text{-}F2}$ as functions of λ, all of which are roughly proportional to each other. The connectors are the primary contributors to the losses observed here, as the fiber losses are largely insignificant for such a short length. A fiber with a length of 10 m was substituted for the 1.5-m F1, and $H_{F1}C_{F1\text{-}F2}$ remeasured. Figure 6.10 shows the result, together with one of the $H_{F1}C_{F1\text{-}F2}$ measurements for the 1.5-m fiber. The fiber losses are clearly more wavelength dependent than are the losses of the connectors.

Since only short lengths of fiber were used here, the coupler was the fiber component which had the greatest effect on $H_S(\lambda)$. The coupler was characterized by directing the lamp's output through fiber F1 into coupler

pigtail CP1. The coupler's output was then directed to the monochromator by aligning fiber CP3 with F2. The measured spectrum was normalized by $i_0(\lambda)$ to obtain a result equivalent to $S_{1\text{-}3}C_{CP3\text{-}F3}$. The transmissivity between coupler ports 2 and 3 was then measured by reversing the light path, from F2 to F1. After normalization, this measurement provided $C_{F3\text{-}CP3}S_{3\text{-}2}$. The product of these measurements, which is denoted $H_{CP}(\lambda)$ and is shown in Fig. 6.11, gives the round-trip transmissivity of the coupler and the mechanically aligned splice.

The reflectivity of the thin-film interferometer $R_F(\lambda)$ can be approximated by $R_f(\lambda)$, where $R_f(\lambda) = H_S(\lambda)/H_{CP}(\lambda)$. This gives

$$R_f(\lambda) = K\frac{C_{F1\text{-}CP1}C_{CP2\text{-}F2}}{C_{F1\text{-}F2}}T_3^2 R_F(\lambda)\,, \qquad (4)$$

where the term K reflects the variability in connector transmissivities due to remating. Figure 6.12 shows $R_f(\lambda)$ for a typical silicon film (sensor 294) together with the best fit that could be obtained using the previously measured dielectric function of sputter-deposited a-Si. Here, the refractive index of the fused-silica fiber was modeled using the dispersion equation of Malitson.[24] The thickness of this 45-min sputtered film was determined to be 1.42 μm.

Figure 6.13 shows a Nomarski-microscope image of a silicon-coated fiber end. The film's surface is fine-textured and apparently flat, except for a ring-shaped feature, which is only visible using the microscope's interference mode. This surface feature is precisely aligned with the optical fiber's inner cladding, which has an I.D. of 100 μm and an O.D. of 115 μm. Therefore, this feature does not affect the guided light. The inner cladding is fused silica that is doped with 4 mole % fluorine.[25] The fluorine dopant lowers the inner cladding's refractive index relative to the core, which is pure fused silica. The outer cladding, which serves no optical function, is incidentally doped with fluorine, ~1 mole %. The ring-shaped feature on the surface of the silicon becomes considerably more pronounced after the silicon is annealed. This feature is probably a depression in the surface, due to the densification of the fiber's inner cladding by volatilization of the fluorine dopant.

6.5 Laser Annealing

Figure 6.14 shows, schematically, the configuration used to anneal the silicon films on the fiber ends. The theoretical intensity distribution of the light incident on the fiber end can be determined using Gaussian-beam optics.[26] The

argon-ion laser's output has a electric field profile,

$$|E(\rho,z)| = E_0(z)\exp[-\rho^2/w^2(z)], \tag{5}$$

where z is the coordinate in the direction of propagation, ρ is the radial coordinate and 2w is the beam diameter. The intensity profile of the beam is

$$I(\rho,z) = \frac{P_0}{2\pi w^2(z)}\exp[-2\rho^2/w^2(z)], \tag{6}$$

where P_0 is the laser's output power. By integrating this equation, the power contained within a radius of ρ can be obtained,

$$P(\rho,z) = P_0[1-\exp[-2\rho^2/w^2(z)]]. \tag{7}$$

At the beam waist, which corresponds to z = 0, w(z) has its minimum value w_0. From the laser's technical specifications, the beam waist is located 1.54 m behind the laser's output mirror, and its diameter is $2w_0$ = 1.3 mm. At any position along the z axis, the beam's electric field profile is completely determined by the beam diameter 2w(z) and the wavefront radius of curvature R(z), which are given by[26]

$$w^2(z) = w_0^2\left[1+(z/z_R)^2\right], \tag{8}$$

and

$$R(z) = z\left[1 + (z_R/z)^2\right], \tag{9}$$

where z_R is

$$z_R = \frac{\pi w_0^2}{\lambda}. \tag{10}$$

As shown in Fig. 6.14, a plano-convex lens is positioned 1.7 m in front of the laser's output mirror, i.e. at $z = z_L$, where $z_L = 3.2$ m. At the lens, the beam diameter is $2w_{L1} = 2.08$ mm, and the wavefront radius of curvature is $R_{L1} = 5.28$ m. The lens, of focal length f, converts the wavefront curvature from R_{L1} to R_{L2}, where

$$\frac{1}{R_{L2}} = \frac{1}{R_{L1}} - \frac{1}{f}. \tag{11}$$

For $f < R_{L1}$, $R_{L2} < 0$, and the output beam is convergent. The beam radius is unchanged through the thin lens, so that $w_{L2} = w_{L1}$.

To determine the waist position of the focused beam, a new coordinate system is defined so that the lens is located at $z' = -z_f$ and $z' = 0$ is the focal

point. Substituting $w(-z_f) = w_{L2}$ and $R(-z_f) = R_{L2}$ into Eqs. 8 and 9, gives, for the waist radius w_f,

$$\frac{1}{w_f^2}=\frac{1}{w_{L2}^2}+\left[\frac{\pi w_{L2}}{R_{L2}\lambda}\right]^2, \tag{12}$$

and for z_f,

$$z_f=R_{L2}\left[w_f^2/w_{L2}^2-1\right]. \tag{13}$$

For f = 750 mm, R_{L2} = -874 mm, so that $2w_f$ = 272 μm and z_f = 859 mm. As the focal length of the lens decreases, z_f is more nearly equal to f.

With the laser operating at a very low power level, ~1 mW, a micropositioner was used to align the silicon-coated fiber end with the focused beam. The degree of alignment was inferred by observing the light reflected from the fiber end. Once aligned, no light was detected at the fiber's uncoated end, which indicates that the light coupled into the film was completely absorbed. Exposure of the silicon film was effected using a timer-driven shutter. After the fiber was aligned, the shutter was closed. The laser's power was then increased to the maximum value, and the exposure initiated.

Initial experiments were performed using an f = 200 mm lens. The fiber end was located 200 mm from the lens, very near to the 66-μm-diameter beam waist. Figure 6.15 shows a Nomarski microscope image of the silicon-coated fiber end after a 2-s anneal at 1 W. The central region of the film, 75 μm in diameter, has an extremely rough surface. This indicates that the film was at least partially melted. This rough region is dark at the center but lighter aroung the circumference. The dark central region has a diameter of 40 μm. Outside the rough region is a ring of finer grained material, with an O.D. of 115 μm. Beyond this fine-grained region, the film surface is smooth.

As shown by Fig. 6.16, an increased exposure time of 10 s caused the very rough region to extend almost to the edge of the fiber. Again, the central region, ~40 μm in diameter, appears dark. Figure 6.17 shows a film that was annealed for 0.5 s at a laser power of 2 W instead of 1 W (for this test, the laser's output was increased by removing the intracavity etalon). The dark area once again has a diameter of 40 μm. In this case the fiber and laser beam were apparently misaligned. The dark region is almost entirely smooth surfaced and has the appearance of a solidified pool of molten silicon. The surrounding material is lighter and rough surfaced. The rough surface may be caused by the formation of argon bubbles when the silicon is melted.[27,28] The

perturbations that result when these bubbles burst through the surface may become frozen in place in regions where the optical energy supplied was not sufficient to drive off all the argon before the exposure was terminated.

Because of the rough surface that results when the silicon is melted, solid-phase crystallization was attempted. The optical intensity was reduced by increasing the spot size, which also improved the intensity uniformity across the surface of the film. A lens with a 750-mm focal length was used, so that $2w_f = 272\ \mu m$ and $z_f = 859$ mm. The fiber end was positioned 680 mm from the lens, where the spot size is calculated to be $2w = 378\ \mu m$. At this position, if the 140-μm fiber is precisely aligned with the beam, 24% of the beam's power will be incident on the silicon film, and the intensity at the fiber's edge will be fully 76% of the intensity at the center. The average power density incident on the film is estimated to be 1.6 kW/cm^2. In practice, the alignment will be imperfect so it is advantageous to have a laser spot which is larger than the fiber, as is the case here. The spot size was measured by translating a 50-μm-diameter pinhole across the beam while monitoring the transmitted power. The diameter at one-half the peak intensity was measured to be $270 \pm 20\ \mu m$, which is $\sim$20% larger than the calculated value.

For a lens-to-fiber separation of 680 mm and a laser power of 1 W, anneals were performed with exposure times ranging from 0.125 s to 10 s. When inspected using the Nomarski microscope, all the annealed films appeared similar to the film shown in Fig. 6.18 (sensor 292), which was annealed for 2 s. The relative degrees of crystallization of the laser-annealed films were inferred from shifts in the absorptivity $\alpha(\lambda)$, as determined through analysis of $R_f(\lambda)$. A cut-on wavelength λ_{co} was arbitrarily defined to be the wavelength at which the interference fringe visibility was 0.5. For a silicon film, this is equivalent to $\alpha(\lambda_{co})L = 0.55$. The variations in L among the nominally 1.4-μm-thick films is not sufficient to affect this approximate analysis. The time required to fully crystallize the silicon was determined to be 1 s, since longer exposures produced no further reduction in λ_{co}. The shifts in $\alpha(\lambda)$ were discontinuous as a function of exposure time; exposures from 0.125 to 0.5 s yielded $\Delta\lambda_{co} = -115$ nm, while exposures from 1 to 10 s produced $\Delta\lambda_{co} = -200$ nm. Figure 6.19 shows the reflectivity $R_f(\lambda)$ of films that were laser annealed for 0.5 s and 2 s.

6.6 Analysis of Annealed Silicon Films

The optical properties of the annealed silicon can be determined more accurately by ellipsometry rather than reflectometry. The ellipsometer's analysis area (spot size), however, is approximately 1 x 2 mm, much larger than the diameter of either the fiber or the focused laser beam. To permit ellipsometric analysis of the annealed silicon, silicon films were sputter-deposited on fused-silica substrates and then rapid thermal annealed at various temperatures in an attempt to reproduce the effects of laser annealing. After it was determined by reflectometry that the effects of laser annealing could be replicated using rapid thermal annealing, ellipsometric measurements of the RTA samples were used to infer the optical properties of the laser-annealed silicon.

Silicon films were sputter deposited on fused-silica cover slips using the same conditions that were used for deposition on fibers. The samples were annealed, in forming gas, in a rapid thermal annealer which heated the samples, which were set on top of a silicon wafer, using infrared radiation. A thermocouple, in contact with the sample, was used for closed-loop temperature control. Following a 10-s temperature ramp, the samples were

held at temperatures from 550 to 900 °C for 30 s. After ellipsometric analysis, each film was reflectively analyzed by aligning it perpendicular to the end of coupler pigtail CP-3. A drop of index-matching fluid was applied, and the fiber and film were then brought into contact. From measurements of $R_f(\lambda)$, it was determined that the films deposited on the cover slips were identical to those deposited on the fibers. For films annealed at 550, 700, and 750 °C, $\Delta\lambda_{co}$ was the same as was produced by laser annealing for 0.5 s. For RTA temperatures of 800 and 900 °C, $\Delta\lambda_{co}$ was equal to that of the 2-s laser anneal. At temperatures of 550 and 900 °C, anneals of 5 min duration were performed. No further shifts in $\alpha(\lambda)$ were observed as a result of the increased annealing time.

The silicon films on cover slips were analyzed by ellipsometry before and after annealing. The ψ and Δ measurements were performed over the range of 250 nm to 1.0 μm, with a 10-nm sampling increment, and the angle of incidence was varied from 55° to 75° with a 5° increment. Because the SiO_2 substrates were only 0.15 mm thick, it was not possible to roughen their back sides. The reflections from the back surface were therefore modeled by incoherently superposing them onto the reflections from the front surface.

The optical properties obtained after laser annealing for 1 s or more were determined by analysis of the 900 °C RTA sample. The ψ and Δ functions of the RTA sample were first fit by using the Bruggemann EMA to model the annealed silicon as a mixture of a-Si, c-Si and void. For the optical properties of c-Si, the measurements of Aspnes and Studna were used.[22] For SiO_2 Bixner's data were used.[29] Both sets of data have been tabulated by Palik.[19] A better fit was obtained by representing the film's amorphous component using the properties of fully relaxed amorphous silicon,[20] rather than those of a-Si that was not annealed.[18] The film's surface roughness was modeled as an overlayer comprised half of the bulk material and half void. The fitting procedure yielded thicknesses of 4 nm for the overlayer and 1.39 μm for the film. The calculated film composition was 25.6% a-Si, 68.9% c-Si, and 5.5% void.

Figure 6.20 shows the experimental and calculated values of ψ, for a 70° angle of incidence. The fit deviates most notably from the experimental results at 360 nm or 3.4 eV. The ε_2 function of c-Si has a peak at 3.4 eV, the E_1 critical point, which is apparently absent from the ε_2 function of the annealed silicon. The strength of this E_1 peak, and therefore the applicability of the three-component EMA, is strongly dependent on the grain size. The

three-component EMA has been used to accurately fit ellipsometric measurements on polycrystalline silicon (poly-Si), as deposited by LPCVD at 650 °C and also after it was annealed with an argon-ion laser.[30] The laser in this case melted the silicon. The c-Si fraction was determined to be 14% as deposited and 88% after annealing. The EMA model was also used to fit measurements performed on similarly deposited poly-Si that was annealed at 950 °C in a furnace.[31] Here, the c-Si fraction was determined to be 57% after annealing. In this case, the fit was not as good; the calculated $<\varepsilon_2>$ exceeded the measured $<\varepsilon_2>$ by more than 5% at the 3.4 eV peak.

Jellison et al.[32] found that the three-component EMA does not accurately represent the dielectric function of fine-grain poly-crystalline silicon. For poly-Si which was known to have a small grain size, their best fit was similar to that of Fig 6.20, in the respect that their EMA model also produced features at 3.4 eV which were absent from the measured ψ and Δ data. The RTA poly-Si, analyzed here, is expected to be fine-grained, based on the results of Serikawa and Okamoto,[5] who obtained 33-nm grains after annealing, in a 950 °C furnace, sputter-deposited silicon that was initially amorphous.

In both of the instances where the annealed films were accurately represented by the three-component EMA, the grain size was presumably large. In the laser-annealed films, a few 1-μm grains were observed.[30] Since the furnace-annealed films were phosphorous doped,[31] the average grain size was probably between 0.5 and 1.0 μm.[33] For the as-deposited LPCVD silicon, which was fairly well fit with a c-Si content of 14%, the crystallite size should have been intermediate, between 0.1 to 0.3 μm.[34]

The three-component EMA was therefore abandoned, and the dielectric function of the RTA Si was determined by an approach similar to that used by Jellison.[32] In the wavelength region of low absorption, $\lambda > 450$ nm, the dielectric function of the poly-Si was represented using the model of Forouhi and Bloomer.[35] By considering the electronic states of an amorphous solid to

be a broadened superposition of molecular-orbital states, Forouhi and Bloomer obtained

$$k(E) = \frac{A(E-E_g)^2}{E^2-BE+C}. \quad (14)$$

Here, E is the photon energy, E_g is the optical band gap, and A, B and C are constants greater than 0 such that $4C-B^2 > 0$. From k(E), Forouhi and Bloomer used the Kramers-Kronig relation to obtain

$$n(E) = n(\infty) + \frac{B_0E+C_0}{E^2-BE+C}, \quad (15)$$

where B_0 and C_0 are determined by A,B,C, and E_g.[35] Using this model, n and k are fully determined by five independent parameters (A, B, C, E_g, and $n(\infty)$).

Over the range from 450 nm to 1.0 μm, the ellipsometric measurements of the 900 °C RTA sample were very well fit by adjusting the Forouhi-Bloomer coefficients, the film thickness, and the thickness and void fraction of a rough-surface overlayer. The MSE was minimized for a film thickness of 1.382 μm, and the overlayer thickness and void fraction were determined to be 6.1 nm and 80%. This implausibly high void fraction caused the overlayer's

refractive index to be nearly equal to that of SiO_2. Since an oxide of this thickness might very well be present, the data was refit using an SiO_2 overlayer instead of the supposed rough surface. This reduced the MSE from 14.1 to 13.7, giving film and oxide thicknesses of 1.384 μm and 5.6 nm. Further support for the validity of the oxide model was given by fitting the data for $\lambda \geq 600$ nm, only. The oxide model provided essentially the same results as were obtained for $\lambda \geq 450$ nm, but the rough-surface model gave a grossly different overlayer void fraction of 35%. As deposited, the silicon thickness was determined to be 1.356 μm, which implies that the density was reduced 2.0% by annealing.

The data were also fit using models with two overlayers, for instance, a mixture of RTA Si and SiO_2 underneath SiO_2 and void. This model was intended to represent the very plausible presence of both roughness and oxide. This additional complexity, however, was not justified, because, for $\lambda \geq 450$ nm, the absorption of RTA Si is so low that RTA Si combined with void is not readily distinguishable from SiO_2. This caused the solution to have a very large uncertainty due to the broadness of the MSE minimum.

To determine the optical properties of the RTA Si for $\lambda < 450$ nm, the thicknesses of the RTA Si and oxide were fixed at the values that were determined using the $\lambda \geq 450$ nm data. Then, at each measurement wavelength from 250 nm to 1.0 μm, n and k were adjusted to best fit the ψ and Δ measurements. At $\lambda = 450$ nm, the directly calculated n and k values differ only slightly from those of the Forouhi-Bloomer model ($\Delta n \approx 1\%$, $\Delta k \approx 10\%$). With increasing wavelength, the two sets of n and k measurements rapidly converge and are essentially identical for $\lambda > 600$ nm. The directly calculated n and k values, however, are fairly noisy in the region where interference effects first appear, 500 nm $< \lambda <$ 600 nm.

Figures 6.21 to 6.24 show the measured and calculated values of ψ and Δ for $\lambda < 500$ nm (all angles) and $\lambda > 500$ nm (70 ° only). Figure 6.25 shows the calculated values of n and k as functions of wavelength, while Figs. 6.26 and 6.27 show ε_1 and ε_2 as functions of photon energy. Figures 6.26 and 6.27 also show the values of ε_1 and ε_2 that were measured for the as-deposited a-Si films, as well as the values, from the literature, for single-crystal silicon.[19]

The ε_2 function of silicon that was annealed at 900 °C (Fig. 6.27) is similar to the ε_2 function of small-grained poly-Si, measured by Jellison.[32] In both instances $\varepsilon_2(E)$ has a single prominent peak, at ~4.1 eV, with no discernable structure at 3.4 eV. The principal difference is the magnitude of the ε_2 peak, which is 4% lower here. Also, the ε_2 peak occurs here at a slightly higher energy, 4.15 eV instead of 4.10 eV. A similar single-peaked ε_2 function was obtained by annealing PECVD a-Si at 1100 °C for 10 min.[36] The imaginary part of the dielectric function was determined by Kramers-Kronig analysis of reflectance measurements. This measurement method is less accurate than ellipsometry. The ε_2 peak, in this case, was located at 4.3 eV and was 6% lower than the peak of the RTA Si.

In the short-wavelength region, the measured dielectric function is extremely sensitive to the condition of the film's surface. Both the composition and thickness of any overlayers must be known if accurate n and k values are to be directly calculated. The two groups that measured single-peaked ε_2 functions both assumed ideal surfaces (the sample analyzed by Jellison was syton polished).[32,36] For the measurements reported here, if surface roughness is indeed present in combination with the assumed oxide, then the measured ε_2 will be somewhat inaccurate in the UV region. Therefore, the ε_2 function of

RTA Si shown in Fig. 6.27 should be regarded as approximate. The general shape of $\varepsilon_2(E)$, however, is not greatly affected by the surface condition. Therefore, it may be concluded that the silicon annealed at 900 °C is polycrystalline, with a small grain size. Also, since the n and k values measured in the long-wavelength region are little affected by the assumed overlayer, a high degree of confidence can be placed in the accuracy of these measurements. This is the wavelength region in which accurate n and k measurements are most necessary, since the optical fibers strongly atttenuate light with $\lambda < 500$ nm.

Figure 6.28 shows the good agreement between the $R_f(\lambda)$ that was measured, after a 2-s laser anneal, and that which was calculated using the ellipsometrically determined n and k values. This annealed silicon film was that of sensor 294, for which $R_f(\lambda)$ before annealing is shown in Fig. 6.12. The measured thicknesses, before and after annealing, imply a density reduction of 3.5%, which is larger than the 2.0% reduction determined by ellipsometry of the 900 °C RTA sample. During ellipsometric analysis of the RTA samples, the same positions were not analyzed each time. Because of the influence of film nonuniformity on the ellipsometric measurement, the density change measured by reflectometry is considered more reliable. Since

amorphous and single-crystal silicon have equal densities,[37] the density reduction observed following laser crystallization must be a product of the polycrystalline film's granularity.

The good agreement of the measured and theoretical R_f functions shows that excellent thickness uniformity is obtained for deposition onto the fiber ends, since no reduction from the theoretical fringe visibility is observed. Also, the coupling of noncollimated light from the fiber to the film is shown to have the negligible effect on fringe visibility that was predicted in section 4. In the case of the laser-annealed films, the good agreement of the measured and theoretical R_f functions shows that the effects of annealing are uniform as well.

The optical properties of the intermediate annealed state were determined by ellipsometric analysis of the 750 °C RTA sample. In this case, the ellipsometric data were very well fit using the dielectric function of a-Si that was deposited at 570 °C by LPCVD.[20] This indicates that annealing at temperatures between 550 and 750 °C (and laser annealing for 0.125 to 0.5 s) reduces the structural disorder of the amorphous silicon but causes negligible crystallization. The a-Si annealed at 750 °C was determined to have a void fraction of 1.1%, relative to the LPCVD a-Si. An overlayer of 50:50 a-Si and

SiO_2 was assumed to be covered with another layer of pure SiO_2. The thicknesses of these layers were determined to be 2.8 nm and 1.1 nm, respectively. This two-overlayer model was supported in this case because the overlayer thicknesses could be determined using the UV ellipsometric data, where a-Si and SiO_2 have markedly different optical properties. Once the surface overlayers were determined, n and k could be calculated for the infrared wavelengths outside the range of the data for LPCVD a-Si.

Figure 6.29 shows the the measured $R_f(\lambda)$, for a 0.5-s laser anneal, together with the $R_f(\lambda)$ that was calculated using the n and k values of the 750 °C RTA sample. In this case, the thickness change caused by laser annealing was roughly equal to the measurement resolution. The implied density reduction was in this case 0.2 ± 0.2 %.

6.7 Conclusion

Optimum conditions were determined for the magnetron-sputter deposition of dense amorphous-silicon films on the ends of optical fibers. The uniformity of these films was found to be excellent. A laser-annealing process was determined which fully crystallized the silicon, without degrading the

optical properties of the thin-film interferometer. The power density was 1.6 kW/cm^2 at a wavelength of 514 nm. Two annealed states were identified. The first was fully relaxed a-Si, which was produced by laser anneals of 0.125 to 0.5 s duration and also rapid thermal anneals at 550 to 750 °C. The second annealed state was poly-Si, which was produced by laser anneals of 1 to 10 s duration and also rapid thermal anneals at 800 and 900 °C. Ellipsometric measurements showed that this material was poly-crystalline silicon with a small grain size. The measured dielectric function of this poly-Si was found to permit accurate modeling of the reflectivity of the silicon thin-film interferometer.

6.8 References

1. S.L. Semjonov, M.M. Bubnov, E.M. Dianov, and A.G. Shchebunyaev, "Reliability of Aluminum Coated Fibers at High Temperature," in **Fiber Optics Reliability and Testing: Benign and Adverse Environments VI,** D.K. Paul and H.H. Yuce, eds., Proc. SPIE 2074, pp. 25-33 (1994).

2. J.R. Hollahan and R.S. Rossler, "Plasma Deposition of Inorganic Thin Films," in **Thin Film Processes**, J.L. Vossen and W. Kern, eds., (Academic Press, New York, 1978) pg. 354.

3. R. Kakkad, J. Smith, W.S. Lau, and S.J. Fonash, "Crystallized Si Films by Low-Temperature Rapid Thermal Annealing of Amorphous Silicon," J. Appl. Phys. 65, 2069 (1989).

4. A. Madan, P.G. LeComber, and W.E. Spear, "Investigation of Density of Localized States in A-Si using Field-Effect Technique," J. Non-Cryst. Solids 20, 239 (1976).

5. A. Okamoto and T. Serikawa, "Magnetron-Sputtered Silicon Films for Gate Electrodes in MOS Devices," J. Electrochem. Soc. 134, 1479 (1987).

6. W.T. Pawlewicz, "Influence of Deposition Conditions on Sputter-Deposited Amorphous Silicon," J. Appl. Phys. 49, 5595 (1978).

7. R.C. Ross and R. Messier, "Microstructure and Properties of RF-Sputtered Amorphous Hydrogenated Silicon Films," J. Appl. Phys. 52, 5329 (1981).

8. Y. Zaka, S.A. Abo-Namous, and R.W. Fane, "Control of Electrical and Optical Properties of Unhydrogenated Neon-Sputtered Amorphous Silicon by Preparation Conditions," Thin Solid Films 125, 47 (1985).

9. A. Bhattackaryya and K.N. Ritz, "Grain Growth Studies in Polysilicon by Ar^{40} Ion Implantation and Thermal Annealing," J. Electrochem. Soc. 131, 2143 (1984).

10. J. Fortner and J.S. Lannin, "Radial-Distribution Functions of Amorphous Silicon," Phys. Rev. B39, 5527 (1989).

11. S. Roorda, J.S. Custer, W.C. Sinke, J.M. Poate, D.C. Jacobson, A. Polman, and F. Spaepen, "Structural Relaxation in Amorphous Silicon and the Role of Network Defects," Nucl. Instr. and Meth. B59/60, 344 (1991).

12. J.E. Fredrickson, C.N. Waddell, W.G. Spitzer, and G.K. Hubler, "Effects of Thermal Annealing on the Refractive Index of Amorphous Silicon Produced by Ion Implantation," Appl. Phys. Lett. 40, 172 (1982).

13. R.A. Lemons, M.A. Bosch, A.H. Dayem, J.K. Grogan, and M.M. Mankiewich, "Laser Crystallization of Si Films on Glass," Appl. Phys. Lett. 40, 469 (1982).

14. G.K. Celler, "Laser Crystallization of Thin Si Films on Amorphous Insulating Substrates," J. Crystal Growth 63, 429 (1983).

15. J.A. Woollam Co., Lincoln, NE 68508.

16. D.E. Aspnes, "Optical Properties of Thin Films," Thin Solid Films 89, 249 (1982).

17. W.H. Press, B.P. Flannery, S.A. Teukolsky, and W.T. Vetterling, **Numerical Recipes** (Cambridge University Press, Cambridge, 1989) pp. 521-528.

18. D.T. Pierce, and W.E. Spicer, "Electronic Structure of Amorphous Si from Photoemission and Optical Studies," Phys. Rev. B 5, 3017 (1972).

19. Handbook of Optical Constants of Solids, edited by E.D. Palik (Academic, Orlando, 1985).

20. D.E. Aspnes, A.A. Studna, and E. Kinsbron, "Dielectric Properties of Heavily Doped Crystalline and Amorphous Silicon From 1.5 to 6.0 eV," Phys. Rev. B 29, 768 (1984).

21. M. Fried, T. Lohner, W.A.M. Aarnik, L.J. Hanekamp, A. van Silfhout, "Determination of Complex Dielectric Functions of Ion Implanted and Implanted-Annealed Amorphous Silicon by Spectroscopic Ellipsometry," J. Appl. Phys. 71, 5260 (1992).

22. D.E. Aspnes and A.A. Studna, "Dielectric Functions and Optical Parameters of Si, Ge, GaP, GaAs, GaSb, InP, InAs, and InSb from 1.5 to 6.0 eV," Phys. Rev. B 27, 985 (1983).

23. R.P. Vasquez, A. Madhukar, and A.R. Tanguay, Jr., "Spectroscopic Ellipsometry and X-Ray Photoelectron Spectroscopy Studies of the Annealing Behavior of Amorphous Silicon Produced By Ion Implantation," J. Appl. Phys. 58, 2337 (1985).

24. I.H. Malitson, "Interspecimen Comparison of the Refractive Index of Fused Silica," J. Opt. Soc. Am. 55, 1205 (1965).

25. Fiberguide Industries, Stirling, NJ 07980.

26. A.E. Siegman, **Lasers** (University Science Books, Mill Valley, California, 1986).

27. S. Matteson, P. Revesz, Gy. Farkas, J. Gyulai, and T.T. Sheng, "Epitaxial Regrowth of Ar Implanted Amorphous Si by Laser Annealing", J. Appl. Phys. 51, 2625 (1980).

28. E. Fogarassy, R. Stuck, M. Toulemonde, P. Siffert, J.F. Morhange, and M. Balanski, "Pulsed Laser Annealing of RF Sputtered Amorphous Si: H Films, Doped with Arsenic," in Laser and Electron-Beam Interactions with Solids, B.R. Appleton and G.K. Celler, eds. (Elsevier, 1982), pp. 553-558.

29. B. Brixner, "Refractive-Index Interpolation for Fused Silica," J. Opt. Soc. Am. 57, 674 (1967).

30. B.G. Bagley, D.E. Aspnes, G.K. Celler, and A.C. Adams, "Optical Characterization of Chemically Vapor Deposited and Laser-Annealed Polysilicon," in **Laser and Electron-Beam Interactions with Solids**, B.R. Appleton and G.K. Celller, eds. (North Holland, New York, 1982) pp. 483-487.

31. B.G. Bagley, D.E. Aspnes, A.C. Adams, and C.J. Mogab, "Optical Properties of Low-Pressure Chemically Vapor Deposited Silicon over the Energy Range 3.0-6.0 eV, Appl. Phys. Lett. 38, 56 (1981).

32. G.E. Jellison, Jr., M.F. Chisholm, and S.M. Gorbatkin, "Optical Functions of Chemical Vapor Deposited Thin-Film Silicon Determined by Spectroscopic Ellipsometry," Appl. Phys. Lett. 62, 3348 (1993).

33. A.C. Adams, "Dielectric and Polysilicon Film Deposition," in **VLSI Technology**, S.M. Sze, ed. (McGraw-Hill, New York, 1983) p. 103.

34. G. Harbeke, L. Krausberger, E.F. Steigmeier, A.E. Widmer, H. Kappert, and G. Neugebauer, "Growth and Physical Properties of LPCVD Polycrystalline Silicon Films," J. Electrochem. Soc. 131, 675 (1984).

35. A.R. Forouhi and I. Bloomer, "Optical Dispersion Relations for Amorphous Semiconductors and Amorphous Dielectrics," Phys. Rev. B 34, 7018 (1986).

36. G.-J. Fan, F.H. Pollak, and R. Tsu, "Optical Properties of Disordered Silicon in the Range 1-10 eV," Solar Energy Materials 8, 241 (1982).

37. P. Baeri and S.U. Campisano, "Heat Flow Calculations," in **Laser Annealing of Semiconductors**, J.M. Poate and J.W. Mayer, eds. (Academic Press, New York, 1982) p. 81.

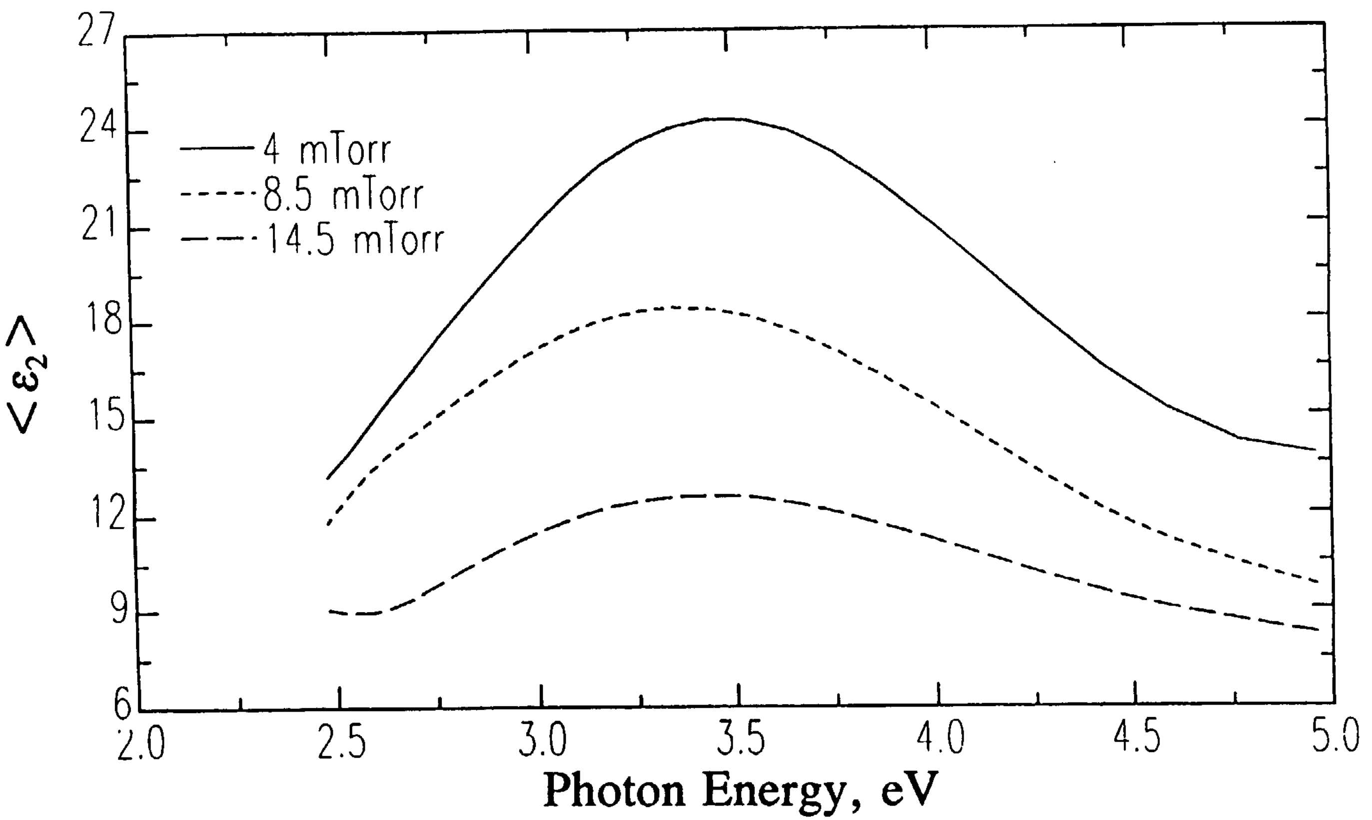

Figure 6.1 Imaginary part of the pseudo-dielectric function $<\varepsilon_2(E)>$, where E is the photon energy, for silicon sputter-deposited at different pressures.

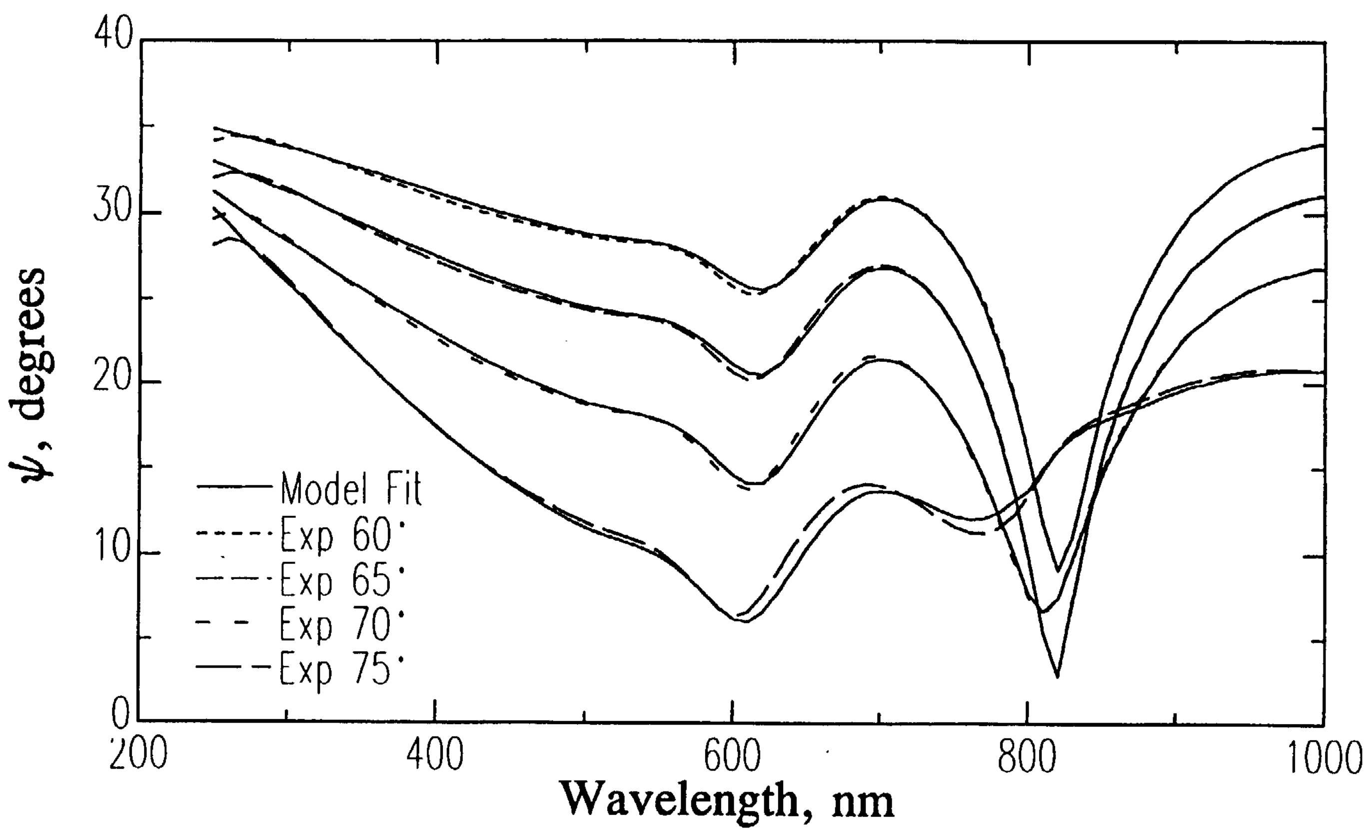

Figure 6.2 Measured and calculated $\psi(\lambda)$ for silicon sputter-deposited at 4.0-mTorr pressure and 400-W RF power.

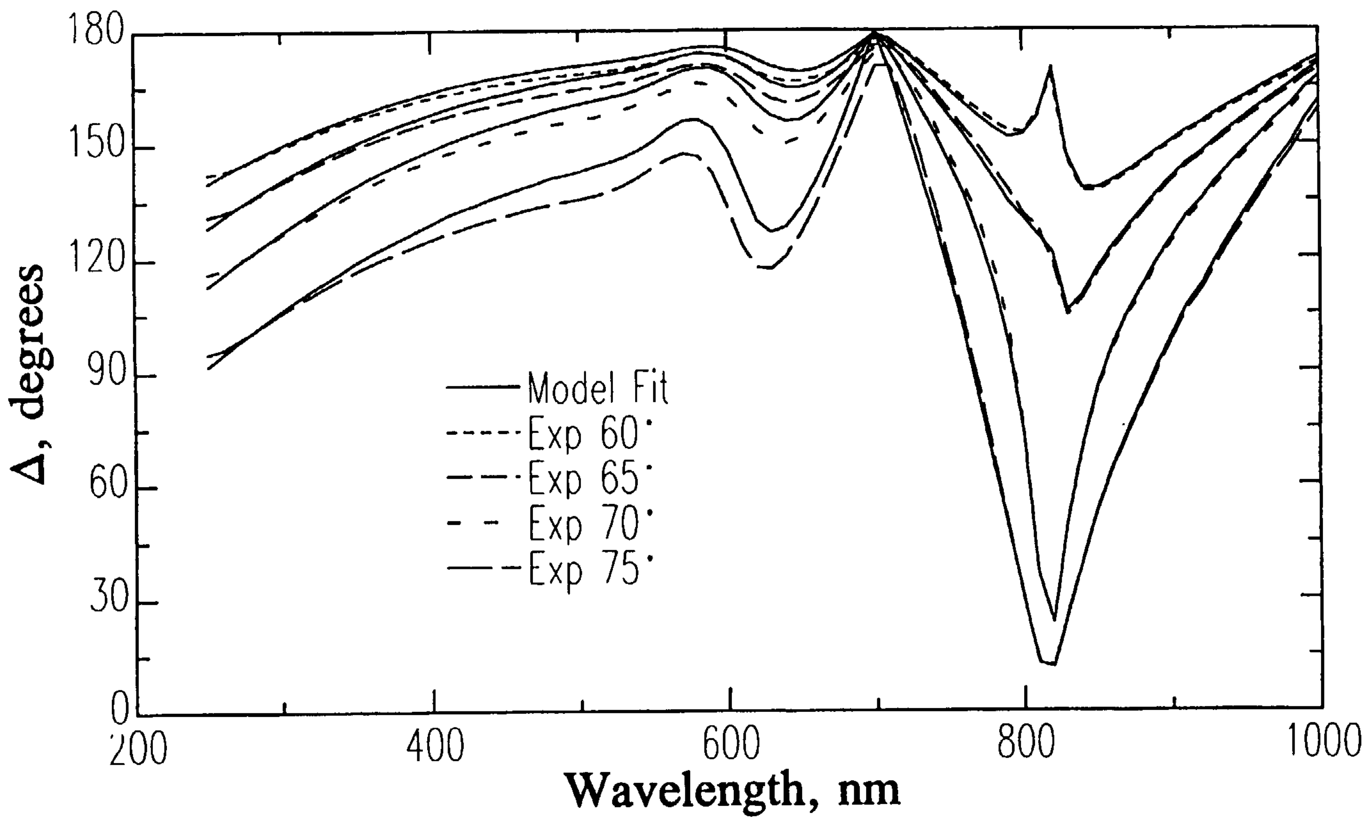

Figure 6.3 Measured and calculated $\Delta(\lambda)$ for silicon sputter-deposited at 4.0-mTorr pressure and 400-W RF power.

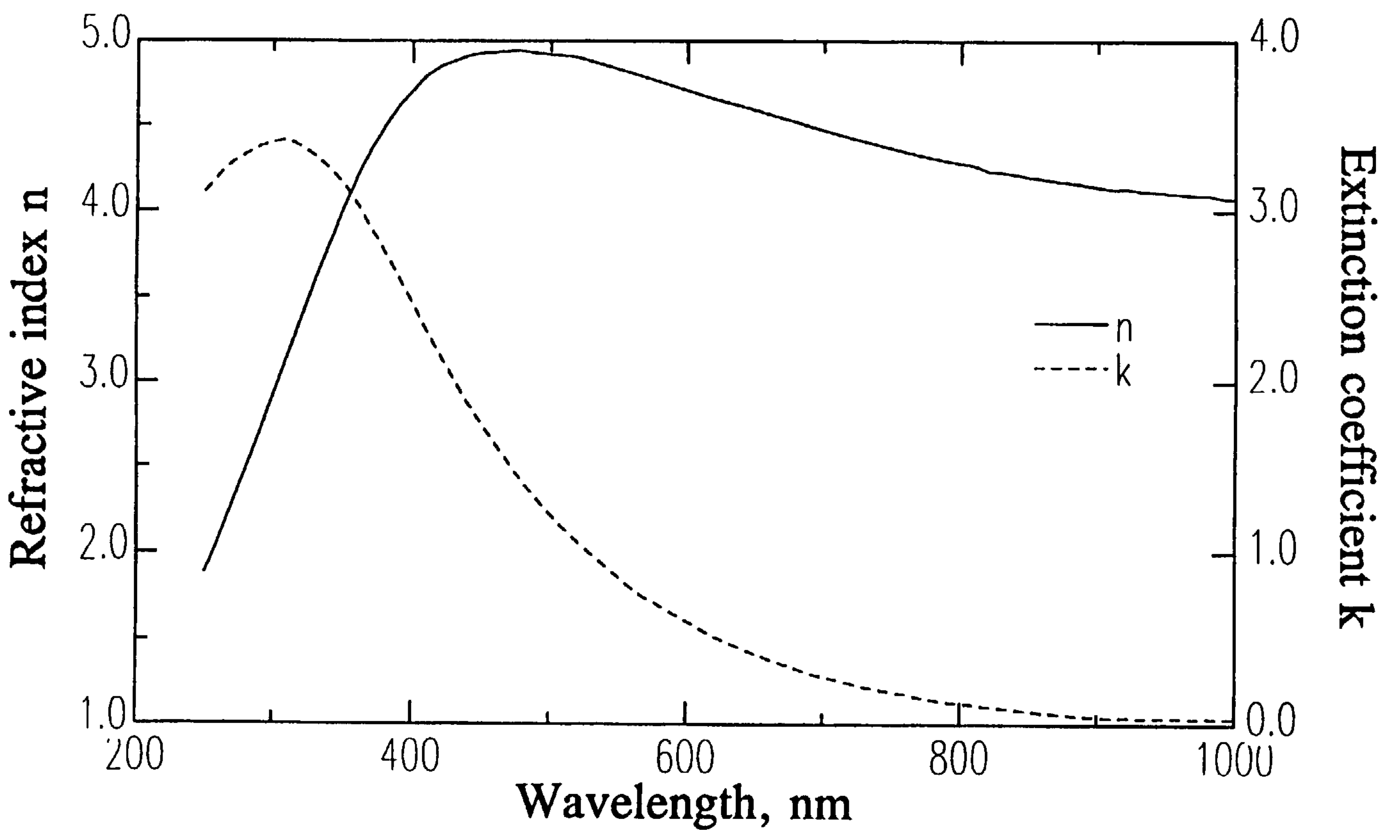

Figure 6.4 Measured $n(\lambda)$ and $k(\lambda)$ for sputter-deposited silicon films.

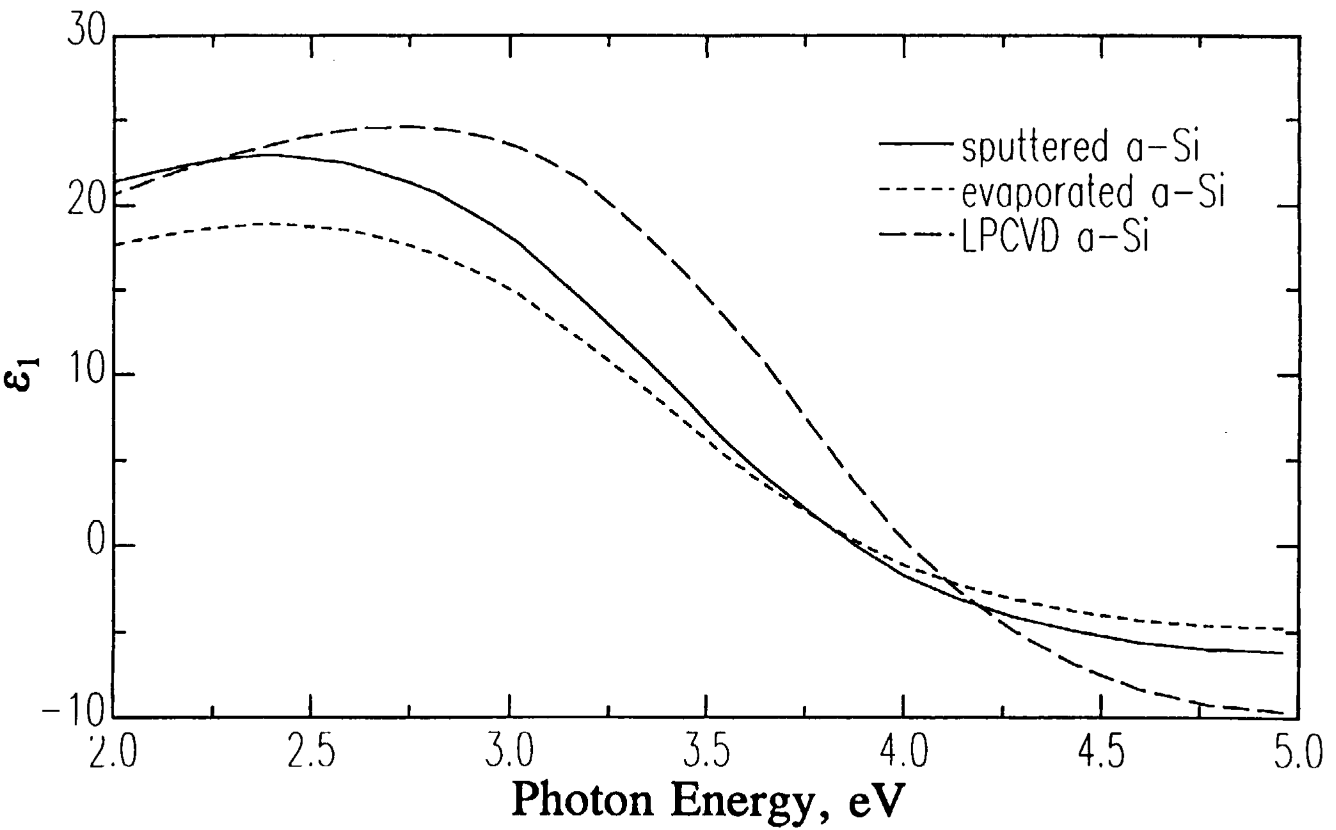

Figure 6.5 Real part of the dielectric function $\varepsilon_1(E)$ for sputter-deposited a-Si, evaporated a-Si and LPCVD a-Si.

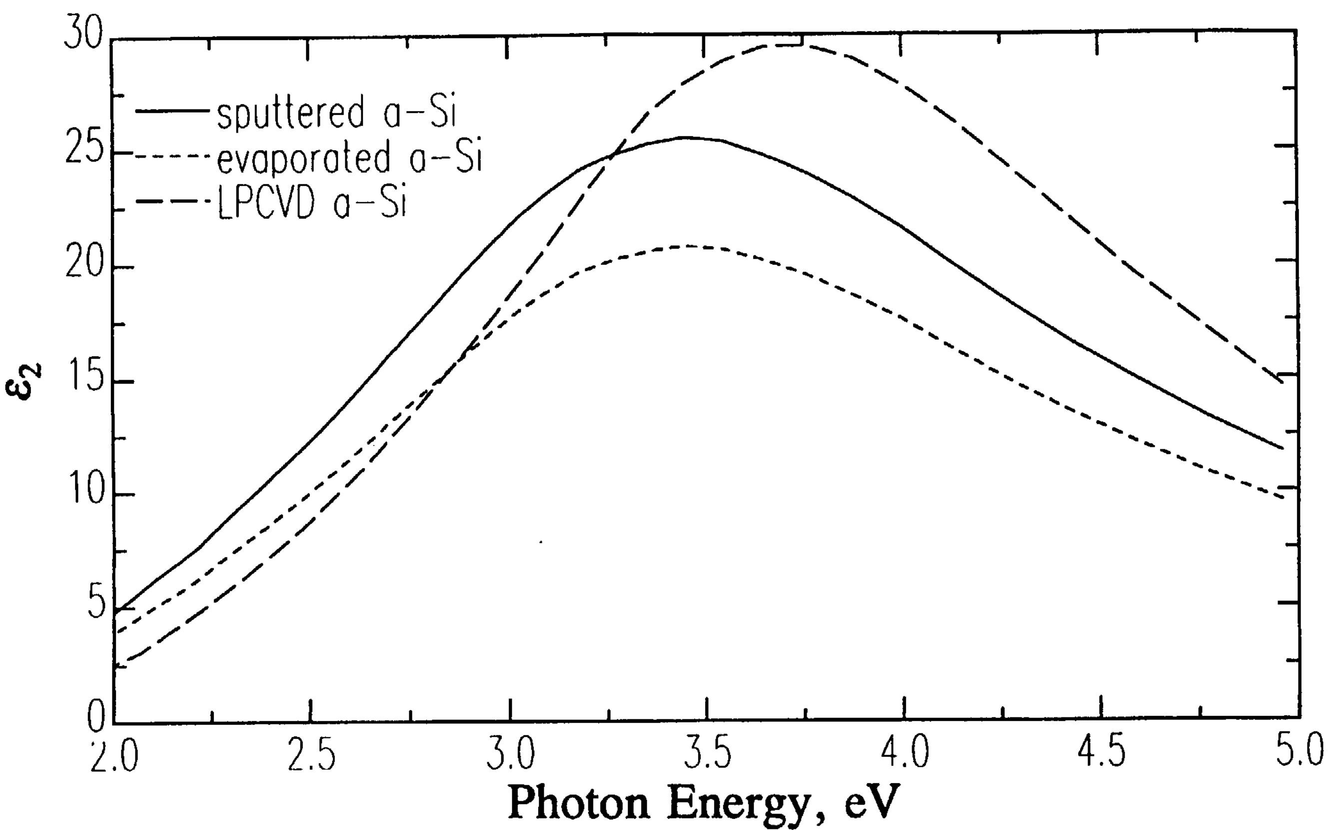

Figure 6.6 Imaginary part of the dielectric function $\varepsilon_2(E)$ for sputter-deposited a-Si, evaporated a-Si and LPCVD a-Si.

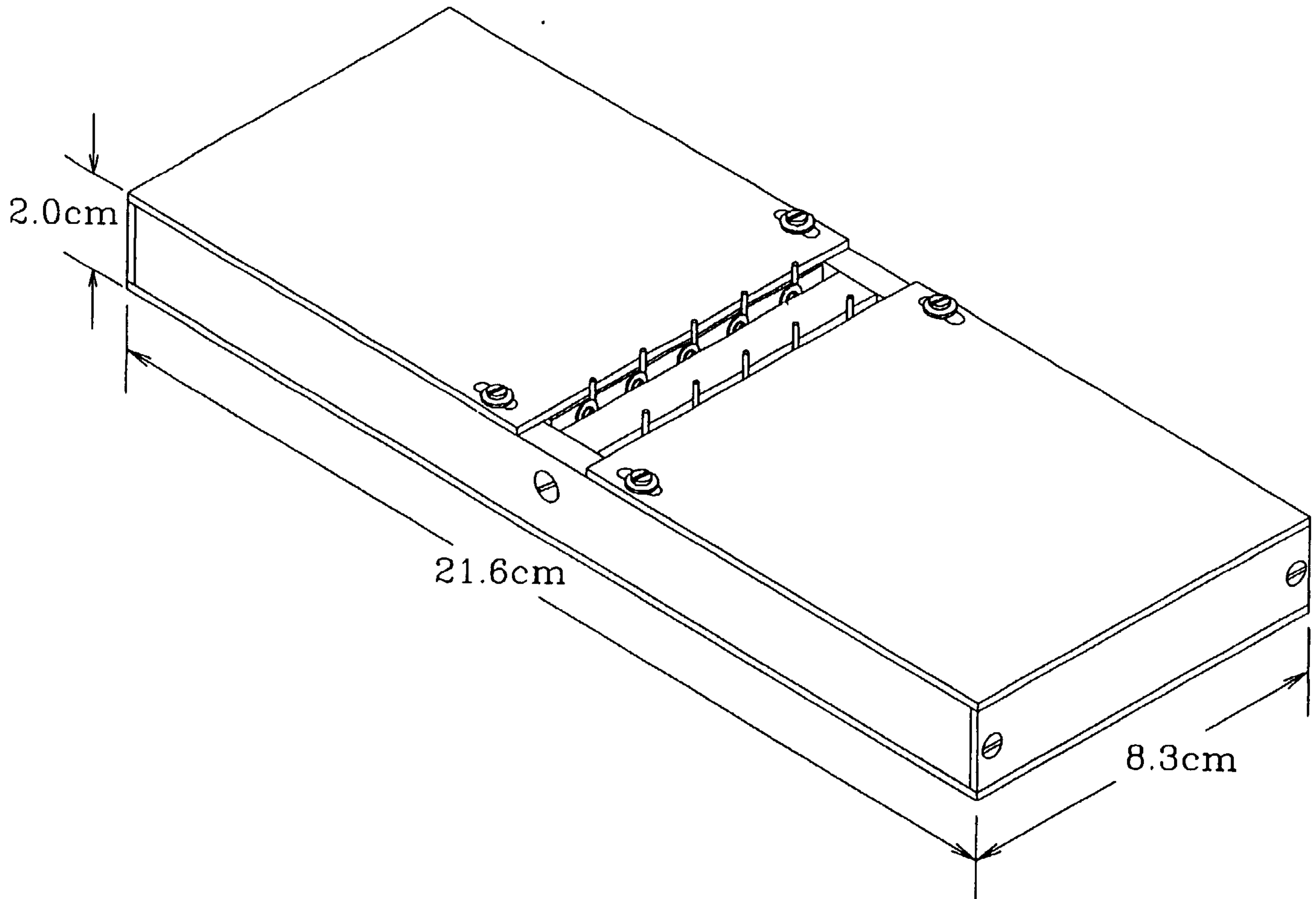

Figure 6.7 Fiber holder for sputter deposition.

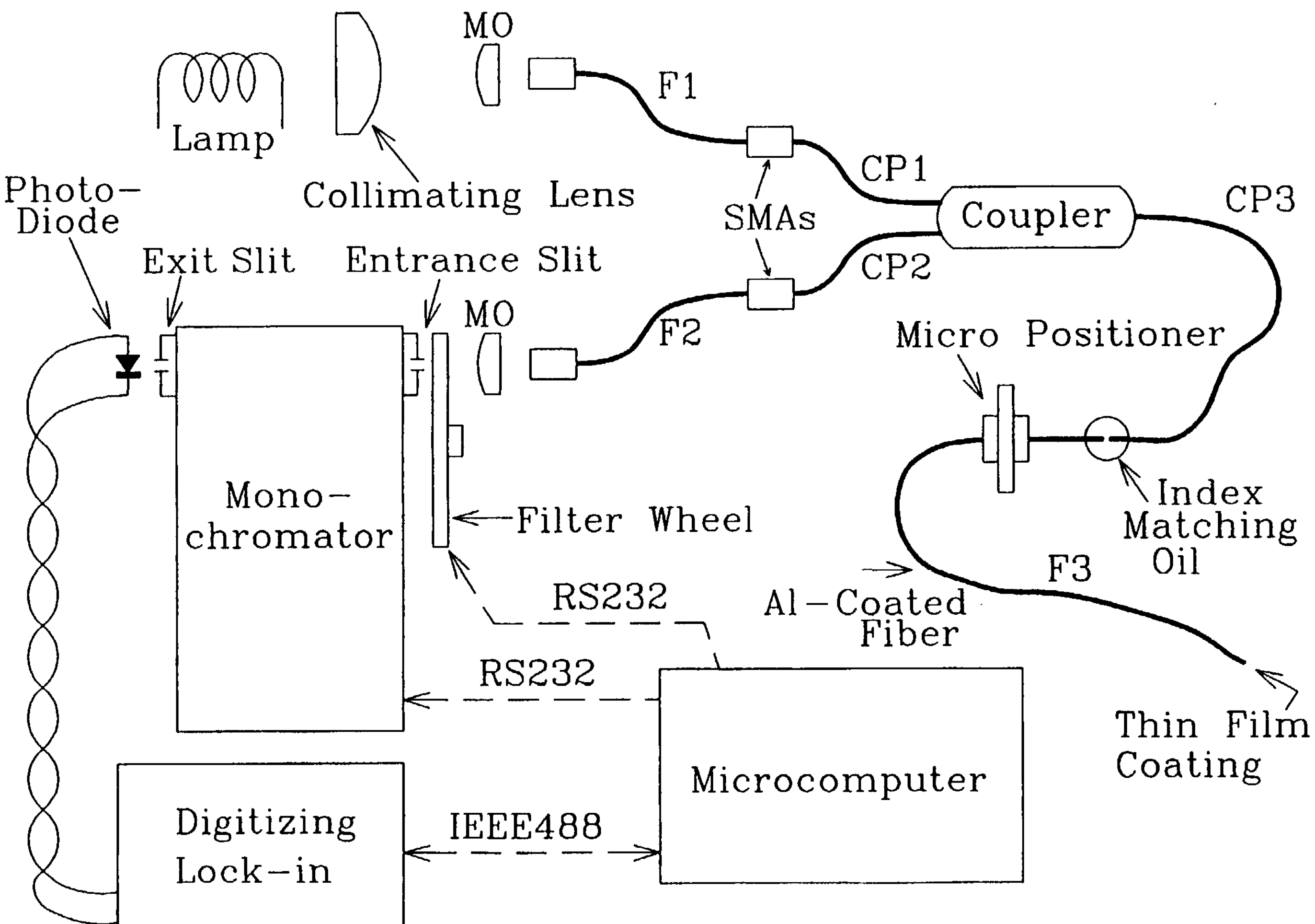

Figure 6.8 Schematic of fiber-coupled spectrometer showing microscope objectives (MO), fibers (F) and coupler pigtails (CP).

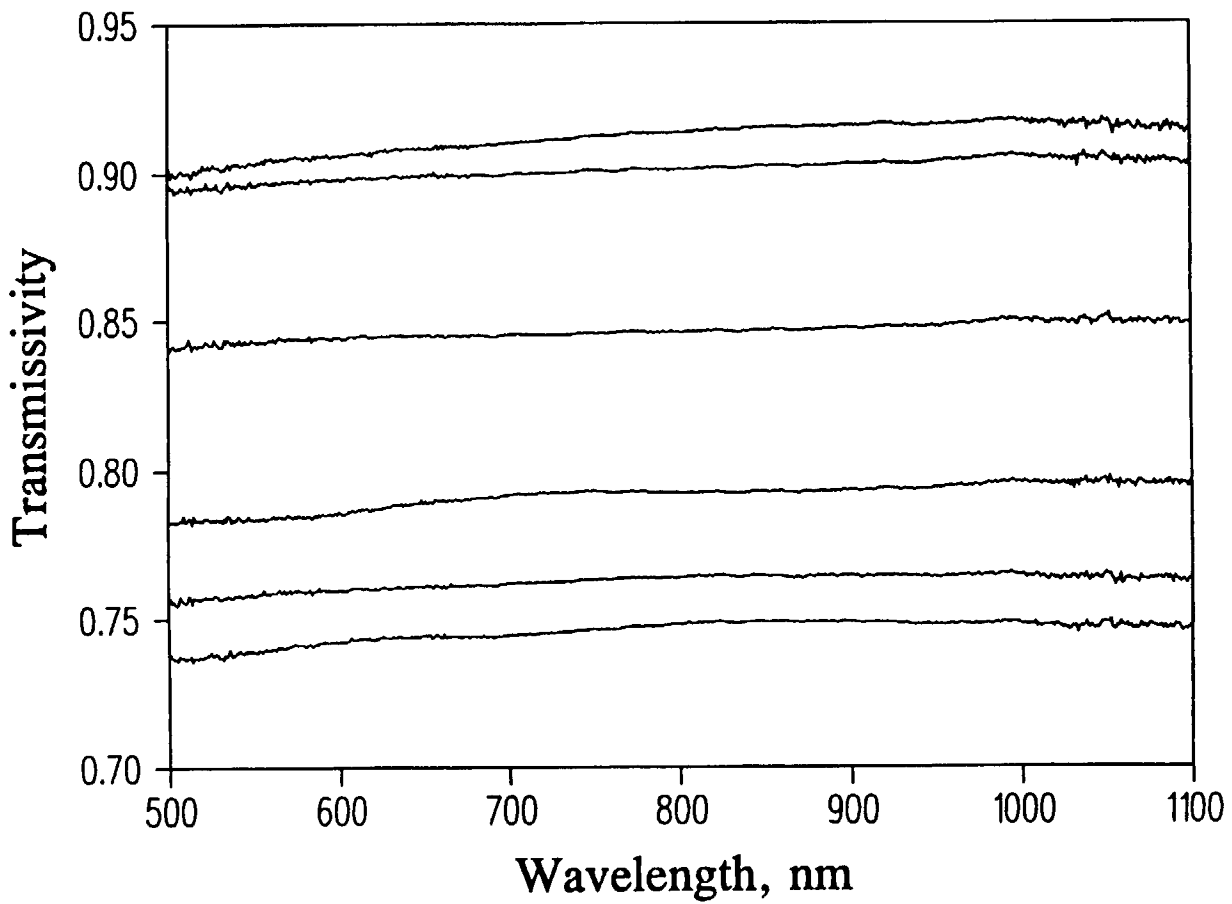

Figure 6.9 Transmissivities of 1.5-m fiber and connector $H_{F1}C_{F1\text{-}F2}(\lambda)$ showing effects of connector remating.

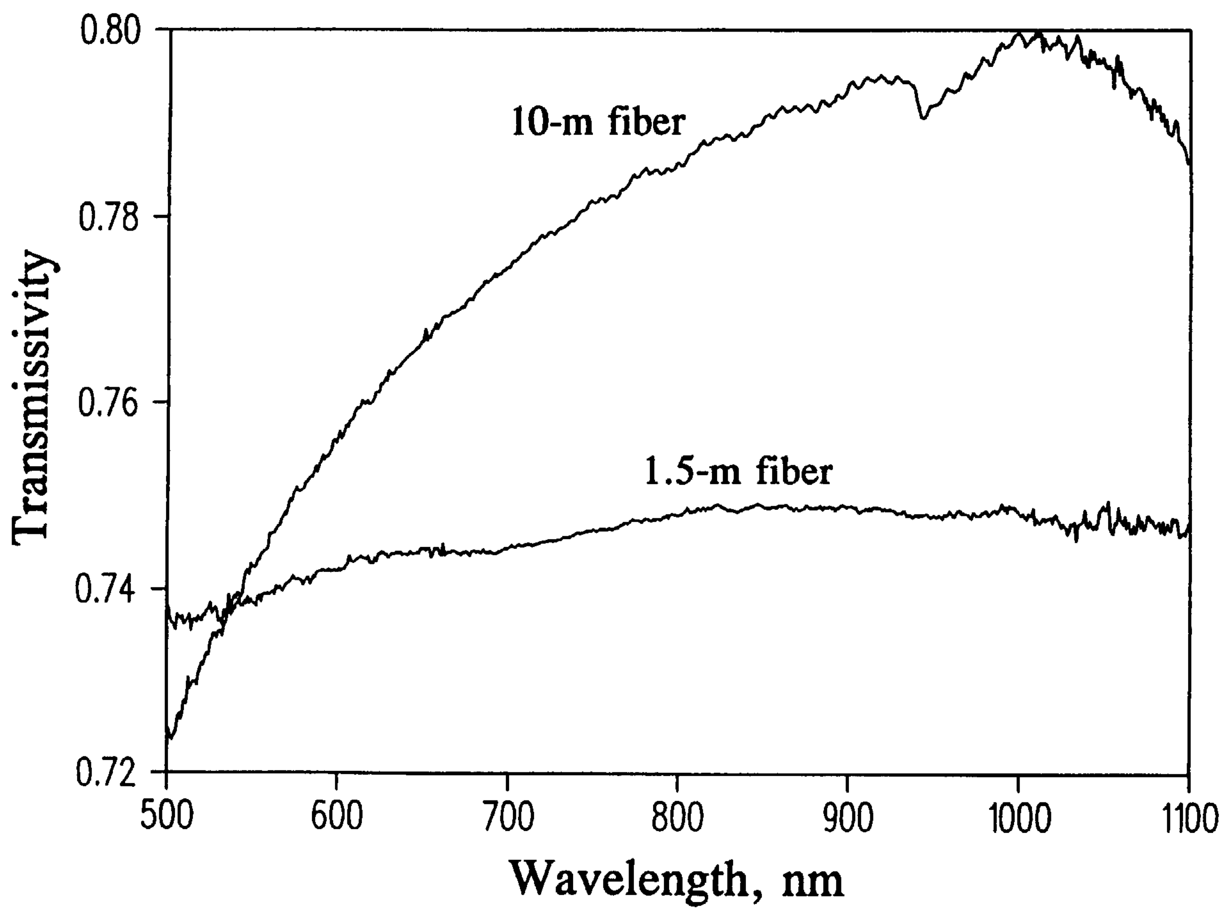

Figure 6.10 Transmissivities of fiber and connector $H_{F1}C_{F1\text{-}F2}(\lambda)$ for 1.5-m and 10-m long fibers.

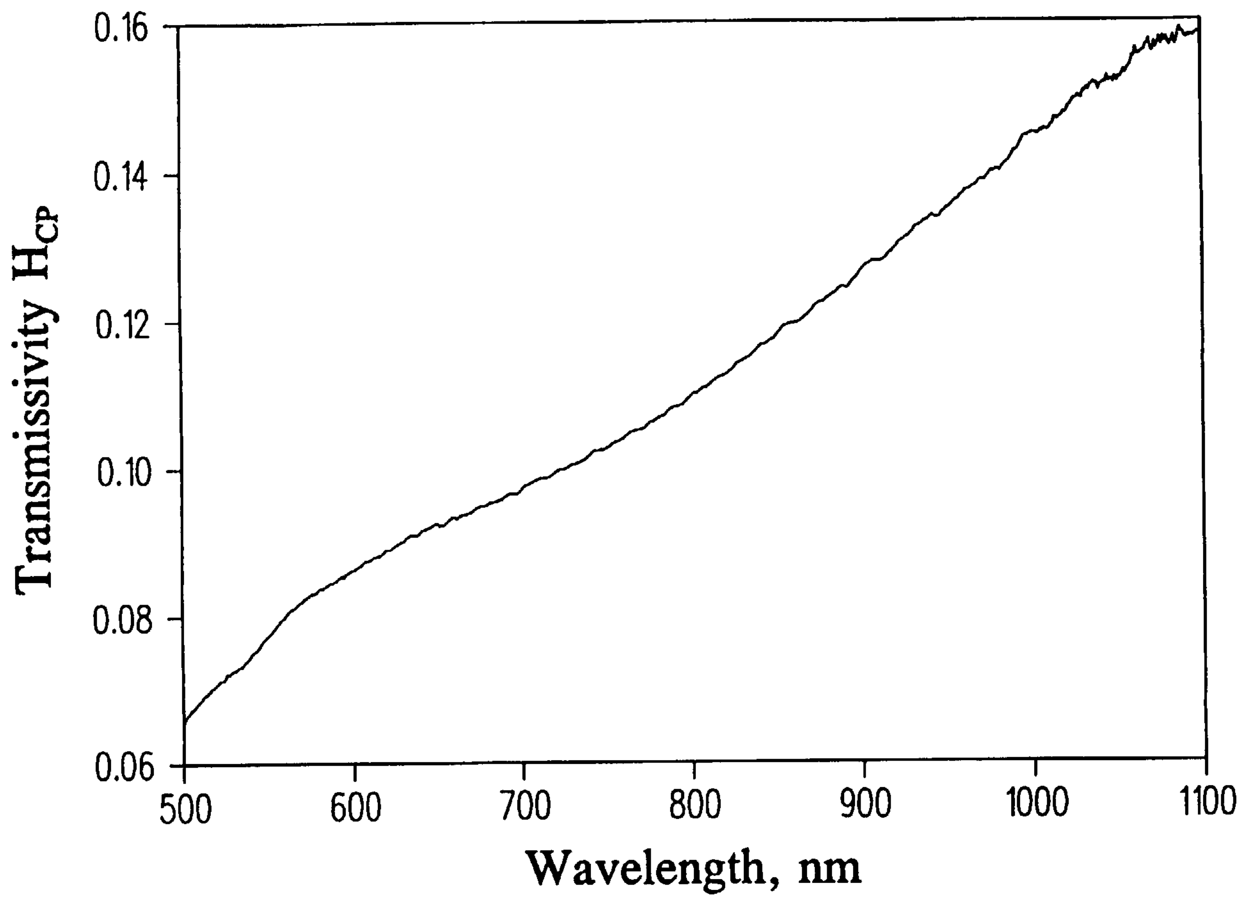

Figure 6.11 Round-trip transmissivity $H_{CP}(\lambda)$ of coupler and mechanically aligned splice.

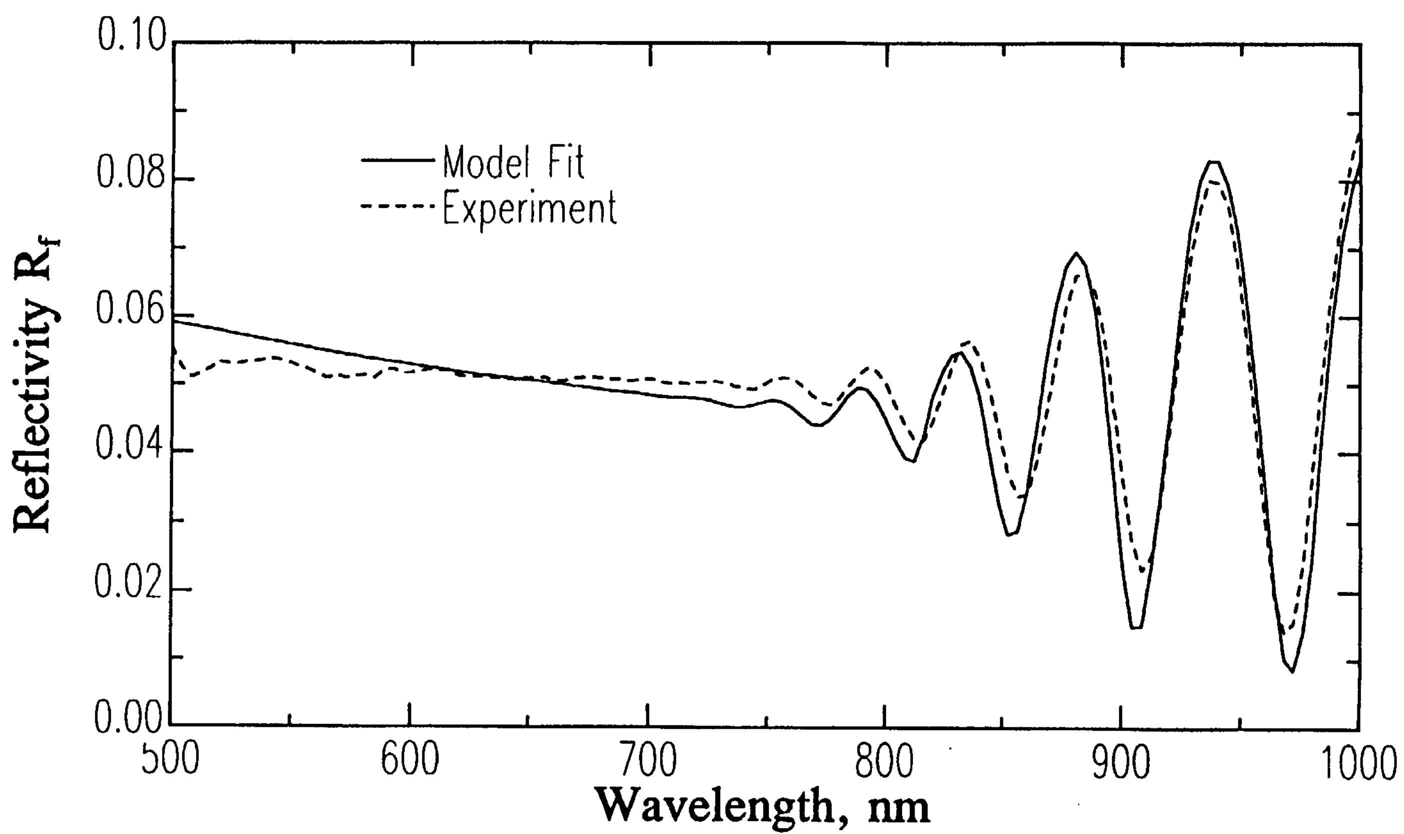

Figure 6.12 Measured and calculated reflectivity $R_f(\lambda)$ of silicon film sputter-deposited on fiber end (sensor 294).

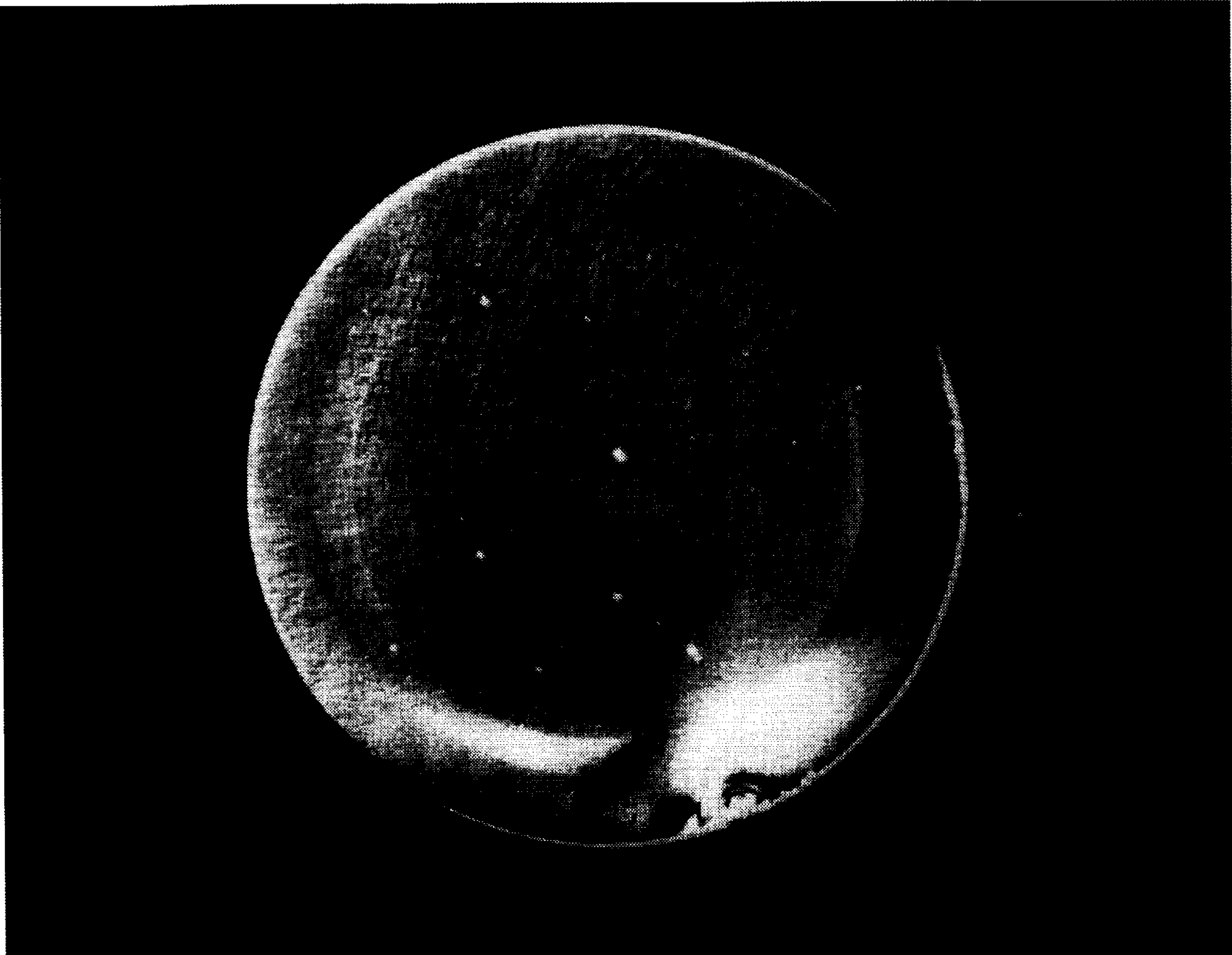

Figure 6.13 Nomarski-microscope image of silicon film sputter-deposited on fiber end.

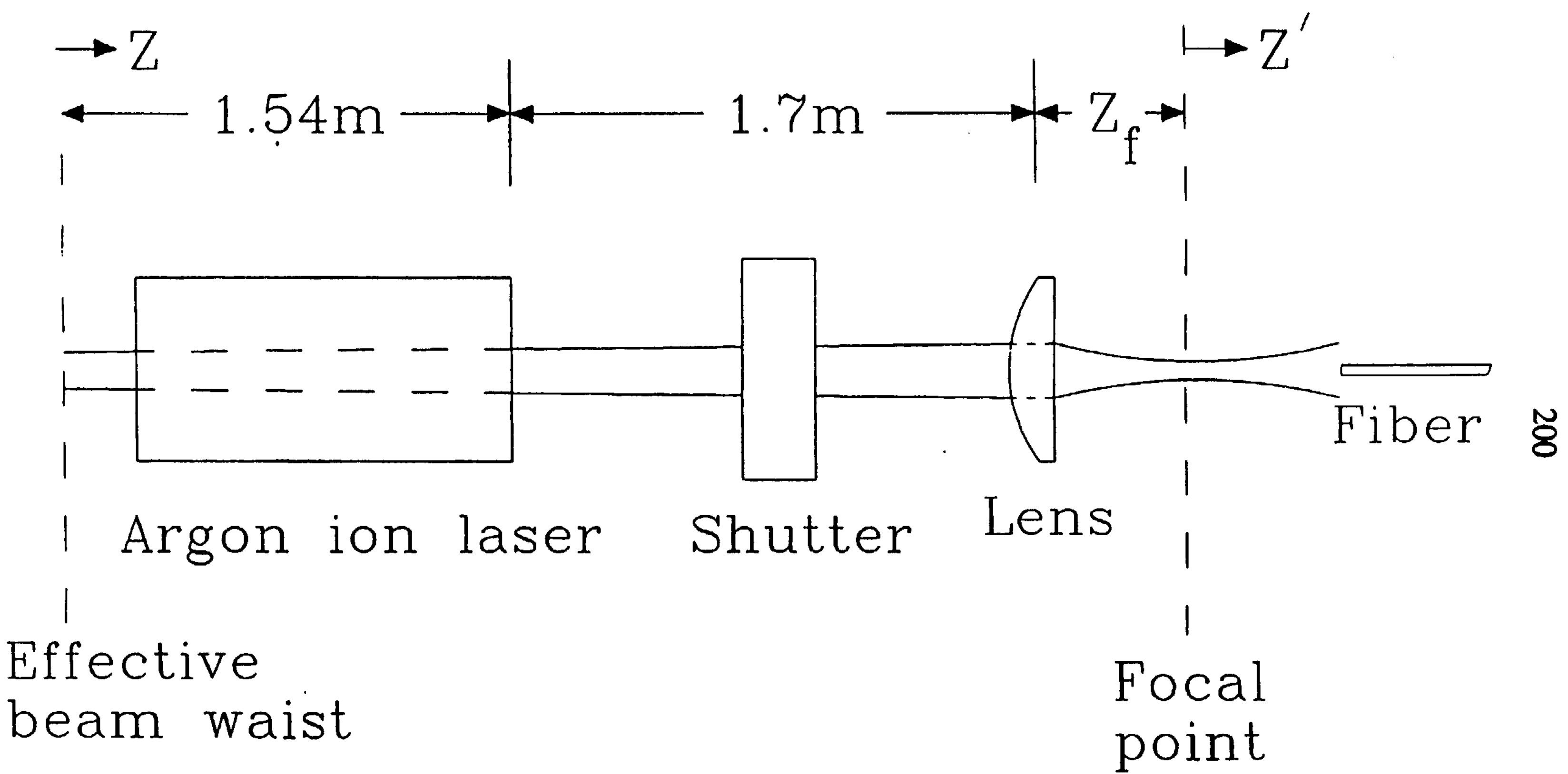

Figure 6.14 Schematic of laser-annealing apparatus.

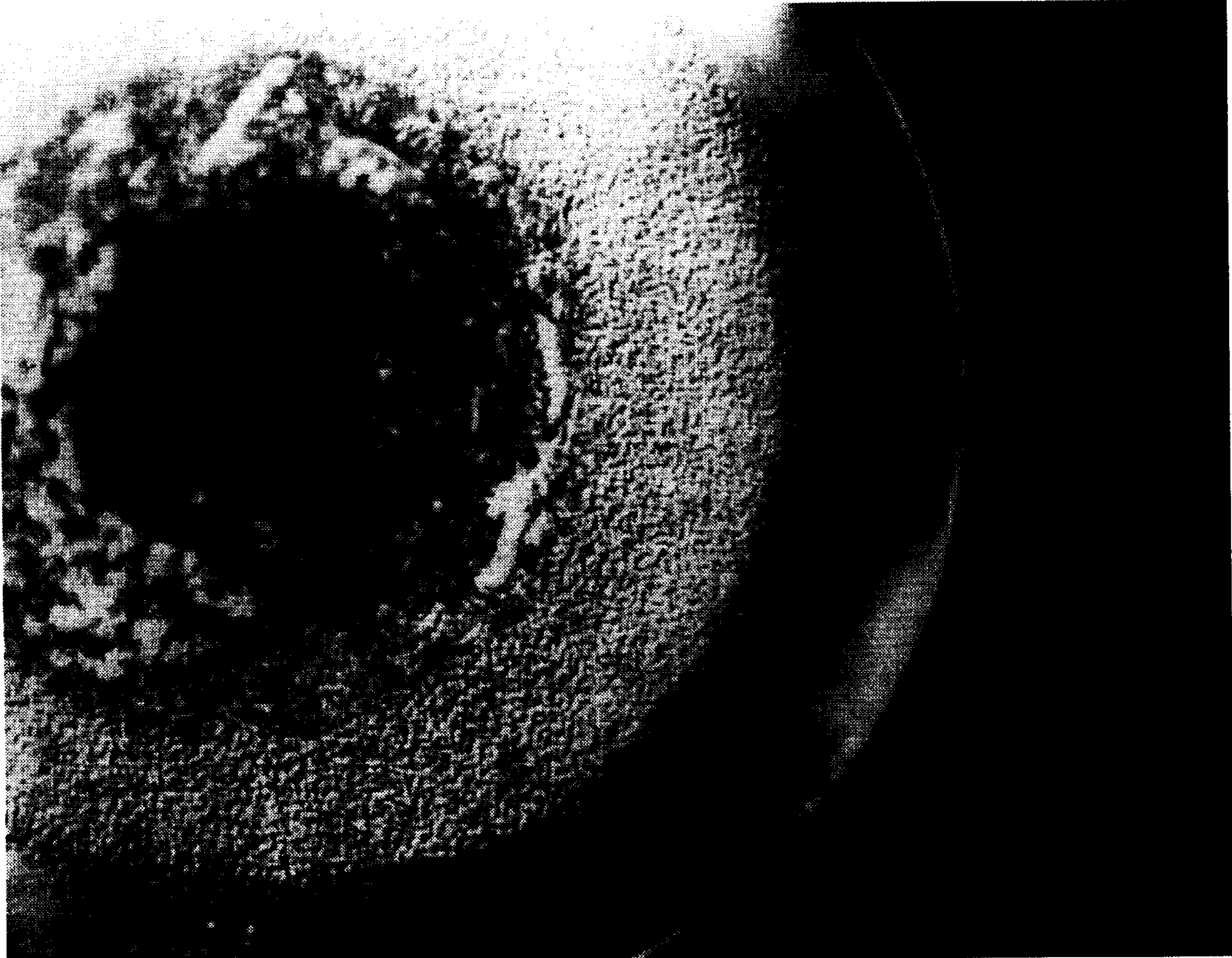

Figure 6.15 Silicon film annealed for 2 s with 1-W laser beam focused to a 66-μm-diameter spot.

Figure 6.16 Silicon film annealed for 10 s with 1-W laser beam focused to a 66-μm-diameter spot.

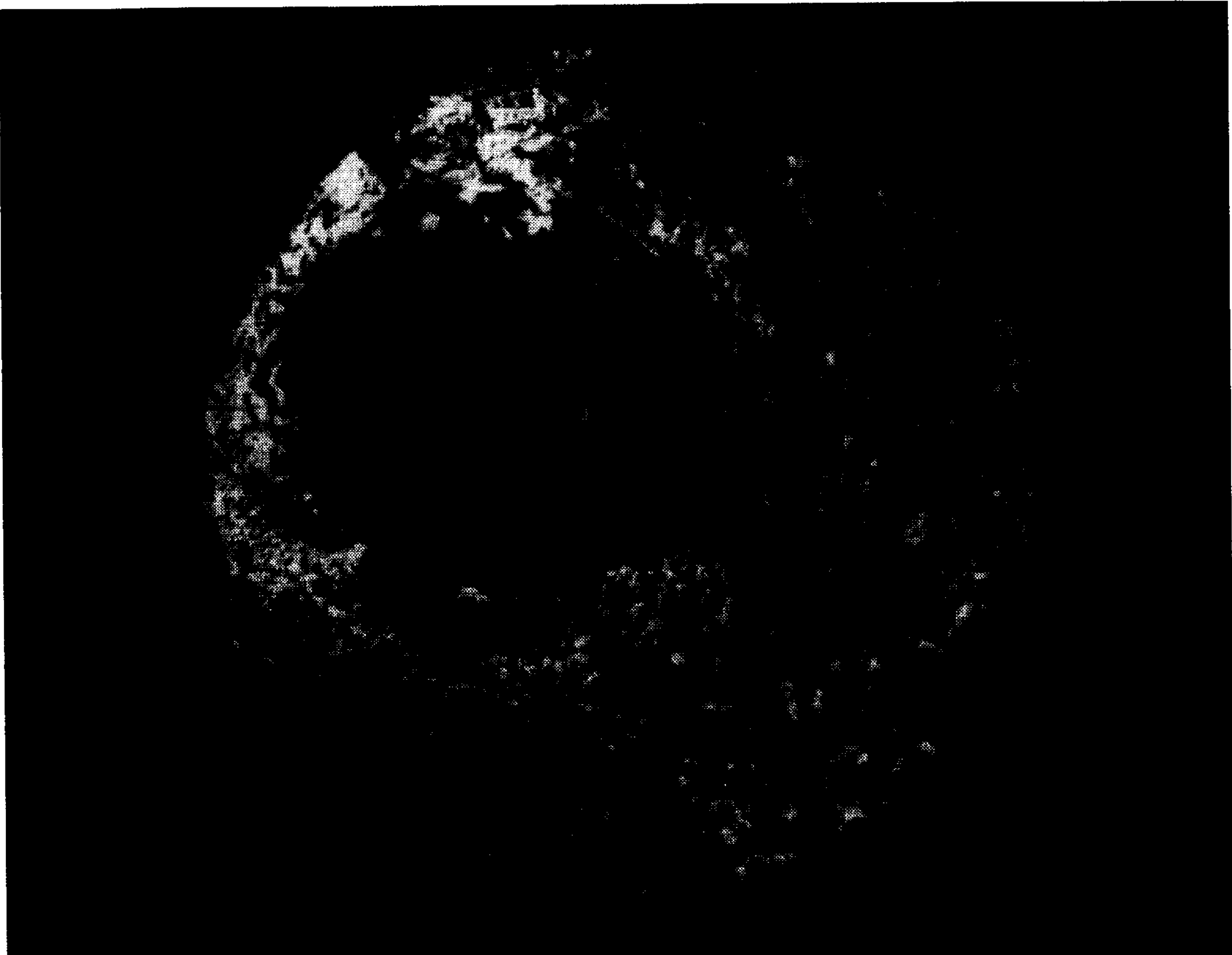

Figure 6.17 Silicon film annealed for 0.5 s with 2-W laser beam focused to a 66-μm-diameter spot.

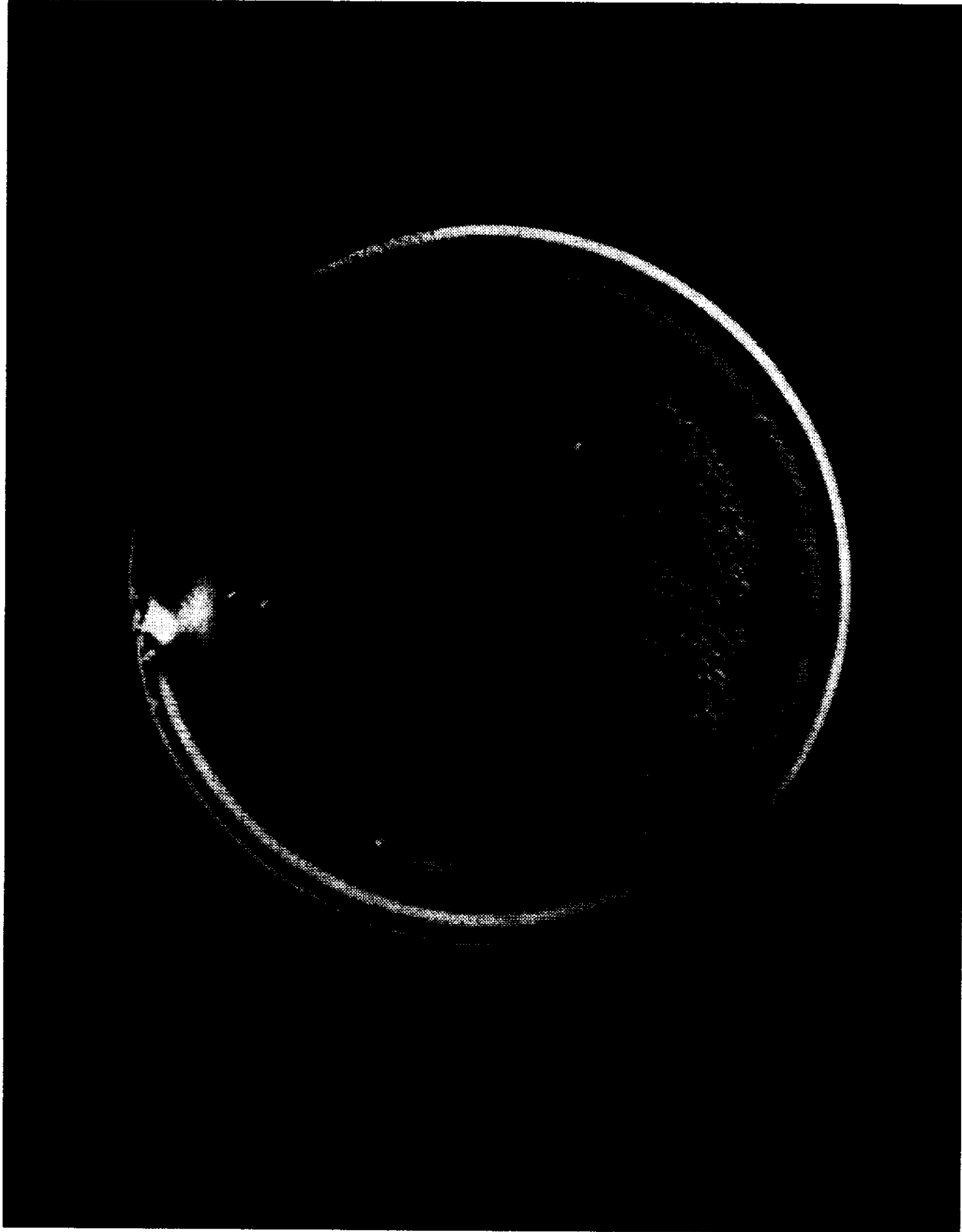

Figure 6.18 Silicon film annealed for 2 s with 1-W laser beam focused to a 378-μm-diameter spot.

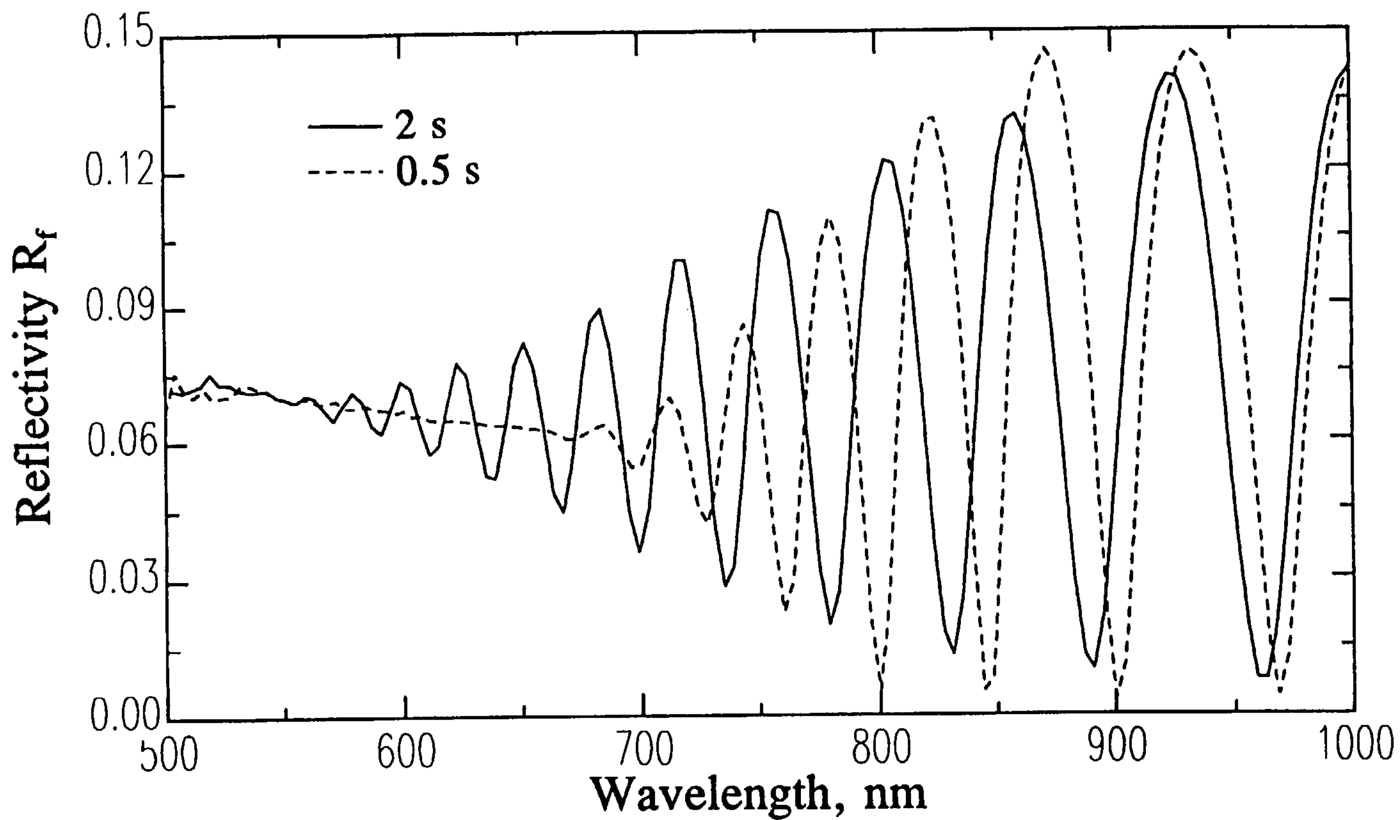

Figure 6.19 Reflectivities $R_f(\lambda)$ of silicon films annealed for 0.5 s and 2 s. For the case of the 0.5 s anneal, the R_f values have been multiplied by 0.58.

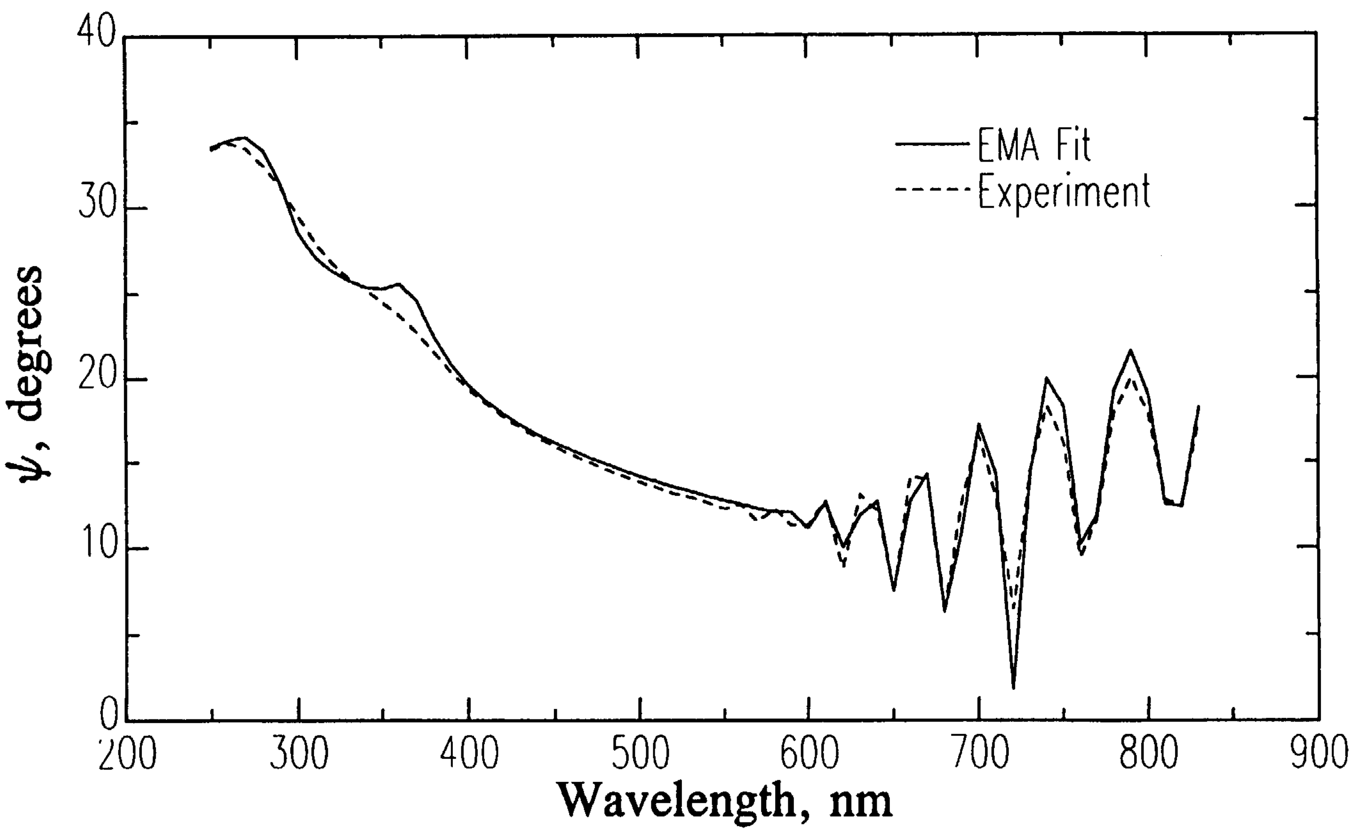

Figure 6.20 Measured and calculated $\psi(\lambda)$ for silicon rapid thermal annealed at 900 °C. Here, an EMA of a-Si, c-Si and void was used to model the film.

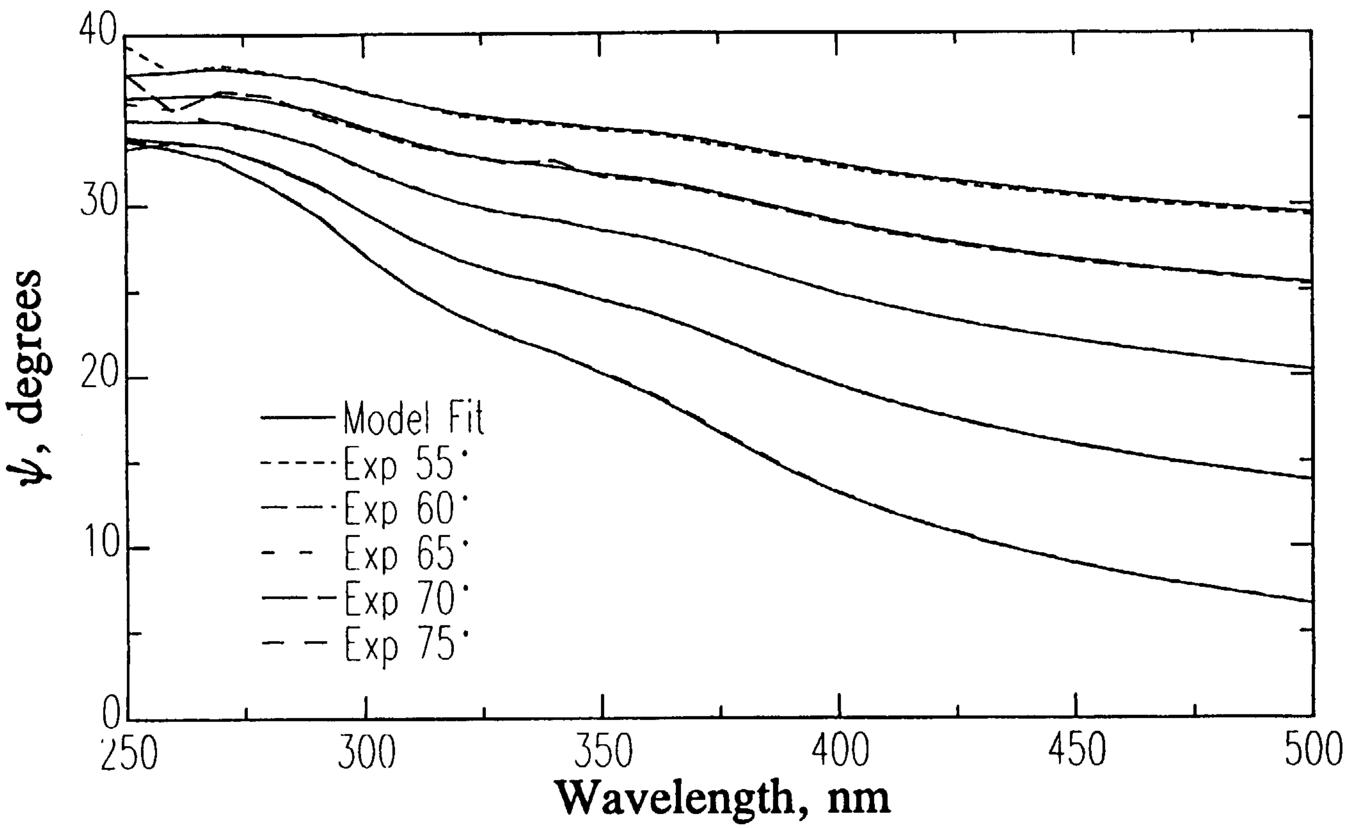

Figure 6.21 Measured and calculated $\psi(\lambda)$ of RTA silicon, for $\lambda < 500$ nm.

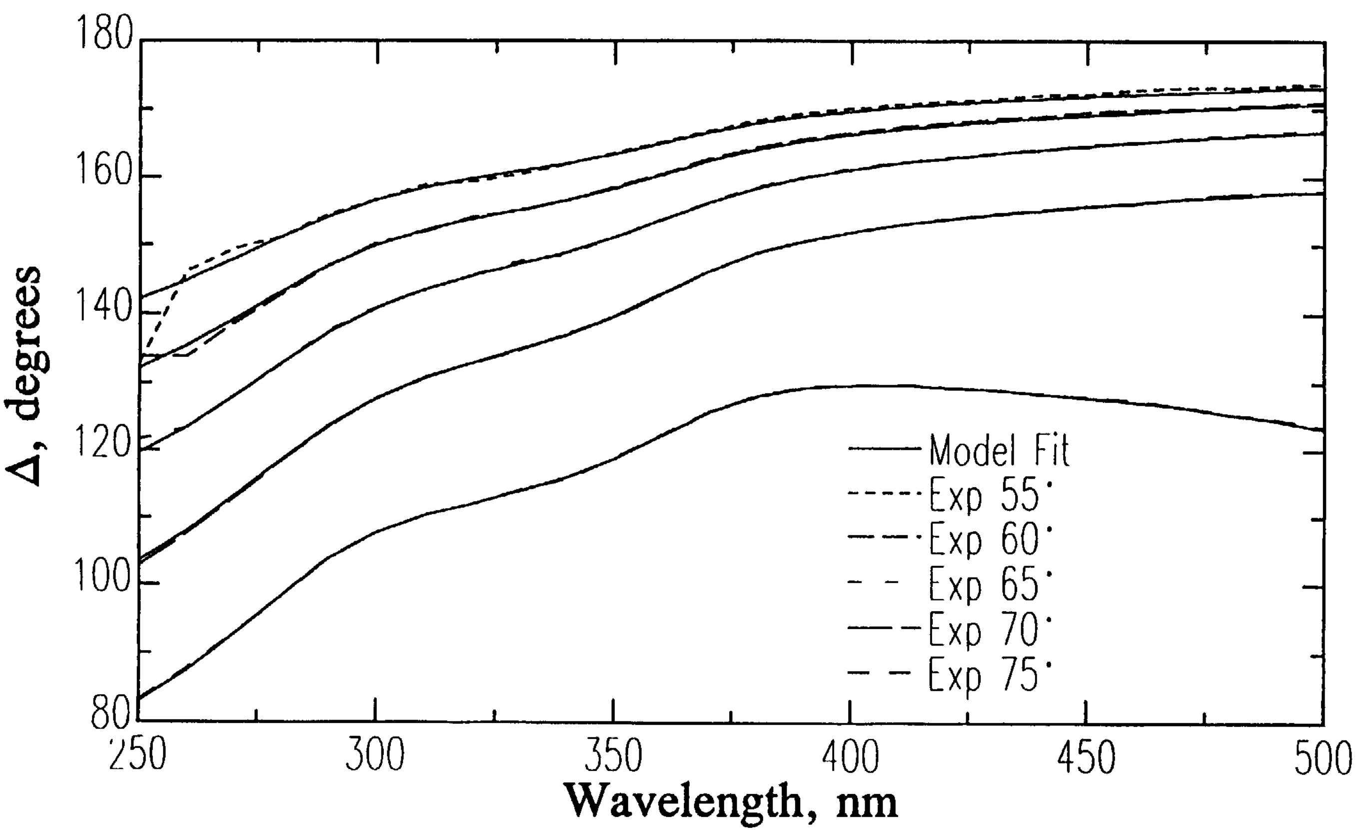

Figure 6.22 Measured and calculated $\Delta(\lambda)$ of RTA silicon, for $\lambda < 500$ nm.

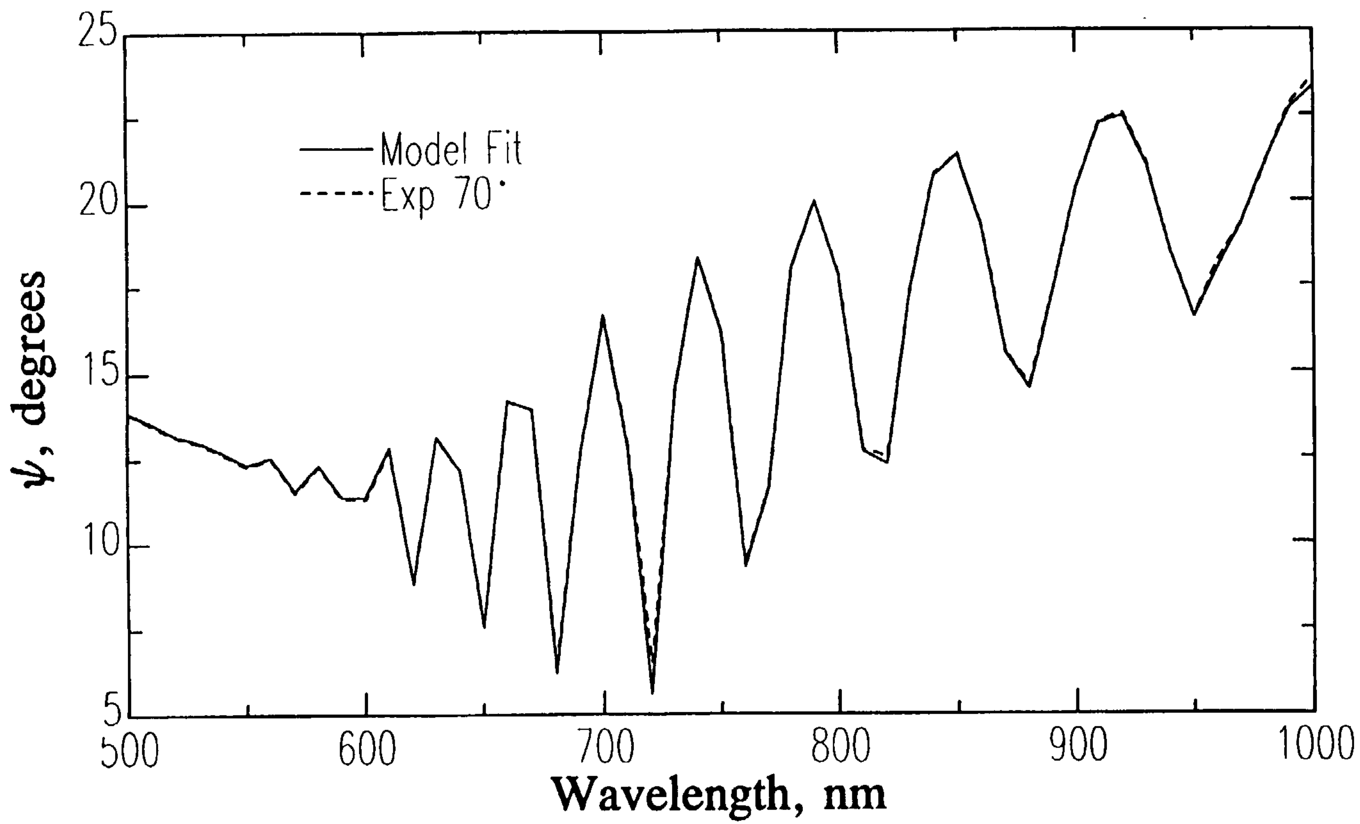

Figure 6.23 Measured and calculated $\psi(\lambda)$ of RTA silicon, for $\lambda > 500$ nm.

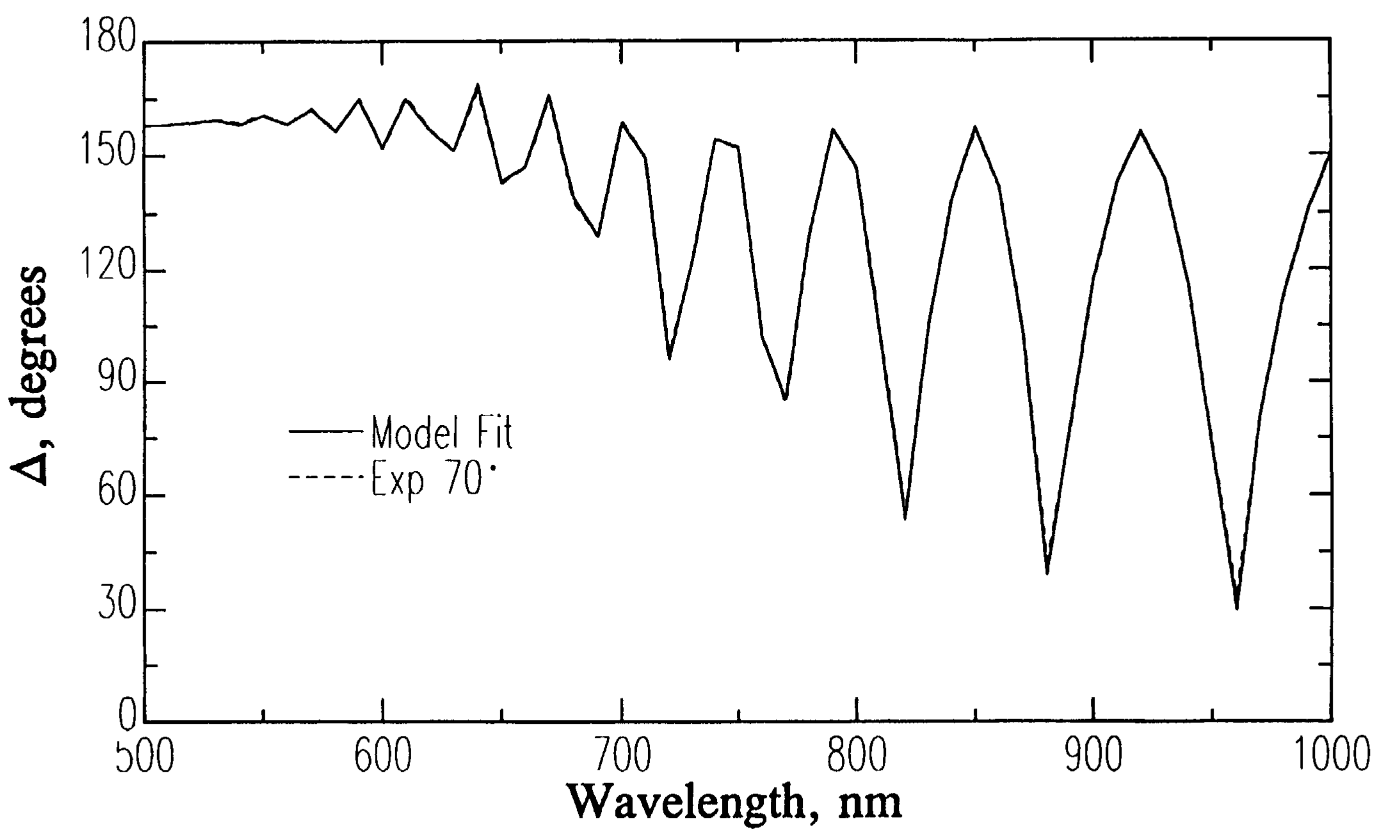

Figure 6.24 Measured and calculated $\Delta(\lambda)$ of RTA silicon, for $\lambda > 500$ nm.

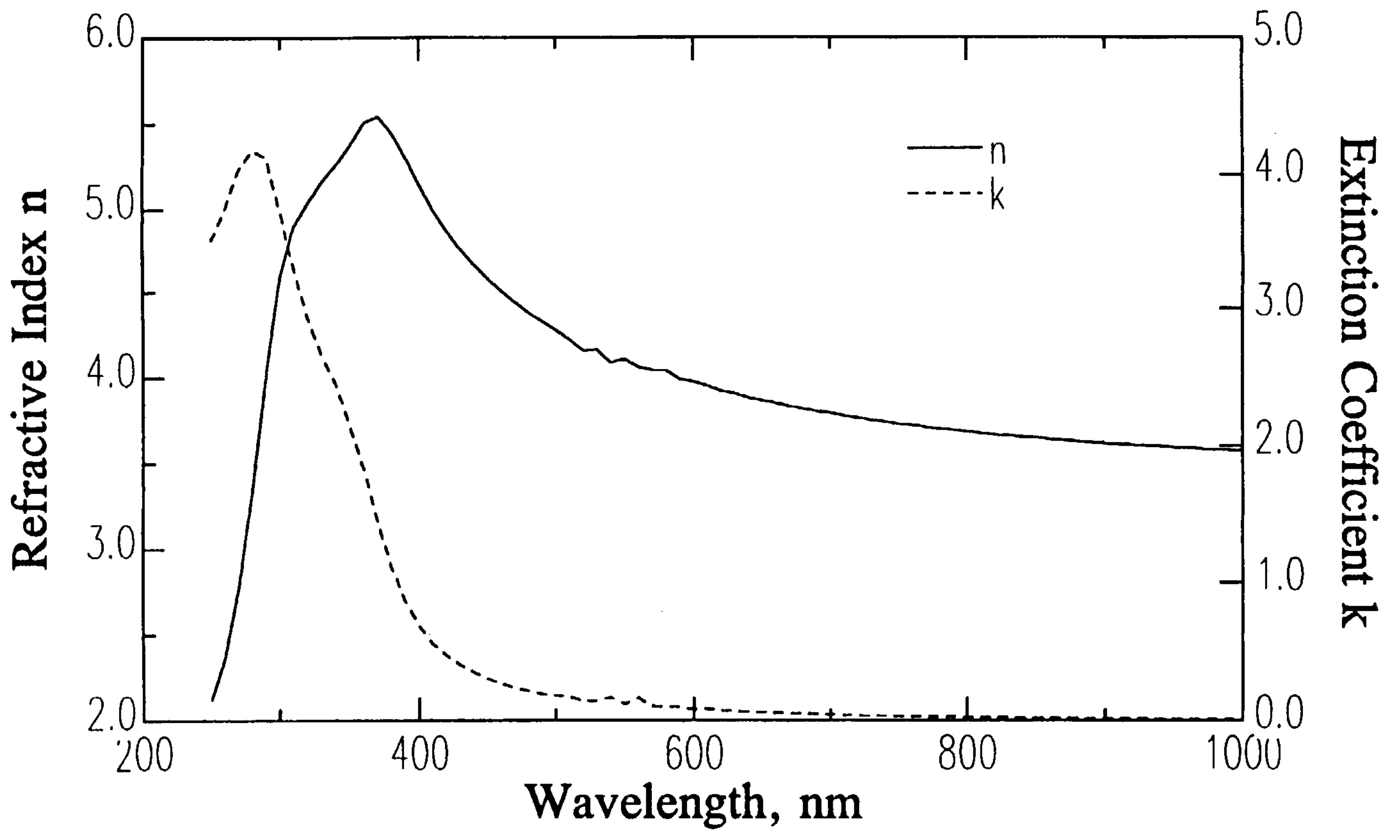

Figure 6.25 Calculated n(λ) and k(λ) for silicon rapid thermal annealed at 900 °C.

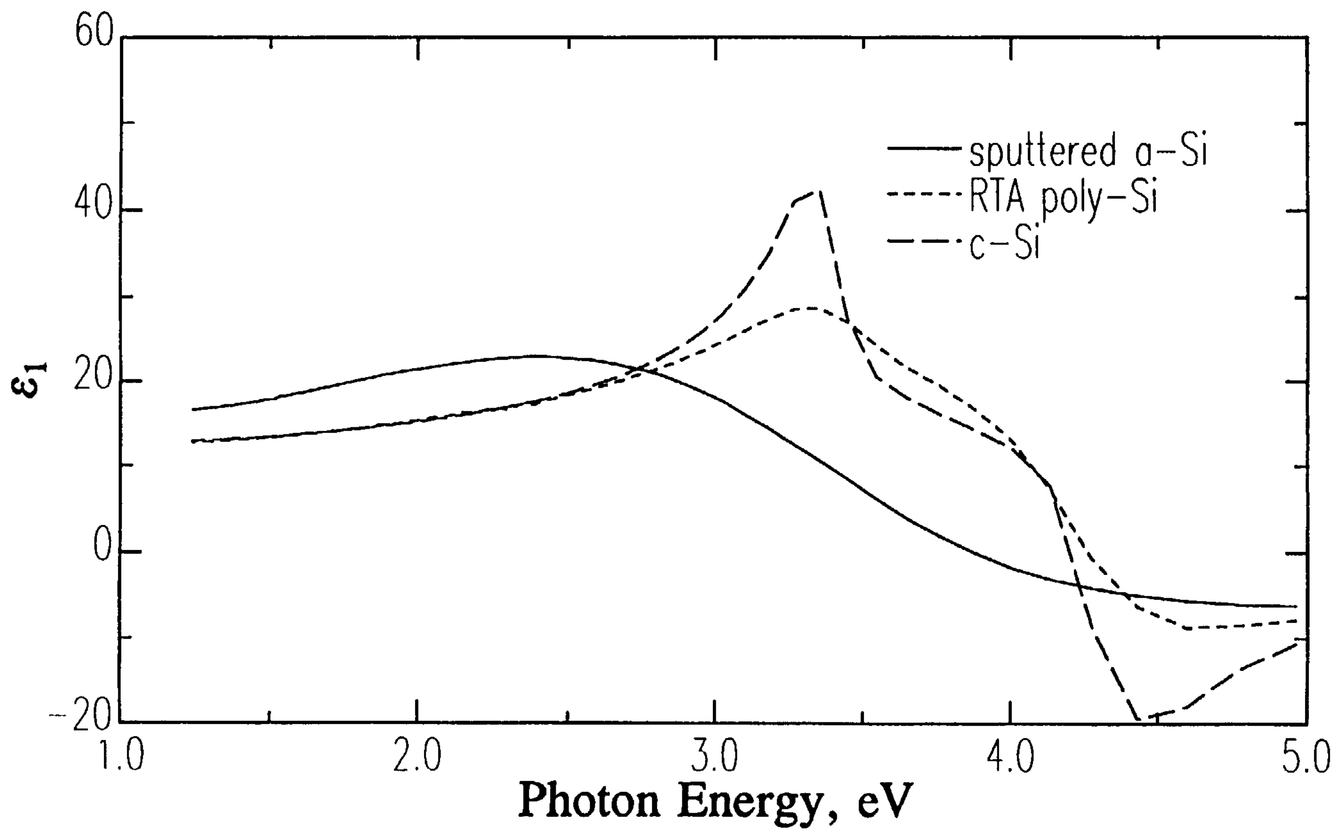

Figure 6.26 Real part of the dielectric function $\varepsilon_1(E)$, where E is the photon energy, for sputter-deposited a-Si, RTA poly-Si and c-Si.

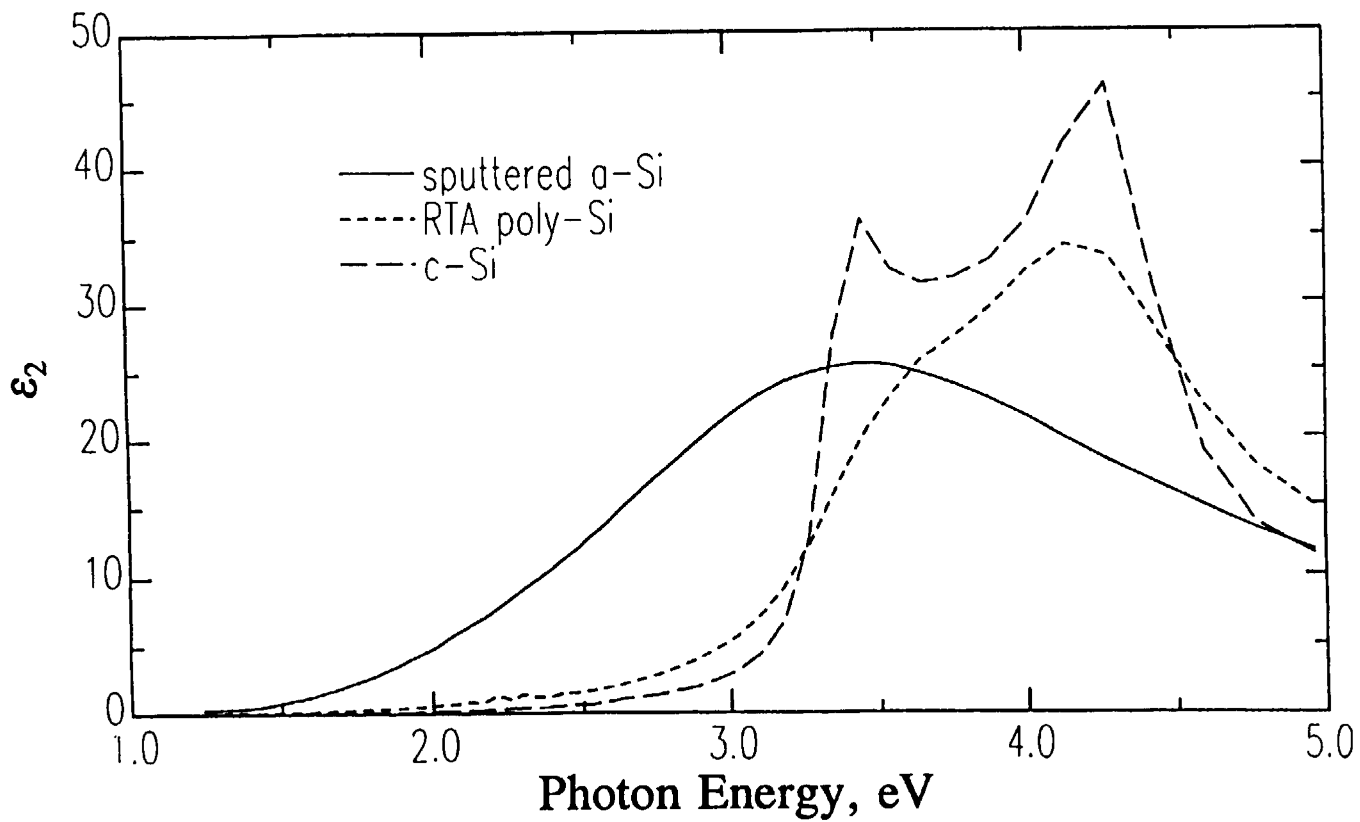

Figure 6.27 Imaginary part of the dielectric function $\varepsilon_2(E)$, where E is the photon energy, for sputter-deposited a-Si, RTA poly-Si and c-Si.

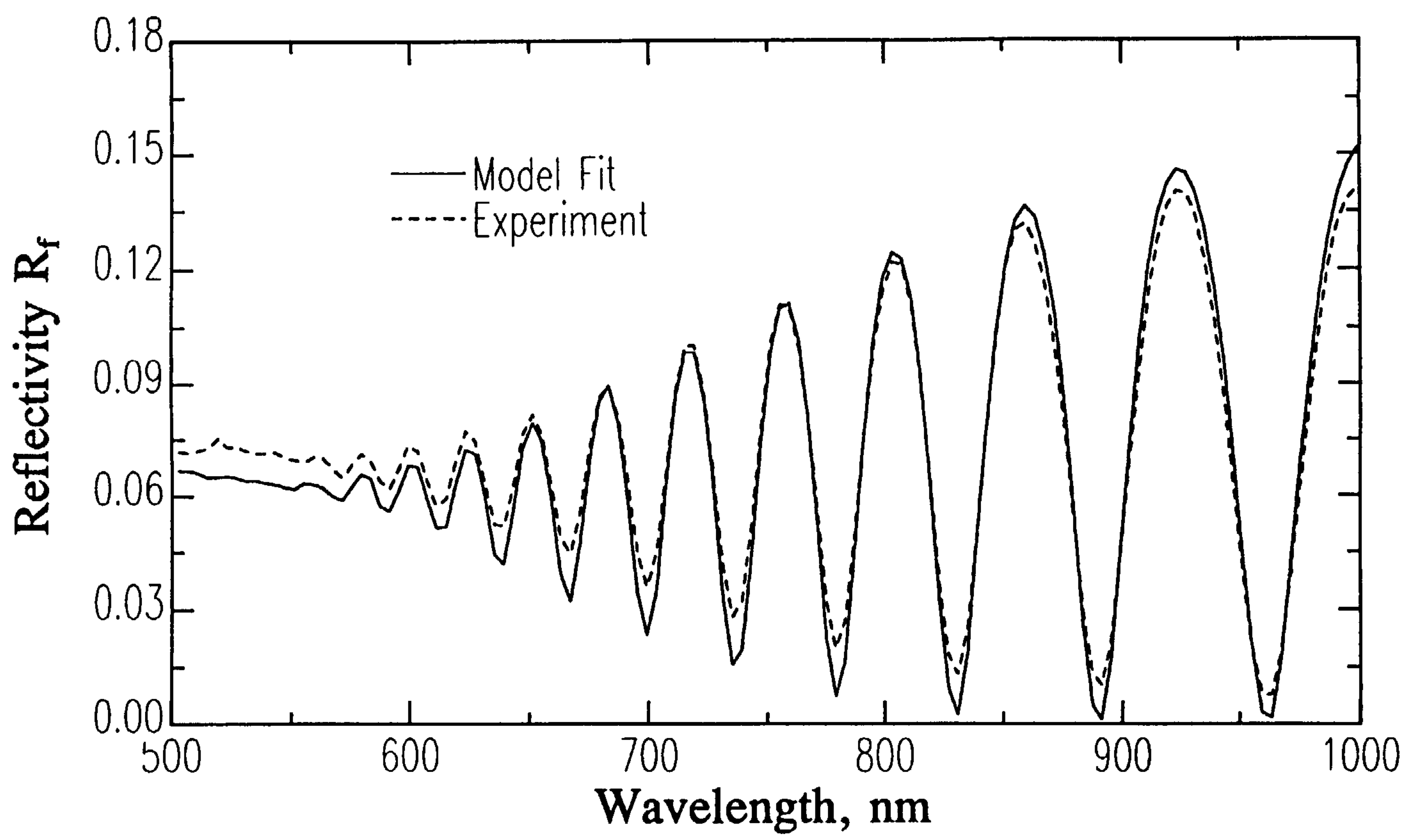

Figure 6.28 Measured and calculated reflectivity $R_f(\lambda)$ of silicon film laser annealed for 2 s (sensor 294).

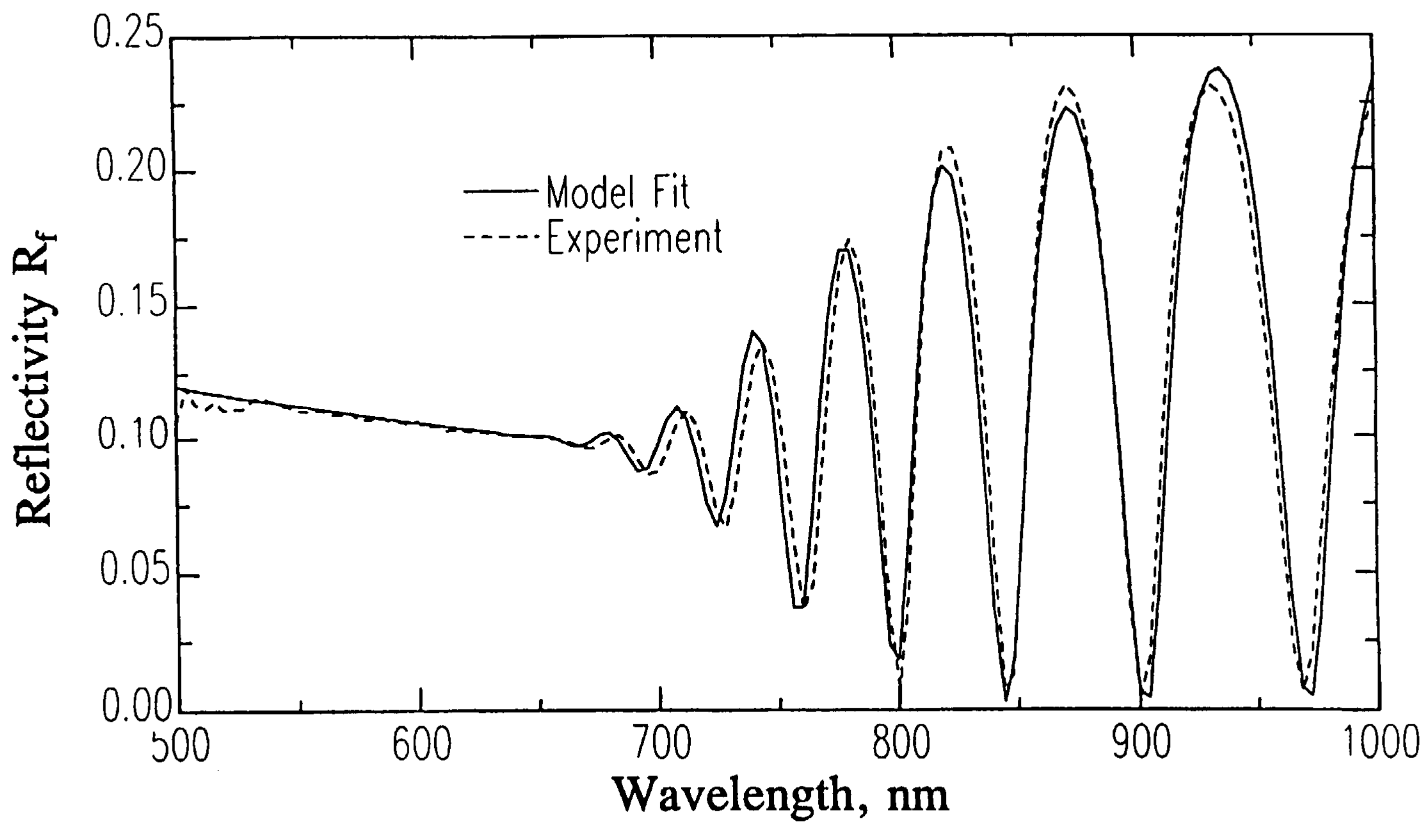

Figure 6.29 Measured and calculated reflectivity $R_f(\lambda)$ of silicon film laser annealed for 0.5 s.

7. TEMPERATURE SENSOR ENCAPSULATION

7.1 Introduction

The encapsulating layers of Si_3N_4 and aluminum were deposited in the magnetron sputtering system used for silicon deposition. Magnetron sputtering was used because it can yield dense films despite a low substrate temperature. Silicon nitride, which is not readily obtained with good stoichiometry by evaporation, was deposited by reactive sputtering in a nitrogen plasma. The aluminum outer layer was sputter-deposited immediately after Si_3N_4 deposition, without breaking vacuum. In this section, optimization of the Si_3N_4 deposition process will be described, and the properties of the Si_3N_4 diffusion barriers will be evaluated. Then the deposition and characteristics of the aluminum films will be discussed.

7.2 Silicon Nitride Deposition Methods

Silicon nitride is widely used to passivate semiconductor devices because it is an excellent barrier to contaminants such as moisture and sodium.[1]

Silicon-nitride passivating layers are usually deposited by PECVD, at temperatures between 250 and 350 °C. This PECVD nitride is termed SiN or SiN_x to emphasize its lack of stoichiometry. It is generally silicon rich ($x = 0.8$ to 1.2), with a large concentration of hydrogen (20 to 25 atomic %). Both these factors cause PECVD SiN_x to be thermally unstable, with a refractive index that is dependent on the film's thermal history. Silicon nitride deposited by PECVD is, therefore, ill-suited for this application, since changes in the refractive index of the silicon-nitride layer can cause the sensor's output to drift. Another disadvantage of PECVD SiN_x is its lower density, compared to stoichiometric and hydrogen-free Si_3N_4. A film with the highest possible density is desired in order to best protect the underlying silicon. Another disadvantage of PECVD SiN_x is the previously cited incompatibility of PECVD with optical fiber substrates.

Hydrogen-free and stoichiometric Si_3N_4 films are most readily deposited, at low substrate temperatures, by RF magnetron or diode sputtering.[2-7] Sputtering a Si_3N_4 target in an inert gas, such as argon, produces a film which is nitrogen deficient. Stoichiometric Si_3N_4 is obtained only by reactive sputtering in nitrogen (argon can be added to increase the deposition rate). Impurities are minimized by using a silicon target, since 99.999% pure Si is

readily available, as opposed to just 99.9% for a Si_3N_4 target. Also, Si_3N_4 targets contain about 1% binder, such as MgO.

In reactive sputtering, the silicon target is bombarded with N_2^+ and N^+ ions which can develop energies in excess of 1 keV as they are accelerated across the cathode dark space. Bombardment by nitrogen ions produces a Si_3N_4 coating on the surface of the target. The steady-state surface condition should therefore be developed by presputtering prior to deposition. The sputtered particles (mostly atoms) typically have several eV of kinetic energy when expelled from the target. These particles will impact the substrate in a manner which is strongly influenced by the gas pressure. With increasing pressure, the sputtered particles suffer more collisions with gas molecules, so that their energies at the substrate are reduced, and the range of their angles of incidence is broadened. Eventually, at a pressure which is inversely proportional to the target-to-substrate spacing, the sputtered particles are thermalized to the average gas energy. Higher impact velocities densify the film by increasing the surface mobilities of the adatoms. Normal incidence, as is obtained at low pressures, also promotes a greater density, since oblique incidence causes shadowing and void formation. A reduced pressure, therefore, aids the development of a dense and stoichiometric Si_3N_4 film.

Nitrogen sputtered from the target is insufficient to produce stoichiometric Si_3N_4 films, as is evidenced by the silicon-rich composition of films sputtered from Si_3N_4 targets in inert gas. Stoichiometric Si_3N_4 is obtained only by reactive sputtering in nitrogen. The ionizing effects of the plasma are essential; the presence of N_2 by itself is insufficient, since molecular nitrogen is not chemisorbed by silicon. A nitrogen plasma supplies reactive species of nitrogen to the film by two mechanisms, in addition to the sputtering of nitrogen from the target. All three means of supplying nitrogen to the film are enhanced at reduced pressures.

Because the insulating film develops a negative potential with respect to the plasma, it is bombarded with N_2^+ ions drawn from the plasma (N^+ bombardment is insignificant because N^+ is produced primarily in the cathode dark space). Dissociation of N_2^+ will yield reactive nitrogen atoms, if these molecular ions impact the film with energies greater than ~9 eV. At low pressures, the substrate self-bias becomes considerably more negative, which increases the energy of bombardment and the nitrogen incorporation in the film.

Another means by which nitrogen is supplied to the film is by the neutralization and reflection of nitrogen ions (N_2^+ and N^+) at the target. These reflected particles are generally quite energetic; their energies can approach the target-plasma potential. Provided the gas pressure is sufficiently low, many of the N_2 molecules reflected by the target will have sufficient energy to dissociate upon impact with the film.

The expected dependence of composition on gas pressure has been confirmed by measurements made on sputter-deposited SiN_x films.[2-7] In all these instances, nitrogen content of the films was found to decrease with increasing gas pressure, with stoichiometric $SiN_{1.33}$ obtained at some intermediate pressure. Serikawa and Okamato[2] measured the effect of gas pressure on the film's density, refractive index, and its etch rate in buffered HF. They found that the refractive index and density were maximized, and the etch rate was minimized, for a pressure of 4.5 mTorr. These films were deposited by RF magnetron sputtering in a 50:50 mixture of N_2 and Ar, with a target-to-substrate distance of 5 cm.

For a pressure of 4.5 mTorr, the SiN_x films of Serikawa and Okamato[2] were slightly nitrogen rich, with x = 1.42. The apparently non-stoichiometric

composition of the maximum-density films may have been the result of inaccurate composition measurements. The film composition was determined from the density and refractive index measurements using Lorentz-Lorenz correlation. As the pressure increased from 4.5 mTorr, the refractive index decreased because of the decreasing density. Here, the decrease in n due to a higher void fraction outweighed the increase due to excess silicon. Etch rate in buffered HF was found to be an extremely sensitive indicator of film quality. The minimum etch rate of 2 nm/min was obtained at 4.5 mTorr. For films deposited using a sputtering gas pressure of 50 mTorr (the maximum pressure), the etch rate was 200 nm/min, and at 2.3 mTorr (the minimum pressure), the etch rate was 10 nm/min.

Hu and Gregor,[3] who did not measure film composition, observed a similar dependence of density on gas pressure for RF diode sputtering in pure nitrogen. The maximum density was obtained at 2.5 mTorr.

Carriere et al.[4] used nuclear reaction analysis to measure the composition of RF-magnetron-sputtered SiN_x, with an accuracy of 6%. They found that the nitrogen content decreased monotonically with increasing pressure, with stoichiometry ($x = 1.33$) obtained at about 7 mTorr. They used

a 50:50 mixture of N_2 and Ar. They also measured refractive index and density and found that both decreased with increasing pressure, from 1.5 to 15 mTorr. The minimum etch rate in buffered HF of 0.6 nm/min was obtained at 4 mTorr.

The accuracies of the composition, density, and refractive index measurements of Carriere et al.[4] were not sufficient to rule out the possibility that stoichiometry and maximum values of refractive index and density were all obtained together at 4 mTorr, the pressure which provided the minimum etch rate. It is also quite possible that, as indicated by their measurements, the maximum density and refractive index were obtained at a pressure of 1.5 mTorr, which produced a somewhat nitrogen-rich film with $x = 1.44$. The densifying effect of more energetic bombardment may well have outweighed the decrease in density due to excess nitrogen. Still, one would expect the minimum etch rate to be obtained together with the maximum density. These films had an appreciable oxygen content, ~2 atomic % at 7 mTorr.

Qui and Gyarmati[5] found that for RF-magnetron-sputtered SiN_x, x decreased from 1.47 at 3.0 mTorr to 1.21 at 61 mTorr sputtering gas pressure.

Stoichiometry, x = 1.33, was obtained at a pressure of 23 mTorr. They used a 50:50 mixture of Ar and N_2, and the target-to-substrate spacing was 4 cm. Film composition was determined using glow discharge optical spectroscopy (GDOS) which was calibrated using Rutherford backscattering spectroscopy (RBS). Like Serikawa and Okamato, and Carriere et al., they found that nitrogen-rich SiN_x was somewhat denser than stoichiometric Si_3N_4. They did not measure refractive index or etch rate.

Mogab and Lugujjo[6,7] deposited SiN_x by RF diode sputtering in pure nitrogen. The target-to-substrate spacing was 5 cm. Film composition was measured using Rutherford backscattering. At the lowest pressure of 4 mTorr, a nitrogen-rich film, with x = 1.59, was obtained. With increasing pressure, x decreased to 1.27 at 12 mTorr and then leveled off. The minimum etch rate of 2 nm/min was obtained at 8 mTorr, the same pressure which produced stoichiometric $SiN_{1.33}$.

7.3 Optimization of Si_3N_4 Deposition Process

To determine the optimum deposition conditions, SiN_x films were deposited by magnetron sputtering in pure N_2 with pressures ranging from 1.8

to 5.3 mTorr. The target-to-substrate distance was 6 cm. The relative quality of these films was assessed by ellipsometric determination of their void fractions, and by measurement of their etch rates in buffered HF. The properties of sputter-deposited SiN_x has been shown to be largely insensitive to the RF power level.[3,7] The RF power, therefore, was fixed at 400 W, which is the maximum power that did not unduly stress the electronics.

Silicon-nitride films were sputter-deposited on silicon wafers and 7059 glass slides. The void fraction, f_V, could be determined more accurately if the substrate was glass. The accuracy of the ellipsometrically determined void fractions, based on the goodness of the fit and its void-fraction sensitivity, was typically $\pm$ 0.2 percentage points for glass substrates and $\pm$ 0.5 points for silicon. The pressure dependence of f_V for SiN_x films on glass was determined on four separate occasions. Figure 7.1 shows the results. The deposition rate increased only moderately with increasing pressure; the rate increased by ~20% for a factor of 2 increase in pressure. Deposition series A and series B were performed about one month apart; these were followed one year later by series C, and two months after C, series D. Film thicknesses were 50-70 nm for A, B and C, and 100-110 nm for D.

The sputter-deposited SiN_x films were modeled using the Bruggeman effective-medium approximation (EMA), assuming a composition of Si_3N_4 and void. For void-free Si_3N_4, the n and k data of Phillip, as tabulated by Palik,[8] were used. The refractive index of the 7059 glass was determined by ellipsometry. The roughness of the film's surface was modeled by an overlayer comprised of 50% void. The thickness of this overlayer was found to increase with increasing pressure. For instance, for deposition series D, the overlayer thickness increased from 0.9 nm at 2.3 mTorr to 2.6 nm at 4.7 mTorr. The rougher surfaces produced at higher pressures are most likely the result of less energetic bombardment of the substrate. Besides increasing the surface mobilities of adatoms, bombardment of the film with high-energy particles can cause the re-emission of loosely bound atoms. The measured void fraction of the bulk of the film, f_V, was found to be insensitive to the assumed void fraction of the overlayer, so the overlayer composition was fixed at that of the film plus 50% void. Also f_V was found to be unchanged if a surface oxide was assumed to be present in combination with voids due to roughness, as SiO_2 and void are here indistinguishable.

The ellipsometric data were fit using this effective-medium model in the region of negligible absorption, $\lambda > 300$ nm. A good fit could not be

obtained for $\lambda < 300$ nm, where the sputter-deposited SiN_x is absorptive, because the pyrolitic Si_3N_4 analyzed by Phillip was essentially lossless for $\lambda > 250$ nm. The variation of the percent f_V as a function of position on a given slide was about $\pm$ 0.2 points. The variation of the percent f_V between runs could be much larger, sometimes several points, due to the extremely high sensitivity of this process to contaminants. Oxygen, for instance, is readily incorporated into the films, since it is considerably more reactive than nitrogen.

Considerable care was exercised to minimize contamination of the sputtering system. If the sputtering system was previously used to deposit some other material, the first Si_3N_4 film was generally of poor quality, as indicated by a high void fraction and a poor fit (i.e. large MSE). The film quality generally improved with subsequent depositions, as impurities were gettered from the interior of the chamber (there was no provision for bake-out). Once Si_3N_4 films with a low f_V were obtained on a consistent basis, then a series of depositions could be initiated. When contaminants were well controlled, the variation, between runs, of the percent f_V was less than $\pm$ 0.4 points. When the O-ring rotary seal which provided for sample rotation was replaced with a ferro-fluidic seal, Si_3N_4 films having low void fractions were produced more reliably. Still, the modified chamber relied on a number of

O-ring seals. For this critical application a metal-sealed chamber would be preferrable. Pinhole density was quite variable, typically ~100 per cm^2. In this regard, sideways sputtering would be preferrable to the downwards deposition performed here.

The data of Fig. 7.1 show that the maximum refractive index is obtained at a pressure of about 3.5 mTorr. Since the observations of Serikawa and Okamoto[2] should also apply to these similarly deposited films, the films with the maximum refractive index can be expected to have the highest density. With the exception of the first series of depositions, the sensitivity to pressure was not extremely high; a low void fraction was generally obtained for pressures between 3.0 and 3.5 mTorr.

The effect of nitrogen pressure on the quality of the SiN_x films was further assessed by measuring the etch rates in buffered HF. For this test, 270-nm-thick films were sputter deposited on silicon wafers. The wafers were cleaved and samples of each film were etched for 10 min or 30 min. Ellipsometric analysis, at a 70° angle of incidence, was performed at three different positions on each piece, before etching and after. The measured thicknesses were averaged to obtain etch rates which were accurate within

about ± 0.3 nm/min (except for the films deposited at the two highest pressures, which were considerably more nonuniform after etching). Surface roughness was modeled by an overlayer comprised of 50% void. Figure 7.2 shows the etch rate measurements.

Figure 7.3 shows the void fractions of these films, before etching. The accuracy of these percent f_V measurements is only ± 0.8 points, which is much lower than the ± 0.1 points accuracy obtained for thinner films on glass substrates. The lower accuracy of the f_V measurements for SiN_x on silicon is caused by the high degree to which f_V and the film thickness are in this case correlated. The film with the lowest etch rate and void fraction was deposited at 3.5 mTorr, the same pressure which minimized f_V for SiN_x on glass. Lower void fractions were consistently measured for SiN_x deposited on silicon instead of glass; the difference in the percent f_V was typically 2 to 3 points. For the optimum sputter-deposited film, the etch rate was 3.0 nm/min, which is comparable to the minimum rate of 2 nm/min obtained by Serikawa and Okamato, for Si_3N_4 deposited by magnetron sputtering. For comparison, the etch rate of a sample known to be dense stoichiometric Si_3N_4 was measured. The etch rate of this LPCVD Si_3N_4 was found to be significantly lower, 0.8 nm/min.

Silicon-nitride films deposited at 3.5 mTorr were not roughened by etching, however, films deposited at higher pressures were made considerably rougher. The thickness of the rough-surface overlayer was initially in the range of 1 to 3 nm for all the films. After a 30 min etch, it increased to 13 nm and 40 nm for the films deposited at 4.1 mTorr and 4.7 mTorr, respectively. This accounts for the large difference in the 10-min and 30-min etch rates at 4.1 mTorr, because the etch rates were based solely on the changes in the thicknesses exclusive of the rough-surface overlayers. These etch rates are therefore inaccurate if the surface is significantly roughened. The void fractions of the films were unaffected by etching, except for the film deposited at 4.7 mTorr, for which f_V increased from 1.7% to 15%, after etching for 30 min. For SiN_x deposited at high pressures, networks of voids are apparently etched deeply into the films.

The chemical compositions of unetched samples of these films were analyzed using X-ray photoelectron spectroscopy (XPS). The samples were in-situ ion etched, to a depth of 5 nm, to remove the surface oxides before analysis. Figures 7.4 and 7.5 show the survey spectra of electron binding energies for the films deposited at the minimum and maximum pressures (2.3 and 4.7 mTorr), respectively. The film deposited at the optimum pressure of

3.5 mTorr was also analyzed. No differences in the relative fractions of Si and N were observed as a function of deposition pressure. This instrument's resolution in this regard is estimated to be about ± 2 atomic %. The 2:1 range of deposition pressures may have been insufficient to produce a detectable composition variation. The film deposited at 4.7 mTorr had a significantly higher oxygen concentration than did the films deposited at lower pressures, 2.5 atomic % instead of 1.0 atomic %.

Ellipsometric analysis of the composition of the SiN_x films, as a function of sputtering gas pressure, was also performed. Here the full range of ellipsometric data, 250 nm $< \lambda <$ 1000 nm, was used. As noted previously, although the two-component EMA (Si_3N_4 and void) provided a good fit to the ellipsometric data for $\lambda >$ 300 nm, the quality of the fit was poor for $\lambda <$ 300 nm. To model the UV absorption of the sputter-deposited films, a-Si was assumed present in addition to Si_3N_4 and void. A series of 18-min depositions was performed on silicon wafers (together with glass slides, series D of Fig. 7.1), and the model parameters which gave the best fits for these films are provided in Table 7.1. Also shown are the results obtained for an LPCVD Si_3N_4 film.

Table 7.1 Results of ellipsometric analyses of SiN_x films sputter deposited at different pressures. Here, P_{N2} is the pressure of the N_2 sputtering gas in mTorr, the volume fractions f are in % and the thicknesses L are in nm.

P_{N2}	f_V	$f_{a\text{-}Si}$	L	f_{Vsurf}	L_{surf}
2.3	2.0 ±0.5	0.7 ±0.1	85.7 ±7.7	-2.8 ±1.1	23.4 ±7.8
2.9	0.9 ±0.5	0.7 ±0.1	88.9 ±7.0	-3.8 ±1.6	17.3 ±7.0
3.5	0.5 ±0.4	0.7 ±0.1	109.4 ±0.4	50	0.0 ±0.5
4.1	0.7 ±0.4	0.7 ±0.1	116.1 ±0.4	50	0.9 ±0.5
4.7	3.0 ±0.4	0.7 ±0.1	125.2 ±0.4	50	4.7 ±0.5
CVD	0.7 ±0.3	0.3 ±0.1	126.3 ±0.3	50	0.4 ±0.5

In Table 7.1, L and L_{surf} are the thicknesses of the film and the overlayer. The overlayer composition was generally assumed to be the material of the film plus additional voids with a volume fraction of f_{Vsurf}. The data were first fit with f_{Vsurf} = 50% to model the surface roughness of the films. At the two lowest pressures, however, small negative values were obtained for L_{surf}. This unphysical circumstance was found to be resolved by allowing f_{Vsurf} to vary. It was determined that the topmost ~20 nm of these films was denser than the bulk of the films by about 3%. Using this model there was a large uncertainty in the location of the interface between these

layers, $\pm$ 7 nm, but the uncertainty of the total film thickness, $L + L_{surf}$, was only $\pm$ 0.4 nm. There was no evidence of such depth nonuniformities of f_V in the films deposited at pressures of 3.5 mTorr or greater. Figures 7.6 and 7.7 show the ψ and Δ measurements for the film deposited at 3.5 mTorr, together with the best fit provided by the three-component EMA.

As indicated by Table 7.1, for all the SiN_x films sputtered onto silicon, $f_{a\text{-}Si}$ was 0.7%. Again, f_V was minimized at a nitrogen pressure of 3.5 mTorr. The f_V values of Table 7.1 (determined using the three-component EMA) were ~1.4 percentage points higher than the void fractions that were determined by setting $f_{a\text{-}Si} = 0$ and restricting the analysis to $\lambda > 300$ nm (increasing the percent $f_{a\text{-}Si}$ by 1 point and the percent f_V by 2 points produces no net change in n for $\lambda > 300$ nm). Compared to the films deposited at the same time on glass, the percent f_V was consistently ~2 points lower for the silicon substrates. This lower f_V may be caused by the smoother surface and the higher thermal conductivity and lower thermal mass of a silicon wafer relative to a glass slide. The chemical compositions of the surfaces of the substrates were similar, as the native oxide was not stripped from the silicon wafers prior to deposition (it was not found necessary to model the native silicon oxides in order to analyze the much thicker Si_3N_4 layers).

The LPCVD Si_3N_4 film was deposited on a silicon wafer by reaction of NH_3 and $SiCl_2H_2$, with 4:1 relative flow rates, at a temperature of 770 °C and a pressure of 300 mTorr. These LPCVD Si_3N_4 films have been deposited on heavily oxidized silicon wafers for the purpose of fabricating optical waveguides.[9] The losses of these waveguides are lower than 0.5 dB/cm at 630 nm, with the principal loss mechanism being the roughness of the etched side walls. The extremely low absorptivity of these films suggest that they are stoichiometric Si_3N_4, with a very low void fraction as a result of the high deposition temperature. Although the absorptivity of these films is undetectably low for $\lambda > 300$ nm, for $\lambda < 300$ nm the absorption is readily measured and is intermediate between that of the sputtered films and the CVD films analyzed by Phillip. The CVD Si_3N_4 analyzed by Phillip was deposited at 1000 °C by reaction of NH_3 and SiH_4 in the ratio of 40,000:1.

Based on previous work,[2-7] the SiN_x films with the maximum refractive index and minimum etch rate, as obtained here at a pressure of 3.5 mTorr, should have a composition ranging from stoichiometric to slightly nitrogen rich. Here, $f_{a\text{-}Si}$ was found to be 0.7%, regardless of pressure. Note that a uniformly silicon-composition is consistent with the XPS analysis since the compositions of the sputter-deposited SiN_x films were found only to be uniform

over the range of nitrogen pressures used. The value of $f_{a\text{-}Si}$, however, should not be used to infer the excess silicon content of these SiN_x films, because the excess silicon is not present in the form of small grains with the dielectric properties of bulk a-Si. Instead, the film constituents are mixed at an atomic level.

Aspnes and Theeten[10] have shown that the Bruggeman EMA can be used to calculate the dielectric function of stoichiometric to silicon-rich SiN_x by treating the material as a mixture of Si-centered tetrahedra, i.e. $Si\text{-}Si_4$, $Si\text{-}Si_3N$, $Si\text{-}Si_2N_2$, $Si\text{-}Si_1N_4$ and $Si\text{-}N_4$. The volume fractions of these constituents are determined from x, assuming a random distribution of the Si-Si and Si-N bonds. The simple EMA of Si_3N_4 and a-Si represents only the $Si\text{-}Si_4$ and $Si\text{-}N_4$ tetrahedra. Although this simple EMA is incomplete, one might still expect $f_{a\text{-}Si}$ to be correlated with excess silicon content. This is true, however, only for moderately silicon-rich SiN_x. For an excess silicon fraction y, which implies a composition of $Si_y(SiN_{1.33})_{1-y}$, the volume fraction of $Si\text{-}Si_4$ tetrahedra is proportional to y^4. For small y, therefore, the contribution of the $Si\text{-}Si_4$ tetrahedra to the material's dielectric response is negligible, and one would expect to find that $f_{a\text{-}Si} \approx 0$ for such a film, if the dielectric function were modeled using the two-component EMA.

A non-zero $f_{a\text{-}Si}$ can be measured for a near-stoichiometric SiN_x film, if the structural disorder of the film causes the UV absorption edge to be shifted towards the visible.[11] Such distortion of the amorphous material's atomic structure, i.e. variations in the bond angles and lengths, is made probable here by the low substrate temperature during deposition. Further evidence that the UV absorption of the films is due to structural distortion rather than excess silicon was provided by its significant reduction after annealing. The sputter-deposited SiN_x films on silicon substrates were annealed at 1000 °C in dry O_2 for 1 hr, after which $f_{a\text{-}Si}$ was found to decrease from 0.7% to less than 0.1%. Besides shifting the absorption edge further into the UV, annealing also reduced the refractive index of the films. Figure 7.8 shows the values of f_V that were measured before and after anealing. For all the films, annealing increased the percent f_V by about 3.5 points. These f_V values were determined by setting $f_{a\text{-}Si} = 0$ and restricting the analysis to $\lambda > 300$ nm. The annealed films were modeled using an SiO_2 overlayer instead of a rough-surface overlayer. Annealing had a quite different effect on the dielectric properties of the LPCVD Si_3N_4. In this case, the percent f_V decreased by 1 point, while $f_{a\text{-}Si}$ remained unchanged, at about 0.5%.

Similar changes in $f_{a\text{-}Si}$ and f_V were observed when sputter-deposited Si_3N_4 was rapid thermal annealed at 900 °C for 2 min in N_2. This result, together with the Auger results presented in the following subsection, rule out the possibility that the as-deposited films contain excess silicon which is converted to SiO_2 by annealing in O_2, thereby reducing the UV absorption and decreasing n. It is important to show that such a hypothesis is incorrect, because it is inconsistent with the sputter-deposited Si_3N_4 being an effective barrier to oxygen.

Fourrier et al.[12] observed a similar reduction in refractive index after annealing Si_3N_4 films that were deposited by reactive ion-beam sputtering. Fourrier attributed this refractive-index decrease to a reduction in the structural disorder of the film. The Kramers-Kronig relation requires that, at wavelengths beyond than the absorption edge, a refractive index decrease must accompany a shift of the absorption edge towards shorter wavelengths. Through Auger analysis, Fourrier et al. ruled out oxygen incorporation as the cause of the refractive index decrease. Also, they observed the same index change after annealing in N_2.

7.4 Effect of an Oxidizing Environment on Si_3N_4 Encapsulant

To verify that the sputter-deposited Si_3N_4 films are indeed effective barriers to oxygen, a representative film was analyzed, by ellipsometry and Auger electron spectrometry, immediately following deposition and again after exposure to an oxidizing environment. The film was sputtered on silicon in 3.5 mTorr of N_2, and it was oxidized for 2 hrs at 1000 °C in wet O_2. By ellipsometry, the parameters of Table 7.2 were determined.

Table 7.2 Effects of annealing on sputter-deposited Si_3N_4 film.

before annealing;	after annealing;
$f_{a\text{-}Si} = 0.6 \pm 0.1$ %	$f_{a\text{-}Si} = 0.0 \pm 0.1$ %
$f_V = 3.4 \pm 0.3$ %	$f_V = 7.4 \pm 0.1$ %
$L_{ox} = 0.0 \pm 0.5$ nm	$L_{ox} = 12.7 \pm 0.3$ nm

Here, L_{ox} is the thickness of the SiO_2 overlayer. This film was deposited after the vacuum system had been damaged by the operation of a substrate heater without cooling water. Despite efforts to repair the system, the void fractions of the Si_3N_4 films could not be reduced to the levels that were obtained

routinely prior to the incident. As-deposited and oxidized samples of this film were depth profiled using Auger electron spectrometry (AES) with in-situ sputter etching. Figures 7.9 and 7.10 show the concentrations of N, O and Si, as functions of etch depth, for the as-deposited and oxidized samples, respectively. The oxygen concentration inside the film is shown to be unchanged, from its initial value of 1 to 2 atomic %, by exposure to an oxidizing environment. Also, oxygen is not observed to accumulate at the interface of the Si_3N_4 film and the silicon substrate. The sputter-deposited Si_3N_4, therefore, is shown to be an effective barrier to oxygen.

Also investigated was the effect of annealing at a lower temperature. A Si_3N_4 film on a silicon wafer, similar to the sample that was Auger profiled, was annealed for four weeks at 400 °C in air. Initially, and at one week intervals, the film was characterized by ellipsometry. After one week (168 hrs), $f_{a\text{-}Si}$ had decreased from 0.6 $\pm$ 0.1 % to 0.2%. Restricting the analysis to $\lambda > 300$ nm and setting $f_{a\text{-}Si} = 0$, f_V was determined to be 2.1 $\pm$ 0.1 % initially and 3.7% after one week. From the end of the first week to the end of four weeks, no further changes in $f_{a\text{-}Si}$ and f_V were observed.

The oxide growth at 400 °C was difficult to measure. Using the three-component EMA, it was determined that, initially, L_{ox} = 0.0 ± 0.3 nm, and after four weeks (672 hrs), L_{ox} = 0.9 ± 0.8 nm. The approximate nature of the three-component EMA was found to preclude the accurate analysis of thin surface layers. To determine L_{ox} for extremely thin oxides, it was necessary to use the two-component EMA (i.e. $f_{a\text{-}Si}$ = 0) and restrict the analysis to wavelengths far from the absorption edge, i.e. $\lambda > 400$ nm. Using this approach, the initial and final values of L_{ox} were determined to be 7 ± 1 Å and 9 ± 3 Å. The estimated accuracies of these measurements are based on the repeatability of L_{ox} when determined using different portions of the $\lambda > 400$ nm region. It is believed that a few monolayers of surface contamination caused the larger uncertainty in the final value of L_{ox}.

The measured thickness of 7 Å for the Si_3N_4 native oxide is consistent with the observations of Raider et al.,[13] who monitored the oxide growth in room air on a Si_3N_4 film that was first etched in dilute HF. They measured oxide thicknesses L_{ox} of 2 to 3 Å immediately after etching, 3 to 5 Å after 3 days, and 6 to 9 Å after one month.

The considerably lower oxidation rate of Si_3N_4, relative to silicon, has been attributed to the formation of an intermediate silicon-oxynitride phase, which is a more effective barrier than is SiO_2 to the diffusion of oxygen.[12,14-16] Du et al.[14-15] determined that the thickness of this intermediate layer, which was presumed to be stoichometric Si_2N_2O, increased with further oxidation, maintaining about a 1:8 ratio with respect to the SiO_2 thickness. Fourrier et al.[12] measured a 1:4 ratio of Si_2N_2O and SiO_2 thicknesses. Ogbuji and Jayne[16] found that the SiO_xN_y composition, for oxidation in dry O_2, was graded, with nitrogen increasingly substituted for oxygen as the unoxidized Si_3N_4 was approached. They also found that the ratio of the SiO_xN_y and SiO_2 thicknesses was highly dependent on the sample preparation, to the extent that the SiO_2 outer scale was in some instances entirely absent. Nitrogen was found on the surfaces of samples which were chemically stripped immediately prior to oxidation in dry O_2, while samples that were allowed to regrow a native oxide prior to oxidation developed an SiO_2 outer scale. The difference was presumed to be caused by the incorporation of moisture from the air into the native oxide, which subsequently promoted the conversion of oxynitride to SiO_2.

The SiO_xN_y inner scale of an oxidized Si_3N_4 film was found to be generally undetectable by ellipsometry, because it is much thinner than the SiO_2 and Si_3N_4 layers, and its refractive index is intermediate to, and not very different from, those of SiO_2 and Si_3N_4. Since SiO_2 has a much higher etch rate in buffered HF than does near-stoichiometric SiO_xN_y, the inner scale is readily exposed for analysis by surface techniques.[14] Etch profiling was found to be a good means to measure the thickness of the inner scale, because of the very different etch rates of the SiO_2 outer scale, the SiO_xN_y inner scale, and the sputter-deposited Si_3N_4. A Si_3N_4 film on silicon, similar to the sample that was Auger profiled, was oxidized in wet O_2 at 1000 °C for 3 hrs. Between ellipsometric analyses, the film was etched for short times in buffered HF. Figure 7.11 shows the results provided by a model consisting of layers of Si_3N_4 and SiO_2, with thicknesses of L and L_{ox}, respectively. The SiO_2 layer, initially 16-nm thick, was completely removed during the first 15-s etch. The etch rate then slowed considerably, as the SiO_xN_y was etched. Once the oxynitride was removed, the Si_3N_4 was etched at a rate intermediate to those of the SiO_xN_y and the SiO_2.

The ellipsometric etch-profile measurements were analyzed using a three-layer model that represented the SiO_xN_y as a 50:50 mixture of Si_3N_4 and

SiO_2. This oxynitride composition gives n = 1.73 at 630 nm, which is the nominal Si_2N_2O index.[14] Table 7.3 gives the results, as a function of cumulative etch time t. Here f_V represents the void fraction of the Si_3N_4 layer, and the thicknesses of the Si_3N_4, Si_2N_2O, and SiO_2 layers are L, $L_{ox\text{-}n}$, L_{ox}, respectively.

Table 7.3 Measured thicknesses of SiO_2, Si_2N_2O and Si_3N_4 layers, L_{ox}, $L_{ox\text{-}n}$ and L, respectively, and void fraction of Si_3N_4 layer f_V as functions of cumulative etch time t in buffered HF. Notes A, B and C are explained in the text.

t, s	L_{ox}, Å	$L_{ox\text{-}n}$, Å	L, Å	f_v, %
0	160 ± 5	0 (A)	1022.9 ± 2.7	6.2 ± 0.2
15	0 (B)	2.9 ± 5.9	1019.9 ± 4.7	6.2
30	0	4.6 ± 7.1	1016.8 ± 5.5	6.0
60	0	0 (C)	1010.7 ± 1.8	6.2
90	0	0	992.0 ± 0.9	6.0
120	0	0	961.6 ± 1.0	6.2

Prior to etching, i.e. t = 0, the Si_2N_2O layer was buried beneath a much thicker SiO_2 layer, and $L_{ox\text{-}n}$ could not be determined. Therefore, at t = 0, $L_{ox\text{-}n}$ was set equal to zero (note A, in the table). After 15 s of etching, the SiO_2 layer was known to be removed, so its thickness was set to zero (note B). After etching for 60 s, $L_{ox\text{-}n}$ could no longer be determined (linear regression

analysis provided $L_{ox-n} < 0$) so it was set to zero (note C). After removal of the SiO_2 layer, the SiO_xN_y layer is readily observed (at t= 15 s and t = 30 s), although its thickness could not be accurately determined because L_{ox-n} and L were correlated.

Since L_{ox-n} and L are correlated, and L is known to be unchanged while the SiO_xN_y is being etched, the thickness changes of the etched SiO_xN_y layer can be more accurately determined by deleting the SiO_xN_y layer from the model, so that L represents the sum of the Si_3N_4 and SiO_xN_y thicknesses. The etch rate of SiO_2 was determined by an independent experiment to be 130 nm/min. Using this result and assuming a uniform SiO_xN_y composition, the etch sequence of Table 7.4 was derived.

Table 7.4 Etch sequence of oxidized Si_3N_4. Provided are the thicknesses of SiO_2, SiO_xN_y and Si_3N_4 etched during each time interval ending at time t. Etch time is in s, thicknesses are in Å, and etch rate is in Å/min.

			[---ETCHED THICKNESS (Å)---]			
t	L_{ox}	L	SiO_2	SiO_xN_y	Si_3N_4	RATE
0	160	1023				
7.5	--	----	160			1300
15	0	1022		1		8
30	0	1020		2		8
52.5	--	----		3		8
60	0	1011			6	48
90	0	992			19	38
120	0	962			30	60
150	0	939			23	46
180	0	918			21	42

The etch rate of the SiO_xN_y inner scale was determined to be 0.8 nm/min, identical to that which was measured for LPCVD Si_3N_4. The variations in the Si_3N_4 etch rates of Table 7.4 are indicative of the uncertainties caused by the use of such short etch intervals. The Si_3N_4 etch rate is somewhat higher than was previously measured because this film had the higher void fraction characteristic of films which were deposited after the sputtering system was damaged. The ratio of SiO_2 to SiO_xN_y thicknesses was determined here to be 25:1.

Enomoto et al.[17] also etch-profiled oxidized Si_3N_4 films, however, their films were deposited by LPCVD instead of sputtering. In 6:1 buffered HF (1 part HF to 6 parts 40% NH_4F) they measured an etch rate of 103 nm/min for SiO_2, which is similar to the rate measured here. They measured an etch rate for the LPCVD Si_3N_4 of 0.9 nm/min, similar to the 0.8 nm/min rate that was measured in section 7.3. Since LPCVD Si_3N_4 and the SiO_xN_y inner scale have the same etch rate, it is understandable why Enomoto's group did not detect the oxynitride layer. It is interesting to note that, despite the low refractive index and high etch rate of the sputter-deposited Si_3N_4, its oxidation produces a layer of SiO_xN_y with apparently ideal composition and density, as indicated by its low etch rate. This would explain the similarity in the oxidation rates of sputter-deposited and LPCVD Si_3N_4 films.[12]

In section 5, it was determined that negligible drift should result due to oxidation of the Si_3N_4 layer, based on the extrapolation to 600 °C of oxidation rates measured at 900 °C and higher.[12,18,19] Lee's group[18] measured the growth of thin oxides, L_{ox} > 10 Å, at 900 °C in wet O_2. The parabolic oxidation kinetics observed by Lee's group were assumed to apply at lower temperatures as well. The wet oxidation measurements of Fourrier's group[12] at 900 °C and 1000 °C were then used to determine parabolic rate constants

that were extrapolated to 600 °C, using an Arrhenius relation. The activation energy of 3.2 eV determined from these data was approximately equal to that measured by Choi's group[19] at higher temperatures. The measurements of all three groups were found to be consistent with each other and the assumption of parabolic growth, i.e. $L_{ox} = Bt^{1/2}$. Measurements by Enomoto's group,[17] however, showed the oxide thickness to be given by $L_{ox} = A_E t^{2/3}$, for the L_{ox} range of interest here.

The oxidation measurements of Enomoto's group, at 900 °C and 1000 °C, actually agree quite well with those reported by Lee and and Fourrier. Further, if the values of A_E of Enomoto's group are extrapolated to 600 °C, and their model applied, essentially the same oxide growth in 5000 hrs is calculated as was determined by extrapolating the parabolic rate constants obtained from the measurements reported by Fourrier. The similarity of the two models can be understood by writing both equations in terms of L_{ox}^2, which gives $L_{ox}^2 = Bt$ and $L_{ox}^2 = A_E^2 t^{4/3}$. Since the activation energy of A_E was determined by Enomoto et al. to be 1.67 eV, that of A_E^2 is 3.3 eV, very similar to that which was measured for B.

To try to assess the validity of the estimated oxidation kinetics at 600 °C, the oxidation rates of the magnetron-sputtered Si_3N_4 films were measured. In order to obtain readily measured oxides for reasonably short anneals, the temperature range of this study was 800 to 1000 °C. The oxidations were performed in wet O_2 to more closely duplicate the operating environment of the sensor. As is the case for the oxidation of silicon, the Si_3N_4 oxidation rate is greatly accelerated by moisture. To provide a partial pressure of water of 640 Torr, O_2 was bubbled through 95 °C deionized water.[20] The Si_3N_4 films were sputter-deposited on silicon substrates, at a pressure of 3.5 mTorr, to a thickness of 100 nm. These films were deposited before the operation of the vacuum system was degraded. The f_V values, measured using the two-component EMA, were in the range of 0 to 2%. The films were oxidized several days to weeks after deposition and were not preannealed. An uncoated silicon control sample was oxidized together with each Si_3N_4 sample. The silicon was boron doped with a resistivity of 1-10 Ω-cm, and its orientation was (100). The native oxides of the silicon and Si_3N_4 samples were not stripped prior to oxidation.

Figure 7.12 shows the measured oxidation kinetics of (100) silicon in wet O_2 at 800, 900 and 1000 °C. The parabolic and linear rate constants, B

and B/A, were determined by fitting straight lines to plots of L_{ox} vs. t/L_{ox} in the manner of Deal and Grove.[20] The two uppermost solid lines in Fig. 7.12 are the linear-parabolic fits to the 900 and 1000 °C data. Insufficient measurements were performed at 800 °C to obtain valid rate constants. Instead, the rate constants at 900 and 1000 °C were extrapolated using Arrhenius relations to 800 °C, and these extrapolated values of B and B/A were used to calculate the oxide growth shown in Fig. 7.12. The measured activation energies were 0.785 eV for B, and 1.72 eV for B/A, which are comparable to the activation energies of 0.71 eV and 1.96 eV measured by Deal and Grove for wet oxidation of (111) silicon.[20]

Table 7.5 shows the rate constants measured at 900 °C and 1000 °C, together with Deal's values of B and B/A for wet oxidation of (100) silicon.[21] The agreement with Deal's measurements is quite good at 900 °C. However, at 1000 °C, although the A values were identical, the measured B was somewhat lower than that determined by Deal. Since B is proportional to C^*, the equilibrium concentration of the oxidant in the oxide, while A is independent of C^*, it seems likely that the lower oxidation rate observed here was the result of a lower than intended partial pressure of H_2O.

Table 7.5 Parabolic rate constants for wet oxidation of (100) Si.

T, °C	[--- B ($\mu m^2/hr$) ---] Measured	Deal[21]	[--- B/A ($\mu m/hr$) ---] Measured	Deal
900	0.138	0.143	0.140	0.150
1000	0.254	0.314	0.531	0.664

Figure 7.13 shows the oxidation kinetics in wet O_2 of the sputter-deposited Si_3N_4 films. The solid lines are theoretical results that will be explained later. Figure 7.14 shows the 900 °C and 1000 °C measurements plotted in log-log format. If L_{ox} is proportional to t^{α}, then $\log(L_{ox})$ as a function of log(t) will be linear with slope α. Linear regression analyses gave $\alpha = 0.70$ at 1000 °C and $\alpha = 0.50$ at 900 °C (the solid lines in Fig. 7.14). The linear-parabolic oxidation model predicts that, for thin oxides, $\alpha = 1$, and for thick oxides, $\alpha = 1/2$. In the region of transition between linear and parabolic growth, α is approximately 2/3, and is within $\pm 10\%$ of this value over a 0.8-decade span of time.[17]

Enomoto et al.[17] studied the oxidation of LPCVD Si_3N_4 in wet O_2 from 900 to 1100 °C, and found that α was equal to 2/3 over more than 2 decades in time. Here, the range of L_{ox} was roughly 50 Å to 1000 Å. When Si_3N_4 is

converted to SiO_2 by reaction with H_2O, NH_3 is produced. By considering the inhibiting effect on reaction rate that is caused by the accumulation of NH_3 at the SiO_2/Si_3N_4 interface, Enomoto's group derived a model for the wet oxidation of Si_3N_4 which greatly extends the transition region between linear and parabolic growth. This provides $L_{ox} = A_E t_{2/3}$ for a prolonged period, in accordance with their observations. In this early study of Si_3N_4 oxidation the presence of the SiO_xN_y inner scale was apparently unknown, so its pronounced blocking effect on the diffusion of H_2O and NH_3 was not considered.

The oxidation kinetics measured at 1000 °C, shown in Fig. 7.14, conform to the observations of Enomoto's group, as α was determined to be 0.70. After 10 hrs the oxide thickness was 370 Å, which is somewhat lower than the thickness of 410 Å measured by Enmoto et al. However, they used a higher partial pressure of water, 720 Torr instead of 640 Torr. The measurement by Fourrier's group for the same time and temperature was L_{ox} = 430 Å, comparable to the measurement by Enomoto's group. Fourrier's group used a mixture of O_2 and steam, for which the partial pressure of water was apparently not precisely known but was stated to be greater than 600 Torr.

At 900 °C, the oxidation kinetics shown in Fig. 7.14 give $\alpha = 0.5$ for L_{ox} ranging from 30 to 150 Å. The measurements by Enomoto's group at this temperature extend from 65 to 140 Å, which may be an insufficient range to accurately determine α (they obtained $\alpha = 2/3$, as they did for higher temperatures). The oxidation measurements performed by Lee's group at 900 °C, for 10 Å < L_{ox} < 60 Å, give $\alpha = 0.5$. Parabolic extrapolation of these measurements to a time of 10 hrs gives L_{ox} = 115 Å. This is slightly higher than the L_{ox} = 105 Å measured here. The partial pressure of water used by Lee's group was not specified but was presumably 640 Torr. After 10 hrs at 900 °C, the oxide thicknesses reported by Enomoto and Fourrier were L_{ox} = 120 Å and L_{ox} = 125 Å, respectively.

It seems implausible that the oxidation mechanism should change from one which provides $\alpha = 2/3$, at 1000 °C, to another which gives $\alpha = 1/2$, at 900 °C. Therefore, the effect of a period of rapid initial growth, prior to the onset of $t^{2/3}$ growth, was investigated. In general, the effect of rapid initial growth can be represented by incorporating a time offset τ into the model that governs the subsequent growth.[20] For the model of Enomoto et al., this gives $L_{ox} = A_E(t+\tau)^{2/3}$ or $L_{ox}^{3/2} = A_E^{3/2}t + L_0^{3/2}$, where $L_0 = A_E\,\tau^{2/3}$. The oxide thickness at which the rapid initial growth terminates is approximately equal to

L_0. At sufficiently high temperatures, L_0 can be expected to be negligible in comparison with L_{ox}, so that $\log(L_{ox})$ as a function of $\log(t)$ will have the expected slope of $\alpha = 2/3$. If L_{ox} is comparable to L_0, however, a lower slope will be observed.

The three sets of measurements, at oxidation temperatures of 800, 900 and 1000 °C, were independently analyzed by fitting $L_{ox}^{3/2}$ as a linear function of t, thereby determining A_E and L_0 at each temperature. An attempt was made to fit the oxidation measurements using a temperature-independent L_0, but these fits were inaccurate. Table 7.6 gives the results, together with the A_E values obtained from the Arrhenius representation provided by Enomoto et al.[17]

Table 7.6 Rate constants for wet oxidation of Si_3N_4, where $L_{ox} = A_E t^{2/3} + L_0$. Here, L_0 is in Å, A_E is in Å/hr$^{2/3}$, and the oxidation temperature T_{ox} is in °C. Note A is explained in the text.

	[---Measured---]		[Enomoto, et al.[17]]	
T_{ox}	L_0	A_E	L_0	A_E
800	34	4.47	0	5.55
900	23	21.3	0	25.8
1000	0 (A)	81.5	0	94.3

At 1000 °C, the linear fit to $L_{ox}^{3/2}$ intercepted $L_{ox} = 0$ at $t = 0.375$ hrs. The slope provided by this implausible solution gave $A_E = 85.9$ Å/hr$^{2/3}$. A more realistic approximation was obtained by fixing L_{ox} at 0 at $t = 0$, which gave $A_E = 81.5$ Å/hr$^{2/3}$ (note A in Table 7.6). At this temperature, the oxidation kinetics are not as sensitive to the value of L_{ox}. The measured values of A_E agree reasonably well with the measurements of Enomoto et al., considering the lower partial pressure of water which was used here. The measured values of L_0 and A_E were used to determine the theoretical oxidation rates shown by the solid lines in Fig. 7.13.

For the conditions of interest here, $T_{ox} = 600$ °C and $L_{ox} < 30$ Å, these results indicate that rapid initial oxidation kinetics would probably apply. Therefore, a model of the initial oxidation kinetics is required in order to extrapolate the results of measurements performed at higher temperatures. The data presented here, however, are insufficient to establish the growth kinetics of such thin oxides.

At the beginning of this research project, because little confidence was placed in the effectiveness of the aluminum layer as a barrier to oxidants, it

was considered prudent to estimate the potential measurement drift due to Si_3N_4 oxidation. For purposes of this worst-case estimate, the Si_3N_4 surface was assumed to be directly exposed to the oxidizing ambient. Analysis of the sputter-deposited aluminum layers, described in the next subsection, have rendered this issue less consequential, as the sputter-deposited aluminum has been found to be an effective barrier to oxygen.

7.5 Characteristics of the Aluminum Encapsulating Layer

The sensor's aluminum encapsulating layer was deposited by magnetron sputtering.[22] For a DC power of 400 W and an argon pressure of 8 mTorr, the deposition rate was 25 nm/min. The aluminum encapsulant was sputter-deposited for 60 min, to a thickness of 1.5 μm.

When inspected under an optical microscope, the surfaces of the sputter-deposited aluminum films appear to be fully comprised of tightly packed pyramidal hillocks, each of which has a width of several μm. Because aluminum is highly reactive, residual oxygen is readily incorporated into the film. The chemisorption of oxygen along the edges of growing grains limits the mobility of atoms between grains, thereby promoting columnar growth.[23]

Although the surfaces of the sputter-deposited aluminum films were diffusely reflective, when viewed through the substrate the films were specular. Therefore, these films were deemed suitable for use as the thin-film interferometer's rear reflector.

At low temperatures, transport through a polycrystalline thin film occurs principally via diffusion along grain boundaries.[24] Because these sputter-deposited aluminum films are comprised of columnar crystallites and voids, little confidence was placed initially in their effectiveness as barriers to oxidants. However, these aluminum films were experimentally determined to be good barriers to oxygen, despite their poor appearance. The volume increase following oxidation of the columnar grains may have closed down the vertical pores, even as the film was being deposited.

A 1.5-μm-thick sputter-deposited aluminum film, on a silicon substrate, was oxidized in dry O_2 at 400 °C for 2 hrs. Figures 7.15 and 7.16 show the atomic concentration of oxygen as a function of depth in the film, as measured using Auger electron spectrometry. These results show that the oxygen content inside the film was unchanged by exposure to the oxidizing environment.

Instability of the Si_3N_4/Al interface is a potential cause of sensor drift. The diffusion of aluminum in Si_3N_4 films was studied by Ogata, et al.[25] From the shift in the KL_2L_3 Auger peak they determined that the diffused aluminum is not metallic but is in the form of an oxide. The oxygen concentration in the film was observed to track that of the diffused aluminum, with a ratio approximately equal to that of Al_2O_3.

The formation of Al_2O_3 then appears necessary for the diffusion mechanism observed by Ogata et al. Possible sources of oxygen for the formation of Al_2O_3 are the Si_3N_4 layer's native oxide and the oxygen impurities in the film. Even at very low temperatures, aluminum in contact with SiO_2 will react, yielding Al_2O_3 and silicon.[26] This reaction causes aluminum to be strongly adherent to SiO_2. For sufficient thickness of SiO_2, this reaction is self limiting, probably because the Al_2O_3 acts as a barrier to the diffusion of aluminum.[27]

In the fabrication of the fiber-optic temperature sensors, the aluminum was sputter deposited immediately after the Si_3N_4 layer, without breaking vacuum. The thickness of the Si_3N_4 surface oxide was thereby minimized, so it may well have been entirely consumed by the sputter-deposited aluminum.

The oxygen impurities in the Si_3N_4 are another source of oxygen for the formation of Al_2O_3 which could then diffuse through the Si_3N_4.

The diffusion of Al_2O_3 in the Si_3N_4 film is not expected to be a significant source of drift. Using the results of section 5, the measured temperature was determined to shift by 1 °C following a 0.4% change in the refractive index of the Si_3N_4 layer. Using the Bruggeman EMA, the refractive index of Si_3N_4 was determined to be essentially unchanged by the addition of significant amounts of Al_2O_3. An Al_2O_3 fraction of fully 3.2%, by volume, was required to produce an index change sufficient to shift the measured temperature by -1 °C.

The effectiveness of the Si_3N_4 layer at keeping the aluminum away from the silicon layer was estimated using the results of Ogata's group,[25] who measured the the diffusion of aluminum in Si_3N_4 over the temperature range of 450 to 530 °C. By extrapolation of their measurements, it was determined that, after 5000 hrs at 300 °C, aluminum should diffuse into the Si_3N_4 by a length $2(Dt)^{1/2}$ of only 18 nm. Thus, an insignificant amount of aluminum would reach the Si_3N_4/Si interface during the operational life of the sensor. The Si_3N_4 layer should be even more effective at blocking the diffusion of

silicon, since the mechanism for this process can be expected to be similar to the mechanism for silicon diffusion in SiO_2, which proceeds very slowly,[28] at a rate comparable to that of silicon self diffusion.

The effects of aluminum diffusion on the optical properties of the Si_3N_4 layer were experimentally determined by annealing an aluminum and Si_3N_4 couple at 530 °C for 10.5 hrs. Based on the measurements of Ogata's group, aluminum was expected to be fully diffused through the 100-nm-thick Si_3N_4 film by this anneal, since the diffusion length $2(Dt)^{1/2}$ was determined to be 170 nm. This diffusion length is equal to that which would be obtained after 10^6 hrs at 300 °C. After sputter deposition on a silicon wafer, the Si_3N_4 film was annealed for 2 hrs at 1000 °C in wet O_2. The thermal oxide was then stripped, and the Si_3N_4 layer was ellipsometrically characterized. Following aluminum deposition, the sample was annealed in argon. Then the aluminum was removed and the Si_3N_4 refractive index remeasured. At 830 nm, the refractive index change was determined to be only 0.2%, roughly half of the index change that would shift the measured temperature by 1 °C.

7.6 Conclusion

The optimum conditions for deposition of the Si_3N_4 diffusion barrier were determined. These magnetron-sputter-deposited Si_3N_4 films were shown to be highly oxidation resistant. The aluminum encapsulating layer was demonstrated to be an effective barrier to oxidants as well. The Si_3N_4 layer was shown to be an effective barrier to the interdiffusion of aluminum and silicon, and the diffusion of aluminum in the Si_3N_4 layer was demonstrated to have a negligible effect on the sensor's output.

7.7 References

1. A.C. Adams, "Dielectric and Polysilicon Film Deposition," in **VLSI Technology**, S.M. Sze, ed. (McGraw-Hill, New York, 1983).

2. T. Serikawa and A. Okamoto, "Properties of Magnetron-Sputtered Silicon Nitride Films," J Electrochem. Soc. 131, 2928 (1984).

3. S.M. Hu and L.V. Gregor, "Silicon Nitride Films by Reactive Sputtering," J. Electrochem. Soc. 114, 826 (1967).

4. T. Carriere, B. Agius, I. Vickridge, J. Siejka, and P. Alnot, "Characterization of Silicon Nitride Films Deposited on GaAs by RF Magnetron Cathodic Sputtering," J. Electrochem. Soc. 137, 1582 (1990).

5. X. Qiu and E. Gyarmati, "Composition and Properties of SiN_x Films Produced by Reactive R.F. Magnetron Sputtering," Thin Solid Films 151, 223 (1987).

6. C.J. Mogab, P.M. Petroff, and T.T. Sheng, "Effect of Reactant Nitrogen Pressure on the Microstructure and Properties of Reactively Sputtered Silicon Nitride Films," J. Electrochem Soc. 122, 815 (1975).

7. C.J. Mogab and E. Lugujjo, "Backscattering Analysis of the Composition of Silicon-Nitride Films by RF Reactive Sputtering," J. Appl. Phys. 47, 1302 (1976).

8. E.D. Palik, ed., **Handbook of Optical Constants of Solids** (Academic, Orlando, 1985).

9. G.N. DeBrabander, J.T. Boyd, and G. Beheim, "Integrated Optical Ring Resonator Wth Micromechanical Diaphragm for Pressure Sensing," IEEE Photonics Technol. Lett. 6, 671 (1994).

10. D.E. Aspnes and J.B. Theeten, "Dielectric Function of Si-SiO_2 and Si-Si_3N_4 Mixtures,' J. Appl. Phys. 50, 4928 (1979).

11. M.J. Rand and D.R. Wonsidler, "Optical Absorption as a Control Test for Plasma Silicon Nitride Deposition," J. Electrochem. Soc. 125, 99 (1978).

12. A. Fourrier, A Bosseboeuf, D. Bouchier, and G. Gautherin, "Thermal Oxidation in Wet Oxygen of Reactive Ion-Beam Sputter-Deposited Silicon Nitride Films," J. Electrochem. Soc. 138, 1084 (1984).

13. S.I. Raider, R. Flitsch, J.A. Aboaf, and W.A. Pliskin, "Surface Oxidation of Silicon Nitride Films," J. Electrochem. Soc. 123, 560 (1976).

14. H. Du, R.E. Tressler, K.E. Spear, and C.G. Pantano, "Oxidation Studies of Crystalline CVD Silicon Nitride," J. Electrochem. Soc. 136, 1527 (1989).

15. H. Du, R.E. Tressler, and K.E. Spear, "Thermodynamics of the Si-N-O System and Kinetic Modeling of Oxidation of Si_3N_4," J. Electrochem. Soc. 136, 3210 (1989).

16. L.U.T. Ogbuji, and D.T. Jayne, "Mechanism of Incipient Oxidation of Bulk Chemical Vapor Deposited Si_3N_4," J. Electrochem. Soc. 140, 759 (1993).

17. T. Enomoto, R. Ando, H. Morita, and H. Nakayama, "Thermal Oxidation of a Si_3N_4 Film and Its Masking Effect against Oxidation of Silicon," Jap. J. Appl. Phys. 17, 1049 (1978).

18. E.G. Lee and H.B. Im, and J.S. Roh, "Effects of Wet Oxidation on the Properties of Sub-10-nm-Thick Silicon Nitride Films," J. Am. Ceram. Soc. 74, 1563 (1991).

19. D.J. Choi, D.B. Fischbach, and W.D. Scott, "Oxidation of Chemically-Vapor-Deposited Silicon Nitride and Single-Crystal Silicon," J. Am. Ceram. Soc. 72, 1118 (1989).

20. B.E. Deal and A.S. Grove, "General Relationship for the Thermal Oxidation of Silicon," J. Appl. Phys. 36, 3770 (1965).

21. B.E. Deal, "Thermal Oxidation Kinetics of Silicon in Pyrogenic H_2O and 5% HCl/H_2O Mixtures," J. Electrochem. Soc. 125, 576 (1978).

22. P.S. MacLeod and L.D. Hartsough, "High-Rate Sputtering of Aluminum for Metallization of Integrated Circuits," J. Vac. Sci. Technol. 14, 263 (1977).

23. K.H. Guenther, "Microstructure of Vapor-Deposited Optical Coatings," Appl. Opt. 23, 3806 (1984).

24. M. Wittmer, "Barrier Layers: Principles and Applications in Microelectronics," J. Vac. Sci. Technol. A 2, 273 (1984).

25. H. Ogata, K. Kanayama, M. Ohtani, K. Fujiwara, H. Abe, and H. Nakayama, "Diffusion of Aluminum into Silicon Nitride Films," Thin Solid Films 48, 333 (1978).

26. Y.E. Strausser and K.S. Majumder, "Abstract: Chemical Structure of the Al-SiO_2 Interface," J. Vac. Sci. Technol. 15, 238 (1978).

27. S.M. Goodnick, M. Fathipour, D.L. Ellsworth, and C.W. Wilmsen, "Effects of a Thin SiO_2 Layer on the Formation of Metal-Silicon Contacts," J. Vac. Sci. Technol. 18, 949 (1981).

28. G. Brebec, R. Seguin, C. Sella, J. Bevenot, and J.C. Martin, "Diffusion du Silicium dans la Silice Amorphe," Acta. Metallurgica 28, 327 (1980).

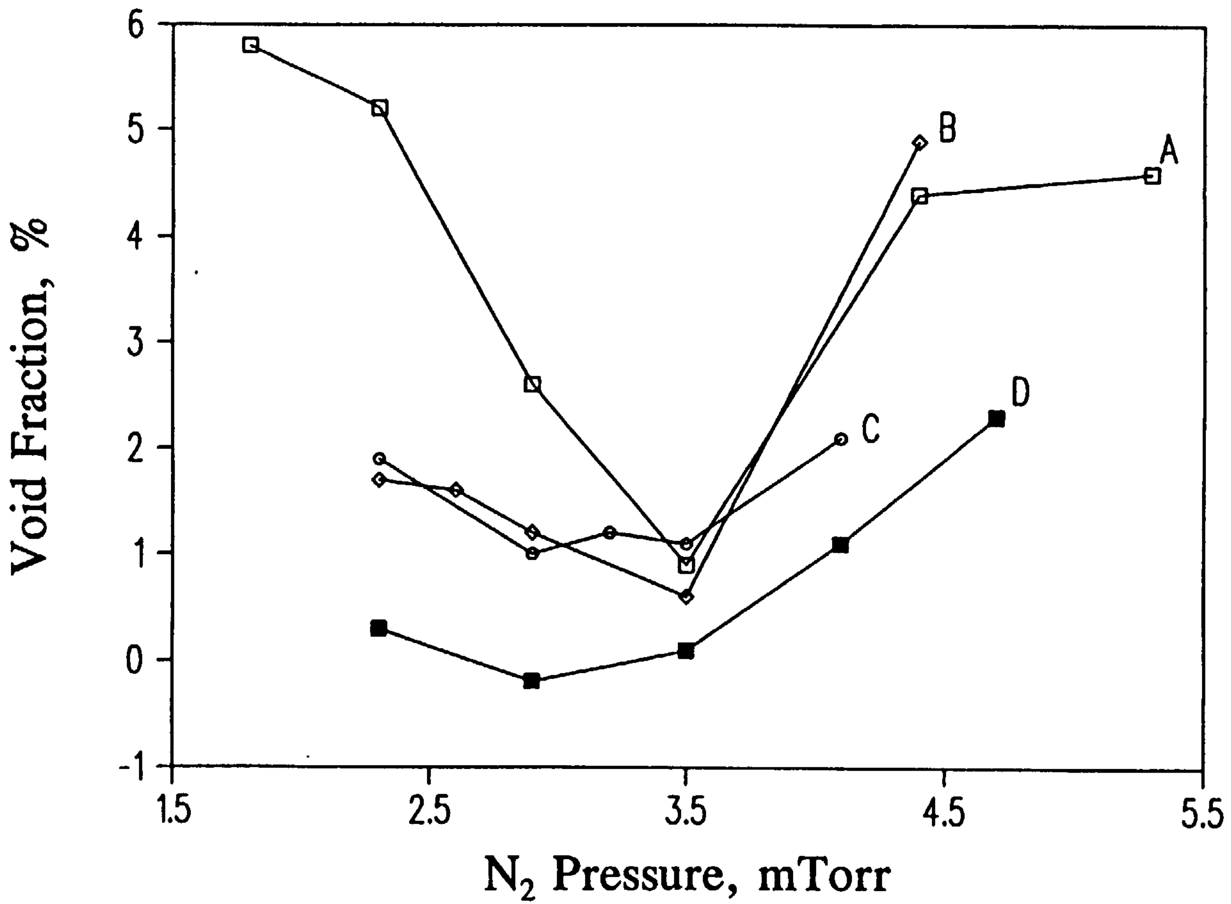

Figure 7.1 Void fractions f_V of SiN_x films as functions of sputtering gas pressure, measured on four different occasions.

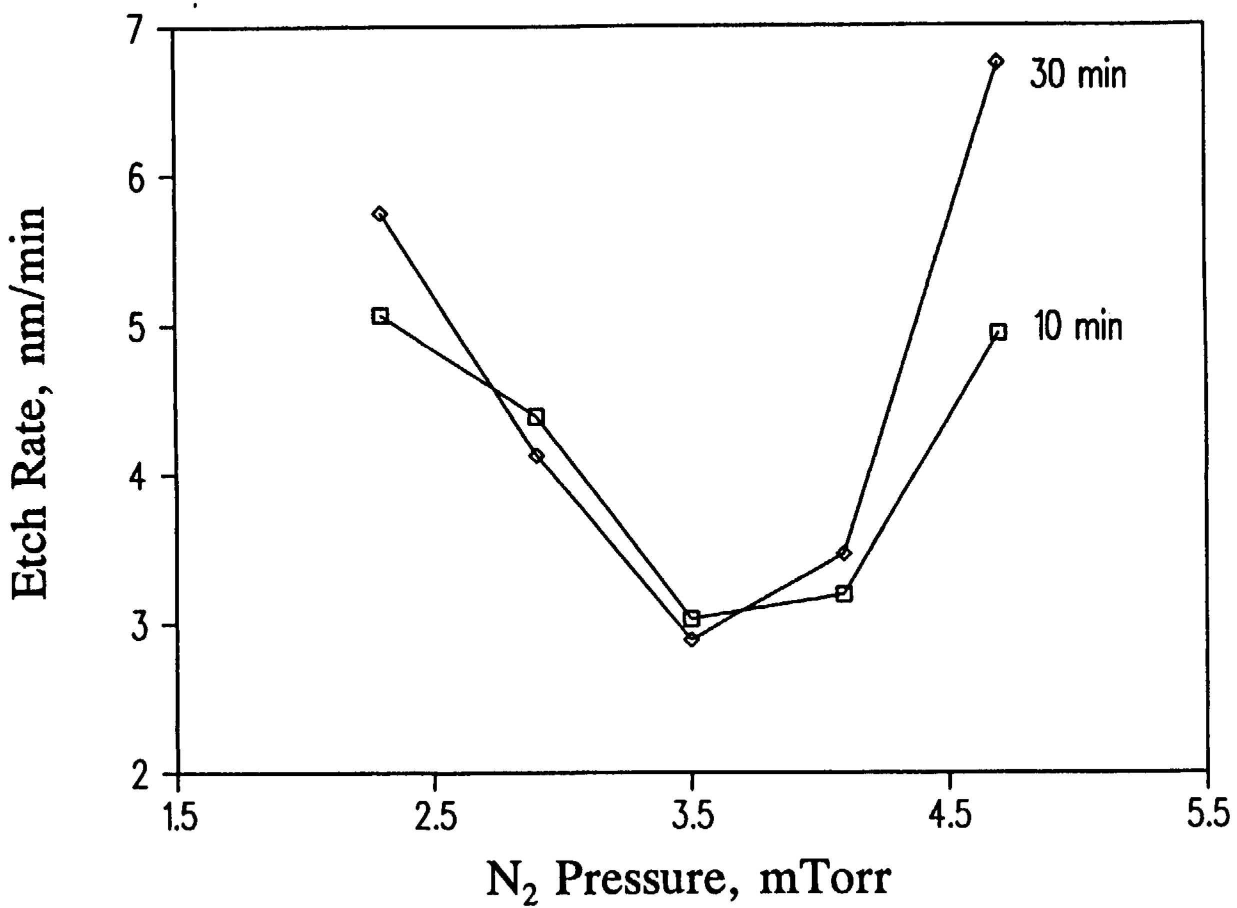

Figure 7.2 Etch rates in buffered HF of SiN_x films as functions of sputtering gas pressure, for 10-min and 30-min etches.

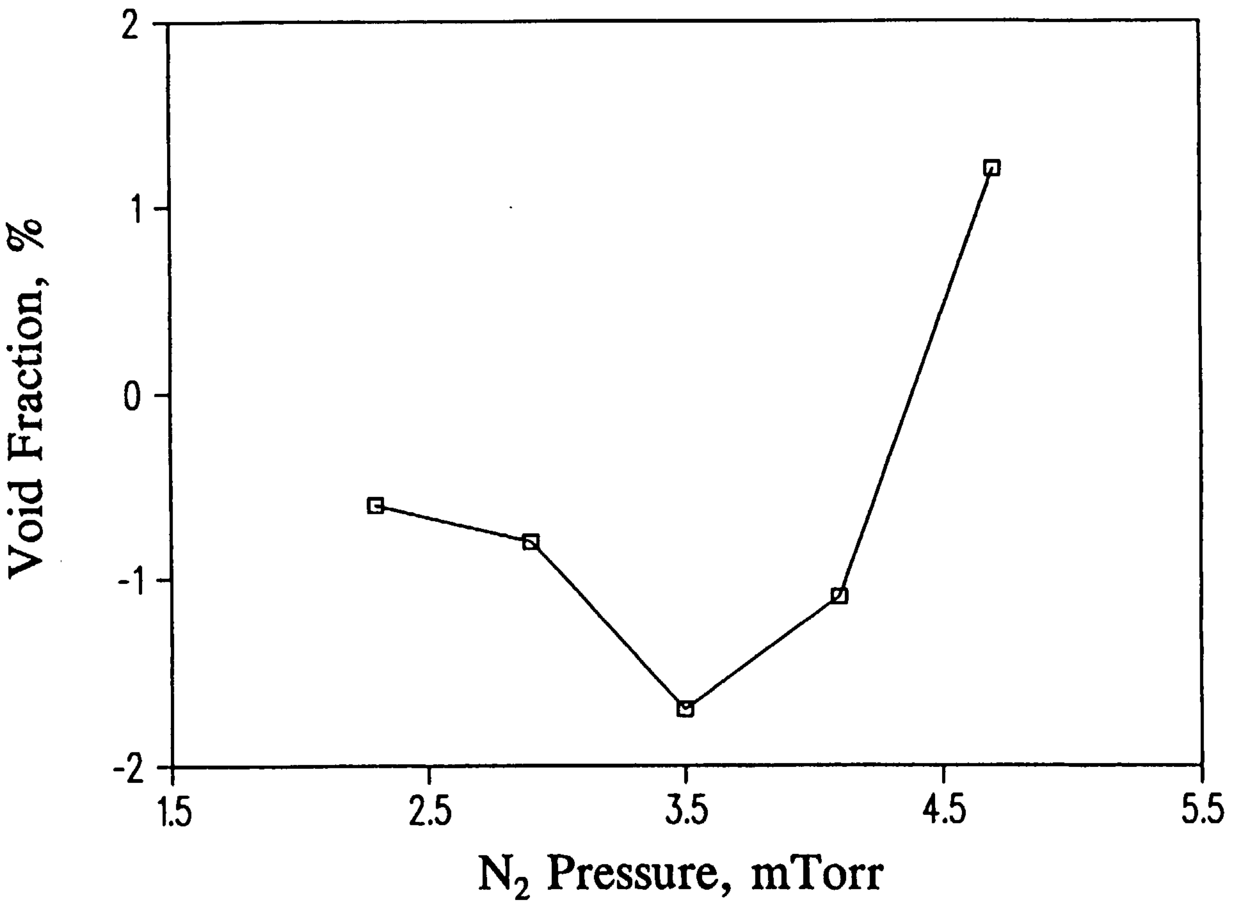

Figure 7.3 Void fraction f_V as a function of sputtering gas pressure for SiN_x films on silicon substrates that were subjected to etch-rate testing.

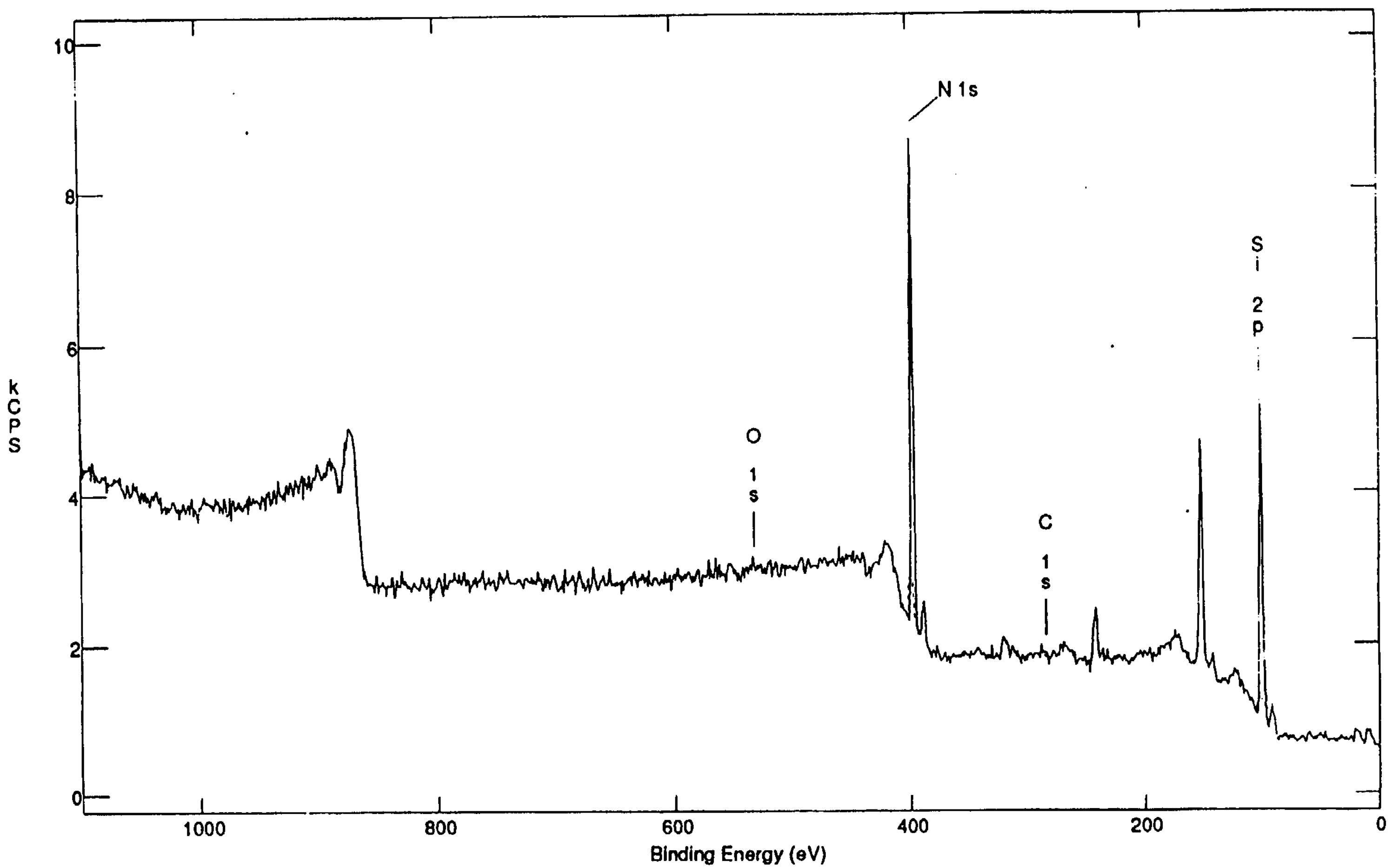

Figure 7.4 Survey spectrum of electron binding energies for SiN_x sputter deposited in 2.3 mTorr N_2.

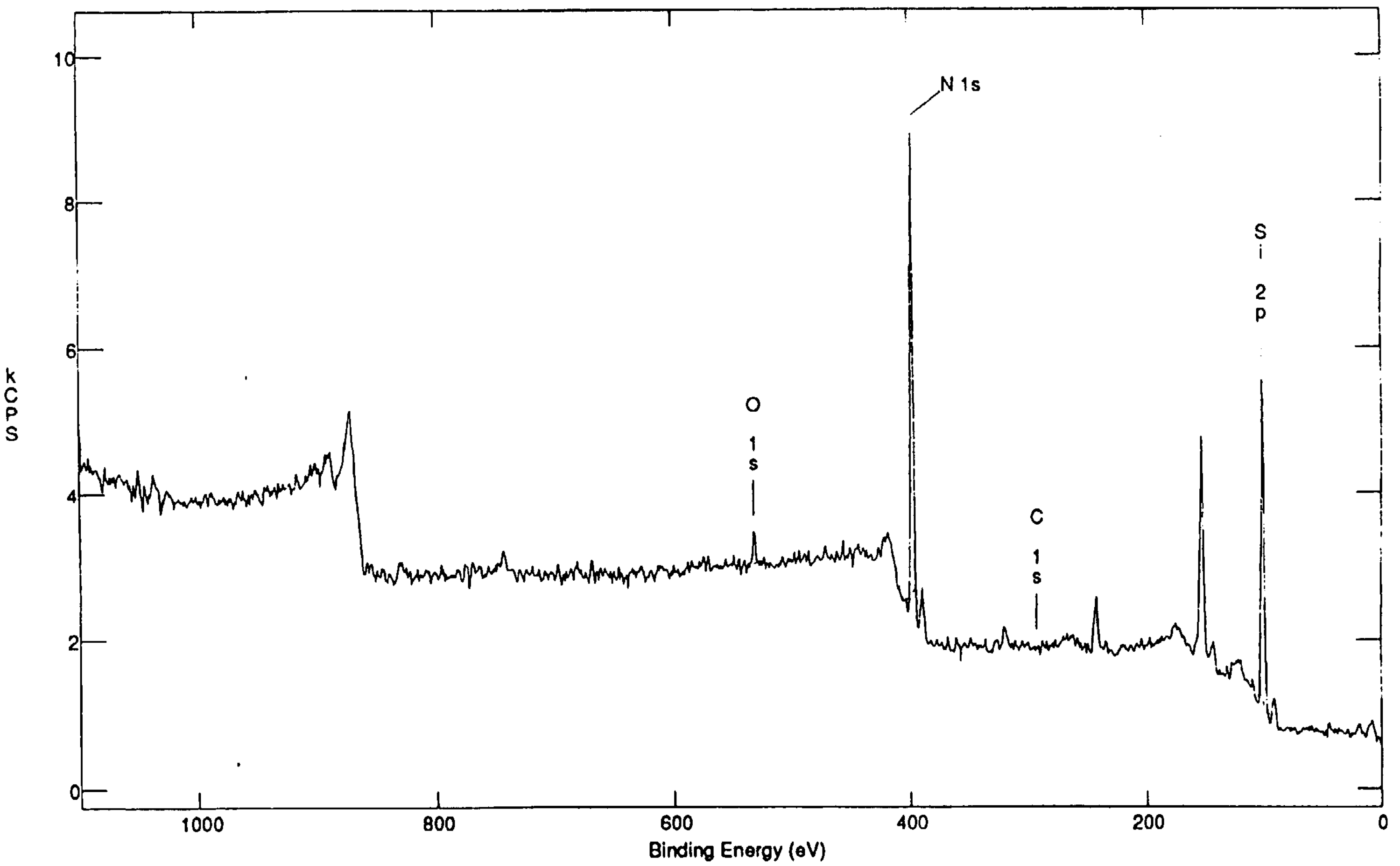

Figure 7.5 Survey spectrum of electron binding energies for SiN_x sputter deposited in 4.7 mTorr N_2.

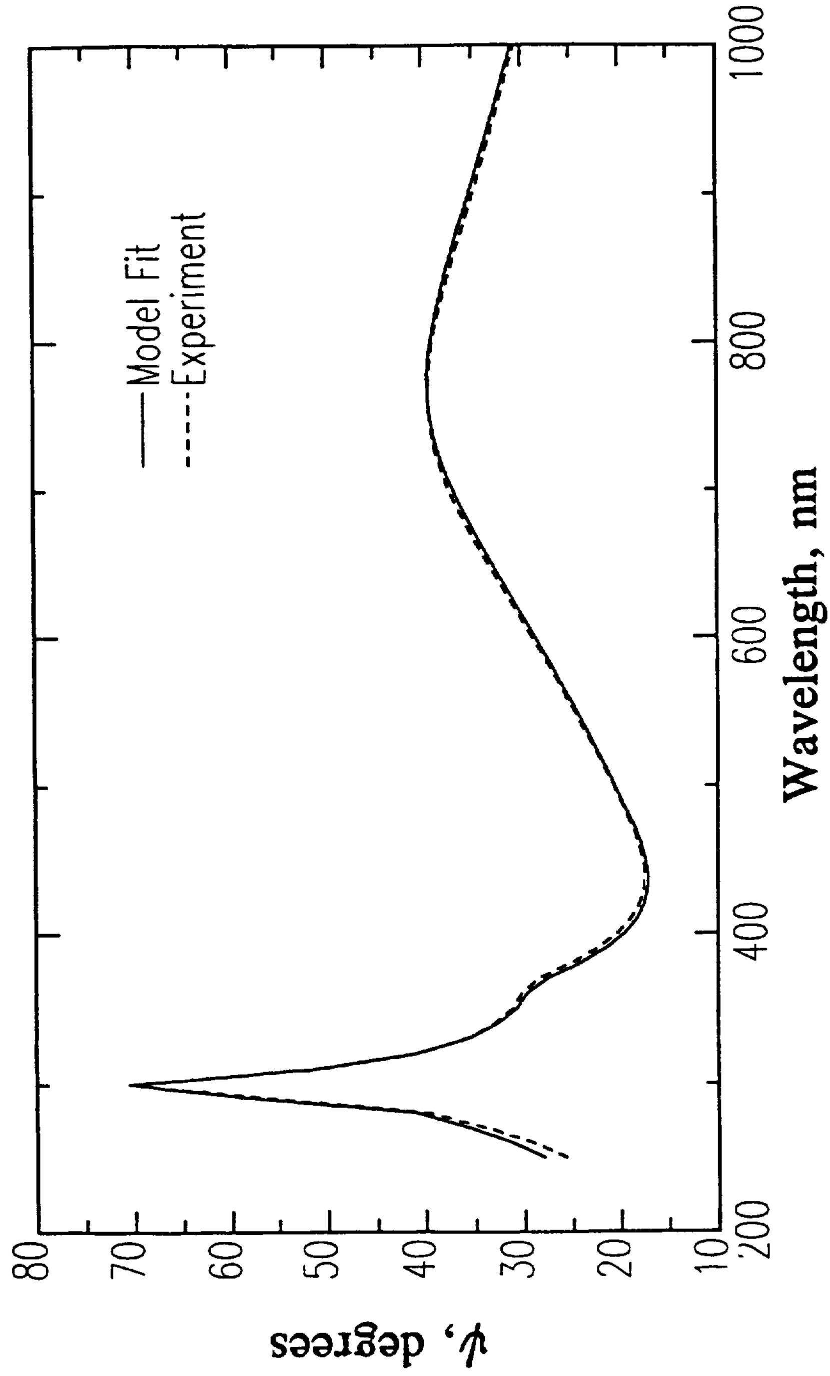

Figure 7.6 Measured and calculated $\psi(\lambda)$ for Si_3N_4 sputter deposited on silicon in 3.5 mTorr N_2.

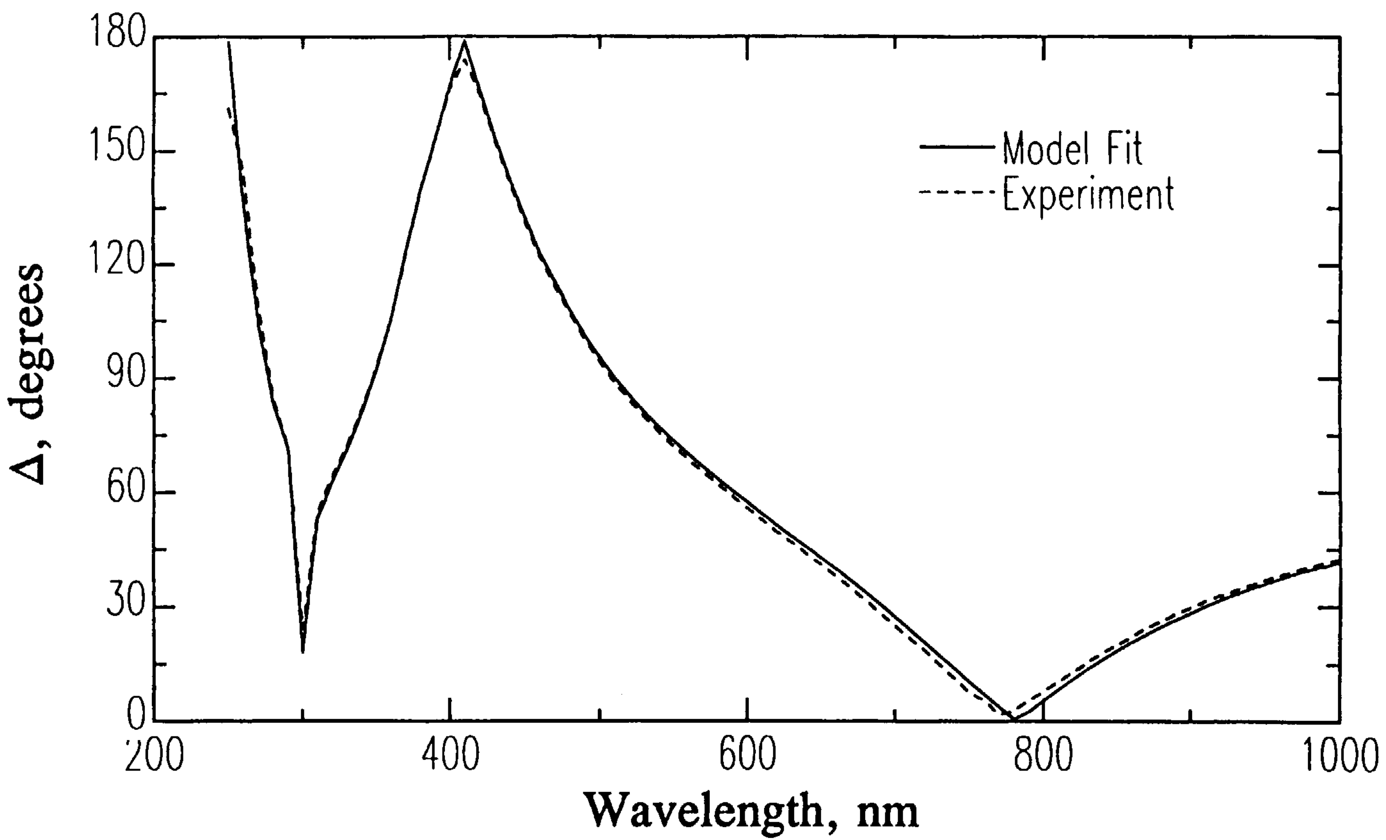

Figure 7.7 Measured and calculated $\Delta(\lambda)$ for Si_3N_4 sputter deposited on silicon in 3.5 mTorr N_2.

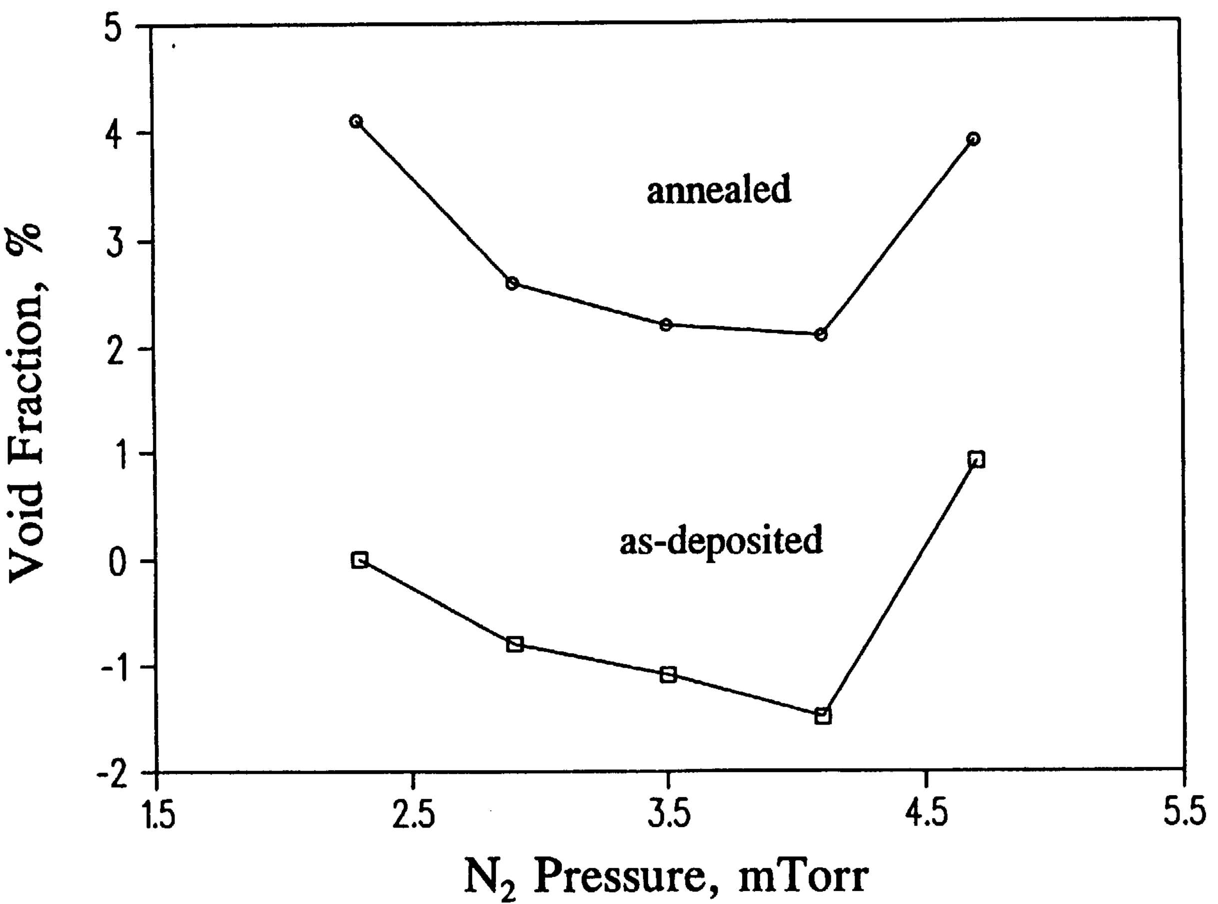

Figure 7.8 Void fractions of Si_3N_4 films on silicon as functions of sputtering gas pressure, as deposited and after annealing.

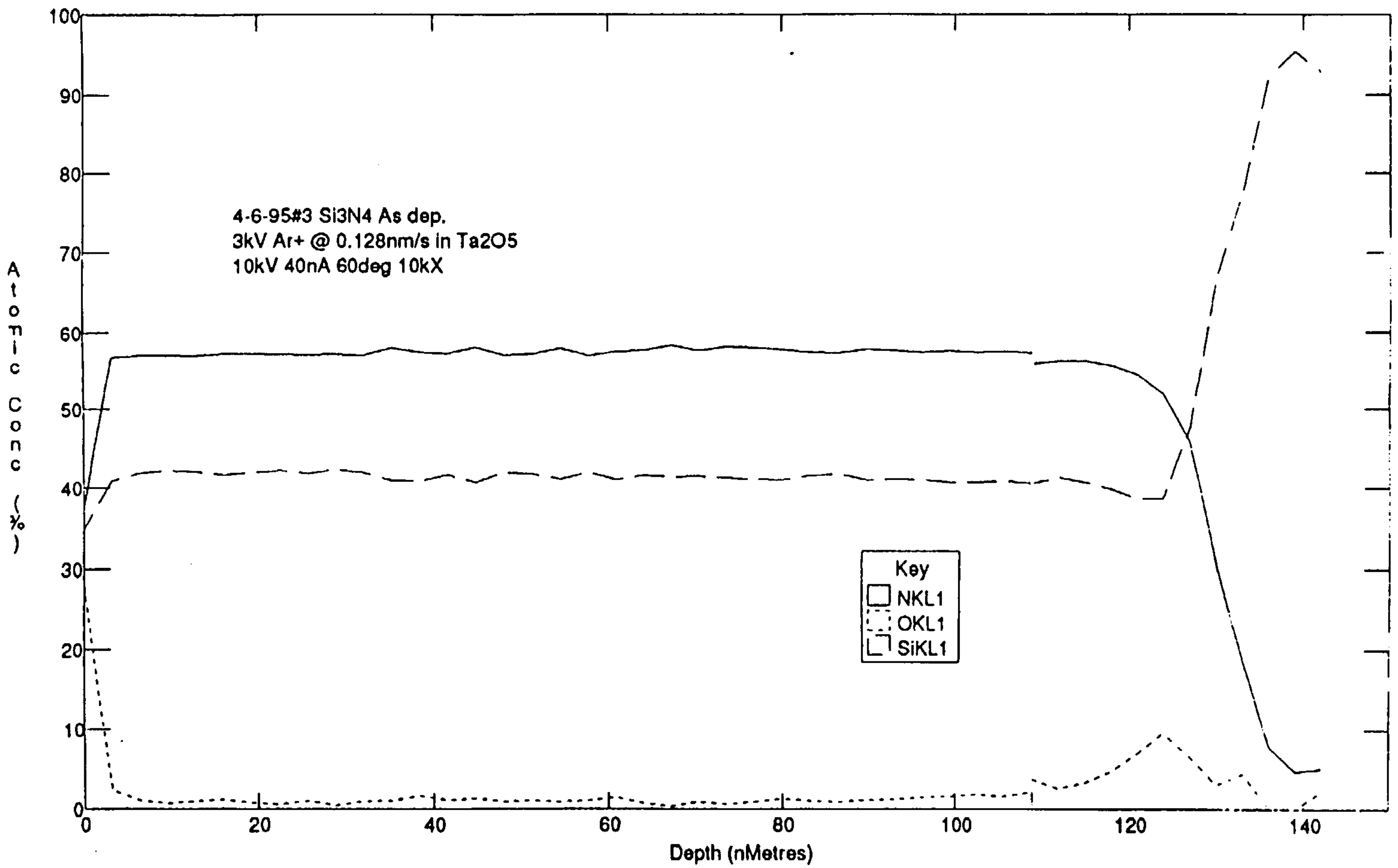

Figure 7.9 Composition profile for Si_3N_4 film on silicon, as sputter deposited.

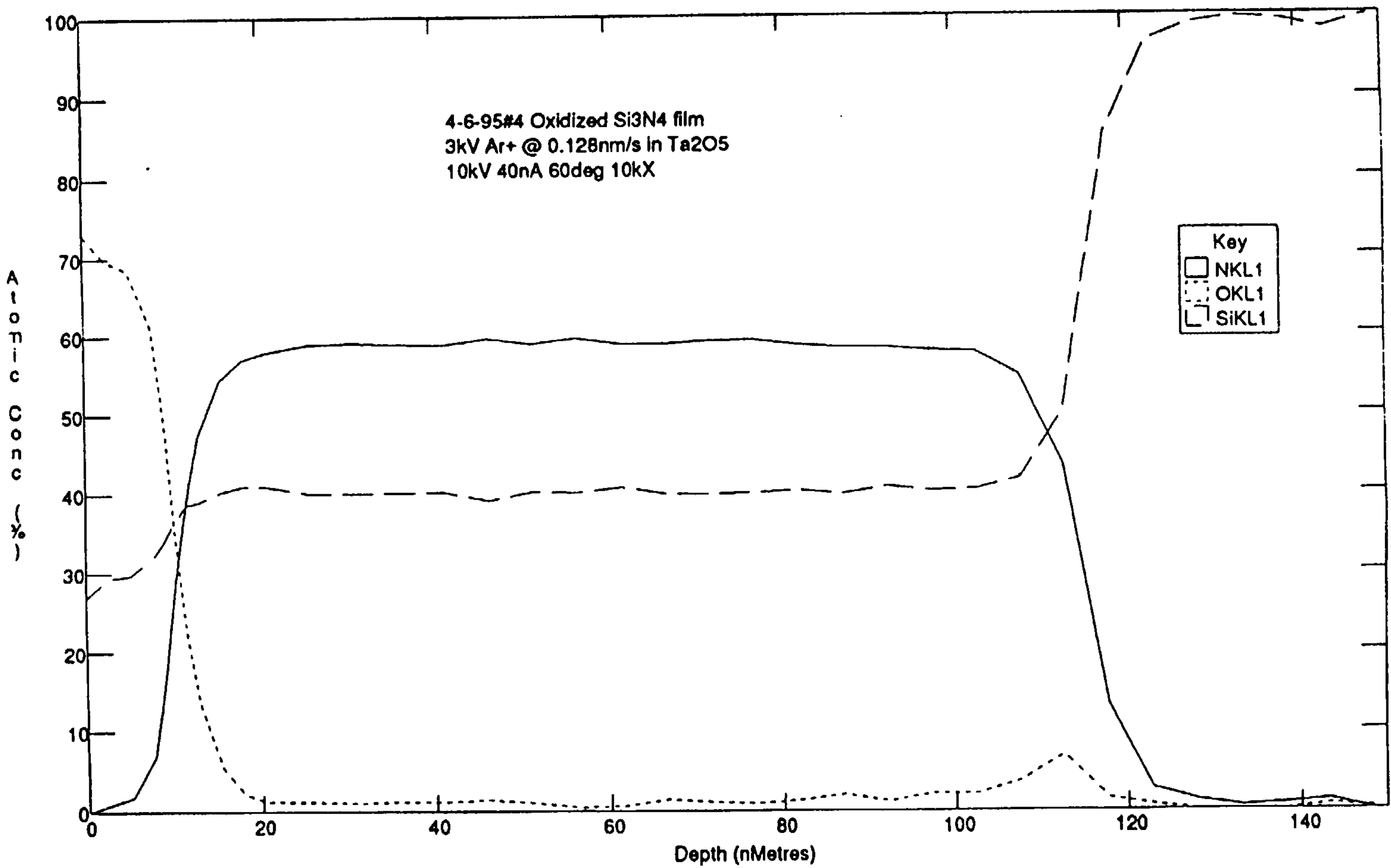

Figure 7.10 Composition profile for oxidized Si_3N_4 film on silicon.

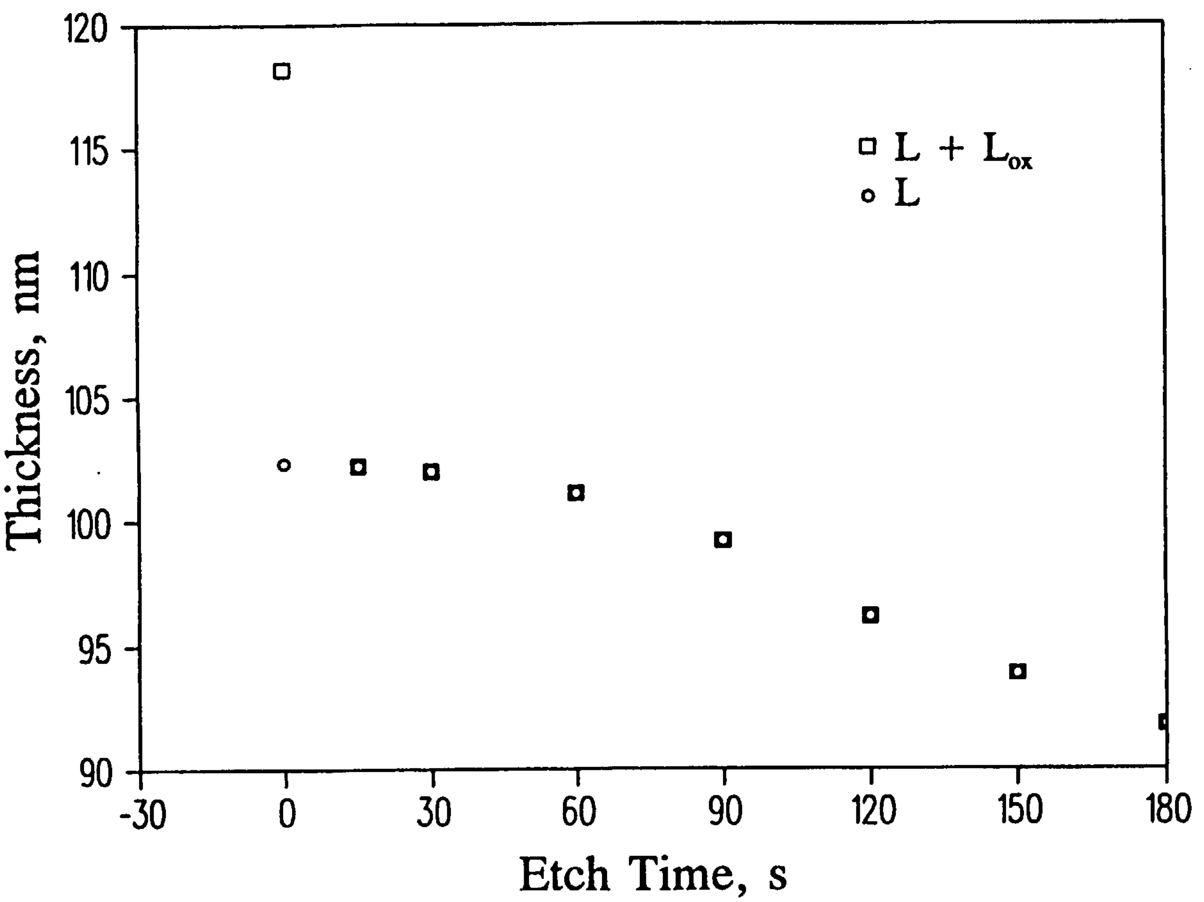

Figure 7.11 Thicknesses of Si_3N_4 and SiO_2 layers, L and L_{ox}, respectively, as functions of etching time in buffered HF.

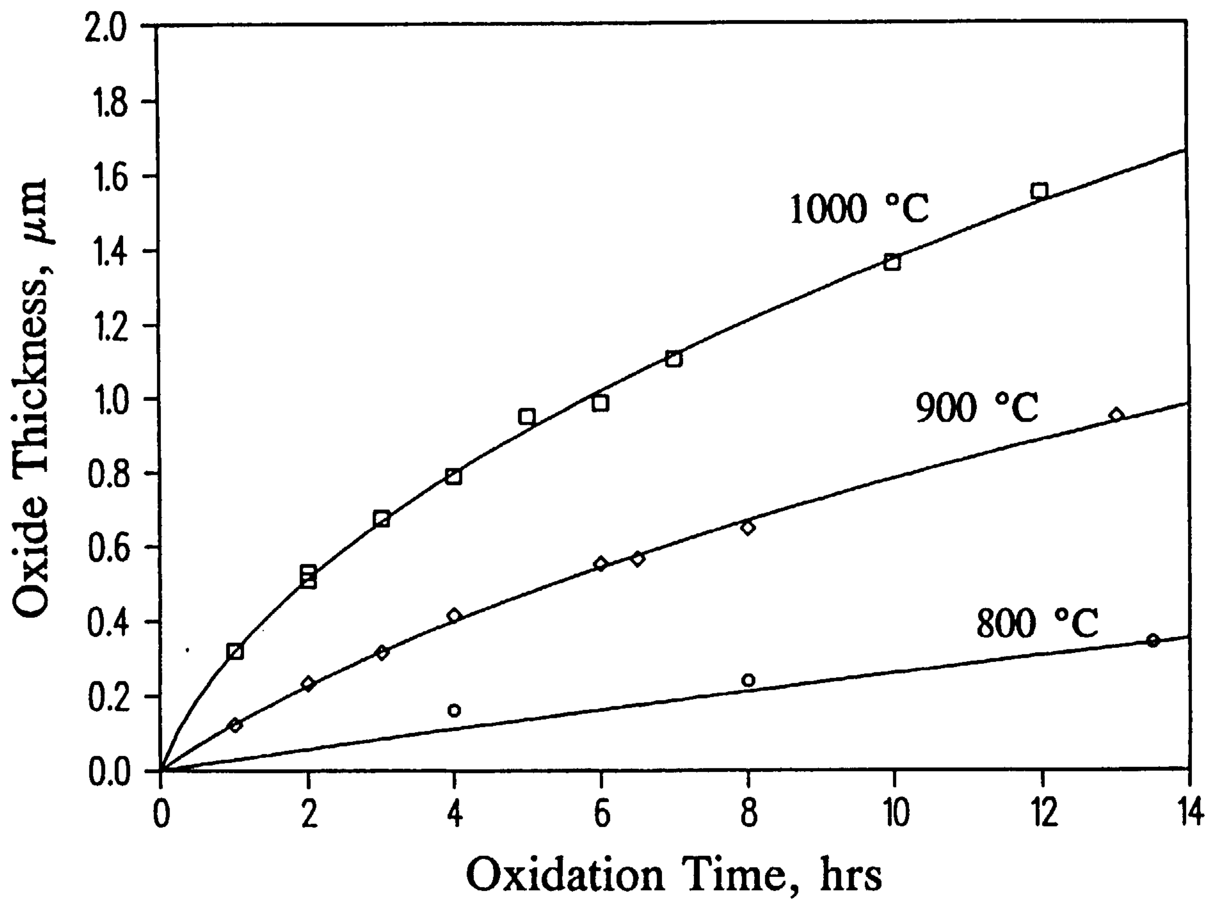

Figure 7.12 Silicon oxidation--measured and calculated thicknesses L_{ox} of SiO_2 layers on silicon as functions of oxidation times in wet O_2, at different temperatures.

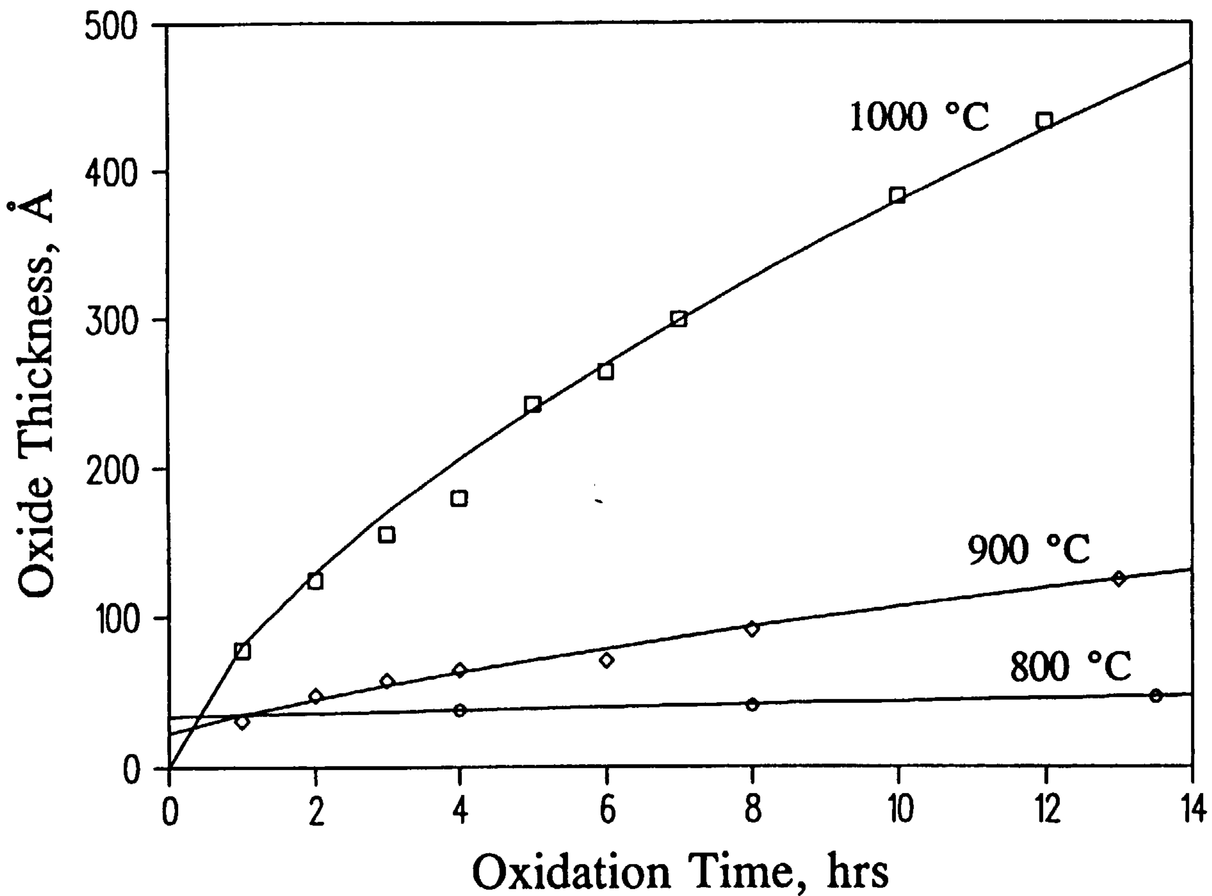

Figure 7.13 Si_3N_4 oxidation--measured and calculated thicknesses L_{ox} of SiO_2 layers on Si_3N_4 as functions of oxidation times in wet O_2, at different temperatures.

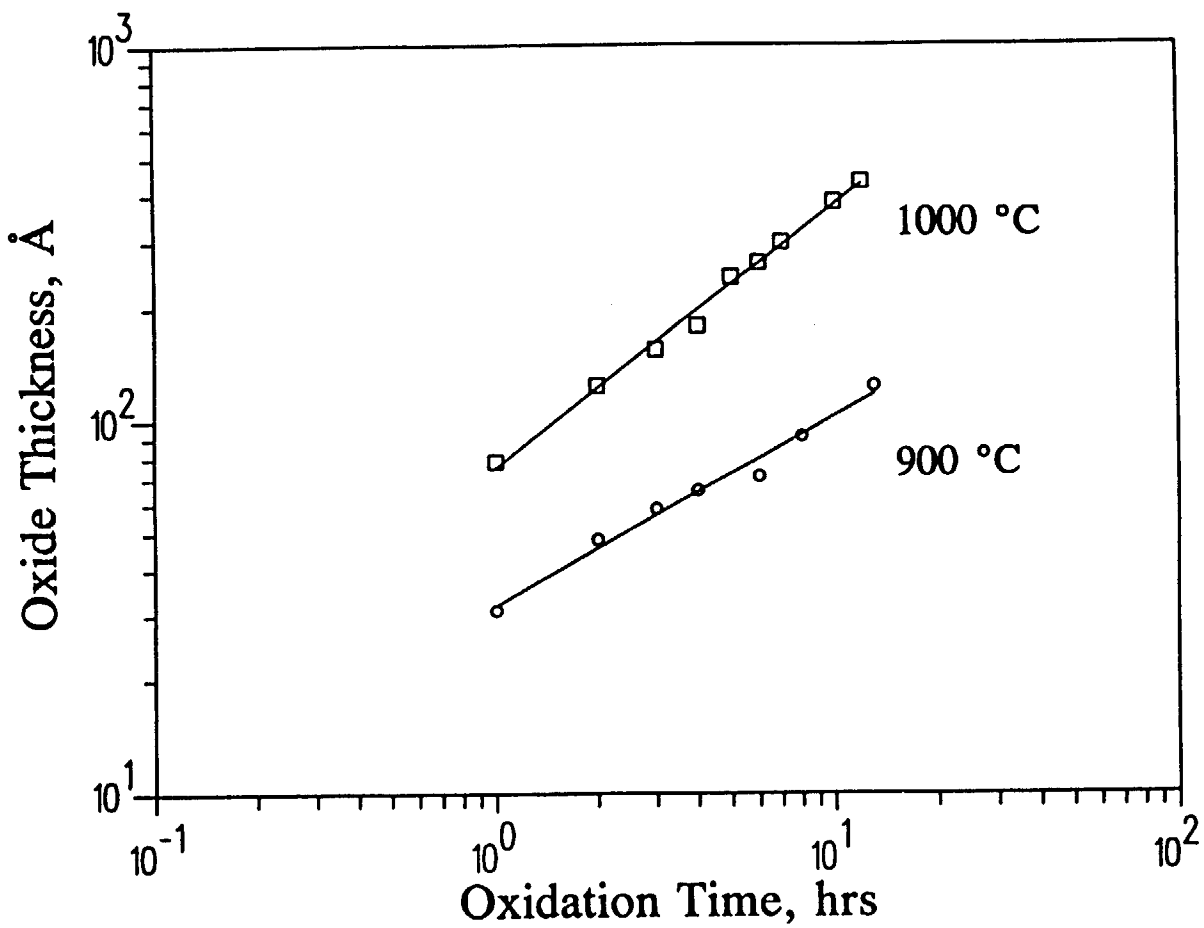

Figure 7.14 Log-log plots of Si_3N_4 oxidation data.

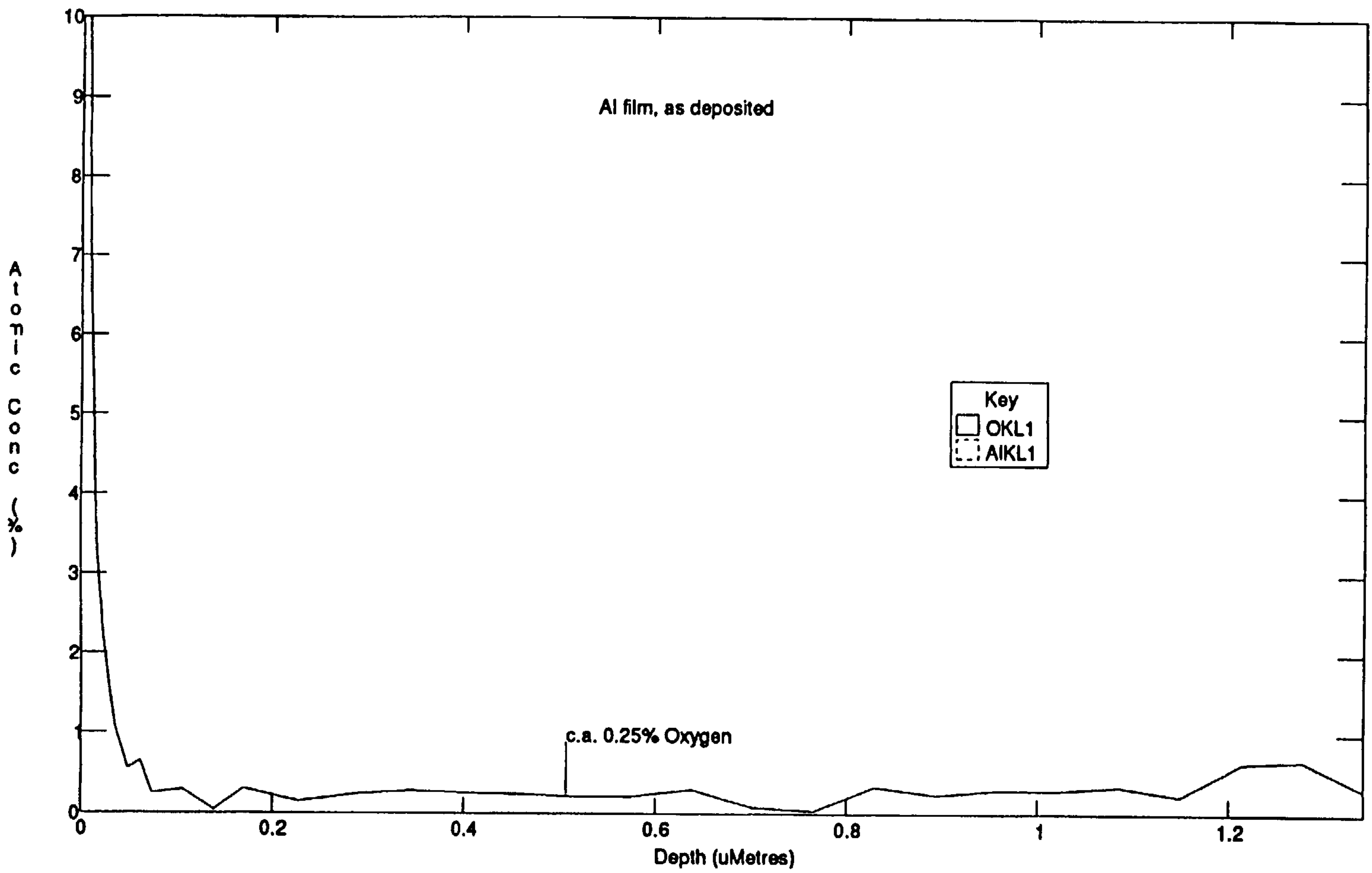

Figure 7.15 Oxygen concentration profile of aluminum film as deposited.

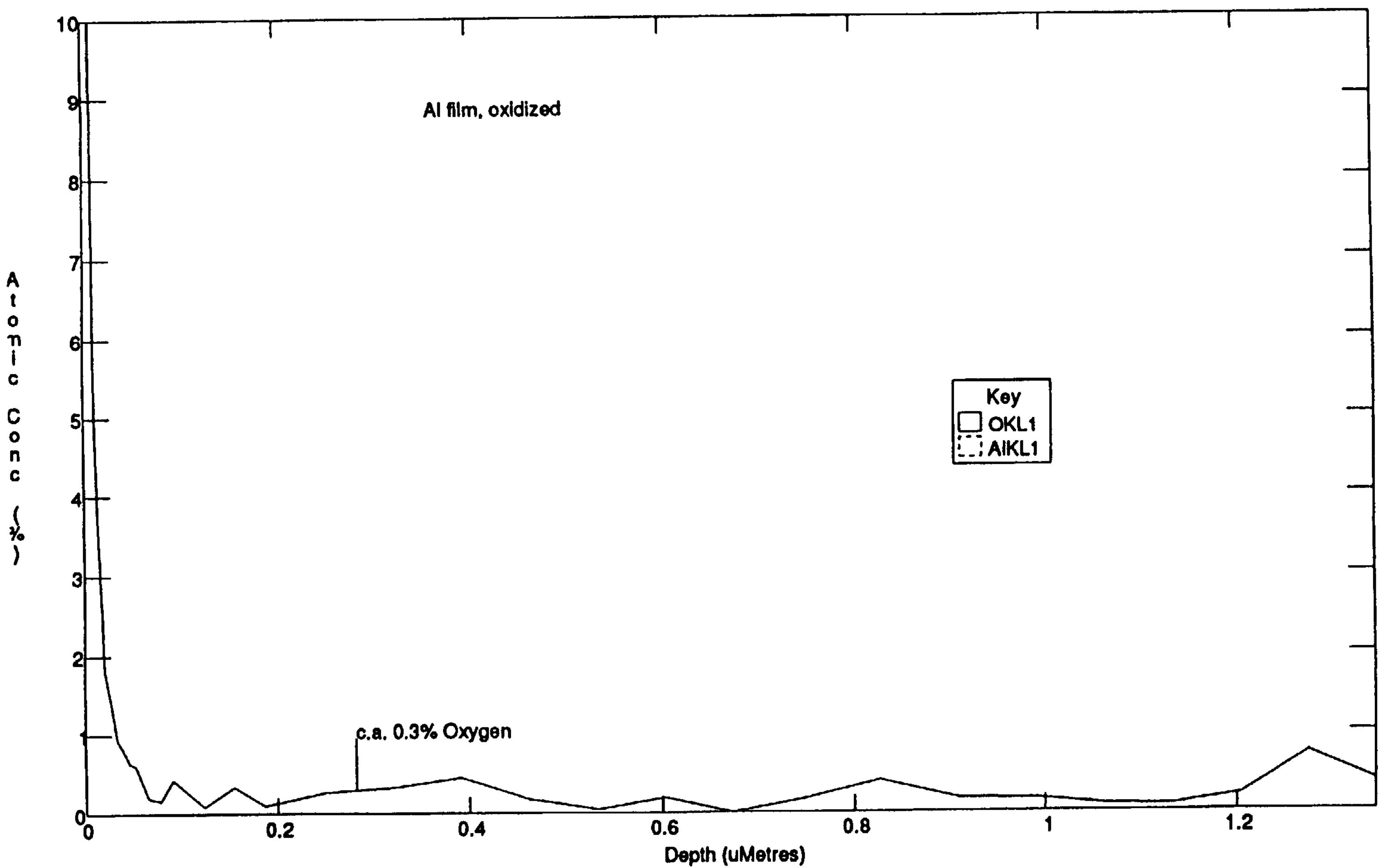

Figure 7.16 Oxygen concentration profile of oxidized aluminum film.

8. TEMPERATURE SENSOR CHARACTERIZATION

8.1 Introduction

Fiber-optic thin-film Fabry-Perot temperature sensors were fabricated using the design and processes described in the preceding sections. Four sensors that were fabricated together were analyzed by reflectometry to determine the properties of the component films. The thermal responses of these sensors were then measured over the -55 to 275 °C range. After the sensors were calibrated, the sensitivities to the most significant sources of drift were studied. Short-term drifts due to remating and fiber bending were measured, as were the long-term drifts resulting from prolonged exposure to an elevated temperature.

8.2 Sensor Fabrication and Initial Characterization

Thin-film interferometric temperature sensors were deposited on the ends of ~0.5-m-long aluminum-coated optical fibers. The fibers were fused silica

with a core diameter of 100 μm and an NA of 0.2. Four sensors, designated 291-294, were fabricated at the same time using the following procedure:

(a) A ~1.4-μm-thick layer of amorphous silicon was magnetron-sputter deposited. The argon pressure was 4 mTorr, the RF power was 400 W, and the deposition time was 45 min.

(b) The silicon films were crystallized using a 1-W argon-ion-laser beam which was focused to a diameter of 270 μm (FWHM). The exposure time was 2 s.

(c) A 90-nm-thick layer of Si_3N_4 was deposited by reactive magnetron sputtering of a silicon target in nitrogen. The pressure was 3.5 mTorr, the RF power was 400 W, and the deposition time was 17 min.

(d) A ~1-μm-thick aluminum layer was sputter deposited immediately after the Si_3N_4 layer, without breaking vacuum. The argon pressure was 8 mTorr, the DC power was 400 W, and the deposition time was 60 min.

The sensors were characterized by spectral reflectometry, as described in section 6. To summarize the nomenclature, the transmitted spectra were

divided by the source spectra to give the sensor transmissivities $H_S(\lambda)$. In terms of the reflectivity of the thin-film interferometer $R_F(\lambda)$, $H_S(\lambda) = H_{FO}(\lambda) R_F(\lambda)$, where H_{FO} is the transmissivity of the fiber-optic link. An approximation to $R_F(\lambda)$ is provided by $R_f(\lambda) = H_S(\lambda)/H_{CP}(\lambda)$, where $H_{CP}(\lambda)$ is the round-trip transmissivity of the coupler.

The effect of laser annealing on the reflectivity of the silicon film can be seen in Fig. 8.1, which gives $R_f(\lambda)$ of the silicon film of sensor 294, before and after it was laser annealed. The sensor reflectivities $R_f(\lambda)$ were modeled by using the methods described in the appendix to calculate $R_F(\lambda)$, which was then multiplied by a coefficient K_{FC}. This λ-independent scale factor approximated the transmissivity of the fiber-optic link exclusive of the coupler, i.e. $K_{FC} \approx H_{FO}(\lambda)/H_{CP}(\lambda)$.

Figure 8.2 shows the experimental $R_f(\lambda)$ for the silicon film of sensor 291, after it was laser annealed, together with the best fit that could be obtained by adjusting K_{FC} and the thickness of the silicon film L_1. The annealed silicon films were modeled using the optical properties of polycrystalline silicon that were measured in section 6. For each of the sensors, before and after annealing, $R_f(\lambda)$ was well fit by the model. The best

fits were obtained for sensors 291-3. Sensor 294 had a slightly reduced fringe visibility, most likely because the film thickness was nonuniform across the fiber core. The cut-on wavelengths at which interference fringes appear are, in each case, shifted by laser annealing by an amount which indicates that the silicon was fully crystallized.

Figure 8.3 shows the experimental and calculated $R_f(\lambda)$ for sensor 291, after the silicon film was encapsulated with the Si_3N_4 and aluminum layers. The dielectric function data of Phillip[1] and Alterowitz[2] were used to model the layers of Si_3N_4 and aluminum, respectively. The measured $R_f(\lambda)$ was fit by adjusting the thickness of the Si_3N_4 layer, L_2, while L_1 was fixed at the value determined prior to encapsulation. Table 8.1 shows the measured values of L_1 and L_2 of all four sensors. The sensed temperature was determined as a function of λ_m, the resonant wavelength of order m. The order of the monitored resonance was chosen so that it could be excited, throughout the entire temperature range, with the emission from an 830-nm-wavelength LED. Table 8.1 provides the values, at 20 °C, of λ_m, together with the fringe orders m, as determined from $m = 2n_1L_1/\lambda_m$. Table 8.1 also provides the interferometric fringe visibilities, η_{VIS}, which were measured after the sensors were spliced to fused-fiber couplers.

Table 8.1 Sensor characteristics measured at T = 20 °C.

Sensor	L_1, μm	L_2, nm	λ_m, nm	m	η_{VIS}
291	1.664	102	815.0	15	0.95
292	1.595	92	832.0	14	0.92
293	1.548	90	811.0	14	0.97
294	1.474	79	827.1	13	0.84

The large variations in the thicknesses of the films were caused by improper positioning of the sputter gun and the fixture holding the fibers. The fiber fixture was placed in the center of the sputtered flux, on the hub of the platen. When the sputtered flux and the fibers were shifted off the axis of rotation, the uniformity was much improved. For example, for sensors 131-134, which will be described later, the range of thicknesses was only $\pm$ 0.020 μm.

The sensor fibers were fusion spliced to 2 X 1 fused-fiber couplers that were specially fabricated for use at high temperatures. The couplers were constructed from fused-silica fibers with polyimide buffer coatings. The fused sections of fiber were encapsulated using high-temperature epoxy. This type

of coupler can withstand 200 °C for prolonged periods, so it could be mounted on the exterior of an aircraft engine. As discussed previously, the coupler and sensor fiber must be joined by a fusion splice. If a dematable connector were used, reflections from the fiber end faces would reduce the sensor's fringe visibility. The non-detachable coupler and sensor must be located in close proximity to facilitate aircraft maintenance.

The fiber-optic thin-film temperature sensors were inserted into an environmental testing chamber. The temperature of the air in the chamber was controlled to within ± 0.5 °C, as measured by a type K thermocouple. A pair of 10-m-long fibers, with SMA connectors, joined each sensor to the ~1-m input and output jumpers that were connected to the lamp and the scanning monochromator (fibers F1 and F2 of Fig. 6.8).

In general, prior to each measurement of $H_S(\lambda)$, the connections between the 10-m fibers and the input and output jumpers were remade, since all the the sensors were usually interrogated at each test condition. Thus, $H_S(\lambda)$ fluctuated from one measurement to the next. However, the λ-independent component of a $H_{FO}(\lambda)$ variation has no effect on the perceived

λ_m, and a λ-dependent change in $H_{FO}(\lambda)$ can be expected to have a small effect if the fringe visibility is sufficiently high, as will be discussed in section 8.5.

Figure 8.4 shows $H_S(\lambda)$ of sensor 292 at the extremes of the operating range, T = -55 °C and T = 278 °C, for 500 nm < λ < 1 μm. In this case, the connectors were not disturbed between the measurements. Once the sensors were spliced to couplers, the resonant wavelengths were determined from the minima in $H_S(\lambda)$. For the completed sensors, $H_S(\lambda)$ is similar in form to $R_f(\lambda)$, except the fused-fiber coupler attenuates $H_S(\lambda)$ in the vicinity of 620 nm. In the 800 to 900 nm range, where the sensor is interrogated, $H_{CP}(\lambda)$ of the fused-fiber coupler is relatively featureless, as is desired.

Figure 8.5 shows $H_S(\lambda)$ for sensor 292, at T = -55 °C and T = 278 °C, over a smaller wavelength range, 800 nm < λ < 900 nm. Again, the connectors were not disturbed between the measurements. For these wavelengths and temperatures, the absorption of the silicon film increases only moderately with increasing temperature (at shorter wavelengths, the absorption change is greater, as shown by Fig. 8.4). For this sensor, the 14th-order resonance is 828.4 nm at -55 °C, and it increases by 18.8 nm as the temperature increases to 278 °C. The total shift of λ_m is approximately 1/2 of

the interferometer's free spectral range of 36 nm. Therefore, almost a factor of 2 increase in L_1 could be accomodated without introducing any measurement ambiguity for the temperature range of -55 to 275 °C. Although $d\lambda_m/dT$ would be unaffected by an increase in L_1, the fringes would be sharpened, which could improve the resolution of λ_m. An increased L_1, however, requires a greater relative uniformity in L_1 across the fiber core in order to provide the same fringe visibility.

8.3 Sensor Calibration

To determine λ_m, the transmissivities $H_S(\lambda)$ were measured using a sampling interval of 0.1 nm. The resonant wavelengths were presumed to correspond to the local minima in the $H_S(\lambda)$ functions, which were located using the following algorithm:

(a) $H_S(\lambda)$ was searched through the range of λ_m for each sensor to locate the wavelength of the minimum value,

(b) a third-order polynomial was fit to $H_S(\lambda)$ in the ± 5 nm region about the minimum,

(c) λ_m was determined by calculating the position of the polynomial's minimum.

This method provided a much greater noise immunity than was obtained by using the minimum value of the unsmoothed $H_S(\lambda)$ data. A quadratic fit, although not extensively tested, was found to be effective as well. A detailed study of signal-processing algorithms is beyond the scope of this research project. This simple algorithm was found to provide a resolution which was adequate for the purposes of calibrating the sensors and assessing their stability.

The four sensors were calibrated by tracking $\lambda_m(T)$ over the -55 to 278 °C range. The normalized resonance shifts were defined to be $\gamma(T) = [\lambda_m(T)-\lambda_m(T_0)]/\lambda_m(T_0)$, where, by arbitrary definition, $T_0 = 96$ °C. Figure 8.6 shows that a quadratic function accurately fits the average of the four $\gamma(T)$ functions. A linear fit to $\gamma_{AVE}(T)$ provides $\kappa_\Phi = 6.9 \times 10^{-5}$/°C, where $\kappa_\Phi = \lambda_m^{-1} d\lambda_m/dT$. Since $\lambda_m \approx 830$ nm, $d\lambda_m/dT \approx 0.06$ nm/°C, which gives an approximate means to convert λ_m changes to changes in the measured temperature T_M.

The measured value of κ_Φ is somewhat lower than the value of $7.9 \times 10^{-5}/°C$ that was determined using the published material properties for single-crystal silicon. A lower thermo-optic coefficient, $n^{-1}dn/dT$, for polycrystalline silicon would account for this discrepancy. Figure 8.7 shows the deviations of each sensor's $\gamma(T)$ from the quadratic fit to $\gamma_{AVE}(T)$. It is apparently not possible to obtain a 2 °C accuracy by a single-point calibration, i.e. a measurement of $\lambda_m(T_0)$. However, if the four $\gamma(T)$ are independently fit using quadratic functions, then the maximum error is only 1.1 °C.

8.4 Effects of Connector Remating

Figure 8.8 shows how $H_S(\lambda)$ is changed by remating two of the fiber link's connectors. These measurements were performed using sensor 291 at T = 278 °C. The changes in $H_S(\lambda)$ are clearly somewhat wavelength dependent and therefore might be expected to influence the measured temperature T_M. The sensitivity of T_M to connector effects was determined by remating the connectors prior to each measurement of a fixed temperature. The principal cause of connector coupling variations is changes in the lateral misalignment of the fiber cores. For this test, the relative angular orientation of the mated ferrules (SMA connectors are not keyed) was changed with each

remating in order to maximize the variability. For each sensor, two connectors were remated prior to each of 20 measurements at a constant 20 °C. The T_M variations of all four sensors were similar so the results were combined. The deviations of T_M from the means are shown in Fig. 8.9, while Fig. 8.10 shows the relative variations of H_{FO}. The T_M deviations had an RMS value of 0.50 °C and a maximum of 1.4 °C, while the relative H_{FO} deviations had an RMS value of 7% and a maximum of 19%.

8.5 Effects of Wavelength-Dependent Changes in the Transmissivity of the Fiber Link

The effects on T_M of λ-dependent changes in the fiber-optic link's transmissivity $H_{FO}(\lambda)$ decrease with increasing interferometric fringe visibility. Since $\eta_{VIS} = \{[H_S]_{MAX}-[H_S]_{MIN}\}/\{[H_S]_{MAX}+[H_S]_{MIN}\}$, the fringe visibility attains its maximum value of unity if $H_S(\lambda_m) = 0$. Table 8.1 lists the fringe visibilities of the four sensors at λ = 830 nm and T = 20 °C. The effects of λ-dependent transmissivity changes were studied using the $H_S(\lambda)$ data for sensor 292 at 20 °C. The transmissivities of sensors with fringe visibilities ranging from 0.3 to 1.0 were modeled by adding the appropriate offsets to these $H_S(\lambda)$ data. Wavelength-dependent changes in the transmissivity of the

fiber-optic link were then simulated by multiplying each of the offset $H_S(\lambda)$ functions by

$$H_{VAR}(\lambda) = 1 + \alpha(\lambda - \lambda_0) \, . \qquad (1)$$

The slope α of this linear function of λ was varied over the range from -0.0125 to 0.0125 nm^{-1} for each value of η_{VIS}. Figure 8.11 shows examples of the modified $H_S(\lambda)$ functions. Here, η_{VIS} = 0.3 and 1.0, and α = -0.0125, 0, and 0.0125 nm^{-1}. For η_{VIS} = 0.3, the shifts in λ_m are apparent.

Figure 8.12 shows the changes in the measured temperature T_M as functions of α, for values of η_{VIS} ranging from 0.3 to 1.0. Since $\eta_{VIS} > 0.8$ for all four sensors, the errors caused by λ-dependent transmissivity changes are expected to be small, less than 1 °C, because the H_{FO} variations observed in practice typically have wavelength sensitivities much smaller than 0.0125 nm^{-1}.

8.6 Effects of Fiber Bending

Fiber bending has the potential to cause significant measurement errors because it can alter the distribution of power among the fiber modes, thereby

changing the effective angle of propagation in the thin-film interferometer. Typically, fiber bending is the most significant cause of changes in the modal power distribution. Changes in the lateral misalignment of the fiber cores within connectors should not change the modal distribution significantly, because the angles of incidence are not affected and the modes are attenuated equally as a function of the offset.

The effects of fiber bending were determined by wrapping the fiber fully around mandrels with radii ranging from 5 mm to 2 cm. This test was performed using sensor 292, at a constant temperature of 20 °C. Measured first were the effects of bending the coupler pigtail that is spliced to the sensor fiber. Figures 8.13 and 8.14 show the effects on T_M and on H_{FO}. Figures 8.15 and 8.16 show the effects on T_M and H_{FO} of bending the 10-m-long fiber that connects the light source to the coupler. In this case, the effects were smaller because the light passes through the bend only once. Also, the greater distance between the bend and the sensor may allow the re-establishment of the equilibrium modal distribution at the sensor.

Significant errors are produced only when the sensor fiber is bent with a radius less than 1.0 cm. The bend sensitivity of this sensor is therefore

entirely satisfactory, since bends with radii less than 1.0 cm should be avoided in any fiber-optic link because of the high losses and mechanical stresses that result. In these tests, one measurement was performed at each bend radius, and this procedure was then repeated four or five times, so the fibers did not lie in precisely the same positions for all the measurements at a given radius. From Figs. 8.13 and 8.15, the scatter in the T_M measurements, at a given bend radius, provides the short-term temperature resolution of this sensor, which is approximately ± 1 °C. This nonrepeatability is greater than the effect of a single fiber bend with a radius greater than 1.0 cm.

8.7 Long-Term Stability

The stabilities of sensors 291-294 were tested at a constant temperature of 278 °C for a total of 5600 hrs. The sensors were fully exposed to the air inside the environmental chamber. They were held in close proximity to each other and the reference thermocouple. The sensors were not pre-annealed and were characterized only at room temperature prior to this test. The environmental chamber was brought to the 278 °C soak temperature and allowed to stabilize for 24 hrs before the baseline $H_S(\lambda)$ measurements were performed. Subsequently, $H_S(\lambda)$ of each sensor was measured at intervals of

one week. The resonant wavelengths were determined using the method described in section 8.3. The shifts in λ_m, relative to the baseline values, were converted to changes in T_M using the measured value of κ_Φ, 6.9 x 10^{-5}/°C.

Figure 8.17 shows the long-term test results. Sensors 291 and 294 drifted excessively, although the rates of drift slowed significantly after ~2000 hrs. Sensors 292 and 293, however, were exceptionally stable. For these sensors, no long-term drift can be perceived, within the limits imposed by the measurement noise. Over the full duration of the test, the temperature measurements of sensors 292 and 293 had standard deviations of 0.8 and 0.6 °C, respectively. Since this test measures the aggregate effects of connector remating, fiber repositioning and prolonged thermal exposure, it is felt that an RMS value of 1 °C accurately represents the stability that these sensors can provide in practice.

After 2300 hrs, the experimental procedure was modified to include a test of the wavelength stability of the spectrometer. Each week, following the $H_S(\lambda)$ measurements, the spectrum of a fiber-coupled HeNe laser was measured and its wavelength, λ_{HeNe}, was determined by the procedure used to determine λ_m. Since the wavelength of the HeNe laser is essentially constant, the

variations in λ_{HeNe} reveal the instabilities of the spectrometer. The changes in T_M corresponding to the measured λ_{HeNe} variations are plotted in Fig. 8.18, together with the T_M changes of the most stable sensors, 292 and 293. These results show that the temperature resolutions of these sensors are limited by the wavelength instability of the fiber-coupled spectrometer.

The measurements of λ_{HeNe} and λ_m, shown in Fig. 8.18, are generally uncorrelated, except for one set of measurements, at 4800 hrs, when all the measured wavelengths are unusually high. The standard deviation of the λ_{HeNe} measurements, 0.42 nm, provides the the wavelength repeatability of the fiber-linked monochromator. The temperature measurements, therefore, can be expected to have a spectrometer-induced noise component of 0.7 °C, which is in fact the observed noise level. It may be possible to reduce the wavelength instability by using a monochromator which has a larger accceptance angle so that the highest-order modes are not extinguished. Also, a larger spectral bandwidth may be beneficial, as this would reduce the effects of mode-mode interference.

Prior to optimization of the laser-annealing process, sensors were fabricated using amorphous-silicon films which were fully relaxed by a 0.5 s

laser exposure (crystallization is obtained only after 1 s of laser annealing). In all other respects these sensors, 131-135, were identical to sensors 291-294, which were laser annealed for 2 s. Figure 8.19 shows the results of a stability test of these sensors at 278 °C. The outputs of the amorphous-silicon Fabry-Perot sensors drifted at a much greater rate than did the sensors fabricated using polycrystalline silicon. For the a-Si sensors, the T_M drift is negative, which indicates that the drift is most likely due to slow crystallization of the silicon.

After the testing of sensors 291-294 was completed, the sensor with the greatest long-term drift, sensor 291, was destructively examined. After removal of the aluminum layer by etching in photoresist developer, the Si_3N_4 layer was observed to be partially delaminated from the underlying silicon. A higher reliability may be attainable by modifying the Si_3N_4 deposition conditions in order to reduce the film stress. A somewat silicon-rich stoichometry has been shown to produce Si_3N_4 films with low residual stresses on GaAs.[3] Also, it would be preferrable to inspect the Si_3N_4 films before aluminum deposition to ensure that the films are free of embedded particles and pinholes. Depositing the aluminum immediately after the Si_3N_4, as was done here, saves only a little time but significantly reduces the reliability, since

pinholes and debris are commonly found in these downward-sputtered Si_3N_4 films.

8.8 Conclusion

In order to obtain a 2 °C accuracy, it was found necessary to separately calibrate each sensor throughout the entire temperature range. Improved control of the thicknesses of the films, however, has the potential to allow a single-point calibration. The temperature sensitivity of the resonant wavelength, $\kappa_\Phi = \lambda_m^{-1} d\lambda_m/dT$, was determined to be 6.9 x 10^{-5}/°C. The measured sensitivity of these polycrystalline-silicon Fabry-Perot interferometers is somewhat lower than the value that was determined using published properties of single-crystal silicon.

This type of sensor was shown to be capable of providing a stability of 1 °C. This RMS stability measurement takes into account the effects of connector remating, fiber bending, and prolonged exposure to an elevated temperature. This high degree of stability was exhibited by two of the four sensors that were tested. All four sensors had short-term stabilities of about

1 °C, but the outputs of two of the sensors drifted slowly when tested at the maximum temperature.

The output of the least stable sensor drifted by 10 °C during 5600 hrs of exposure to 278 °C. Afterwards, it was determined that the Si_3N_4 film of this sensor was partially delaminated from the silicon. This indicates that further work is required to reduce the film stress. Further work should also be directed at reducing the short-term instability of these sensors. The dominant noise source was determined to be the wavelength instability of the fiber-coupled spectrometer. By increasing the numerical aperture and the spectral bandwidth of the monochromator, mode-mode interference effects should be reduced, which should improve the stability of the spectral analysis system.

8.9 References

1. H.R. Phillip, "Optical Properties of Silicon Nitride," J. Electrochem. Soc. 120, 295 (1973).

2. S. Alterowitz, unpublished data provided with WVASE software.

3. T. Carriere, B. Agius, I. Vickridge, J. Siejka, and P. Alnot, "Characterization of Silicon Nitride Films Deposited on GaAs by RF Magnetron Cathodic Sputtering," J. Electrochem. Soc. 137, 1582 (1990).

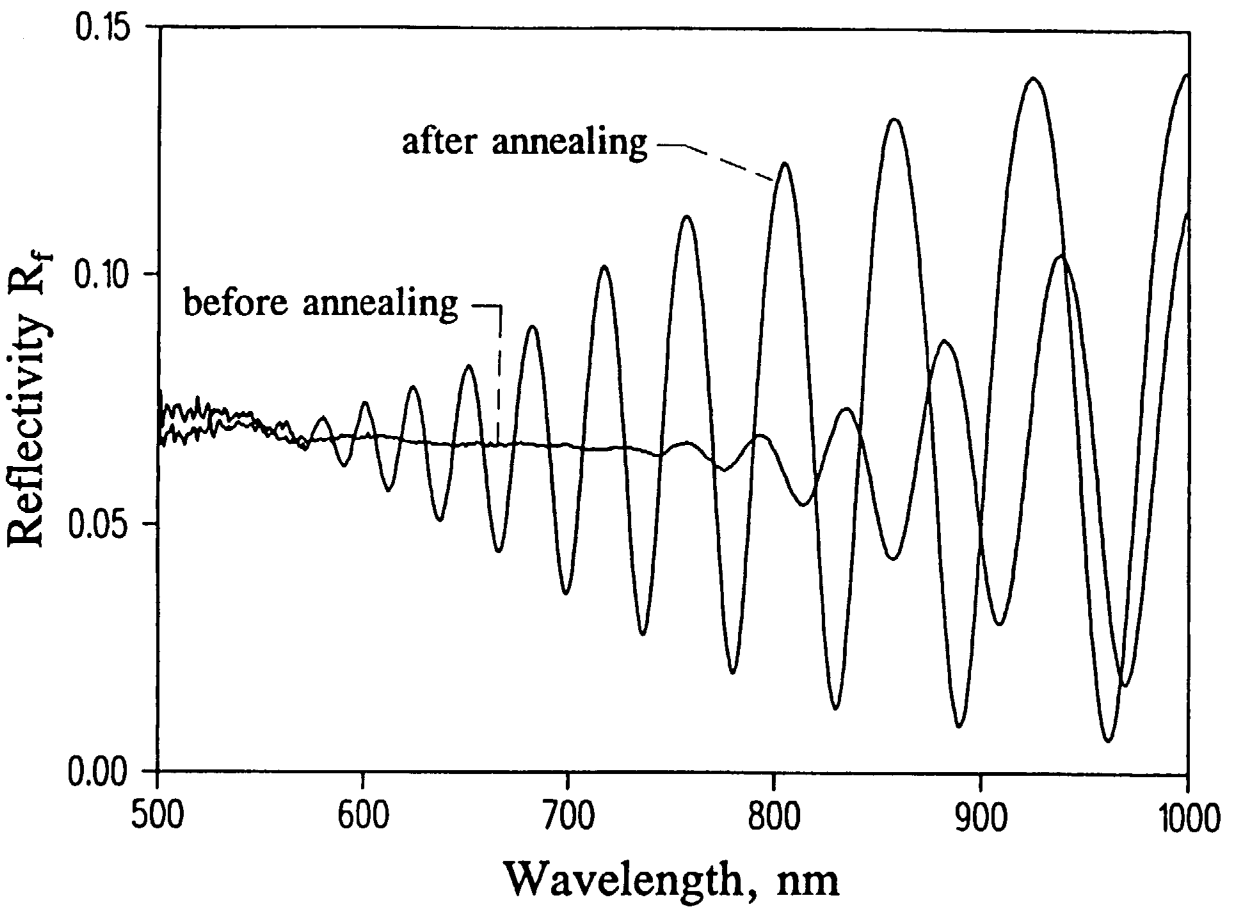

Figure 8.1 Reflectivity $R_f(\lambda)$ of silicon film on fiber end (sensor 294), as sputter-deposited and after laser annealing.

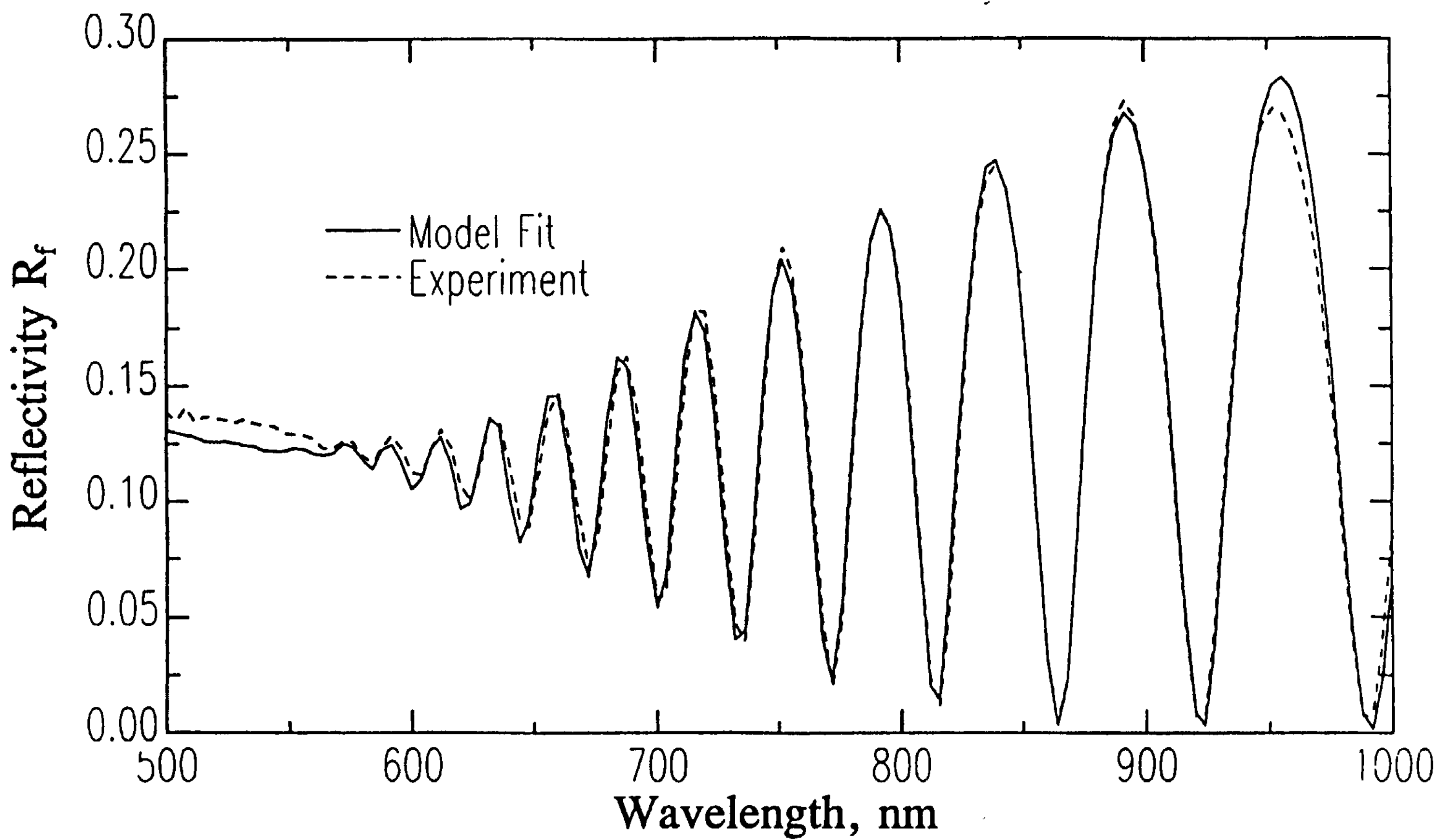

Figure 8.2 Measured and calculated reflectivities $R_f(\lambda)$ of laser-annealed silicon on fiber end (sensor 291).

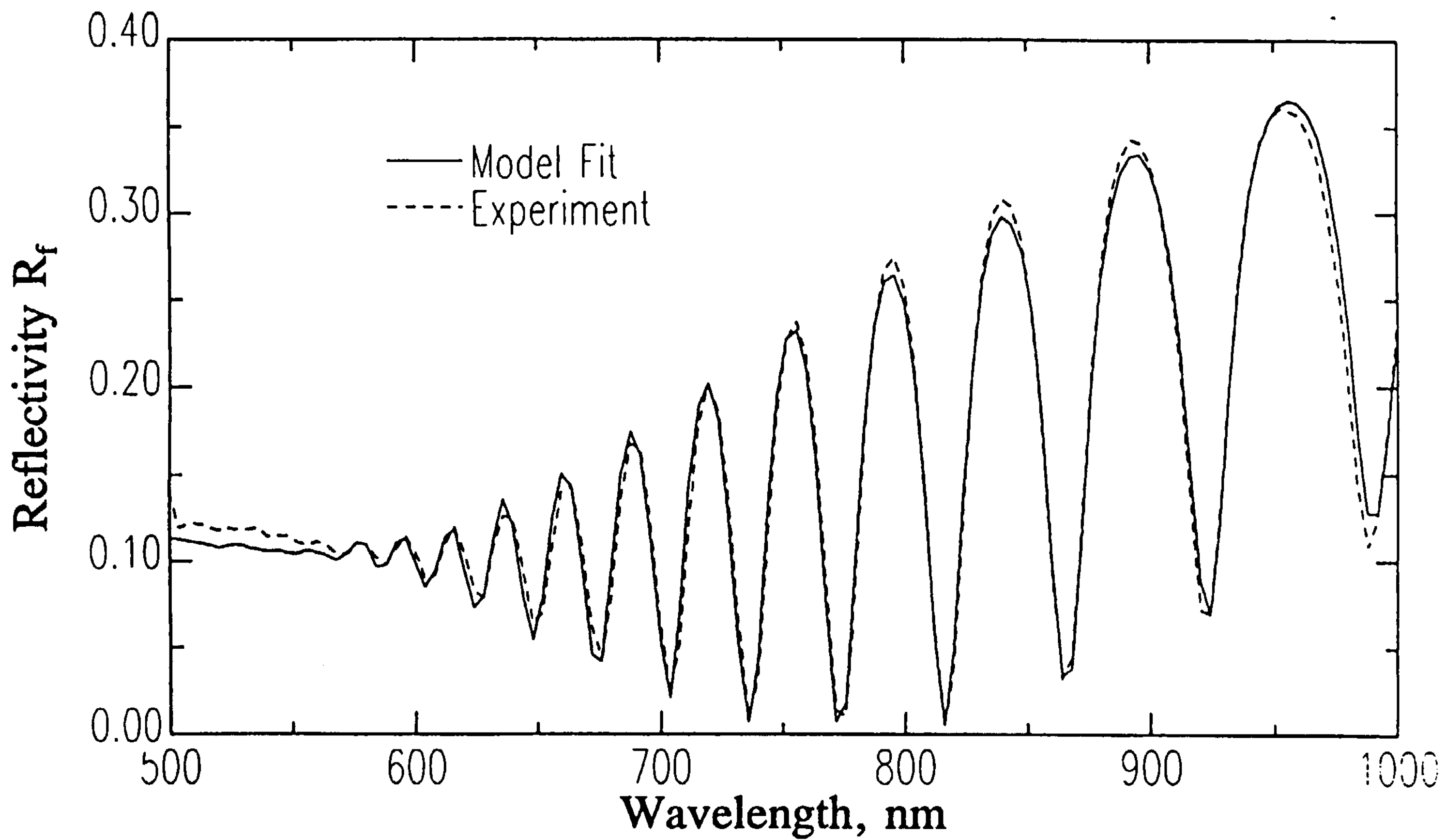

Figure 8.3 Measured and calculated reflectivities $R_f(\lambda)$ of laser-annealed silicon on fiber end after encapsulation with Si_3N_4 and aluminum (sensor 291, fully fabricated).

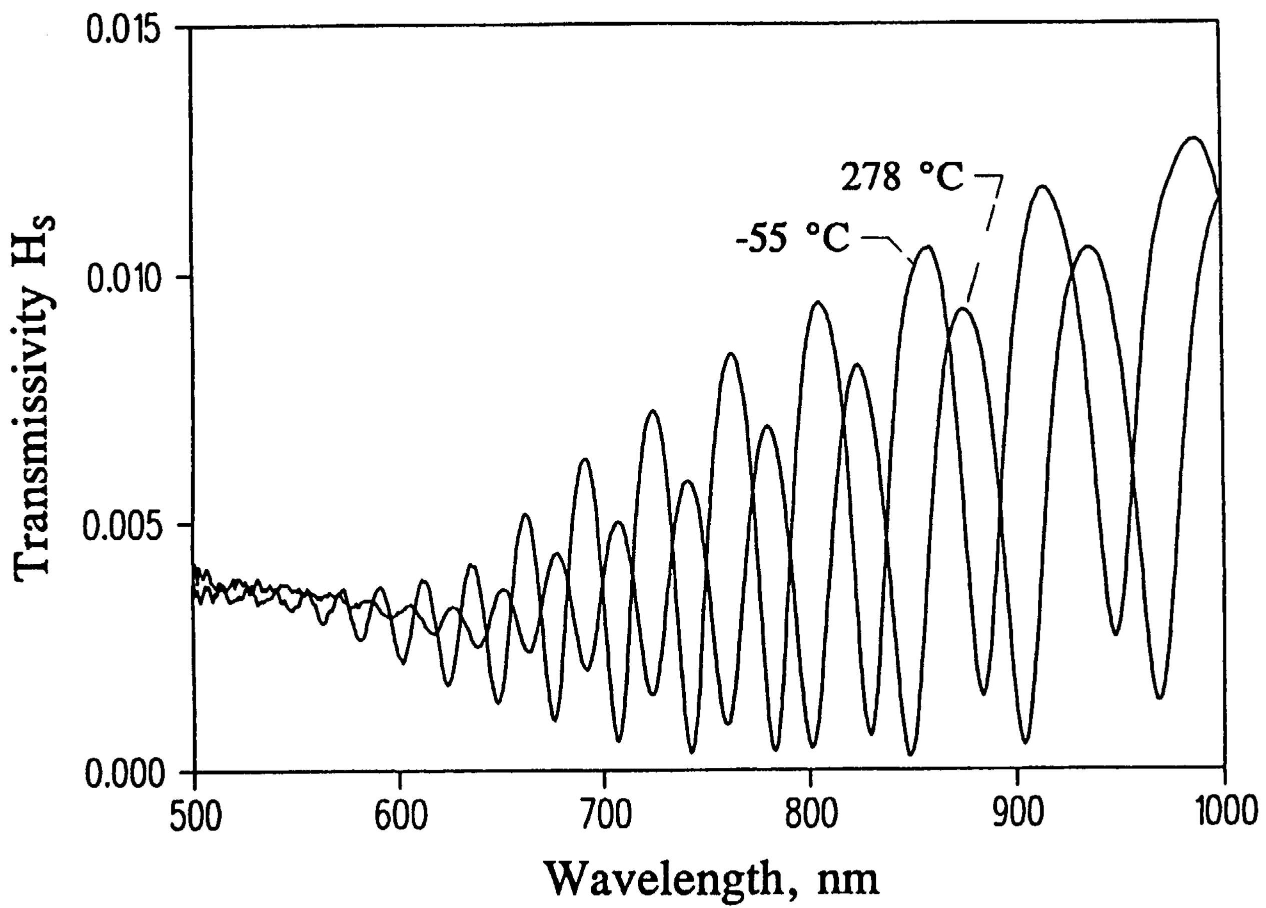

Figure 8.4 Transmissivities $H_s(\lambda)$ of sensor 293 at -55 °C and 278 °C for 500 nm $< \lambda <$ 1 μm.

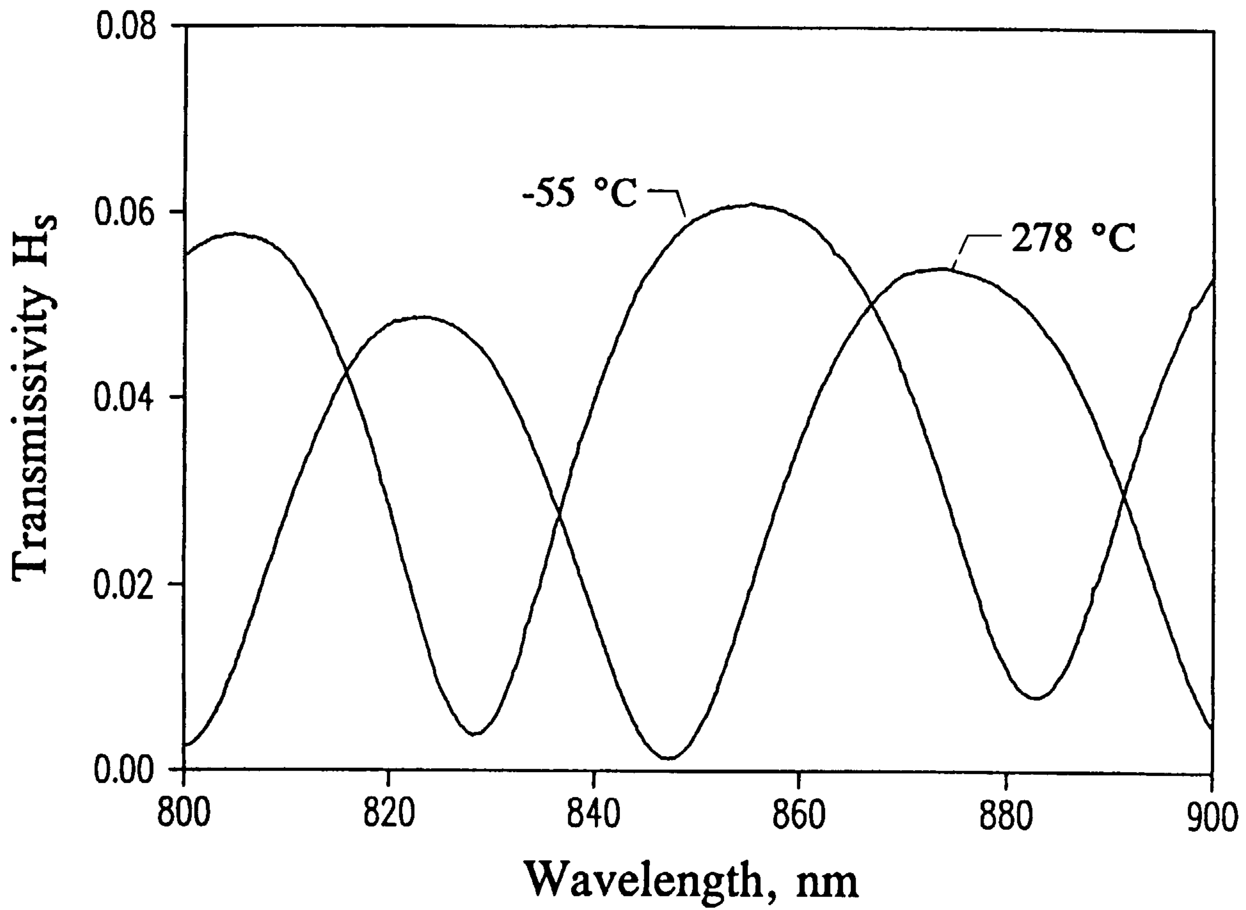

Figure 8.5 Transmissivities $H_S(\lambda)$ of sensor 292 at -55 °C and 278 °C for $800 < \lambda < 900$ nm.

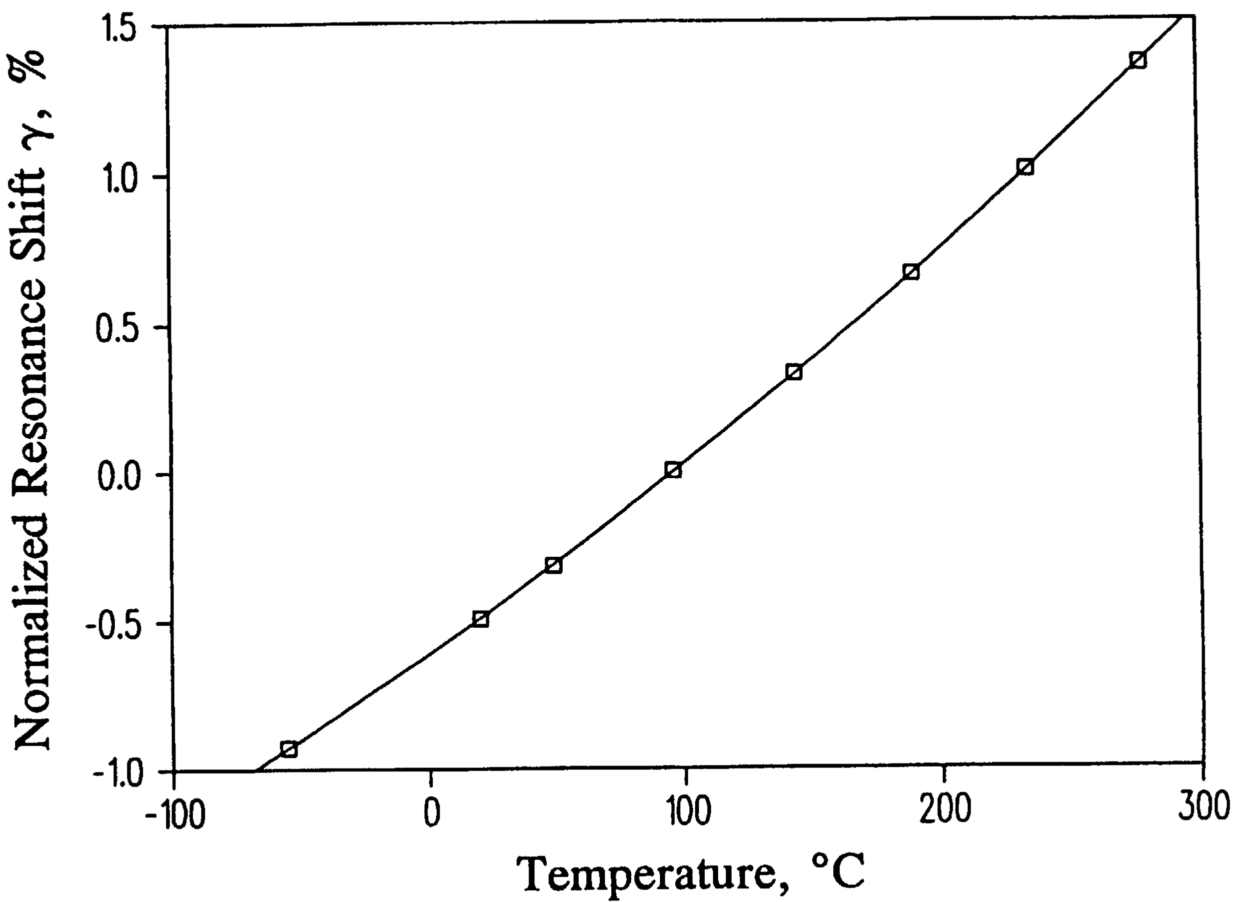

Figure 8.6 Average, for sensors 291-294, of the normalized resonance shifts $\gamma(T) = [\lambda_m(T)-\lambda_m(T_0)]/\lambda_m(T_0)$, where $T_0 = 96$ °C.

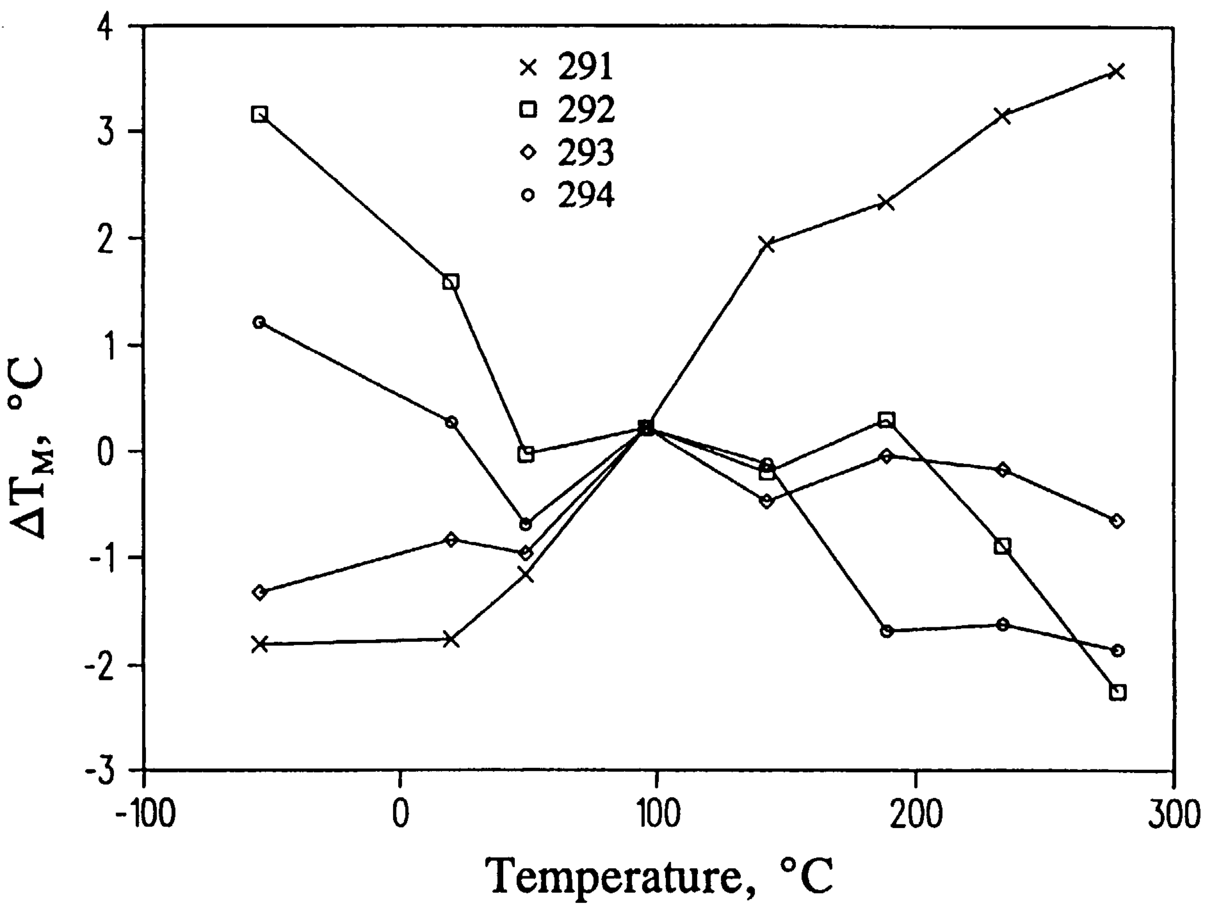

Figure 8.7 Deviations of the normalized resonance shifts $\gamma(T)$ from the quadratic fit to the average, expressed in terms of the measured temperature T_M.

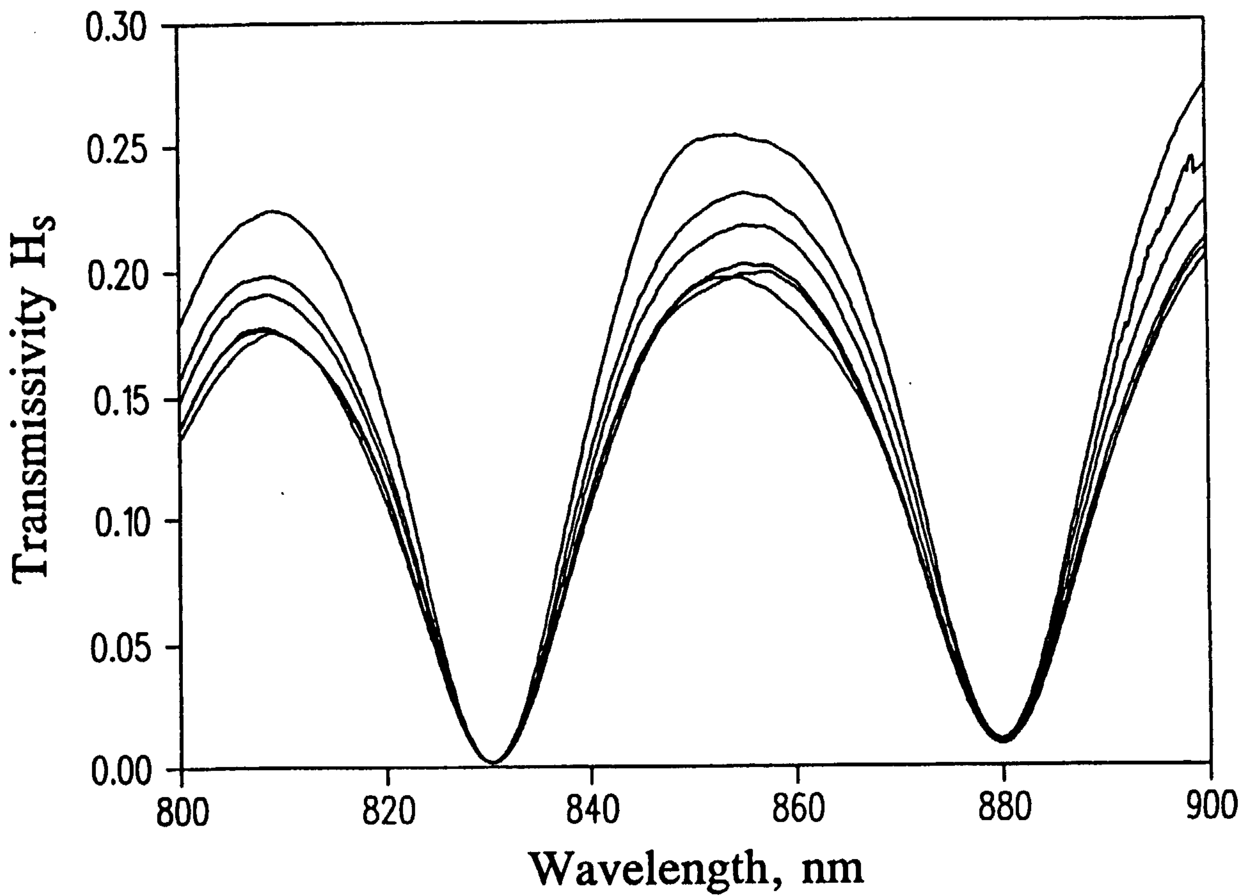

Figure 8.8 Transmissivities $H_S(\lambda)$ of sensor 291 at 278 °C showing effects of remating connectors.

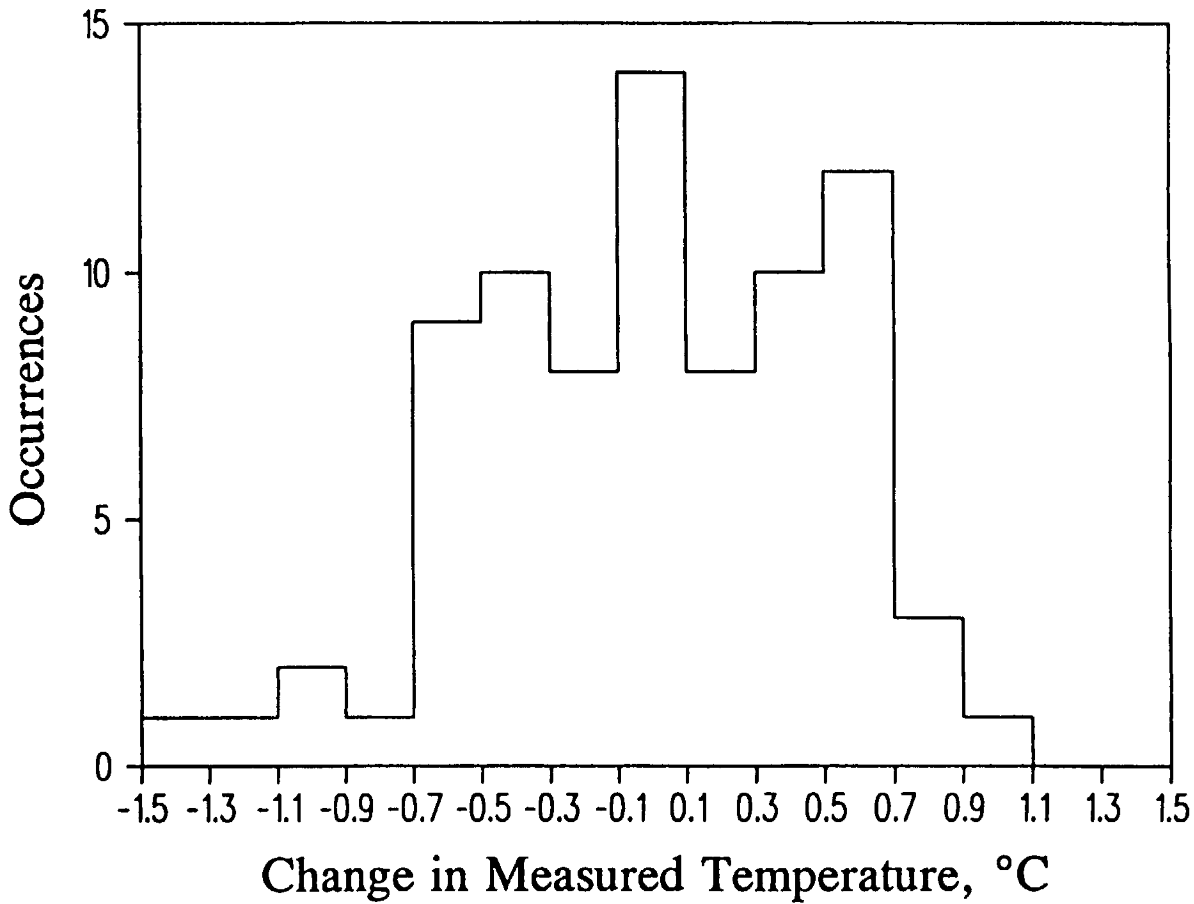

Figure 8.9 Deviations of the measured temperatures T_M from the mean values, at T = 20 °C, caused by remating the connectors (all four sensors).

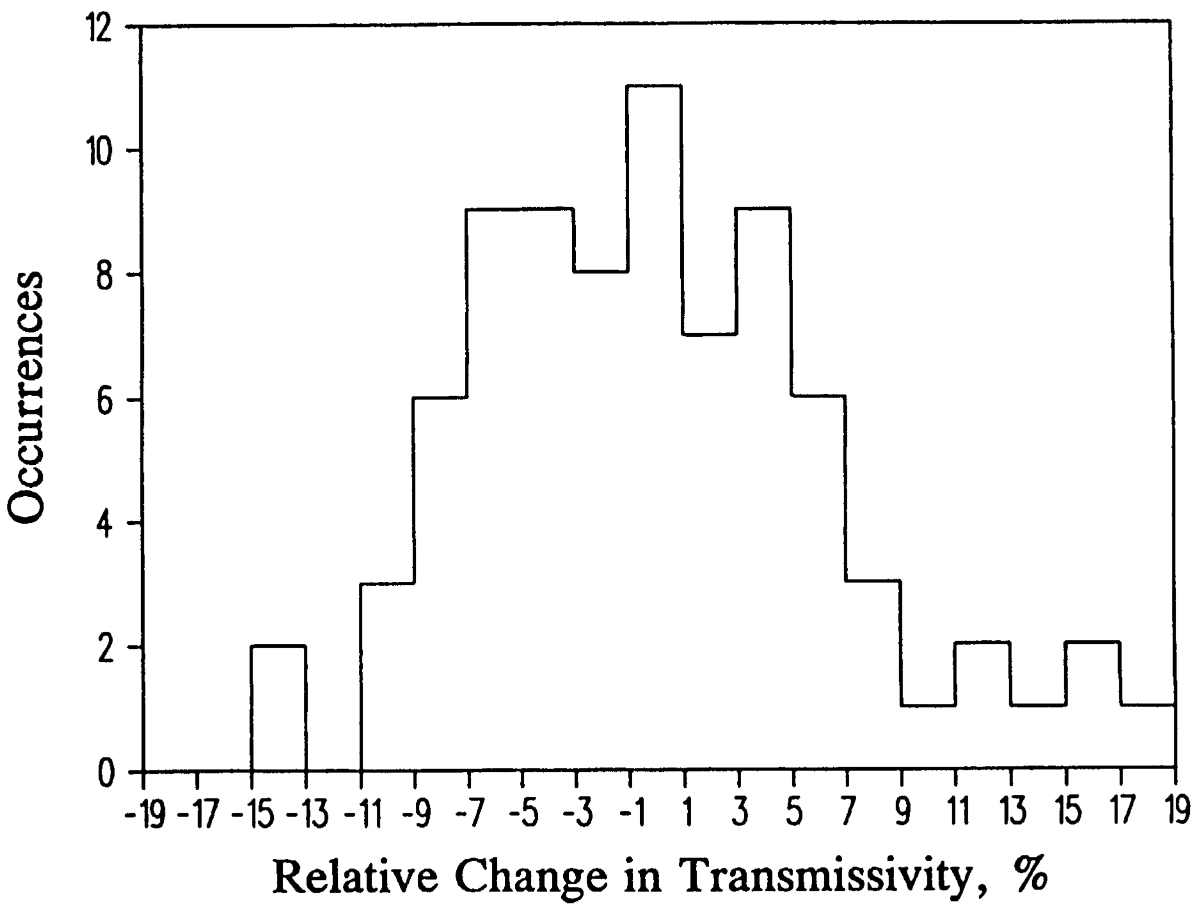

Figure 8.10 Variations in fiber-link transmissivities H_{FO}, relative to the means, caused by remating connectors.

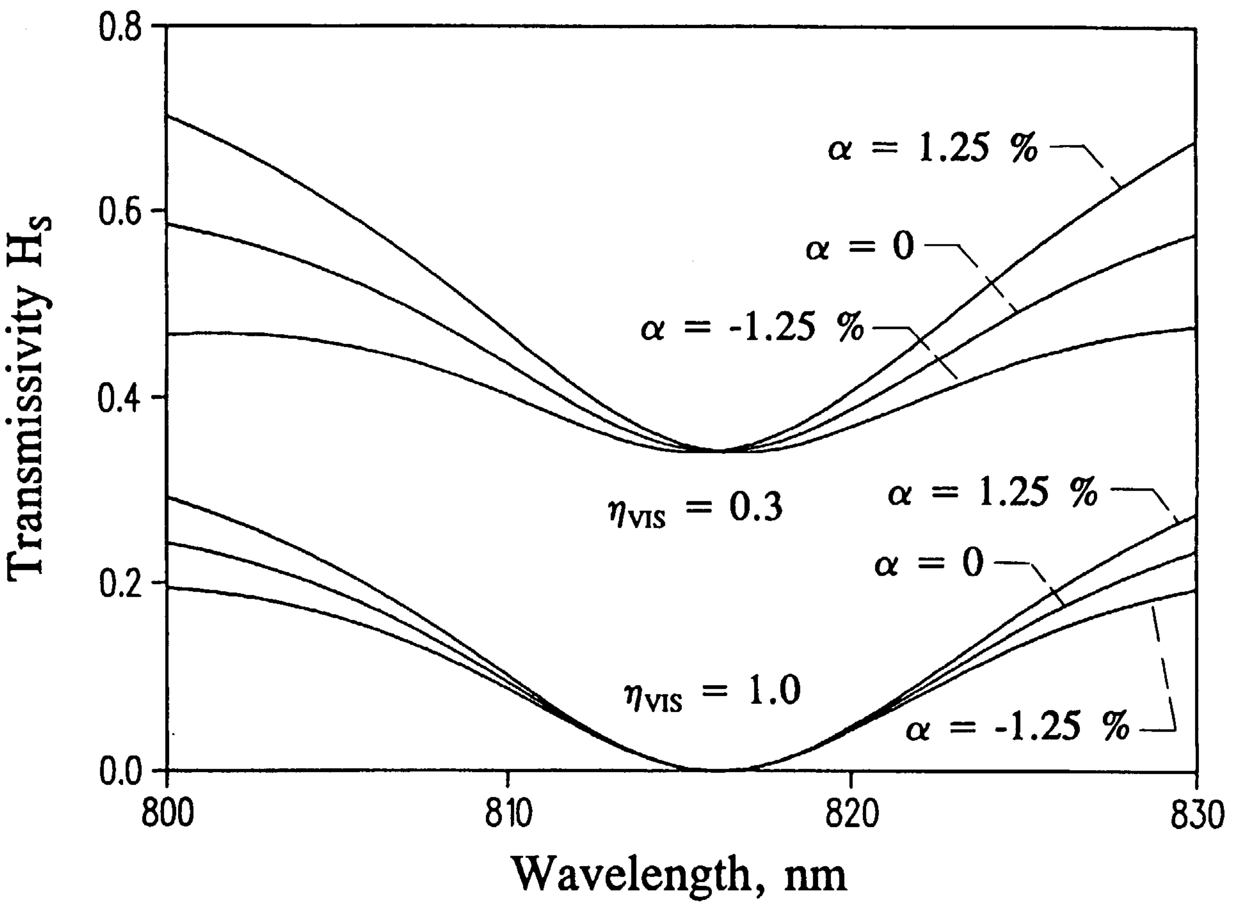

Figure 8.11 Calculated sensor transmissivities $H_S(\lambda)$ showing effects of wavelength-dependent transmissivity changes with different slopes α (in units of nm^{-1}) for sensors having different fringe visibilities η_{VIS}.

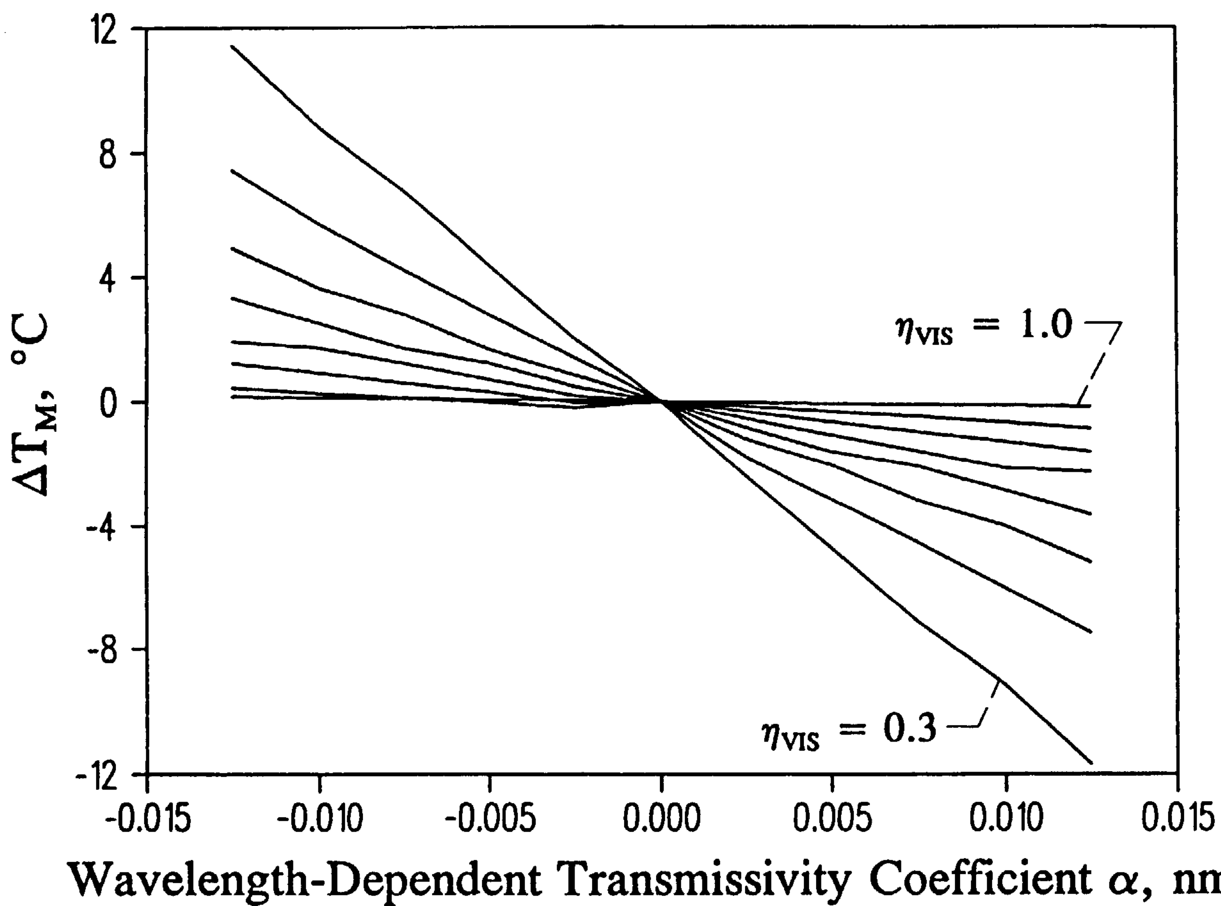

Figure 8.12 Changes in measured temperatures T_M caused by wavelength-dependent transmissivity changes for sensors having fringe visibilities η_{VIS} ranging from 0.3 to 1.0 in increments of 0.1.

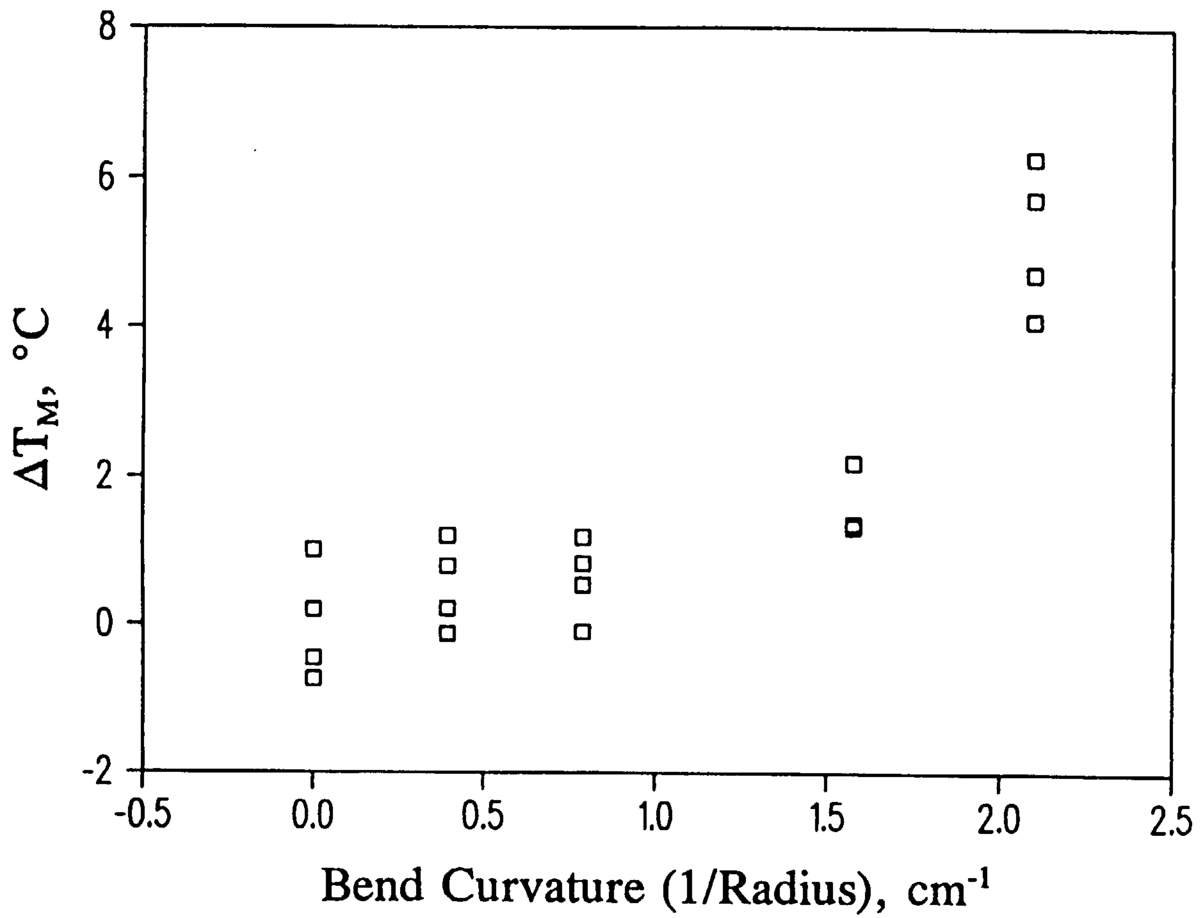

Figure 8.13 Changes in measured temperature T_M caused by bending sensor fiber.

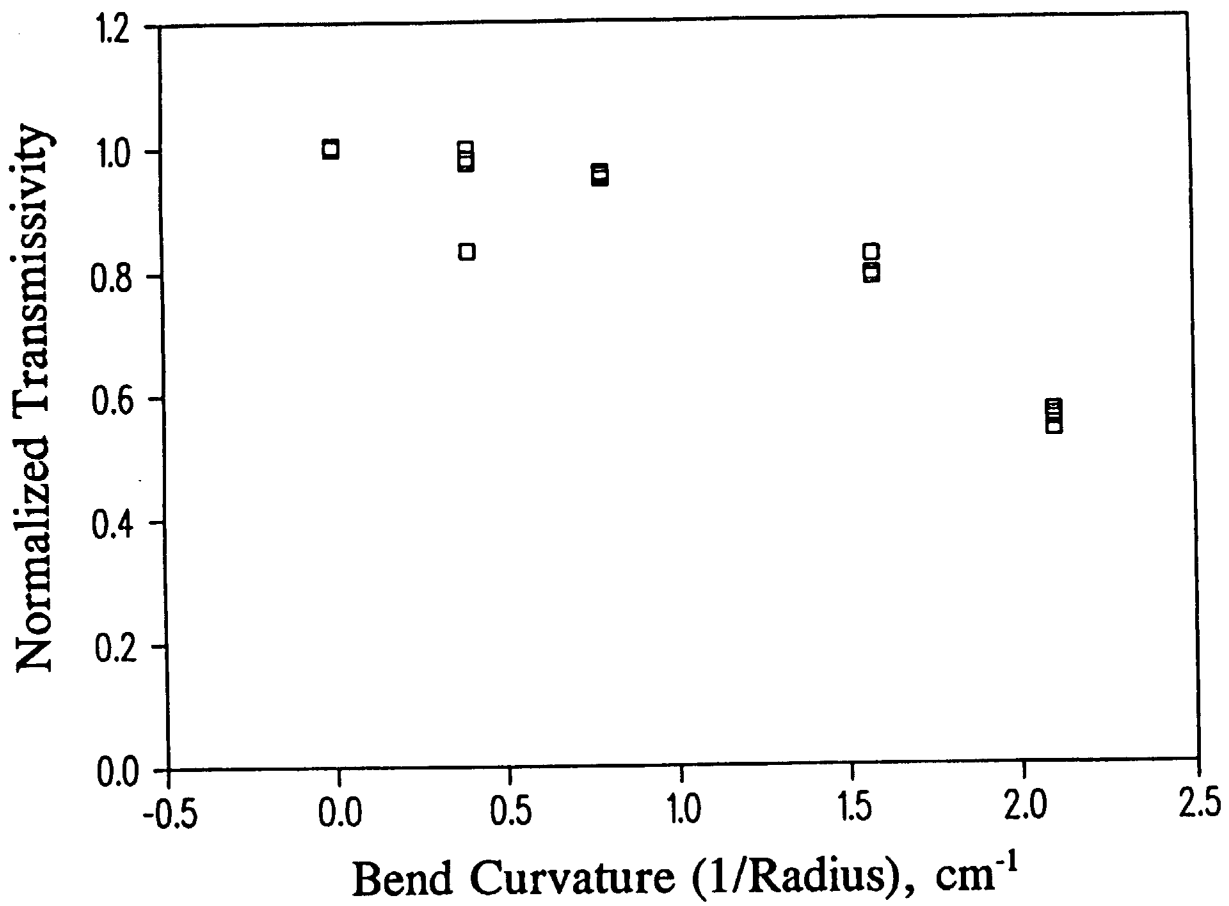

Figure 8.14 Changes in fiber-link transmissivity H_{FO} caused by bending sensor fiber.

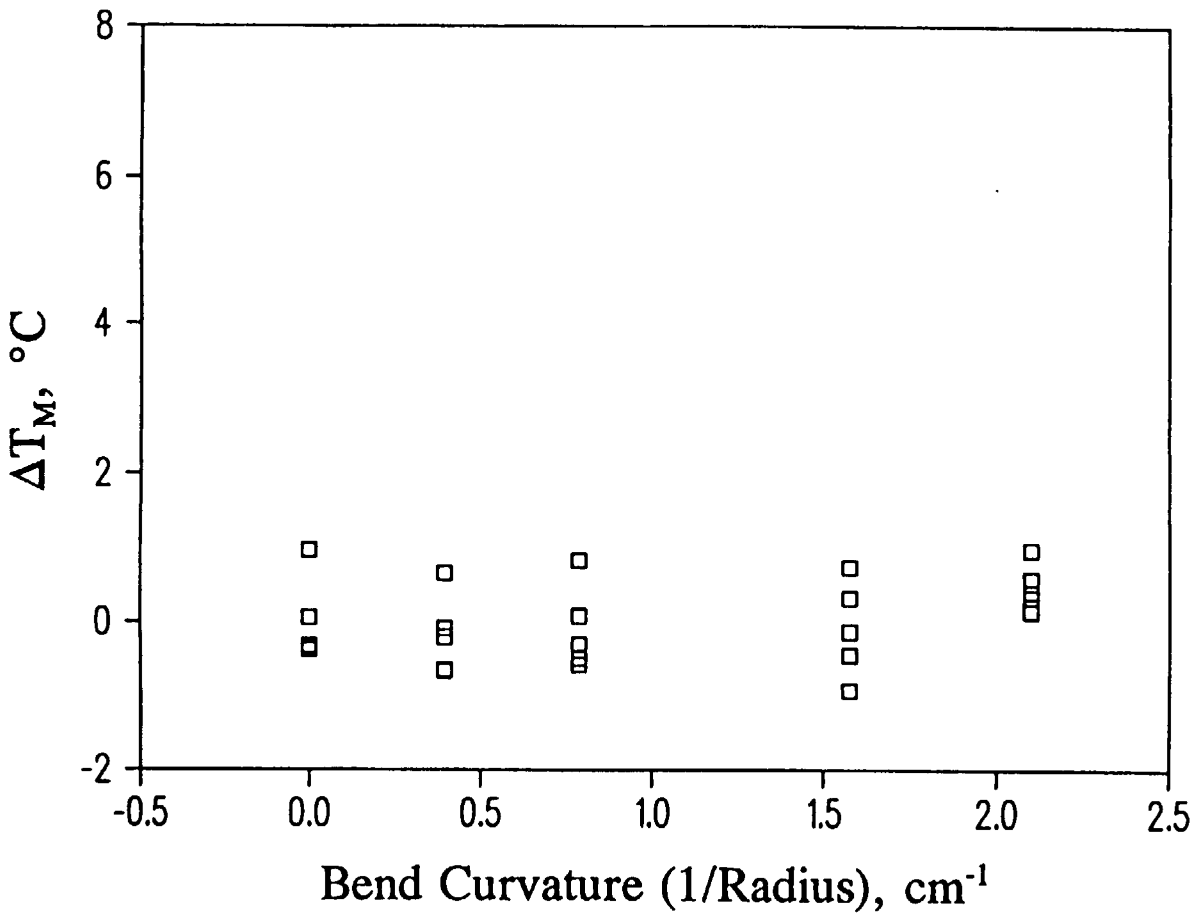

Figure 8.15 Changes in measured temperature T_M caused by bending input fiber.

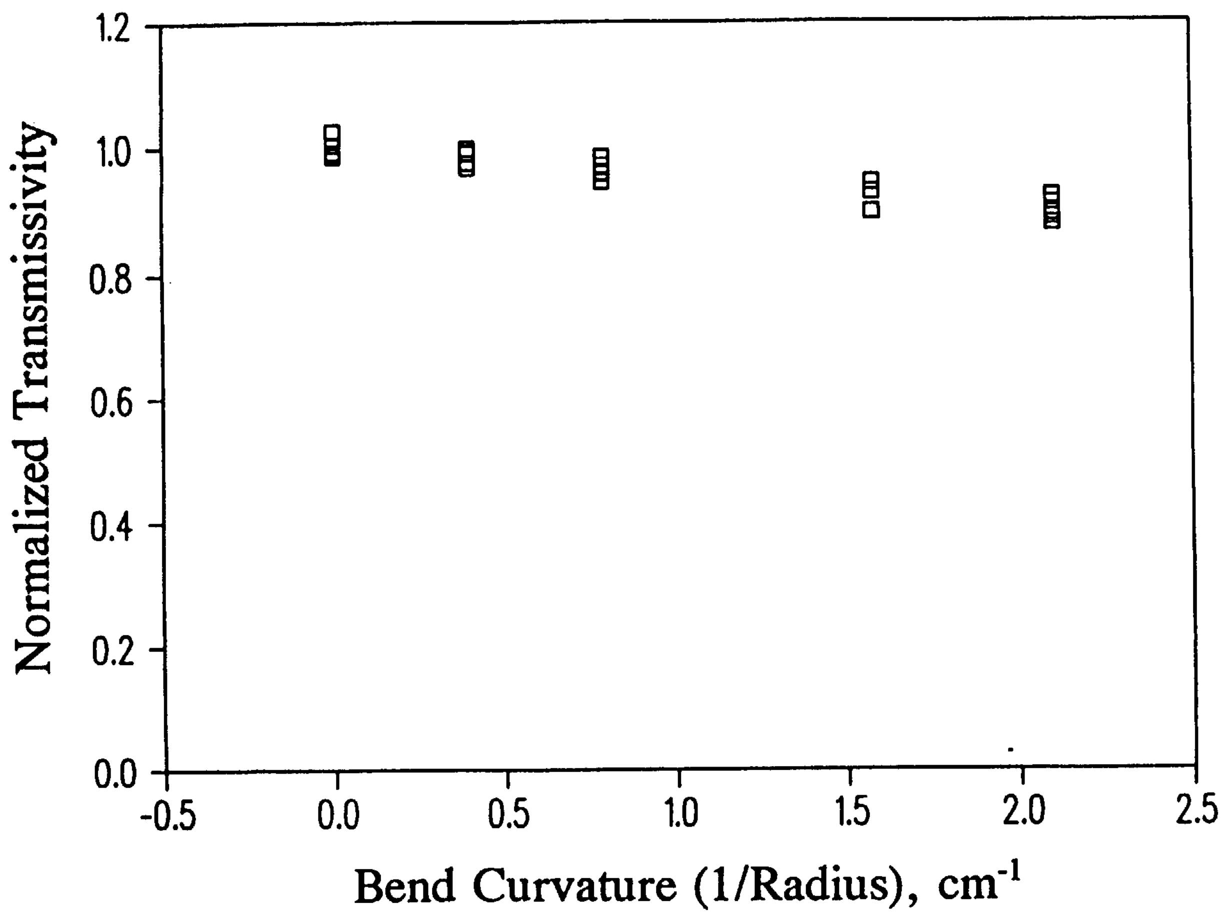

Figure 8.16 Changes in fiber-link transmissivity H_{FO} caused by bending input fiber.

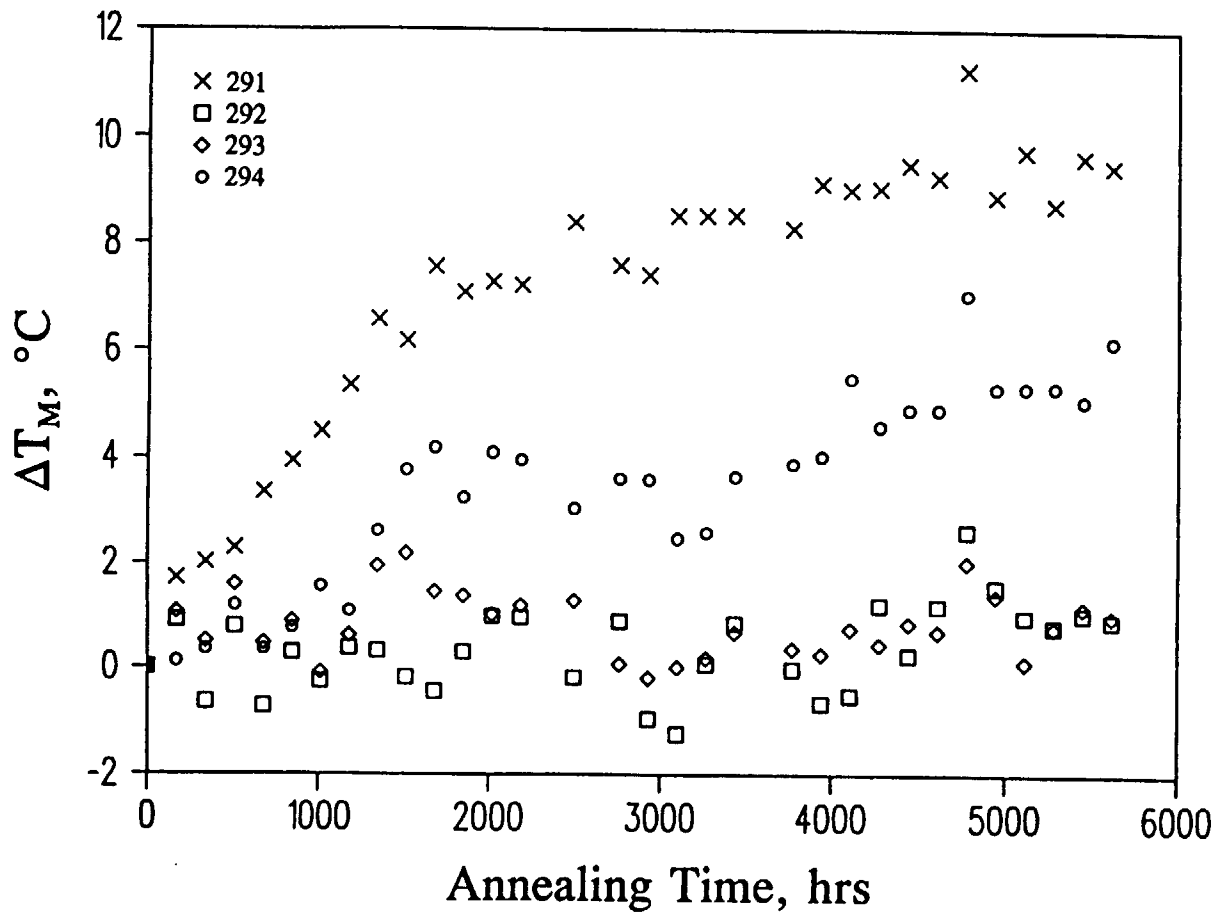

Figure 8.17 Changes in measured temperatures T_M as functions of time of exposure to 278 °C.

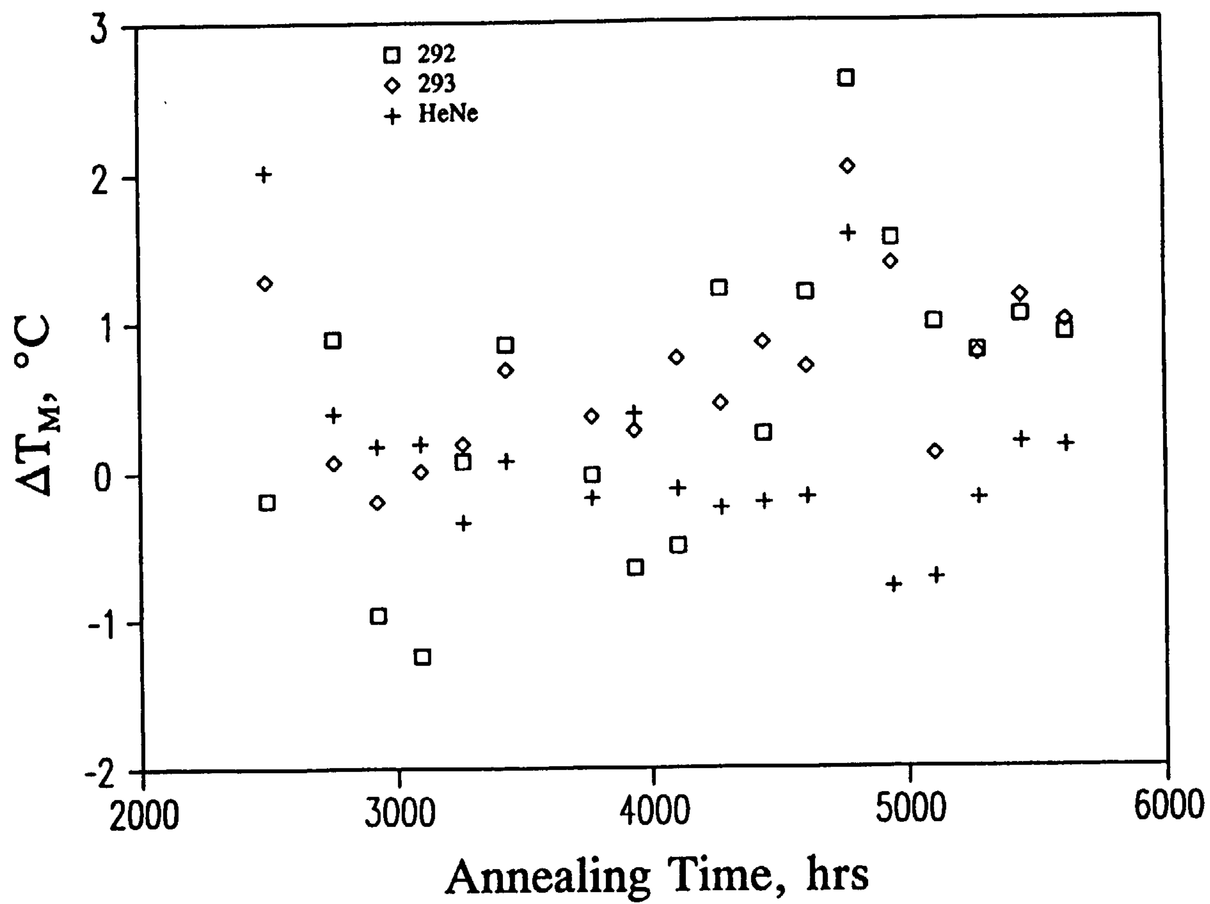

Figure 8.18 Changes in measured temperatures T_M that were calculated based on the changes in the resonant wavelengths of sensors 292 and 293 and the emission wavelength of the HeNe laser, as functions of time.

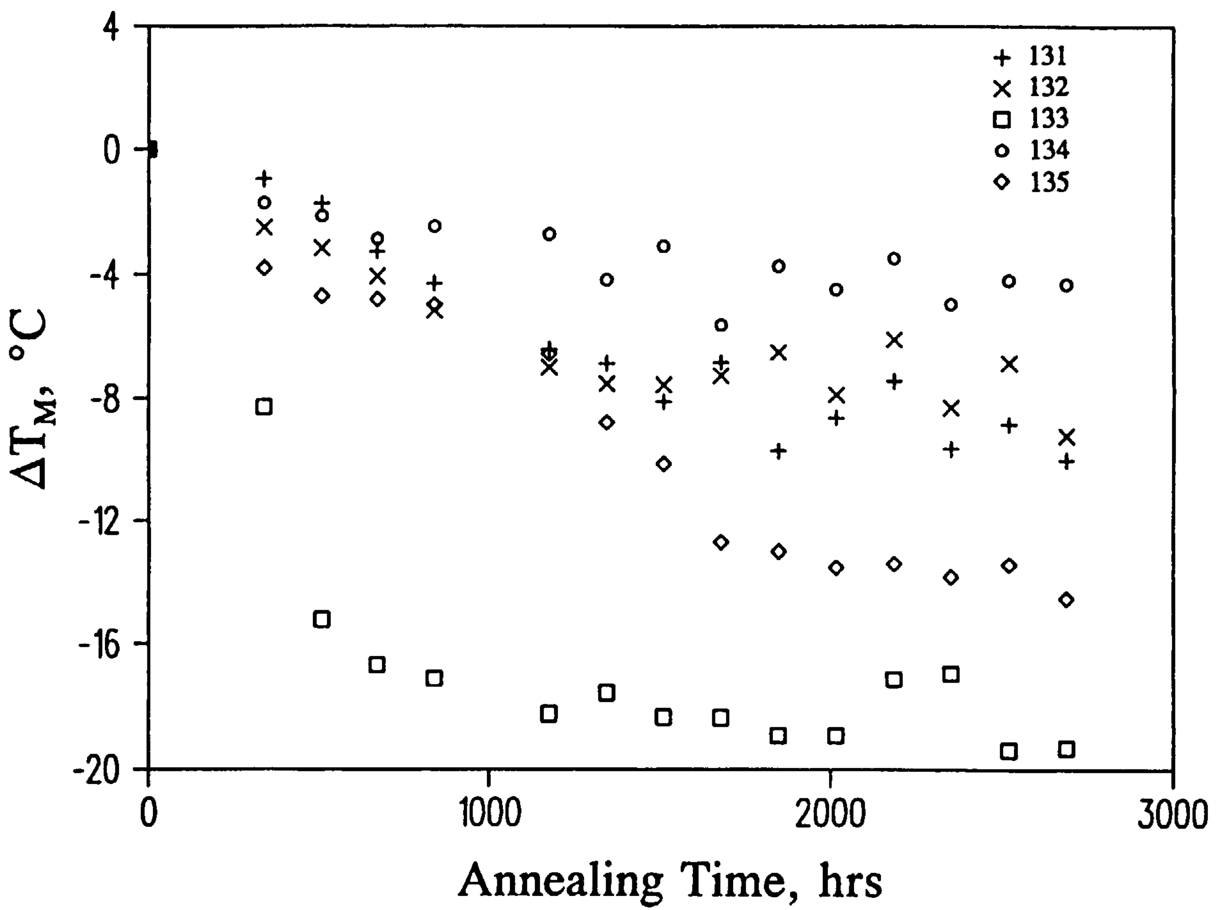

Figure 8.19 Changes in the measured temperatures T_M as functions of time of exposure to 278 °C for a-Si sensors (131-135).

9. CONCLUSION

A fiber-optic temperature sensor that uses a thin-film Fabry-Perot interferometer was shown to be capable of providing an accuracy of ± 2 °C over the temperature range of -55 to 275 °C, throughout a lifetime of 5000 hrs. This sensor, therefore, is well suited for the measurement of inlet-air temperatures in aircraft engine control systems.

A thin-film Fabry-Perot interferometer was deposited directly onto the end of an optical fiber. This approach provides for an extremely compact and rugged sensor that can be inexpensively fabricated using batch processes. Further, this sensor's wavelength-encoded output is not readily corrupted by transmission through optical fibers. The design of the sensor and the development of the fabrication process were largely directed towards overcoming the principle drawback of this approach, which is the tendency of thin films towards instability in severe environments. The sensor design also attempted to minimize short-term instabilities caused by disturbances to the fiber link such as connector remating and fiber bending.

Tests of four prototype sensors proved the soundness of the sensor design and the fabrication process, as outstanding stabilities were demonstrated. Short-term nonrepeatability, due to cable and connector effects, was 1 °C RMS. This measurement noise could be reduced by increasing the wavelength stability of the fiber-coupled spectrometer. Long-term drift was less than 1 °C, after 5000 hrs at 275 °C, for two of the four sensors. The yield of satisfactorily stable sensors could be increased by better inspection procedures and by modifying the Si_3N_4 deposition process to provide lower-stress films.

10. BIBLIOGRAPHY

Adams, A.C., "Dielectric and Polysilicon Film Deposition," in **VLSI Technology**, S.M. Sze, ed. (McGraw-Hill, New York, 1983).

Akhavan Leilabady, P. and M. Corke, "All-Fiber-Optic Remote Sensing of Temperature Employing Interferometric Techniques," Opt. Lett. 12, 772 (1987).

Angelidis, D. and P. Parsons, "Optical Micromachined Pressure Sensor for Aerospace Applications," Opt. Eng. 31, 1638 (1992).

Appels, J.A., E. Kooi, M.. Paffen, J.J. Schatorjé, and W.H.C.G. Verkuylen, "Local Oxidation of Silicon and its Application in Semiconductor-Device Technology," Phillips Res. Repts. 25, 118 (1970).

Aspnes, D.E., "Optical Properties of Thin Films," Thin Solid Films 89, 249 (1982).

Aspnes, D.E. and A.A. Studna, "Dielectric Functions and Optical Parameters of Si, Ge, GaP, GaAs, GaSb, InP, InAs, and InSb from 1.5 to 6.0 eV," Phys. Rev. B 27, 985 (1983).

Aspnes, D.E., A.A. Studna, and E. Kinsbron, "Dielectric Properties of Heavily Doped Crystalline and Amorphous Silicon From 1.5 to 6.0 eV," Phys. Rev. B 29, 768 (1984).

Aspnes, D.E. and J.B. Theeten, "Dielectric Function of Si-SiO_2 and Si-Si_3N_4 Mixtures," J. Appl. Phys. 50, 4928 (1979).

Aspnes, D.E. and J.B. Theeten, "Spectroscopic Analysis of the Interface Between Si and Its Thermally Grown Oxide," J. Electrochem. Soc. 127, 1359 (1980).

Baeri, P. and S.U. Campisano, "Heat Flow Calculations," in **Laser Annealing of Semiconductors**, J.M. Poate and J.W. Mayer, eds. (Academic Press, New York, 1982).

Bagley, B.G., D.E. Aspnes, A.C. Adams, and C.J. Mogab, "Optical Properties of Low-Pressure Chemically Vapor Deposited Silicon over the Energy Range 3.0-6.0 eV," Appl. Phys. Lett. 38, 56 (1981).

Bagley, B.G., D.E. Aspnes, G.K. Celler, and A.C. Adams, "Optical Characterization of Chemically Vapor Deposited and Laser-Annealed Polysilicon," in **Laser and Electron-Beam Interactions with Solids,** B.R. Appleton and G.K. Celller, eds. (North Holland, New York, 1982).

Ballard, S.S., K.A. McCarthy, W.L. Wolfe, "Optical Materials for Instrumentation," University of Michigan Report No. 2389-11-S (1959).

Bauer, K.A., S. Gerson, D.M. Griffith, A.K. Trikha, and E.J. Woods, "Fly-By-Light/Power-By-Wire Integrated Requirements Analysis and Preliminary Design--Boeing Results," NASA CR-4590 (1994).

Beheim, G., "Fiber-Optic Thermometer Using Semiconductor-Etalon Sensor," Electron. Lett. 22, 238 (1985).

Beheim, G. and K. Fritsch, "Spectrum-Modulating Fiber-Optic Sensors for Aircraft Control Systems," NASA TM-88968 (1987).

Beheim, G., K. Fritsch, and D.J. Anthan, "Fiber-Optic Temperature Sensor Using a Spectrum-Modulating Semiconductor Etalon," in **Fiber Optic and Laser Sensors** V, R.P. DePaula and E. Udd, eds., Proc. SPIE 838, pp. 238-246 (1987).

Beheim, G., K. Fritsch, J.M. Flatico, and M. Tabib-Azar, "Silicon-Etalon Fiber Optic Temperature Sensor," in **Fiber Optic and Laser Sensors VII**, E. Udd and R.P. DePaula, eds., Proc. SPIE 1169, pp. 504-511 (1990).

Beheim, G., K. Fritsch, and M. Tabib-Azar, "Sputtered Thin-Film Fiber-Optic Temperature Sensor," Proceeding Sensors Expo, Cleveland, Ohio, September 12-14, 1989, paper #204B (Helmers Publishing, Peterborough, NH, 1989).

Beheim, G., K. Fritsch, and M. Tabib-Azar, "Sputtered Thin Film Fiber-Optic Temperature Sensor," Sensors Vol. 7, No. 1, January, 1990, pp. 37-43.

Beheim, G., J.L. Sotomayor, M.L. Tuma, and M. Tabib-Azar, "Fiber-Optic Temperature Sensor Using Laser Annealed Silicon Film," in **Integrated Optics and Microstructures II**, Proc. SPIE 2291, M. Tabib-Azar, D.L. Polla, and K.K. Wong, eds., pp. 92-98 (1994).

Berthold, J.W., S.E. Reed, and R.G. Sarkis, "Simple, Repeatable, Fiber Optic Intensity Sensor for Temperature Measurement," in **Fiber Optic and Laser Sensors VII**, E. Udd and R.P. DePaula, eds., Proc. SPIE 1169, pp. 512-520 (1990).

Berthold, J.W., S.E. Reed, and R.G. Sarkis, "Reflective Fiber Optic Temperature Sensor Using Silicon Thin Film," Optical Eng. 30, 524 (1991).

Bhattackaryya, A. and K.N. Ritz, "Grain Growth Studies in Polysilicon by Ar^{40} Ion Implantation and Thermal Annealing," J. Electrochem. Soc. 131, 2143 (1984).

Boreman, G., R. Walters, and D. Lester, "Fiber Optic Thin Film Temperature Sensor," in **Fiber Optic and Laser Sensors III**, E.L. Moore and O.G. Ramer, eds., Proc. SPIE 566, 312-316 (1986).

Born, M. and E. Wolf, **Principles of Optics** (Pergammon Press, London, 1959).

Brebec, G., R. Seguin, C. Sella, J. Bevenot, and J.C. Martin, "Diffusion du Silicium dans la Silice Amorphe," Acta. Metallurgica 28, 327 (1980).

Brixner, B., "Refractive Index Interpolation for Fused Silica," J. Opt. Soc. Am. 57, 674 (1967).

Cabrera, N. and N.F. Mott "Theory of the Oxidation of Metals," Rep. Prog. Phys. 12, 163 (1948-9).

Carriere, T., B. Agius, I. Vickridge, J. Siejka, and P. Alnot, "Characterization of Silicon Nitride Films Deposited on GaAs by RF Magnetron Cathodic Sputtering," J. Electrochem. Soc. 137, 1582 (1990).

Celler, G.K., "Laser Crystallization of Thin Si Films on Amorphous Insulating Substrates," J. Crystal Growth 63, 429 (1983).

Chao, H.C. and G.W. Neudeck, "Polysilicon Fabry-Perot Cavities Deposited With Dichlorosilane in a Reduced Pressure Chemical Vapor Deposition Reactor for Thermal Sensing," Electron. Lett. 30, 80 (1994).

Choi, D.J., D.B. Fischbach, and W.D. Scott, "Oxidation of Chemically-Vapor-Deposited Silicon Nitride and Single-Crystal Silicon," J. Am. Ceram. Soc. 72, 1118 (1989).

Christensen, D.A., "Temperature Measurement Using Optical Etalons," Annual Meeting of the Optical Society of America, Houston, Texas, October 15-18, 1974.

Christensen, D.A., "An Optical Etalon Temperature Probe for Biomedical Applications," 28th ACEMB, Paper D4a.1, Fairmont Hotel, New Orleans, Louisiana, Sept. 20-24, 1975.

Cocorullo, G. and I. Rendina, "Thermo-Optical Modulation at 1.5 μm in Silicon Etalon," Electron. Lett. 28, 83 (1992).

Cox, E.R. and B.E. Jones, "Fibre Optic Colour Sensors Based on Fabry-Perot Interferometry", **Fibre Optic Sensors** IEE CP-221 (IEE, London, 1983) pp. 122-126.

Dakin, J.P. and D.J. Pratt, "Distributed Optical Fibre Raman Temperature Sensor Using a Semiconductor Light Source and Detector," Electron Lett. 21, 570 (1985).

Deal, B.E., "Thermal Oxidation Kinetics of Silicon in Pyrogenic H_2O and 5% HCl/H_2O Mixtures," J. Electrochem. Soc. 125, 576 (1978).

Deal, B.E. and A.S. Grove, "General Relationship for the Thermal Oxidation of Silicon," J. Appl. Phys. 36, 3770 (1965).

DeBrabander, G.N., J.T. Boyd, and G. Beheim, "Integrated Optical Ring Resonator Wth Micromechanical Diaphragm for Pressure Sensing," IEEE Photonics Technol. Lett. 6, 671 (1994).

Dils, R.R., "High-Temperature Optical Fiber Thermometry," J. Appl. Phys. 54, 1198 (1983).

Driscoll, W.G., ed., **Handbook of Optics** (McGraw-Hill, New York, 1978).

Du, H., R.E. Tressler, and K.E. Spear, "Thermodynamics of the Si-N-O System and Kinetic Modeling of Oxidation of Si_3N_4," J. Electrochem. Soc. 136, 3210 (1989).

Du, H., R.E. Tressler, K.E. Spear, and C.G. Pantano, "Oxidation Studies of Crystalline CVD Silicon Nitride," J. Electrochem. Soc. 136, 1527 (1989).

Enomoto, T., R. Ando, H. Morita, and H. Nakayama, "Thermal Oxidation Rate of a Si_3N_4 Film ad Its Masking Effect Against Oxidation of Silicon," Japanese J. Appl. Phys. 17, 1049 (1978).

Fan, G.-J., F.H. Pollak, and R. Tsu, "Optical Properties of Disordered Silicon in the Range 1-10 eV," Solar Energy Materials 8, 241 (1982).

Farries, M.C., M.E. Fermann, R.I. Laming, S.B. Poole, D.N. Payne, and A.P. Leach, "Distributed Temperature Sensor Using Nd^{3+}-Doped Optical Fibre," Electron. Lett. 22, 418 (1986).

Fehlner, F.P., "Formation of Ultrathin Oxide Films on Silicon," J. Electrochem. Soc. 119, 1723 (1972).

Fehlner, F.P., "Low Temperature Oxidation of Metals and Semiconductors," J. Electrochem. Soc. 131, 1645 (1984).

Fernicola, V. and L. Crovini, "A High-Temperature Digital Fiber-Optic Thermometer," in **Tenth International Conference on Optical Fiber Sensors**, B. Culshaw and J.D.C. Jones, eds., Proc. SPIE 2360, pp. 211-214, 1994).

Fiorina, L., S. Mezetti, and P.L. Pizzolati, "Thermometry in Geothermal Wells: An Optical Approach," Appl. Opt. 24, 402 (1985).

Fogarassy, E., R. Stuck, M. Toulemonde, P. Siffert, J.F. Morhange, and M. Balanski, "Pulsed Laser Annealing of RF Sputtered Amorphous Si: H Films, Doped with Arsenic," in **Laser and Electron-Beam Interactions with Solids**, B.R. Appleton and G.K. Celler, eds. (Elsevier, 1982), pp. 553-558.

Forouhi, A.R. and I. Bloomer, "Optical Dispersion Relations for Amorphous Semiconductors and Amorphous Dielectrics," Phys. Rev. B 34, 7018 (1986).

Fourrier, A., A. Bosseboeuf, D. Bouchier, and G. Gautherin, "Thermal Oxidation in Wet Oxygen of Reactive Ion-Beam Sputter-Deposited Silicon Nitride Films," J. Electrochem. Soc. 138, 1084 (1991).

Fortner, J. and J.S. Lannin, "Radial-Distribution Functions of Amorphous Silicon," Phys. Rev. B39, 5527 (1989).

Fraser, D.B., "Metallization," in **VLSI Technology**, S.M. Sze, ed. (McGraw-Hill, New York, 1983).

Fredrickson, J.E., C.N. Waddell, W.G. Spitzer, and G.K. Hubler, "Effects of Thermal Annealing on the Refractive Index of Amorphous Silicon Produced by Ion Implantation," Appl. Phys. Lett. 40, 172 (1982).

Fried, M., T. Lohner, W.A.M. Aarnik, L.J. Hanekamp, A. van Silfhout, "Determination of Complex Dielectric Functions of Ion Implanted and Implanted-Annealed Amorphous Silicon by Spectroscopic Ellipsometry," J. Appl. Phys. 71, 5260 (1992).

Fritsch, K. and G. Beheim, "Wavelength-Division Multiplexed Digital Optical Position Transducer," Opt. Lett. 11, 1 (1986).

Giallorenzi, T.G., J.A. Bucaro, A. Dandridge, G.H. Sigel, Jr., J.H. Cole, S.C. Rashleigh, and R.G. Priest, "Optical Fiber Sensor Technology," IEEE J. Quantum Electron. QE-18, 626 (1982).

Glomb, W.L., Jr., "Electro-Optic Architecture (EOA) for Sensors and Actuators in Aircraft Propulsion Systems," NASA CR-182270 (1989).

Goodman, A.M. and J.M. Breece, "Thin Tunnelable Layers of Silicon Dioxide Formed by Oxidation of Silicon," J. Electrochem. Soc. 117, 982 (1970).

Goodnick, S.M., M. Fathipour, D.L. Ellsworth, and C.W. Wilmsen, "Effects of a Thin SiO_2 Layer on the Formation of Metal-Silicon Contacts," J. Vac. Sci. Technol. 18, 949 (1981).

Goodwin, C.A., "The Use of Silicon Nitride in Semiconductor Devices," Ceram. Eng. & Sci. Proc. 5, 109 (1985).

Grattan, K.T.V., A.W. Palmer, and C.A. Willson, "A Miniaturized Microcomputer-Based Neodymium 'Decay-Time' Temperature Sensor," J. Phys. E: Sci. Instrum. 20, 1201 (1985).

Grattan, K.T.V., R.K. Selli, and A.W. Palmer, "Phase Measurement Based Ruby Fluorescence Fiber Optic Temperature Sensor," **Optical Fiber Sensors, 1988 Technical Digest Series**, Vol. 2, pp. 490-494 (Optical Society of America, Washington, D.C. 1988).

Grimblot, J. and J.M. Eldridge, "Oxidation of Al Films," J. Electrochem. Soc. 129, 2369 (1982).

Guenther, K.H., "Microstructure of Vapor-Deposited Optical Coatings," Appl. Opt. 23, 3806 (1984).

Harbeke, G., L. Krausberger, E.F. Steigmeier, A.E. Widmer, H. Kappert, and G. Neugebauer, "Growth and Physical Properties of LPCVD Polycrystalline Silicon Films," J. Electrochem. Soc. 131, 675 (1984).

Harris, R.J., G.T. Johnston, G.A. Kepple, P.C. Krok, and H. Mukai, "Infrared Thermooptic Coefficient Measurement of Polycrystalline ZnSe, ZnS, CdTe, CaF_2, and BaF_2, Single Crystal KCl, and TI-20 Glass," Appl. Opt. 16, 436 (1977).

Hartl, J.C., E.W. Saaski, and G.L. Mitchell, "Fiber Optic Temperature Sensor Using Spectral Modulation," in **Fiber Optic and Laser Sensors V**, R.P. DePaula and E. Udd, eds., Proc. SPIE 838, pp. 257-261 (1987).

Heavens, O.S., **Optical Properties of Thin Solid Films** (Dover Publications, New York, 1965).

Hollahan, J.R. and R.S. Rossler, "Plasma Deposition of Inorganic Thin Films," in **Thin Film Processes**, J.L. Vossen and W. Kern, eds. (Academic Press, New York, 1978).

Hu, S.M. and L.V. Gregor, "Silicon Nitride Films by Reactive Sputtering," J. Electrochem. Soc. 114, 826 (1967).

Icenogle, H.W., B.C. Platt, W.L. Wolfe, "Refractive Indexes and Temperature Coefficients of Germanium and Silicon," Appl. Opt. 15, 2348 (1976).

Iida, O., T. Iwamura, K. Hashiba, Y. Kurosawa, "A Fiber Optic Distributed Temperature Sensor for High-Temperature Measurements," in **Temperature: Its Measurement and Control in Science and Industry**, J.F. Schooley, ed., Vol. 6, Part 2, pp. 745-749 (American Institute of Physics, New York, 1992).

Izutsu, M., A. Enokihara, and T. Sueta, "Integrated Optic Temperature and Humidity Sensors," J. Lightwave Technol. LT-4, 833 (1986).

Jackson, J.D., **Classical Electrodynamics**, 2nd Edition (John Wiley & Sons, New York, 1975).

James, K. and W. Quick, "Fiber-Optic, Fabry-Perot Temperature Sensor," NASA CR-174712 (1984).

James, K.A., W.H. Quick, and V.H. Strahan, "Analysis and Preliminary Design of Optical Sensors for Propulsion Control," NASA CR-159519 (1979).

James, K.A., W.H. Quick, and V.H. Strahan, "Optical Temperature Sensors for Propulsion Control Systems (Fabry-Perot)," NASA Report No. C81-341/201 (1981).

James, K.A., W.H. Quick, and V.H. Strahan, U.S. Patent 4,329,058 (11 May 1982).

Jellison, G.E., Jr., M.F. Chisholm, and S.M. Gorbatkin, "Optical Functions of Chemical Vapor Deposited Thin-Film Silicon Determined by Spectroscopic Ellipsometry," Appl. Phys. Lett. 62, 3348 (1993).

Jellison, G.E., Jr., and F.A. Modine, "Optical Functions of Silicon at Elevated Temperatures," J. Appl. Phys. 76, 3758 (1994).

Jensen, S.C., S.D. Tilstra, G.A. Barnabo, D.C. Thomas, and R.W. Phillips, "A Fiber Optic Temperature Sensor for Aerospace Applications," in **Fiber Optic Systems for Mobile Platforms**, N.E. Lewis and E.L. Moore, eds., Proc. SPIE 1369, pp. 87-95 (1990).

Johnson, L.M., F.J. Leonberger, and G.W. Pratt, Jr., "Integrated Optical Temperature Sensor," Appl. Phys. Lett. 41, 134 (1982).

Kakkad, R., J. Smith, W.S. Lau, and S.J. Fonash, "Crystallized Si Films by Low-Temperature Rapid Thermal Annealing of Amorphous Silicon," J. Appl. Phys. 65, 2069 (1989).

Kamigaki, J. and Y. Itoh, "Thermal Oxidation of Silicon in Various Oxygen Partial Pressures Diluted by Nitrogen," J. Appl. Phys. 48, 2891 (1976).

Kaufmann, M. and L. Shultheis, UK Patent Application GB 2,204,948A (11 May 1988).

Kist, R., S. Drope, and H. Wolfelshneider, "Fiber-Fabry-Perot (FFP) Thermometer for Medical Applications," **Second International Conference on Optical Fiber Sensors,** Proc. SPIE 514, pp. 165-170 (1984).

Knox, J.M., P.M. Marshall, and R.T. Murray, "Birefringent Filter Temperature Sensor," in **Optical Fibre Sensors,** IEE CP-221 (IEE, London, 1983) pp. 1-5.

Kyuma, K., S. Tai, T. Sawada and M. Nunoshita, "Fiber-Optic Instrument for Temperature Measurement," IEEE J. Quantum Electron. QE-18, 676 (1982).

Lee, C.E., R.A. Atkins, and H.J. Taylor, "Performance of a Fiber-Optic Temperature Sensor From -200 to 1050 °C," Opt. Lett. 13, 1038 (1988).

Lee, C.E. and H.F. Taylor, "Interferometric Optical Fiber Sensors Using Internal Mirrors," Electron. Lett. 24, 193 (1988).

Lee, C.E. and H.F. Taylor, "Fiber-Optic Fabry Perot Temperature Sensor Using a Low-Coherence Light Source," J. Lightwave Technol. 9, 129 (1991).

Lee, E.G., H.B. Im, and J.S. Roh, "Effects of Wet Oxidation on the Properties of Sub-10-nm-Thick Silicon Nitride Films," J. Am. Ceram. Soc. 74, 1563 (1991).

Lemons, R.A., M.A. Bosch, A.H. Dayem, J.K. Grogan, and M.M. Mankiewich, "Laser Crystallization of Si Films on Glass," Appl. Phys. Lett. 40, 469 (1982).

Li, H.H., "Refractive Index of Silicon and Germanium and its Wavelength and Temperature Derivatives," J. Phys. Chem. Ref. Data 9, 561 (1980).

Lu, W.J., A.J. Steckl, T.P. Chow, and W. Katz, "Thermal Oxidation of Sputtered Silicon Carbide Thin Films," J. Electrochem. Soc. 131, 1907 (1984).

MacLeod, P.S. and L.D. Hartsough, "High-Rate Sputtering of Aluminum for Metallization of Integrated Circuits," J. Vac. Sci. Technol. 14, 263 (1977).

Madan, A., P.G. LeComber, and W.E. Spear, "Investigation of Density of Localized States in A-Si using Field-Effect Technique," J. Non-Cryst. Solids 20, 239 (1976).

Malitson, I.H., "Interspecimen Comparison of the Refractive Index of Fused Silica," J. Opt. Soc. Am. 55, 1205 (1965).

Mariller, C. and M. Lequime, "Fiber-Optic White Light Birefringent Temperature Sensor," in **Fiber Optic Sensors II**, A.M. Scheggi, ed., Proc. SPIE 798, pp. 121-130 (1987).

Marple, D.T.E., "Refractive Index of GaAs," J. Appl. Phys. 35, 1241 (1964).

Martin, P.J., "Review of Ion-Based Methods for Optical Thin Film Deposition," J. Mater. Sci. 21, 1 (1986).

Mathewson, A.G. and H.P. Myers, Phys. Scr. 4, 291 (1970).

Matteson, S., P. Revesz, Gy. Farkas, J. Gyulai, and T.T. Sheng, "Epitaxial Regrowth of Ar Implanted Amorphous Si by Laser Annealing", J. Appl. Phys. 51, 2625 (1980).

McFarlane, G.G. and V. Roberts, "Infrared Absorption of Silicon Near the Lattice Edge," Phys. Rev. 98, 1865 (1955).

Mogab, C.J. and E. Lugujjo, "Backscattering Analysis of the Composition of Silicon-Nitride Films by RF Reactive Sputtering," J. Appl. Phys. 47, 1302 (1976).

Mogab, C.J., P.M. Petroff, and T.T. Sheng, "Effect of Reactant Nitrogen Pressure on the Microstructure and Properties of Reactively Sputtered Silicon Nitride Films," J. Electrochem. Soc. 122, 815 (1975).

Molarius, J.M., E. Kolawa, K. Morishita, M-A. Nicolet, J.L. Tandon, J.A. Leavitt, and L.C. McIntyre, Jr., "Tantalum-Based Encapsulants For Thermal Annealing of GaAs," J. Electrochem. Soc. 138, 834 (1991).

Morey, W.W., G. Meltz, and W.H. Glenn, "Bragg-Grating Temperature and Strain Sensors," **Optical Fiber Sensors Proceedings of the 6th International Conference**, H.J. Arditty, J.P. Dakin, and R.T. Kersten, eds. (Springer-Verlag, Berlin, 1989) pp. 526-531.

Morey, W.W., G. Meltz, and J.M. Weiss, "High Temperature Capabilities and Limitations of Fiber Grating Sensors," in **Tenth International Conference on Optical Fiber Sensors**, B. Culshaw and J.D.C. Jones, eds., Proc. SPIE 2360 pp. 234-237 (1994).

Movchan, B.A. and A.V. Deshishin, Fiz. Metalloved. 28, 653 (1969).

Murphy, K.A., M.F Gunther, A.M. Vengsarkar, and R.O. Claus, "Quadrature Phase-Shifted, Extrinsic Fabry-Perot Optical Fiber Sensors," Opt. Lett. 16, 273 (1991).

Ogata, H., K. Kanayama, M. Ohtani, K. Fujiwara, H. Abe, and H. Nakayama, "Diffusion of Aluminum into Silicon Nitride Films," Thin Solid Films 48, 333 (1978).

Ogbuji, L.U.T. and D.T. Jayne, "Mechanism of Incipient Oxidation of Bulk Chemical Vapor Deposited Si_3N_4," J. Electrochem. Soc. 140, 759 (1993).

Ohte, A., K. Akiyama and I. Ohno, "Optically-Powered Transducer with Optical-Fiber Data Link," in **Fiber Optic and Laser Sensors II**, E.L. Moore and O.G. Ramer, eds., Proc. SPIE 478, 33-38 (1985).

Okamoto, A. and T. Serikawa, "Magnetron-Sputtered Silicon Films for Gate Electrodes in MOS Devices," J. Electrochem. Soc. 134, 1479 (1987).

Ovren, C., M. Adolfsson, and B. Hok, "Fiber-Optic Systems For Temperature and Vibration Measurements in Industrial Applications," **Proc Int. Conf. on Optical Techniques in Process Control** (BRHA Fluid Engineering Publications, Cranfield, UK, 1983) pp. 67-81.

Palik, E.D., ed., **Handbook on Optical Constants of Solids** (Academic Press, Orlando, Florida, 1985).

Pawlewicz, W.T., "Influence of Deposition Conditions on Sputter-Deposited Amorphous Silicon," J. Appl. Phys. 49, 5595 (1978).

Petersen, K.E., "Silicon as a Mechanical Material," Proc. IEEE 70, 420 (1982).

Petuchowski, S.J., T.G. Giallorenzi, and S.K. Sheem, "A Sensitive Fiber-Optic Fabry-Perot Interferometer," IEEE J. Quantum. Electron. QE-17, 2168 (1981).

Phillip, H.R., "Optical Properties of Silicon Nitride," J. Electrochem. Soc. 120, 295 (1973).

Phillips, R.W. and S.D. Tilstra, "Design of a Fiber Optic Temperature Sensor for Aerospace Applications," in **Temperature: Its Measurement and Control in Science and Industry**, J.F. Schooley, ed., Vol. 6, Part 2, pp. 721-724 (American Institute of Physics, New York, 1992).

Pierce, D.T. and W.E. Spicer, "Electronic Structure of Amorphous Si from Photoemission and Optical Studies," Phys. Rev. B 5, 3017 (1972).

Pitt, G.D., P. Extance, R.C. Neat, D.N. Batchelder, R.E. Jones, J.A. Barnett and R.H. Pratt, "Optical-Fibre Sensors," IEE Proc. 132, Pt. J, 214 (1985).

Poppel, G.L. and W.M. Glasheen, "Electro-optic Architecture for Servicing Sensors and Actuators in Advanced Aircraft Propulsion Systems," NASA CR-182269 (1989).

Poppel, G.L., W.M. Glasheen, J.C. Russell, "Fiber Optic Control System Integration", NASA CR-179568 (1987).

Poumakis, D.J. and W.J. Davies, "Fiber Optic Control System Integration," NASA CR-179569 (1986).

Press, W.H., B.P. Flannery, S.A. Teukolsky, and W.T. Vetterling, **Numerical Recipes** (Cambridge University Press, Cambridge, 1989).

Primak, W., "Refractive Index of Silicon," Appl. Opt. 10, 759 (1971).

Quick, W.H., K.A. James, and J.E. Coker, "Fiber Optics Sensing Techniques," in **Fibre Optic Sensors**, IEE CP-221 (IEE, London, 1983) pp. 6-9.

Qiu, X. and E. Gyarmati, "Composition and Properties of SiN_x Films Produced by Reactive R.F. Magnetron Sputtering," Thin Solid Films 151, 223 (1987).

Raider, S.I., R. Flitsch, J.A. Aboaf, and W.A. Pliskin, "Surface Oxidation of Silicon Nitride Films," J. Electrochem. Soc. 123, 560 (1976).

Rand, M.J. and D.R. Wonsidler, "Optical Absorption as a Control Test for Plasma Silicon Nitride Deposition," J. Electrochem. Soc. 125, 99 (1978).

Roorda, S., J.S. Custer, W.C. Sinke, J.M. Poate, D.C. Jacobson, A. Polman, and F. Spaepen, "Structural Relaxation in Amorphous Silicon and the Role of Network Defects," Nucl. Instr. and Meth. B59/60, 344 (1991).

Ross, R.C. and R. Messier, "Microstructure and Properties of RF-Sputtered Amorphous Hydrogenated Silicon Films," J. Appl. Phys. 52, 5329 (1981).

Saaski, E. and J. Hartl, U.S. Patent 4,678,904 (7 July 1987).

Saaski, E.W. and J.C. Hartl, "Thin-Film Fabry Perot Temperature Sensors," in **Temperature: Its Measurement and Control in Science and**

Industry, J.F. Schooley, ed., Vol. 6, Part 2, pp. 731-734 (American Institute of Physics, New York, 1992).

Saaski, E.W., J.C. Hartl, G.L. Mitchell, R.A. Wolthuis, and M.A. Afromowitz, "A Family of Fiber Optic Sensors Using Cavity Resonator Microshifts," Technical Digest OFS '86: 4th International Conference on Optical Fiber Sensors, Tokyo, October 7-9, 1986, pp. 11-14 (Institute of Electronics and Communications Engineers of Japan, Tokyo, 1986).

Seal, D.W., T.L. Weaver, B.L. Kessler, C.A. Bedoya, R.E. Mattes, "Fiber Optic Control System Integration for Advanced Aircraft," NASA CR-191194 (1994).

Semjonov, S.L., M.M. Bubnov, E.M. Dianov, and A.G. Shchebunyaev, "Reliability of Aluminum Coated Fibers at High Temperature," in **Fiber Optics Reliability and Testing: Benign and Adverse Environments VI**, D.K. Paul and H.H. Yuce, eds., Proc. SPIE 2074, pp. 25-33 (1994).

Serikawa, T. and A. Okamoto, "Properties of Magnetron-Sputtered Silicon Nitride Films," J Electrochem. Soc. 131, 2928 (1984).

Shimizu, M., M. Shimoishizaka, and S. Yoshida, "Radiometric Temperature Measurement Using Infrared Optical Fibers," in **Second International Conference on Optical Fiber Sensors**, Proc. SPIE 514 161-164 (1984).

Shultheis, L., "A Simple Fiber-Optic Fabry-Perot Temperature Sensor," in **Optical Fiber Sensors, 1988 Technical Digest Series**, Vol. 2, (Optical Society of America, Washington, D.C., 1988) pp. 506-509.

Shultheis, L., H. Amstutz, and M. Kaufmann, "Fiber-Optic Temperature Sensing With Ultrathin Silicon Etalons," Opt. Lett. 13, 782 (1988).

Siegman, A.E., **Lasers** (University Science Books, Mill Valley, California, 1986).

Snitzer, E., W.W. Morey and W.H. Glenn, "Fiber Optic Rare Earth Temperature Sensors," in **Optical Fiber Sensors**, IEE CP-221 (IEE, London, 1983) pp. 79-82.

Strausser, Y.E. and K.S. Majumder, "Abstract: Chemical Structure of the Al-SiO_2 Interface," J. Vac. Sci. Technol. 15, 238 (1978).

Sun, M., "Fiberoptic Thermometry Based on Photoluminescent Decay Times," in **Temperature: Its Measurement and Control in Science and Industry**, J.F. Schooley, ed., Vol. 6, Part 2, pp. 731-734 (American Institute of Physics, New York, 1992).

Sze, S.M., **Physics of Semiconductor Devices**, 2nd edition (John Wiley and Sons, New York, 1981).

Thornton, J.A., "Influence of Apparatus Geometry and Deposition Conditions on the Structure and Topography of Thick Sputtered Coatings," J. Vac. Sci. Technol. 11, 666 (1974).

Tilstra, S.D., "A Fluorescence-Based Fiber Optic Temperature Sensor for Aerospace Applications," in **Specialty Fiber Optic Systems for Mobile Platforms**, N.E. Lewis and E.L. Moore, eds., Proc. SPIE 1589, pp. 32-37 (1991).

Tregay, G.W., P.R. Calabrese, M.J. Finney, and K.B. Stukey, "Durable Fiber Optic Sensor for Gas Temperature Measurement in the Hot Section of Turbine Engines," in **Fly-by-Light**, E. Udd and D. Varyshneya, eds., Proc. SPIE 2295 (1995).

Tregay, G., P. Calabrese, P. Kaplin, and M. Finney, "Fiber Optic Sensor for Turbine Engine Gas Temperature from 600 to 1900 °C," NASA CR-187048 (1990).

van de Vaart, H, S.M. Emo, DM. Gualtieri, J. Hou, T.R. Kinney, and R.C. Morris, "Fringe Pattern Analysis of a Birefringent Modified Spectrum to Determine Environmental Temperature," US Patent #5255068 (1993).

Vasquez, R.P., A. Madhukar, and A.R. Tanguay, Jr., "Spectroscopic Ellipsometry and X-Ray Photoelectron Spectroscopy Studies of the Annealing Behavior of Amorphous Silicon Produced By Ion Implantation," J. Appl. Phys. 58, 2337 (1985).

Wakami, T. and S. Tanaka, "1.55 μm Long-Span Fiber-Optic Distributed Temperature Sensor," in **Tenth International Conference on Optical Fiber Sensors**, B. Culshaw and J.D.C. Jones, eds., Proc. SPIE 2360, pp. 134-137 (1994).

Wang, A., S. Gollapudi, K.A. Murphy, R.G. May, and R.O. Claus, "Saphire-Fiber-Based Intrinsic Fabry-Perot Interferometer," Opt. Lett. 17, 1021 (1992).

Wickersheim, K.A., "A New Fiberoptic Thermometry System for Use in Medical Hyperthermia," in **Optical Fibers in Medicine II**, A. Katzir, ed., Proc. SPIE 713, pp. 150-157 (1986).

Wittmer, M., "Barrier Layers: Principles and Applications in Microelectronics," J. Vac. Sci. Technol. A 2, 273 (1984).

Yeh, Y., C.E. Lee, R.A. Atkins, W.N. Gibler, and H.F. Taylor, "Fiber Optic Sensor for Substrate Temperature Monitoring," J. Vac. Sci. Technol. A 8, 3247 (1990).

Yoshino, T., K. Kurosawa, K. Itoh, and T. Oze, "Fiber-Optic Fabry-Perot Interferometer and Its Sensor Applications," IEEE J. Quantum. Electron. QE-18, 1624 (1982).

Zaka, Y., S.A. Abo-Namous, and R.W. Fane, "Control of Electrical and Optical Properties of Unhydrogenated Neon-Sputtered Amorphous Silicon by Preparation Conditions," Thin Solid Films 125, 47 (1985).

11. APPENDIX ON OPTICAL THEORY

11.1 Plane Wave Propagation in Homogeneous Media

Expressed in terms of the electric and magnetic field intensities, **E** and **H**, Maxwell's equations, for an isotropic medium which is nonconductive, nonmagnetic and charge-free, are

$$\nabla \cdot [(\varepsilon \varepsilon_0) \boldsymbol{E}] = 0, \tag{1}$$

$$\nabla \cdot \boldsymbol{H} = 0, \tag{2}$$

$$\nabla \times \boldsymbol{E} = -\mu_0 \frac{\partial \boldsymbol{H}}{\partial t}, \tag{3}$$

$$\nabla \times \boldsymbol{H} = \varepsilon \varepsilon_0 \frac{\partial \boldsymbol{E}}{\partial t}. \tag{4}$$

Here ε_0 and μ_0 are the permittivity and permeability of free space, and ε is the medium's relative permittivity or dielectric constant. In general, ε is complex with real part ε_1 and imaginary part ε_2.

After taking the curl of both sides of Eqs. 3 and 4, if one assumes that ε is uniform throughout the medium, one obtains the wave equations in **E** and **H**,

$$\nabla^2 \boldsymbol{E} = \frac{\varepsilon}{c^2} \frac{\partial^2 \boldsymbol{E}}{\partial t^2}, \tag{5}$$

$$\nabla^2 \boldsymbol{H} = \frac{\epsilon}{c^2} \frac{\partial^2 \boldsymbol{H}}{\partial t^2}. \tag{6}$$

The plane wave solution of these equations is given by

$$\boldsymbol{E}(\boldsymbol{r}, t) = \boldsymbol{E}_0 expj\left(\frac{\omega N}{c}\boldsymbol{u}\cdot\boldsymbol{r} - \omega t\right), \tag{7}$$

and

$$\boldsymbol{H}(\boldsymbol{r}, t) = \frac{N}{Z_0}\boldsymbol{u}\times\boldsymbol{E}_0 expj\left(\frac{\omega N}{c}\boldsymbol{u}\cdot\boldsymbol{r} - \omega t\right), \tag{8}$$

where **u** is the normalized propagation vector (i.e. $\mathbf{u}\cdot\mathbf{u} = 1$), which must be perpendicular to $\mathbf{E}_0$ (i.e. $\mathbf{u}\cdot\mathbf{E}_0 = 0$).

The speed of light in free space c is

$$c=\frac{1}{\sqrt{\varepsilon_0\mu_0}}, \tag{9}$$

and the impedance of free space Z_0 is

$$Z_0=\sqrt{\frac{\mu_0}{\varepsilon_0}}. \tag{10}$$

The medium's complex refractive index N is defined to be

$$N=\sqrt{\varepsilon}. \tag{11}$$

In general, N will vary as a function of ω. To emphasize its ω dependence, the relative permittivity ε is commonly designated the dielectric function. The real and imaginary parts of N are designated n and k, i.e. $N = n + jk$. The refractive index n determines the wave's phase velocity $v_p = c/n$, and the extinction coefficient k gives the absorption coefficient $\alpha = 4\pi k/\lambda$, where the wavelength in free space λ is equal to $2\pi c/\omega$.

From the definition of N,

$$\varepsilon_1 = n^2 - k^2, \tag{12}$$

and

$$\varepsilon_2 = 2nk. \tag{13}$$

The magnitude and direction of the wave's energy flux are given by the time-average Poynting vector,

$$\boldsymbol{S}_{av} = \frac{1}{2} Re\ \boldsymbol{E} \times \boldsymbol{H}^*, \tag{14}$$

and the wave's intensity, I, is simply the magnitude of $\mathbf{S}_{av}$.

In the case of a nonabsorptive medium, where k = 0, **u** is real and it is perpendicular to the planes of constant phase. For an absorptive medium that is entered at a normal angle of incidence, **u** is again real and it is perpendicular to the planes of constant amplitude and constant phase. If a plane wave enters an absorptive material at other than normal incidence, then **u** is complex, and in this case the normals to the planes of constant amplitude and constant phase are not necessarily coincident, as they are parallel to Re(N**u**) and Im(N**u**), respectively.

11.2 Reflection and Transmission at an Interface Between Two Materials

Consider a plane wave, incident on a medium of complex refractive index N_1 from a medium of index N_0, at an angle of θ_0 from the normal to the interface, as shown in Fig. 11.1. The xy plane is the plane of incidence and the x axis is perpendicular to the interface so that the incident wave's normalized propagation vector is given by

$$\boldsymbol{u}_i = \hat{\boldsymbol{x}}\cos\theta_0 + \hat{\boldsymbol{y}}\sin\theta_0 . \qquad (15)$$

Satisfaction of Maxwell's equations requires continuity of the tangential components of **E** and **H** across the interface. The reflected wave, therefore, must have a normalized propagation vector,

$$\boldsymbol{u}_r = -\hat{\boldsymbol{x}}\cos\theta_0 + \hat{\boldsymbol{y}}\sin\theta_0 . \qquad (16)$$

For the transmitted wave,

$$\boldsymbol{u}_t = \hat{\boldsymbol{x}}\cos\theta_1 + \hat{\boldsymbol{y}}\sin\theta_1, \tag{17}$$

where

$$N_1\sin\theta_1 = N_0\sin\theta_0. \tag{18}$$

This last equation is Fresnel's law of refraction. If $k_0 = 0$, then

$$N_1\boldsymbol{u}_t = \hat{\boldsymbol{x}}\sqrt{(n_1^2 - k_1^2 - n_o^2\sin^2\theta_0) + j2n_1k_1} + \hat{\boldsymbol{y}}\sin\theta_0. \tag{19}$$

Continuity of the tangential **E** and **H** components also determines the amplitude reflection and transmission coefficients, $r = E_{0r}/E_{0i}$ and $t = E_{0t}/E_{0i}$. The amplitudes of the reflected and transmitted waves are most readily determined if the incident wave's electric field vector $\mathbf{E}_0$ is decomposed into its components parallel and perpendicular to the plane of incidence. These eigenpolarization states, p and s, respectively, are maintained after reflection or transmission by the interface. The responses to an arbitrarily polarized input, therefore, can be obtained by superposition of the responses to the

input's p and s components. These are determined using Fresnel's amplitude coefficients,[1]

$$r_p = \frac{-N_1\cos\theta_0 + N_0\cos\theta_1}{N_1\cos\theta_0 + N_0\cos\theta_1}, \tag{20}$$

$$r_s = \frac{N_0\cos\theta_0 - N_1\cos\theta_1}{N_0\cos\theta_0 + N_1\cos\theta_1}, \tag{21}$$

$$t_p = \frac{2N_0\cos\theta_0}{N_1\cos\theta_0 + N_0\cos\theta_1}, \tag{22}$$

$$t_s = \frac{2N_0\cos\theta_0}{N_0\cos\theta_0 + N_1\cos\theta_1}. \tag{23}$$

11.3 Reflection From a Single Layer

Consider now the reflection of light from a Fabry-Perot interferometer, which, as shown in Fig. 11.2, is comprised of a single film having a thickness L and complex refractive index N_1. If the angle of incidence is θ_0, and the refractive indexes of the ambient and substrate are N_0 and N_2, respectively, then the amplitude reflectance of the film is[1]

$$\begin{aligned} r_F = r_{01} + t_{01} t_{10} r_{12} \exp(j2\Omega) \\ \times [1 + r_{10} r_{12} \exp(j2\Omega) + r_{10}^2 r_{12}^2 \exp(j4\Omega) + \ldots], \end{aligned} \tag{24}$$

where

$$\Omega = \frac{2\pi}{\lambda} N_1 L \cos\theta_1. \tag{25}$$

The angle of incidence inside the film, θ_1, is determined using Fresnel's law (θ_1 may be complex). The variables r_{ij} and t_{ij} are the Fresnel amplitude coefficients, for the appropriate polarization states, for a wave incident from medium i into medium j.

Using $r_{01} = -r_{10}$ and $t_{01}t_{10} = 1-r_{10}^2$, which follow from Eqs. 20-23, gives

$$r_F = \frac{-r_{10} + r_{12}\exp(j2\Omega)}{1 - r_{10}r_{12}\exp(j2\Omega)}. \tag{26}$$

The film's amplitude transmittance may be obtained by similar means, and is given by

$$t_F = \frac{t_{01}t_{12}\exp(j\Omega)}{1 - r_{10}r_{12}\exp(j2\Omega)}. \tag{27}$$

Consider first an ideal Fabry-Perot interferometer, which is both lossless and symmetric, so that all $k = 0$ and $n_2 = n_0$. If one also assumes that $n_1 > n_0$, then the phase change on internal reflection is zero and the reflectivity is given by

$$R_F = \frac{2R - 2R\cos(2\Phi)}{1 + R^2 - 2R\cos(2\Phi)}, \tag{28}$$

where

$$R = |r_{10}|^2, \tag{29}$$

and

$$\Phi = \frac{\pi}{\lambda}\Lambda_{OPD}. \tag{30}$$

Here, the interferometer's optical path difference or OPD is given by

$$\Lambda_{OPD} = 2n_1 L \ \cos\theta_1. \tag{31}$$

The reflectivity can be rewritten as

$$R_F = \frac{F\sin^2(\Phi)}{1 + F\sin^2(\Phi)}. \tag{32}$$

where

$$F = \frac{4R}{(1 - R)^2}. \tag{33}$$

The transmissivity of the ideal Fabry-Perot interferometer is given by

$$T_F = \frac{1}{1 + F\sin^2(\Phi)}. \tag{34}$$

As expected, for zero loss, $T_F + R_F = 1$. The reflectivity is a minimum, and the transmissivity a maximum, at the resonance condition, $\Phi = \pi m$, where m is an integer. The coefficient F determines the resonance width (finesse, $\pi/2\ F^{1/2}$, is a useful concept only for large R). A larger R narrows the reflectance minima, or fringes, as shown by Fig. 11.3, where $R_F(\Phi)$ is plotted for different values of R.

Consider now the reflectivity of an absorptive Fabry-Perot interferometer. The analysis is considerably simplified if $\theta_0 = 0$. Then,

$$R_F = \frac{|r_{10}|^2 + |r'_{12}|^2 - 2|r_{10}||r'_{12}|\cos(2\Phi - \phi_{10} + \phi_{12})}{1 + |r_{10}|^2|r'_{12}|^2 - 2|r_{10}||r'_{12}|\cos(2\Phi + \phi_{10} + \phi_{12})}. \tag{35}$$

Here, ϕ_{10} and ϕ_{12} are the phase changes on reflection, such that

$$r_{10} = |r_{10}|\exp(j\phi_{10}), \tag{36}$$

$$r_{12} = |r_{12}|\exp(j\phi_{12}), \tag{37}$$

and r'_{12} is the apparent amplitude reflectivity of the film's second surface when viewed from the first surface, i.e.

$$r'_{12} = r_{12}\exp(-\alpha_1 L). \tag{38}$$

The absorption coefficient of the resonator material is given by $\alpha_1 = 4\pi k_1/\lambda$.

The transmissivity of the absorptive Fabry-Perot interferometer, for normal incidence, is

$$T_F = \frac{|N_2/N_0|\,|t_{01}|^2|t_{12}|^2\exp(-\alpha_1 L)}{1+|r_{10}|^2|r'_{12}|^2-2|r_{10}|\,|r'_{12}|\cos(2\Phi+\phi_{10}+\phi_{12})}. \tag{39}$$

Assume that α_1 is independent of λ, then $T_F(\lambda)$ is a minimum when the resonance condition is satisfied, i.e. $\Phi = \Phi_m$, where m is an integer and

$$2\Phi_m + \phi_{10} + \phi_{12} = 2\pi m. \tag{40}$$

The reflectivity R_F, on the other hand, is a minimum at precisely $\Phi = \Phi_m$ only if $\phi_{10} = 0$ or π. This is caused by the difference in the signs associated with ϕ_{10} in the numerator and denominator of Eq. 35. For the Fabry-Perot temperature sensor, ϕ_{10} is small, and it has little effect on the positions of the minima of $R_F(\lambda)$. For a silicon film in an SiO_2 ambient, ϕ_{10} is only 1.3 mrad at $\lambda = 830$ nm. In practice, α_1 will vary as a function of λ, which will cause the minima of both $R_F(\lambda)$ and $T_F(\lambda)$ to be shifted off-resonance. Since there is no direct means of measuring Φ, the somewhat imprecise practice will be adopted here of equating resonance with the minima in $R_F(\Phi)$.

11.4 Reflection From a Multilayer Stack of Films

The reflectivity of a multilayer stack of films can be calculated by starting with the last film and repeatedly applying the equation for the amplitude reflectance of a single film (Eq. 26). A method that is generally more satisfactory is attributed to Abelès and described in the book by Heavens.[2] This matrix method is widely used to design optical interference filters. As shown in Fig. 11.4, the multilayer structure consists of n films plus the ambient (or superstrate), which is designated layer 0, and the substrate, which is layer n+1. The electric field in layer m, which is either p- or s-polarized, is the sum of a forward (+) and a backward (-) traveling wave, i.e.

$$\begin{aligned} E &= E_m^{+}\exp[j\chi_m(z-c_m)] \\ &\quad + E_m^{-}\exp[-j\chi_m(z-c_m)], \end{aligned} \tag{41}$$

where the time dependence has been suppressed, and

$$\chi_m = \frac{2\pi}{\lambda} N_m \cos\theta_m, \tag{42}$$

and

$$c_m = \sum_{k=0}^{m-1} L_k, \tag{43}$$

where L_0 is defined to be 0.

At the interface between the ambient and the first film, continuity of the tangential E and H components requires

$$E_1^+ = t_{01} E_0^+ + r_{10} E_1^-, \tag{44}$$

$$E_0^- = r_{01} E_0^+ + t_{10} E_1^-. \tag{45}$$

Continuity at the interface between layers m-1 and m gives the more general result,

$$E_m^+ = t_{m-1,m}\exp(j\Omega_{m-1})E_{m-1}^+ + r_{m,m-1}E_m^-, \tag{46}$$

$$\exp(-j\Omega_{m-1})E_{m-1}^- = r_{m-1,m}\exp(j\Omega_{m-1})E_{m-1}^+ + t_{m,m-1}E_m^-, \tag{47}$$

where

$$\Omega_m = \chi_m L_m. \tag{48}$$

To conform to Heavens' nomenclature, $r_{m-1,m}$ is replaced with r_m and $t_{m-1,m}$ with t_m. The relationships $r_{m,m-1} = -r_m$ and $t_{m,m-1} = (1-r_m^2)/t_m$ are then used to give

$$E_{m-1}^{+} = \frac{1}{t_m}\exp(-j\Omega_{m-1})E_m^{+} + \frac{r_m}{t_m}\exp(-j\Omega_{m-1})E_m^{-}, \tag{49}$$

and

$$E_{m-1}^{-} = \frac{r_m}{t_m}\exp(j\Omega_{m-1})E_m^{+} + \frac{1}{t_m}\exp(j\Omega_{m-1})E_m^{-}. \tag{50}$$

Repeated application of these equations gives

$$\begin{pmatrix} E_0^+ \\ E_0^- \end{pmatrix} = \frac{(C_1)(C_2)\ \dots\ (C_{n+1})}{t_1 t_2\ \dots\ t_{n+1}} \begin{pmatrix} E_{n+1}^+ \\ E_{n+1}^- \end{pmatrix}, \tag{51}$$

where

$$(C_m) = \begin{pmatrix} \exp(-j\Omega_{m-1}) & r_m \exp(-j\Omega_{m-1}) \\ r_m \exp(j\Omega_{m-1}) & \exp(j\Omega_{m-1}) \end{pmatrix}. \tag{52}$$

If the matrix product has elements a, b, c, d, such that

$$\begin{pmatrix} a & b \\ c & d \end{pmatrix} = (C_1)(C_2)\ \dots\ (C_{n+1}), \tag{53}$$

then, since $E^-_{n+1} = 0$,

$$\frac{E_0^-}{E_0^+} = \frac{c}{a}. \tag{54}$$

In addition,

$$\frac{E_{n+1}^{+}}{E_{0}^{+}}=\frac{t_1 t_2 \ldots t_{n+1}}{a}. \tag{55}$$

The reflectivity of the multilayer stack is then given by

$$R_F=\left|\frac{c}{a}\right|^2, \tag{56}$$

and the transmissivity is

$$T_F=\left|\frac{N_{n+1}}{N_0}\right|\left|\frac{t_1 t_2 \ldots t_{n+1}}{a}\right|^2. \tag{57}$$

11.5 Basic Ellipsometric Relations

A spectroscopic ellipsometer measures two parameters, ψ and Δ, as functions of wavelength, at an angle of incidence θ_0. The real values of ψ and Δ are related to the amplitude reflection coefficients of the sample by

$$\frac{r_p}{r_s} = \tan(\psi)\exp(j\Delta). \tag{58}$$

In the case of a multilayer stack of films, the amplitude reflection coefficients r_p and r_s can be determined using Eq. 54. A useful ellipsometric parameter is the pseudodielectric function $<\varepsilon>$ which is given by

$$\begin{aligned} <\varepsilon> &= \sin^2\theta_0 \\ &+ \sin^2\theta_0 \tan^2\theta_0 \, [(1-\rho)/(1+\rho)]^2, \end{aligned} \tag{59}$$

where

$$\rho = \tan(\psi)\exp(j\Delta). \tag{60}$$

The pseudodielectric function, which has real and imaginary parts $<\varepsilon_1>$ and $<\varepsilon_2>$, is the dielectric function of a hypothetical substrate, the analysis of which would provide the measured values of ψ and Δ.

11.6 Effective Medium Theory

It is sometimes necessary to determine the optical properties of heterogeneous mixtures of materials. For instance, the dielectric function of a thin film typically differs from that of the bulk material due to highly deposition-dependent defects such as voids and impurities. The dielectric functions of such films can be determined by modeling the films as mixtures of the composite materials and voids using the effective medium theory.[3]

Consider an inhomogeneous material which is comprised of a host medium, with a (complex) dielectric function ε_H, into which are embedded grains of a material with a dielectric function of ε_A. The fraction by volume of the embedded material is f_A. The embedded grains are assumed to be small compared to the optical wavelength, i.e. less than about 0.1λ, yet not so small that the grains no longer retain the dielectric response of the bulk material. The ε_A grains are modeled as uniformly sized spheres, each of which has a volume of V, so that the number of these spheres per unit volume is f_A/V.

In order to determine the material's macroscopic dielectric function ε_M, assume that an electric field is applied which produces, in the absence of the

ε_A spheres, a uniform field of $\mathbf{E}_0$ in the host medium. The effect of embedding one ε_A sphere in the host will be analyzed first. The polarization inside this sphere is uniform and is given by[4]

$$\boldsymbol{P}_A = 3\varepsilon_H \varepsilon_0 \frac{\varepsilon_A - \varepsilon_H}{\varepsilon_A + 2\varepsilon_H} \boldsymbol{E}_0. \tag{61}$$

Outside the sphere, the electric field is equal to $\mathbf{E}_0$ plus the field produced by an electric dipole of moment $\mathbf{P}_A V$. The dipole's contribution to the average electric field in the host medium is equal to $-\mathbf{P}_A V/(3\varepsilon_H \varepsilon_0)$. This result is obtained by integrating the dipole field over a large spherical volume containing the ϵ_A microsphere.[4]

If the host medium is then filled, to a volume fraction of f_A, with randomly positioned ε_A spheres, then the average electric field is given by

$$\boldsymbol{E} = \boldsymbol{E}_0 - \frac{f_A \boldsymbol{P}_A}{3\varepsilon_H \varepsilon_0}. \tag{62}$$

Also, since the average polarization in the material is $f_A P_A$,

$$(\varepsilon_M - \varepsilon_H)\varepsilon_0 E = f_A P_A. \tag{63}$$

The preceding three equations can be combined to determine ε_M, the dielectric function of the inhomogeneous medium, which is given by

$$\frac{\varepsilon_M - \varepsilon_H}{\varepsilon_M + 2\varepsilon_H} = f_A \frac{\varepsilon_A - \varepsilon_H}{\varepsilon_A + 2\varepsilon_H}. \tag{64}$$

This equation is known as the Maxwell-Garnett effective medium expression. If the host medium is vacuum, then $\varepsilon_H = 1$, so that the Maxwell-Garnett expression indicates that $(\varepsilon_M - 1)/(\varepsilon_M + 2)$ should be proportional to the material's density, which is the Clausius-Mosotti result.

Now consider a heterogenous material comprised of grains of two materials which are randomly mixed. To analyze this mixture of materials A and B, spheres having dielectric functions of ε_A and ε_B are embedded in the host medium, with volume fractions of f_A and f_B. In this case, the embedded materials fill the entire volume so that $f_B = 1 - f_A$. Voids may be modeled as

grains with unity dielectric constant. The previously described method of analysis gives

$$\frac{N_M^2-N_H^2}{N_M^2+2N_H^2}=f_A\frac{N_A^2-N_H^2}{N_A^2+2N_H^2}+f_B\frac{N_B^2-N_H^2}{N_B^2+2N_H^2}, \tag{65}$$

where the dielectric functions have been replaced by the squares of the complex refractive indexes. A self-consistent choice is now made for the host medium, i.e. $N_H = N_M$, which gives the Bruggeman effective medium approximation or EMA, which is

$$0=f_A\frac{N_A^2-N_M^2}{N_A^2+2N_M^2}+f_B\frac{N_B^2-N_M^2}{N_B^2+2N_M^2}. \tag{66}$$

It is this two-component Bruggemann EMA, and its generalization to three components, which is used here to model the dielectric responses of the sputter-deposited films.

11.7 References

1. M. Born and E. Wolf, **Principles of Optics** (Pergammon Press, London, 1959).

2. O.S. Heavens, **Optical Properties of Thin Solid Films** (Dover Publications, New York, 1965).

3. D.E. Aspnes, "Optical Properties of Thin Films," Thin Solid Films 89, 249 (1982).

4. J.D. Jackson, **Classical Electrodynamics**, 2nd Edition (John Wiley & Sons, New York, 1975) pp. 147-152.

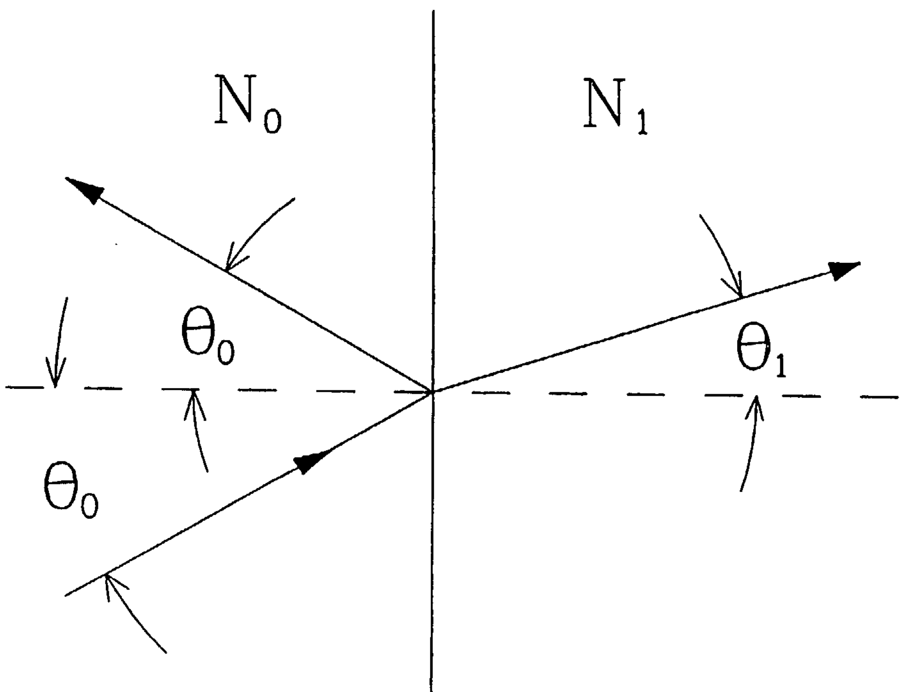

Figure 11.1 Transmission and reflection at an interface between two materials with complex refractive indexes N_0 and N_1.

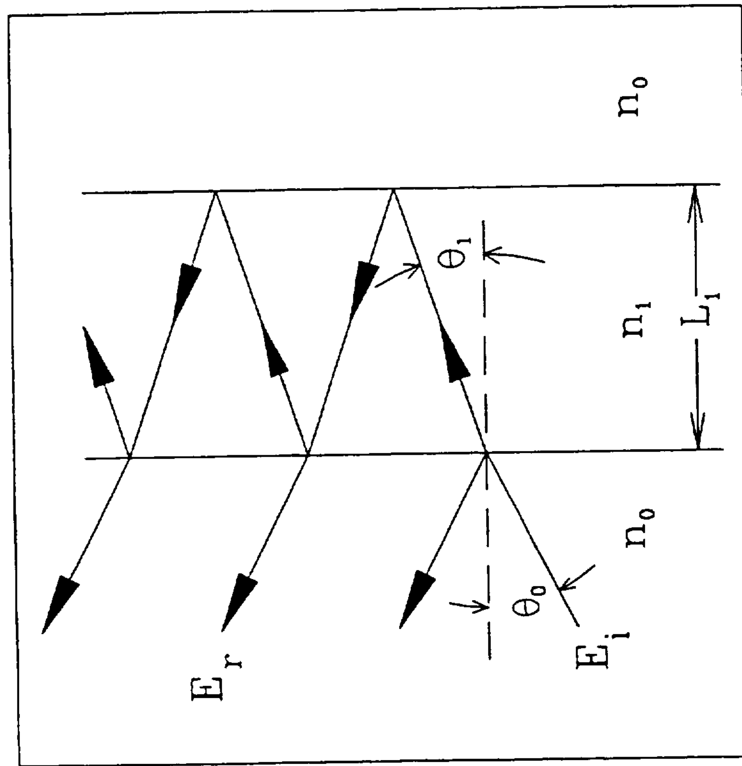

Figure 11.2 Transmission and reflection from a single film.

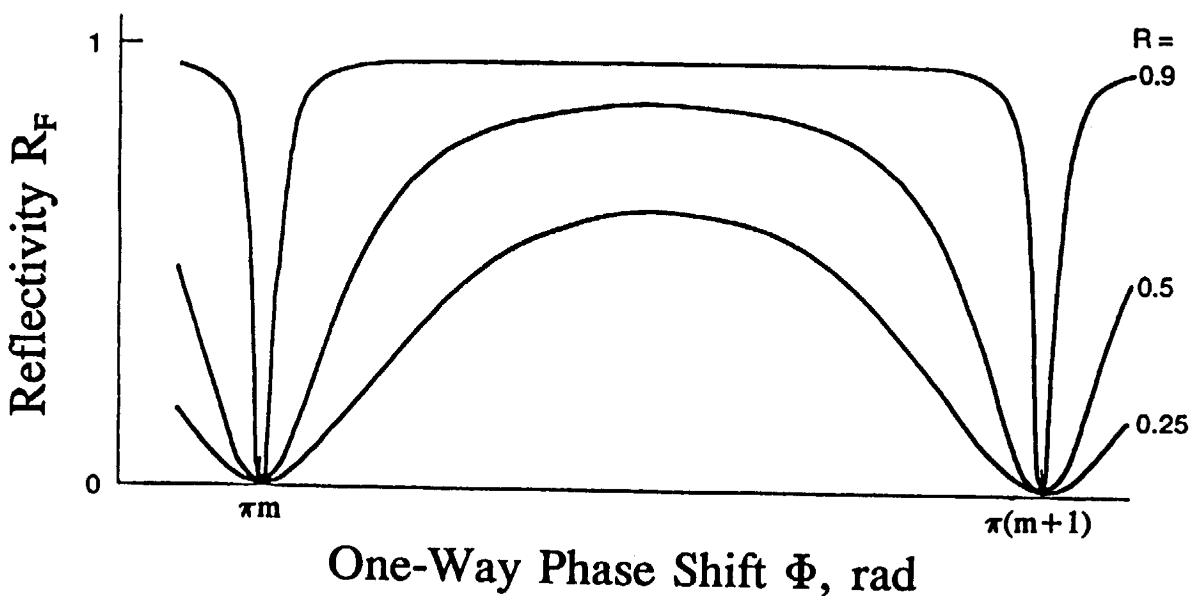

Figure 11.3 Reflectivities R_F of ideal Fabry-Perot interferometers as functions of the one-way phase shift Φ, for different mirror reflectivities R.

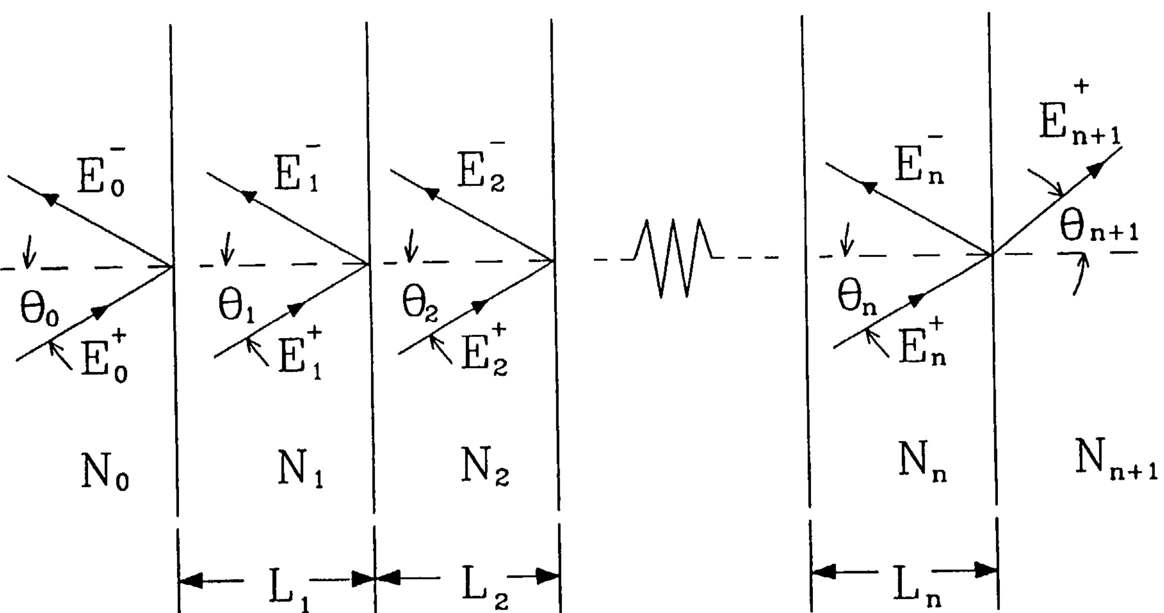

Figure 11.4 Transmission and reflection from a multilayer stack.

REPORT DOCUMENTATION PAGE

Form Approved
OMB No. 0704-0188

Public reporting burden for this collection of information is estimated to average 1 hour per response, including the time for reviewing instructions, searching existing data sources, gathering and maintaining the data needed, and completing and reviewing the collection of information. Send comments regarding this burden estimate or any other aspect of this collection of information, including suggestions for reducing this burden, to Washington Headquarters Services, Directorate for Information Operations and Reports, 1215 Jefferson Davis Highway, Suite 1204, Arlington, VA 22202-4302, and to the Office of Management and Budget, Paperwork Reduction Project (0704-0188), Washington, DC 20503.

1. AGENCY USE ONLY (*Leave blank*)	2. REPORT DATE	3. REPORT TYPE AND DATES COVERED
	May 1997	Technical Memorandum

4. TITLE AND SUBTITLE

Fiber-Optic Temperature Sensor Using a Thin-Film Fabry-Perot Interferometer

5. FUNDING NUMBERS

WU–523–21–13

6. AUTHOR(S)

Glenn Beheim

7. PERFORMING ORGANIZATION NAME(S) AND ADDRESS(ES)

National Aeronautics and Space Administration
Lewis Research Center
Cleveland, Ohio 44135–3191

8. PERFORMING ORGANIZATION REPORT NUMBER

E–10745

9. SPONSORING/MONITORING AGENCY NAME(S) AND ADDRESS(ES)

National Aeronautics and Space Administration
Washington, DC 20546–0001

10. SPONSORING/MONITORING AGENCY REPORT NUMBER

NASA TM–107459

11. SUPPLEMENTARY NOTES

This report was submitted as a dissertation in partial fulfillment of the requirements for the degree Doctor of Philosophy to Case Western Reserve University, Cleveland, Ohio, May 1996. Responsible person, Glenn Beheim, organization code 5510, (216) 433–3847.

12a. DISTRIBUTION/AVAILABILITY STATEMENT

Unclassified - Unlimited
Subject Category 35

This publication is available from the NASA Center for AeroSpace Information, (301) 621–0390.

12b. DISTRIBUTION CODE

13. ABSTRACT *(Maximum 200 words)*

A fiber-optic temperature sensor was developed that is rugged, compact, stable, and can be inexpensively fabricated. This thin-film interferometric temperature sensor was shown to be capable of providing a ±2 °C accuracy over the range of -55 to 275 °C, throughout a 5000 hr operating life. A temperature-sensitive thin-film Fabry-Perot interferometer can be deposited directly onto the end of a multimode optical fiber. This batch-fabricatable sensor can be manufactured at a much lower cost than can a presently available sensor, which requires the mechanical attachment of a Fabry-Perot interferometer to a fiber. The principal disadvantage of the thin-film sensor is its inherent instability, due to the low processing temperatures that must be used to prevent degradation of the optical fiber's buffer coating. The design of the stable thin-film temperature sensor considered the potential sources of both short and long term drifts. The temperature-sensitive Fabry-Perot interferometer was a silicon film with a thickness of ~2 µm. A laser-annealing process was developed which crystallized the silicon film without damaging the optical fiber. The silicon film was encapsulated with a thin layer of Si_3N_4 overcoated with aluminum. Crystallization of the silicon and its encapsulation with a highly stable, impermeable thin-film structure were essential steps in producing a sensor with the required long-term stability.

14. SUBJECT TERMS

Temperature sensors; Fiber-optic sensors

15. NUMBER OF PAGES

388

16. PRICE CODE

A17

17. SECURITY CLASSIFICATION OF REPORT	18. SECURITY CLASSIFICATION OF THIS PAGE	19. SECURITY CLASSIFICATION OF ABSTRACT	20. LIMITATION OF ABSTRACT
Unclassified	Unclassified	Unclassified	

NSN 7540-01-280-5500

Standard Form 298 (Rev. 2-89)
Prescribed by ANSI Std. Z39-18
298-102